

Final Technical Report
Grant N00014-93-1-G013
UW 144-DK48

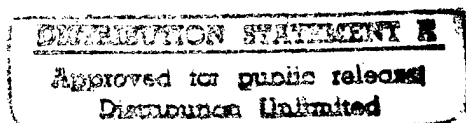
**The Measurement of Cirrus Cloud Structure
and Optical Properties with a High Spectral
Resolution Lidar and a Volume Imaging Lidar**

E. W. Eloranta
Principal Investigator

University of Wisconsin
Space Science and Engineering Center
1225 W. Dayton St.
Madison, Wis
Tel (608)-262-7327

Bill Hoppel, ONR Program Manager

September 7, 1997



THIS QUALITY INSPECTED 2

19970918 080

1 Introduction

Scientific progress achieved under the support of this research grant has been reported in a series of conference presentations, student thesis and published papers. Copies of these documents comprise the body of this report.

2 Journal Papers

- Piironen, P., and E. Eloranta, 1994: Demonstration of an iodine absorption filter based high spectral resolution lidar, *Optics Letters*, **19** pp 234-236
- Ackerman, S., E. Eloranta, C. Grund, R. Knuteson, H. Revercomb, W. Smith, and D. Wylie, 1993: University of Wisconsin Cirrus Remote Sensing Experiment, *Bulletin of the American Meteorological Society*, **74**, pp 1041-1049.

3 Phd and Masters Thesis

- Piironen, P., 1994: A High Spectral Resolution Lidar Based on an Iodine Absorption Filter, *University of Joensuu, PhD thesis*, Joensuu, Finland pp 113
- DeSlover, D. H., 1996: Analysis of visible and infrared cirrus cloud optical Properties using high spectral resolution remote sensing, *University of Wisconsin-Madison MS thesis*, Madison, Wisconsin, pp 93

4 Conference Presentations

- Eloranta, E. W. and P. Piironen, *Statistics on the optical properties of cirrus clouds measured with the high spectral resolution lidar*, Cloud Impacts on Defense Systems and Operations Conference, Bedford, MA. October 24-26, 1995.
- Eloranta, E. W. and P. Piironen, *An error analysis for high spectral resolution lidar measurements*, Presented at the Optical Society of America topical meeting on Remote Sensing of the Atmosphere, February, 1995, Salt Lake City, NV.
- Eloranta, E. W. and P. Piironen, *Depolarization measurements with the high spectral resolution lidar*, Seventeenth International Laser Radar Conference, Sendai, Japan, 1994.
- Eloranta, E. W. and P. Piironen, *High spectral resolution lidar measurements of particle size*, 7th International Workshop on Multiple Scattering, Ciba, Japan July 21-23, 1994.

- Eloranta, E. W. and P. Piironen, *Remote Particle size measurements with the University of Wisconsin high spectral resolution lidar*, Presented at the annual meeting of the American Meteorological Society, Jan 1994, Nashville, TN.
- Wylie, D., W. Wolf and E.W. Eloranta, *Visible and infrared radiative relationships as measured by satellite and lidar*, 1994 annual meeting of the American Meteorological Society, Jan 1994, Nashville, TN.
- Eloranta, E.W. and P. Piironen, *An I_2 absorption filter based high spectral resolution lidar for measurement of the optical properties of aerosols and clouds*, invited paper, SPIE Atmospheric Propagation III meeting, April 1994, Orlando, FL.
- Eloranta, E. W. *A Practical Model for the Calculation of Multiply Scattered Lidar Returns*. Presented at the Optical Society of America topical meeting on Remote Sensing of the Atmosphere, March 1993, Salt Lake City, NV.
- Piironen, P, and E.W. Eloranta, *Initial Data from a New High Spectral Resolution Lidar* Presented at the Optical Society of America topical meeting on Remote Sensing of the Atmosphere. March 1993, Salt Lake City, NV.
- Eloranta, E. W. and P. Piironen, *Adaptation of the University of Wisconsin High Spectral Resolution Lidar for Use in the ARM Program*. Presented at the Annual Meeting of the American Meteorological Society, January 1993, Anaheim, CA.

Demonstration of a high-spectral-resolution lidar based on an iodine absorption filter

P. Piironen and E. W. Eloranta

Department of Atmospheric and Oceanic Sciences, University of Wisconsin, 1225 West Dayton Street, Madison, Wisconsin 53706

Received September 7, 1993

A high-spectral-resolution lidar that uses an iodine absorption filter and a tunable, narrow-bandwidth Nd:YAG laser is demonstrated. Measurements of aerosol scattering cross section and optical depth are presented. The iodine absorption filter provides better performance than the Fabry-Perot étalon that it replaces.

The University of Wisconsin high-spectral-resolution lidar (HSRL) measures optical properties of the atmosphere by separating the Doppler-broadened molecular backscatter return from the unbroadened aerosol return.¹ The molecular signal is then used as a calibration target that is available at each point in the lidar profile. This calibration permits unambiguous measurements of aerosol scattering cross section and optical depth. The HSRL employs a Fabry-Perot étalon with a 0.5-pm bandpass to separate the aerosol and molecular scattering.

The HSRL based on the Fabry-Perot étalon produces accurate measurements of clear air, thin cirrus, and stratospheric aerosols. However, when this system is used to probe dense water clouds, the detected aerosol signal in the molecular channel becomes of the order of 10^3 larger than the molecular return. Therefore the inversion coefficients used to separate the aerosol and molecular signals must be known with better than 0.01% accuracy; otherwise some of the aerosol return will appear in the separated molecular return. Since the inversion coefficients for the étalon-based system are known with only 0.1% accuracy, the measurements of dense water clouds are subject to error. For a reduction in the required calibration precision, a filter is required that provides greater rejection of the aerosol signal in the molecular channel.

The performance of a Fabry-Perot étalon is limited by its finesse and the angular distribution of incoming light. The étalon is operated in a pressure- and temperature-controlled environment, since keeping the filter performance stable requires a better than 0.1-mbar pressure tuning accuracy and a 0.1 °C temperature stability.

Shimizu *et al.*² proposed the use of a narrow-band atomic absorption filter in a HSRL, and She *et al.*³ reported HSRL measurements of the temperature and the aerosol extinction coefficient with a barium atomic absorption filter. These studies have shown that an absorption filter can offer high rejection against aerosol scattering and therefore make the separation between molecular and aerosol scattering easier. Another advantage of an absorption filter is the stability of the absorption characteristics.² Furthermore, the transmission characteristics of a molecular absorption filter are not dependent on the

mechanical alignment of the filter² or the angular dependence of the incoming light. Also, a wide dynamic range in rejection against aerosol scattering is achieved by a simple change in the vapor pressure² or the length of the cell.

In this Letter we present what are to our knowledge the first results from a HSRL that uses an iodine absorption filter. The advantage of iodine compared with barium is that instead of a dye laser's being required, a narrow-bandwidth, frequency-doubled Nd:YAG laser can be used. Also, strong absorption is obtained in a short cell at room temperature. Even though iodine has extensive hyperfine structure, the absorption linewidth is similar to the barium linewidth, which is broadened by operation at a temperature of ~500 °C.

Iodine has many absorption peaks; eight of them are easily reached by thermal tuning of a frequency-doubled Nd:YAG laser.⁴ Our HSRL uses a continuously pumped, Q-switched, injection-seeded, frequency-doubled Nd:YAG laser operating at a 4-kHz pulse repetition rate.⁵ The frequency-doubled output is tunable over a 124-GHz frequency range by temperature tuning of the seed laser under computer control.

We measure the iodine spectrum by scanning the laser wavelength. A small amount of laser light is directed into a 100-m-long fiber-optic delay (Fiber 1 in Fig. 1) and sent to the receiver to create a calibration light source. Since some of the laser shots are unseeded, the delay is necessary so that the measured Q-switch buildup time of each pulse can be used as a quality control to trigger the data system to record only seeded pulses. We calibrate the absorption spectrum by simultaneously measuring the signal reflected from the high-spectral-resolution étalon (Fig. 1) and the signal transmitted through the absorption cell. The pressure in the étalon is held constant while the laser wavelength is scanned. The free spectral range of the étalon is used to define the temperature-wavelength dependence of the scan. The measured spectrum has been compared with a published spectrum,⁶ and an ~0.01-pm wavelength agreement in relative line positions was observed. The measured iodine spectrum is presented in Fig. 2.

The receiver is shown in Fig. 3. The system is a combined interferometer-molecular absorption lidar,

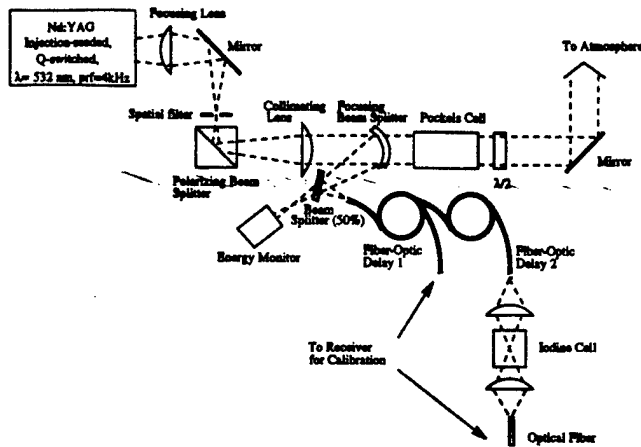


Fig. 1. HSRL transmitter. A sample of each transmitted pulse is directed to a pair of optical fibers, delayed, and injected back to the receiver for system calibrations. The length of the fibers is set so that the time-separated pulses can be recorded into the data profile. A 4-cm-long iodine cell is used for frequency locking the laser: the seed laser temperature is dithered, and by maximization of the ratio between the first and the second calibration fiber signal the laser output is locked to the center of the absorption peak.

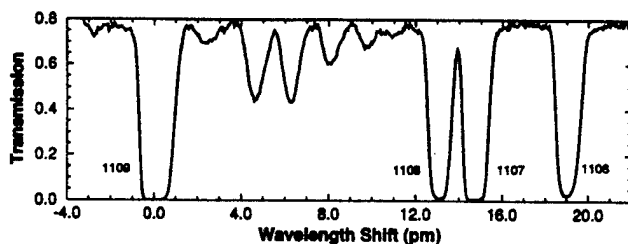


Fig. 2. Transmission of the 43-cm iodine cell as a function of wavelength shift. The identification line numbers are from Ref. 6.

which can be used in either mode. When the iodine absorption cell is used, one can use the high-resolution étalon as a reflector by pressure tuning it out from the transmission peak. When the high-resolution étalon is used, we disconnect the iodine cell by simply removing the beam splitter and the last turning mirror (mirror 4).

For initial HSRL measurements line 1109 (Ref. 6; peak wavelength 532.26 nm), which is well isolated from the neighboring lines, was chosen. The narrower line 1106 would be a better candidate, but it is located close to a mode hop of the seed laser. For the first HSRL measurements a 43-cm-long cell was made. The cell with iodine crystals in a side arm was evacuated and kept at 27 °C.

A comparison between high-resolution étalon performance and iodine absorption filter performance is presented in Fig. 4. For the aerosol backscatterer a 2:1 separation between channels by the étalon [Fig. 4(b)] is measured, compared with a 1000:1 separation in the iodine cell when it is operated at 27 °C [Fig. 4(a)]. The determination of the system calibration for the amount of detected aerosol backscatterer is limited by the photon-counting statistics. With the current calibration for the iodine-absorption-based system the effective aerosol

rejection in the inverted molecular profile is $\sim 1:5000$. With an improved calibration procedure, currently in progress, the determination accuracy of system calibration coefficients is expected to be improved. The molecular transmission in Figs. 4(a) and 4(b)

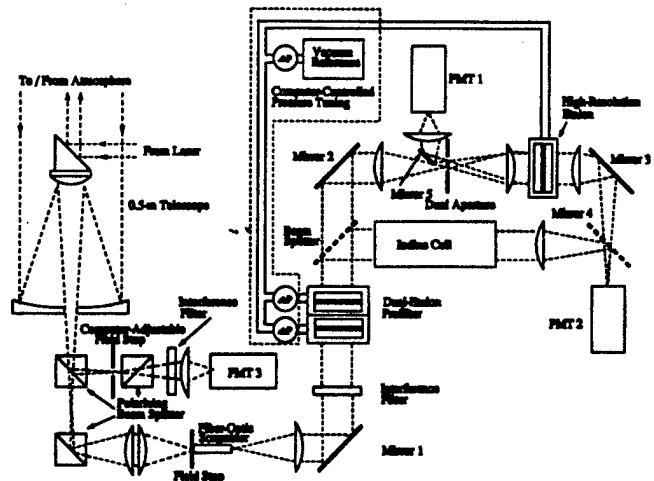


Fig. 3. HSRL receiver. The received backscatter signal is prefiltered for the background with an interference filter and a low-resolution étalon pair before being directed into a beam splitter. The signal detected with photomultiplier tube PMT1 contains the information about the total aerosol and molecular backscatter signal. The signal directed through the iodine cell and detected by photomultiplier tube PMT2 is a combination of the amount of aerosol backscatter signal that passes through the absorption cells and the wings of the molecular backscatter signal.

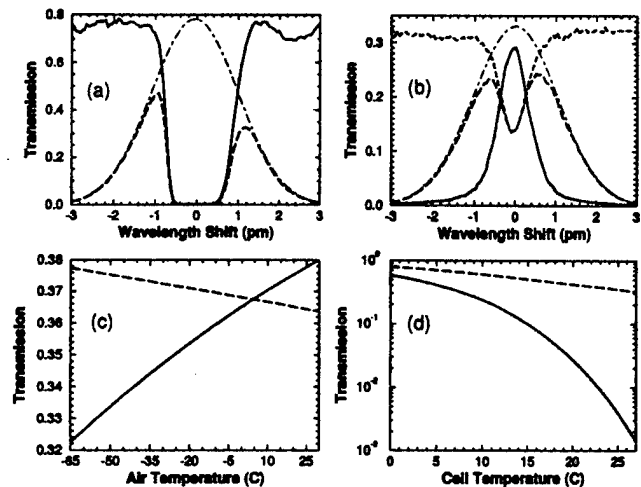


Fig. 4. (a) Transmission of a 43-cm cell (solid curve) together with the molecular transmission (dashed curve) at -65°C air temperature as a function of wavelength shift. The dashed-dotted curve shows the calculated molecular spectrum at -65°C . (b) Étalon transmission (solid curve), reflection (dashed curve) and calculated molecular transmission of the molecular channel (PMT1) (long-dashed curve) as a function of wavelength shift. The dashed-dotted curve shows the calculated molecular spectrum at -65°C . (c) Comparison of the molecular transmission of the molecular channel (PMT1) (dashed curve) and the iodine cell (solid curve) as a function of air temperature. (d) Iodine cell aerosol (solid curve) and molecular (dashed curve) transmission as a function of cell temperature.

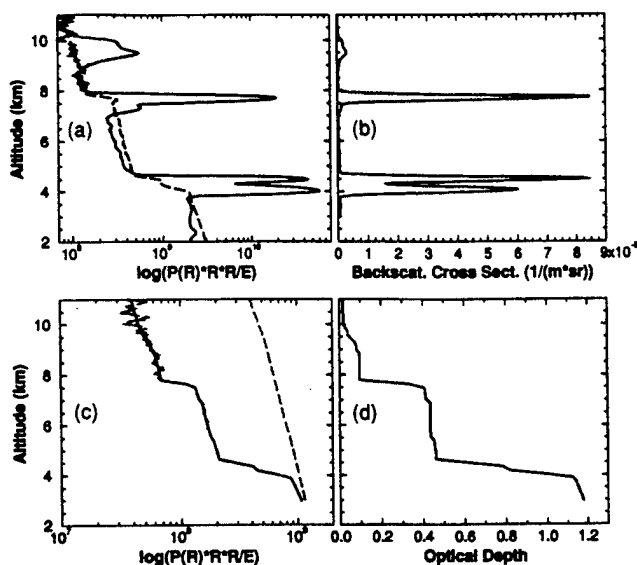


Fig. 5. HSRL Measurements obtained on July 21, 1993. (a) Signals detected with PMT1 (solid curve) and PMT2 (dashed curve). (b) Aerosol backscatter cross section. (c) A constrained nonlinear regression fit (solid curve) to the inverted molecular signal (dashed curve at left) together with the calculated clear air molecular return (dashed curve at right). (d) Optical depth through the cloud layers.

is calculated by the Doppler-broadened molecular spectrum at -65°C . This temperature is close to the lowest temperature measured at the tropopause. The molecular transmissions of the high-resolution étalon and the iodine absorption filter are similar [Fig. 4(c)]. Owing to a wide absorption linewidth, the molecular transmission of the iodine filter is more dependent on the air temperature than is the étalon. The temperature dependence of the cell transmission is modeled by the table values of iodine vapor pressure⁷ [Fig. 4(d)]. By changing the cell temperature from 27 to 0°C , we can tune on-line transmission from 0.08% to 60%.

Figure 5 shows an example from data obtained on July 21, 1993, with the iodine-absorption-filter-based HSRL. A multilayer water cloud structure together with a cirrus cloud at 9 km is shown. The signal measured by photomultiplier tube PMT1 contains information about the total aerosol and molecular scattering. The signal measured by photomultiplier

tube PMT2 shows the molecular return. Notice that only a small aerosol cross talk in the raw molecular signal is visible at the densest parts of the clouds. This is easily removed by the inversion. The measured signals show the large dynamic range achieved in HSRL measurements. The aerosol backscatter cross section [Fig. 5(b)] is obtained from the aerosol-to-molecular-backscatter ratio and an estimate of the atmospheric gas-density profile measured by a radiosonde.

The optical depth is obtained from the ratio of the inverted molecular return to the return predicted for pure molecular scattering. The inverted molecular signal together with the fitted signal is shown in Fig. 5(c). Figure 5(d) shows that an optical depth of 1.2 is measured through the layer. Because the cross talk between channels can be accurately corrected and because the $160\text{-}\mu\text{rad}$ field of view of the HSRL effectively suppresses multiple scattering, the optical depths inside a cloud can be measured. Our first measurements with the iodine-absorption-based HSRL have been so successful that we no longer use the high-resolution étalon.

This study was supported by the Naval Research Laboratory, U.S. Department of the Navy, under grant N00014-93-1-G013 and by the University of Joensuu, Finland.

References

1. S. T. Shipley, D. H. Tracy, E. W. Eloranta, J. T. Trauger, J. T. Sroga, F. L. Roesler, and J. A. Weinman, *Appl. Opt.* **22**, 3716 (1983).
2. H. Shimizu, S. A. Lee, and C. Y. She, *Appl. Opt.* **22**, 3716 (1983).
3. C. Y. She, R. J. Alvarez II, L. M. Caldwell, and D. A. Krueger, *Opt. Lett.* **17**, 541 (1992).
4. J. A. Harrison, M. Zahedi, and J. W. Nibler, *Opt. Lett.* **18**, 149 (1993).
5. C. J. Grund and E. W. Eloranta, *Opt. Eng.* **30**, 6 (1991).
6. S. Gerstenkorn and P. Luc, *Atlas du spectre d'absorption de la molécule d'iode* (Centre National de la Recherche Scientifique, Paris, 1978).
7. A. Das, M. Frenkel, N. M. Gadalla, K. N. Marsh, and R. C. Wilhout, *TRC Thermodynamic Tables (Non-hydrocarbons)* (Thermodynamic Research Center, Texas A&M University, College Station, Tex., 1986), pp. k-190, ka-190.

University of Wisconsin Cirrus Remote Sensing Pilot Experiment

Steven A. Ackerman,*
Ed W. Eloranta,**
Chris J. Grund,+
Robert O. Knuteson,++
Henry E. Revercomb,++
William L. Smith,* and
Donald P. Wylie++

Abstract

During the period of 26 October 1989 through 6 December 1989 a unique complement of measurements was made at the University of Wisconsin—Madison to study the radiative properties of cirrus clouds. Simultaneous observations were obtained from a scanning lidar, two interferometers, a high spectral resolution lidar, geostationary and polar orbiting satellites, radiosonde launches, and a whole-sky imager. This paper describes the experiment, the instruments deployed, and, as an example, the data collected during one day of the experiment.

1. Introduction

Uncertainties in model predictions of the climate response to increased greenhouse gas concentrations are largely due to inadequate parameterization of clouds and cloud–climate feedbacks (Cess et al. 1989). Clouds affect climate by exerting a strong influence on radiative heating and cooling distribution within the atmosphere and at the earth's surface. There is an urgent need for measurements that guide and verify for the development of improved methods of treating cloud radiative properties in climate models. This paper describes the University of Wisconsin Cirrus Remote Sensing Pilot Experiment, designed to investigate visible and infrared (IR) optical properties of cirrus clouds and the effects of cloud spatial distribution on the scaling of point measurements to satellite and general circulation model (GCM) grid-scale averages.

Clouds affect the radiative balance of the earth/atmosphere system by reflecting incoming solar radiation and by trapping outgoing longwave radiation. The difference between a clear-sky and a cloudy-sky ra-

diative energy budget is termed cloud radiative forcing. Observations from the Earth Radiation Budget Experiment (ERBE) recently provided estimates of shortwave and longwave cloud radiative forcing (Ramanathan et al. 1989). For the global mean, shortwave cloud radiative forcing is approximately -48 W m^{-2} , while the longwave cloud radiative forcing is approximately 31 W m^{-2} . Thus, the present average cloud cover produces a net radiative cooling of approximately 17 W m^{-2} . In contrast, models suggest that an instantaneous doubling of CO_2 would produce a radiative heating of approximately 4 W m^{-2} . By modification of radiative heating distribution, the increased greenhouse gas concentrations in the atmosphere are likely to change planetary circulation patterns and result in a redistribution of moisture and cloudiness. Thus, greenhouse warming trends could produce substantial cloud feedbacks that may serve to moderate or augment the actual global thermal response. Understanding the radiative effects of clouds is therefore crucial to the evaluation of greenhouse gas impacts on climate. In addition to modifying the radiative energy budget at the top of the atmosphere, clouds also modify the radiative heating of the atmosphere and surface.

Cirrus clouds are important modulators of earth's radiative balance because of their large areal extent, seasonal persistence, and typically high-altitude location. These clouds have only recently been subject to detailed measurements (*Mon. Wea. Rev.*, **118**, 2259–2248). Climate models suggest that cirrus may produce a positive or a negative feedback response to global warming depending on cloud optical depth, altitude, and particle size distribution (Roeckner et al. 1987; Stephens et al. 1990). In order to address some specific issues concerning the remote sensing and radiative parameterizations of cirrus clouds, simultaneous observations were made at the University of Wisconsin—Madison during the Cirrus Remote Sensing Pilot Experiment (CRSPE). CRSPE employed a unique complement of instruments in conjunction with satellite and National Weather Service meteorological observations. Section 2 describes CRSPE science

*Cooperative Institute for Meteorological Satellite Studies, Madison Wisconsin.

+Space Science and Engineering Center, Madison, Wisconsin.

**Department of Meteorology, University of Wisconsin, Madison, WI 53706

++NOAA/ERL Wave Propagation Laboratory, Boulder, Colorado

©1993 American Meteorological Society

objectives and section 3 gives a brief description of instruments deployed. Section 4 presents a qualitative description of how the data support the scientific objectives by presenting examples of data collected on 1 December 1989.

2. Science objectives

Development of cirrus radiative parameterizations for model applications is particularly challenging for several reasons. Cirrus are composed largely of ice crystals exhibiting a wide range of shapes, sizes, and orientations. Cirrus are spatially inhomogeneous and often exhibit coherent structures in all size regimes, from tens of meters to the synoptic scale. While

Ultimately, global measurement and monitoring of cirrus cloud cover and radiative properties are necessary. Current satellite-borne passive instrumentation can provide the needed global coverage, but cloud property retrieval techniques require verification and calibration.

accurate and detailed measurements of the radiative, microphysical, and morphological properties of cirrus are needed, cloud variability and high cloud altitudes hamper in situ particle and radiation measurements.

Ultimately, global measurement and monitoring of cirrus cloud cover and radiative properties are necessary. Current satellite-borne passive instrumentation can provide the needed global coverage, but cloud property retrieval techniques require verification and calibration.

Interpretation of satellite radiometric measurements is often based on simplified model calculations or ground-based point observations. Scaling point measurements or theoretical calculations of cloud optical properties to satellite pixel-sized areal averages, or to GCM grid volumes, are not trivial due to spatial and temporal inhomogeneity of cirrus. To improve the radiation parameterization in global climate models using information from a densely instrumented site, an estimation of radiation fields averaged over GCM grid boxes must be produced from the point measurements. CRSPE was designed to provide a database suitable for addressing the problems of extrapolating point measurements to the GCM scales. Specific science objectives are listed below.

1) Characterization of the effect of horizontal and vertical cloud inhomogeneities on satellite- and ground-based observations. The ground-based high spectral resolution lidar and the interferometers (see next

section) will provide "point" observations of the cirrus cloud with a field of view (FOV) of less than 1 km. The combination of scanning lidar and satellite data will be used to describe the horizontal and vertical structure of the cloud on the mesoscale, the portion of the cloud that passed over the central site, and the changes in the clouds during the period of the observations.

2) Parameterization of visible and infrared cirrus optical properties. Cloud radiative parameterizations will be developed from the measured visible properties and the infrared emissivities derived from the ground- and satellite-based observations from a variety of cirrus cloud types. The effects of cloud inhomogeneities on these relationships will be investigated.

3) Verification of satellite cloud retrieval methods.

Satellite- and ground-based cloud detection schemes will be compared and verified with lidar observations. Cloud optical properties derived from satellite and ground-based radiometric observations will be cross validated.

4) Statistical description of cirrus spatial scales. Autocorrelations of lidar backscatter will be used to determine statistics of cirrus cloud spatial characteristics.

5) Database for comparisons with radiative transfer models. The interferometers provide accurate measurements of downward infrared radiance spectra under clear-sky conditions for comparison with radiative transfer model calculations. Pristine skies are not observed in nature and the lidars therefore play a vital role in detecting and locating aerosol and subvisible cirrus. Radiosonde observations provide in situ measurements necessary to define the detailed atmospheric temperature and moisture structure required for radiative calculations.

3. The field experiment

The experiment was conducted over south-central Wisconsin from 1 November to 6 December 1989. This was also the location of the FIRE-Cirrus IFO in October 1986 (Cox et al. 1987; Starr 1987). Ground- and satellite-based observations of clear skies and various cirrus cloud systems were made during this one-month period. At the central site, located on the University of Wisconsin—Madison campus, four primary instrument systems operated: two calibrated interferometers with a spectral resolution of approxi-

mately 1 cm^{-1} , the high spectral resolution lidar, a Scripps Whole-Sky Imager (WSI), and an NCAR CLASS radiosonde system. Located 24 km west of the central site, the volume imaging lidar (VIL) was operated with a clear line of sight over the central site. Satellite-based observations over the region were captured in real time by the McIDAS system (Suomi et al. 1983), located at the central site. These instruments are discussed in detail below.

High Spectral Resolution Lidar (HSRL) provides calibrated measurements of the vertical profile of the cirrus backscatter cross section, optical depth, and backscatter phase function at a wavelength of 0.532 μm . Using a two-channel multiwavelength receiver, the HSRL spectrally separates molecular backscatter from cloud particle and aerosol backscatter. The separation is possible because the thermal motions of molecules Doppler broadens the molecular backscatter spectrum, while the Brownian motions of particles produce insignificant broadening of the particle backscatter spectrum (Grund and Eloranta 1991). HSRL observations are also used for diagnosing cloud-base altitude, geometric thickness (for optically thin cloud), and vertical distribution.

High-Spectral Resolution Interferometer Sounder (HIS). Two Michelson interferometers were located at the ground site. The first was the aircraft version that was flown on the NASA ER-2 during FIRE I (Revercomb 1987). The second was based on a Bomem M-120 spectrometer that was being developed for use in the Department of Energy's Atmospheric Radiation Measurement (ARM) Program. A motor-driven mirror directs infrared energy into the M-120 from one of three sources: an ambient blackbody cavity, a cold blackbody source, or the atmosphere. The blackbody views are used to remove the effect of instrument emission from sky radiance through the use of a standard linear calibration. The demonstrated rms noise is approximately 0.1% of ambient temperature. The interferometers provide high spectral resolution (on the order of 1 cm^{-1}) observations of cirrus clouds in the 3.5–20- μm spectral band. The observed spectra allow detailed comparisons with line-by-line radiative transfer models such as FASCOD (Clough et al. 1988; Revercomb et al. 1989). Observations also provide variability estimates of the infrared spectral emissivity of clouds. Atmospheric temperature and moisture profiles are also retrieved from these observations.

Volume Imaging Lidar (VIL) produces 3D reconstructions of cirrus cloud backscatter by assembling successive 2D crosswind scans. The VIL scans 120-km-wide segments of cirrus at a resolution of approximately 60 m in 20 s. During the experiment, one scan plane was oriented above the central site, while a second scan plane was oriented perpendicular to the

mean wind direction or perpendicular to the central site scan plane. During CRSPE, the VIL scan over the central site provided a 2D view of cirrus clouds with 100-m resolution. Time composites of the VIL crosswind scans provide the 3D structure of the cloud, thus describing vertical and horizontal variations of the cirrus cloud backscatter. The VIL observations provide a means for investigating effects of subpixel-scale variability and cloud vertical distribution on the retrieval of cloud height and optical properties from current meteorological satellite sensors and ground-based instruments.

Satellite observations include multispectral data from the polar-orbiting NOAA AVHRR (both GAC and HRPT), HIRS/2 and MSU, and GOES-7 VISSR and VAS data captured in real time by the McIDAS system. These radiometers produce multispectral images of the earth's upwelling radiance with resolutions of 1–8 km depending on wavelength and instrument. The meteorological satellites observe clouds on the scale of tens to thousands of kilometers, thus bridging the gap between the scale of site observations and the regional scales used in GCMs. Satellite visible and infrared observations can be used for diagnosing large-scale geometric and radiative cloud structure.

NCAR Cross-chain Loran Atmospheric Sounding System (CLASS) produces accurate in situ radiosonde determination of atmospheric profiles of temperature, water vapor, and wind speed and direction. A unique feature of the CLASS is that it uses the Loran-C navigation system to determine accurate positions from which to calculate wind speed and direction as a function of altitude during the balloon ascents. The CLASS soundings of temperature and moisture represent point measurements along the balloon flight path but possess the vertical resolution and accuracy required for comparing infrared radiance observations with theoretical calculations from atmospheric radiation models. The temperature and moisture profiles provide thermodynamic properties of the cloud and the surrounding atmosphere as well as density profiles to calibrate HSRL optical depths. Wind speed and direction profiles from the CLASS are used to construct the 3D images from VIL scans.

SCRIPPS Whole-Sky Imager (WSI) generates a time record of sky conditions through a 170° FOV fish-eye CCD camera. Regularly spaced digital "snapshots" through red, blue, and neutral density filters are provided to facilitate cloud detection and accommodate varying light conditions (Johnson et al. 1989).

National Weather Service surface and radiosonde observations. These routine observations are available through McIDAS and describe the synoptic condition associated with the cirrus clouds.

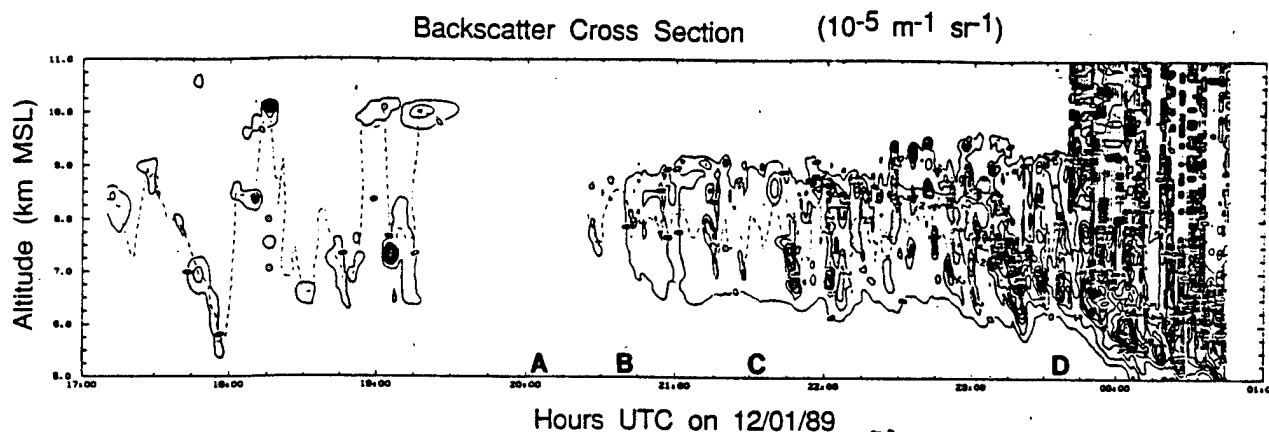


Fig. 1. HSRL-observed backscatter cross section as a function of altitude on 1 December 1989.

4. Case study (1 December 1989)

This section illustrates types of data collected during CRSPE from examples collected on 1 December 1989. The two interferometers (results are shown only for the Bomem M-120) collected data from approximately 1400 to 2400 UTC; the HSRL operated from 1345 to 0110 UTC and the VIL from 1800 to 2330 UTC. Four CLASS sondes were launched and the WSI imaged the sky throughout the day. The NOAA-11 satellite flew over Madison at approximately 1350 UTC. Examples of data products are first presented separately for each instrument; an integrated example of the data is presented at the end of the section.

Figure 1 depicts the HSRL-measured backscatter cross section as a function of altitude for eight hours on 1 December 1989. Contour intervals are $2 \times 10^{-5} \text{ m}^{-1} \text{ sr}^{-1}$. The dashed line marks the optical midcloud altitude (midpoint in optical depth). Between approximately 1930 and 2015 UTC, the HSRL backscatter measurements indicate that the upper troposphere is essentially free of cirrus and aerosol. No clouds were observed visually during this time. Prior to 1930 UTC, the HSRL backscatter cross-section measurements indicate the presence of a cirrus cloud or aerosol layers with backscatter cross sections ranging from approximately 1×10^{-7} to $12 \times 10^{-5} \text{ m}^{-1} \text{ sr}^{-1}$, and optical midcloud altitude ranging from 5.5 to 10 km. Visual observations of sky conditions during this period indicated the presence of thin cirrus fibratus. These visual cirrus are associated with regions of high backscatter cross section at approximately 1815 and 1910 UTC. After approximately 2020 UTC, the HSRL backscatter cross-section measurements coincide with a visually observed cirrus cloud layer. The HSRL-measured cloud top is above 9 km with cloud base at approximately 6.5 km, which begins to descend around 2330

UTC. As the cloud base descends, the cloud optical depth increases so that at approximately 2340 UTC the HSRL lidar beam cannot penetrate through the cloud (optical depth greater than 2.7, indicated by vertical hatching).

The temperature and moisture profiles measured by the CLASS are depicted in Fig. 2, for launch times of 1445, 1800, 2124, and 2356 UTC. Between 1445 and 2124 there is a general warming trend below 800 mb, while a cooling trend exists between 2124 and 2356 UTC. During the period 1445 to 1800 UTC, a significant moistening of the atmospheric layer between 300 and 500 mb occurs. The existence of a

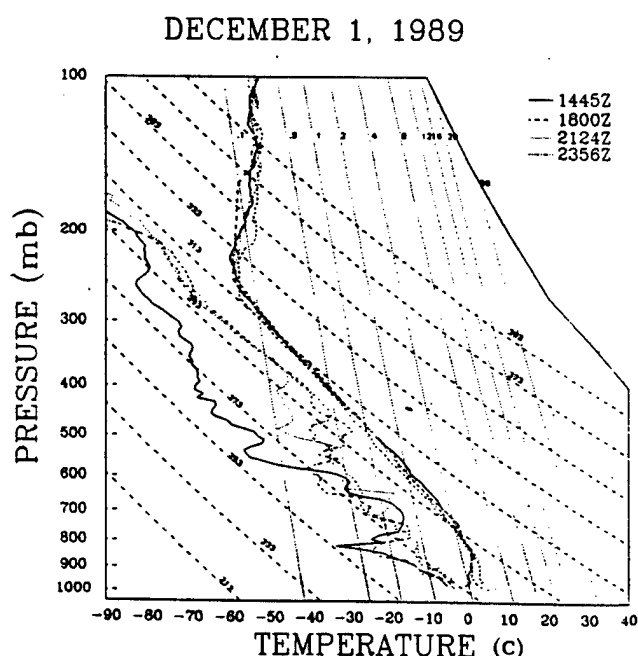


Fig. 2. Temperature and moisture profiles measured by the CLASS at four time periods.

cirrus cloud is suggested from an increase in the dewpoint at approximately 5.6 km (497 mb) at 1800 UTC, 7.3 km (390 mb) at 2124 UTC, and 5.9 km (475 mb) at 2356 UTC. The radiosonde cloud-base altitudes are higher than indicated by the lidar due in part to the time response lag of the hygistor. Similarly, the cloud-top altitude inferred from the radiosonde temperature and moisture profile is higher than indicated by the lidar backscatter signal. Some difference in cloud-top height may also be due to the CLASS sonde sampling a different portion of the atmosphere than the lidar, as well as measurement errors associated with the low humidities of the upper troposphere (Finger and Schmidlin 1991; Elliott and Gaffen 1991).

An example of the observed infrared spectra is depicted in Fig. 3 in terms of brightness temperature as a function of wavenumber. These spectra were collected over a 5-min sampling period at 2006, 2043, 2138, and 2337 UTC (these times are depicted on the HSRL backscatter cross-section time series of Fig. 1). Several gaseous absorption bands are denoted in Fig. 3. The 620–700-cm⁻¹ carbon dioxide band is a strong absorption band that indicates changes in surface air temperature. This band has been used to retrieve low-level temperature inversions (Smith et al. 1990). The 1040-cm⁻¹ (9.6- μ m) ozone band is clearly evident in the clear-sky spectra, but as the cloud opacity increases the signature weakens as the emission from stratospheric ozone is attenuated by the cloud. Several water vapor absorption bands are clearly evident in the 800–1200-cm⁻¹ (8–12- μ m) window region. Figure 4 is an enlargement of Fig. 3 for the 800–1000-cm⁻¹ region, a common spectral interval covered by narrowband radiometers. Techniques for retrieving cirrus cloud properties from narrowband radiometer observations must remove the effects of these absorption lines by using coincident atmospheric temperature and moisture profiles along with model calculations. An advantage of high-spectral resolution observations is that analysis can be done between the absorption lines; however, absorption due to the water vapor continuum must still be accounted for.

The HSRL and CLASS observations are point measurements of the atmospheric vertical structure. While time series analyses give some indication of atmospheric variability, scene variability within the HSRL and the interferometer field of view is unknown. The horizontal and vertical variability of the cirrus cloud observed at 2153 UTC is depicted from the VIL observations in Fig. 5. The top portion of the figure depicts the scan perpendicular to the wind direction and the bottom portion is for the scan in the direction of the ground site. The location of the central site (24 km from the VIL) is depicted in the lower portion of the figure. The VIL scans clearly indicate the heteroge-

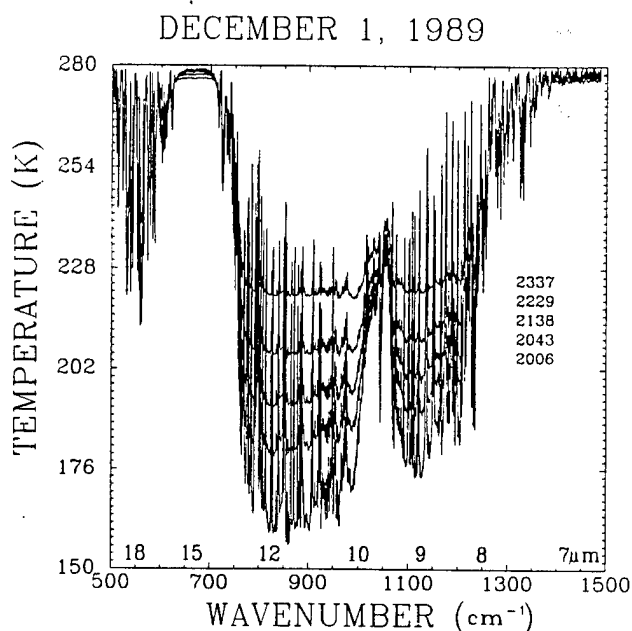


FIG. 3. Five BOMEM-120-observed infrared spectra, in terms of brightness temperature, for the 500–1500 cm⁻¹ (wavelength in microns is also shown). Cloud cover increases during this time period.

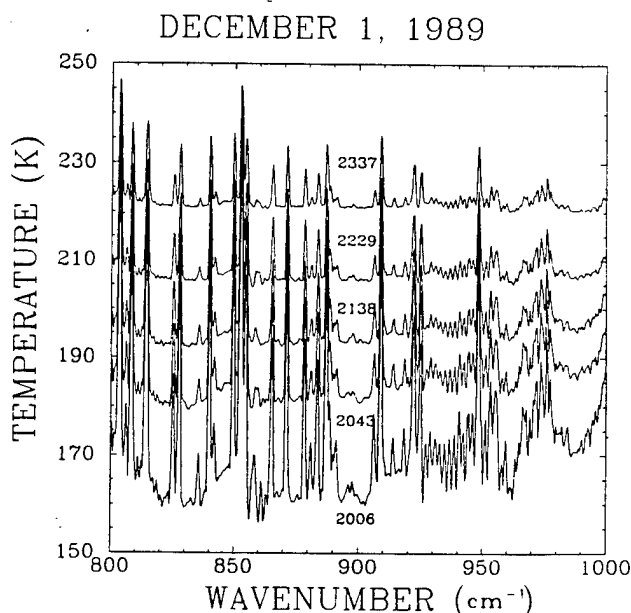


FIG. 4. Enlargement of the 800–1000-cm⁻¹ spectral region for the five spectra depicted in Fig. 3.

neous nature of cirrus cloud, which appears to consist of several individual layers. The VIL data also indicate that ice crystals are falling out of the cloud base at approximately 6.5 km and evaporating. Images from the VIL suggest that single point measurements (e.g., HSRL or M-120) of mean quantities may exhibit large fluctuations due to the heterogeneous nature of the cloud. Temporal averaging of the data may not reduce

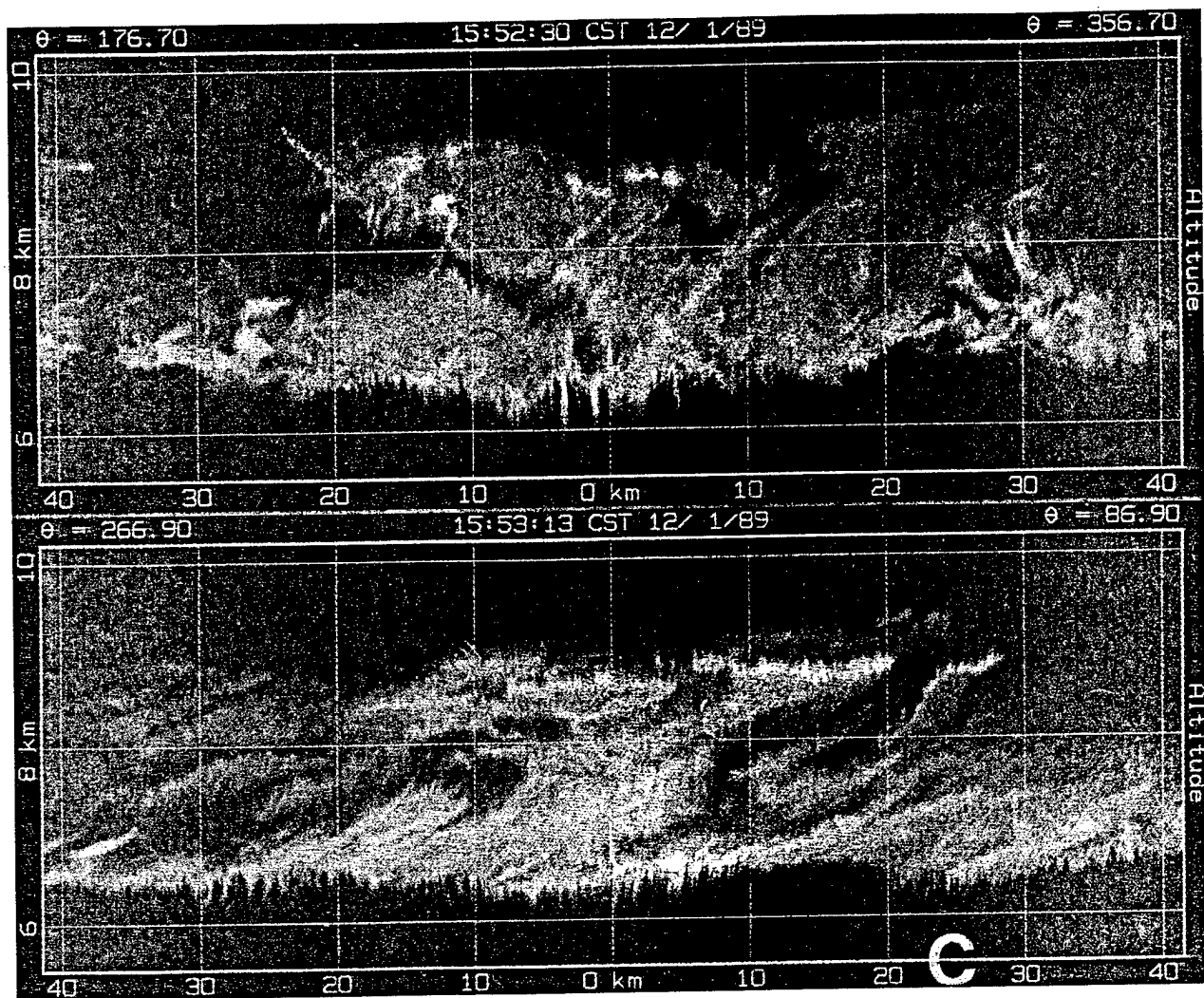


Fig. 5. VIL observations of the cloud field at 2153 UTC (1553 CST). The ordinate is altitude and the abscissa is distance from the VIL. The top portion of the figure depicts the scan perpendicular to the wind direction and the bottom portion is for the scan in the direction of the ground site, located 24 km from the VIL.

this variability due to the large spatial scales and temporal evolution of the cloud.

This sampling problem is graphically illustrated in Fig. 6, which shows a top-down reconstruction of a portion of the cirrus cloud field observed by the VIL. The field is analyzed in terms of observed cloud fraction in two separate 1-h periods, as would be observed by vertically oriented point sensors spaced approximately 10 km apart. This image presents north-south distance on the vertical axis and observation time along the sloping lines. The rectangular grid squares represent 50 km each. In the north-south direction, these are actual measured distances. The distances on the x axis have been computed from wind velocities measured by the CLASS radiosonde. The lidar data used to generate this image consists of approximately 120 north-south lidar scans, each composed of approximately 900 profiles each containing

1024 data points. A signal threshold is chosen and a surface is drawn such that backscatter regions larger than the cloud threshold are enclosed by the surface. The cloud cover figures are shown for 12 different observation points placed at 10-km intervals along a north-south line. The cloud cover percentages on the left of the figure are for times between 14:30 and 15:30 CST and the percentages on the right for the times between 13:30 and 14:30 CST. Notice that even for 1-h averages, cloud cover percentages are highly variable between closely spaced observations points. For the period 13:30 to 14:30, cloud cover varies between 36% and 87%, while in the next hour cloud cover varies spatially between 0% and 73%. These variations make point measurements difficult to compare with area averages over a satellite pixel. Coincident HSRL, interferometer, and VIL data allow the capability to characterize the effect of the cloud horizontal and

vertical inhomogeneities on single, time-averaged point measurements.

Satellite observations depict large-scale structure of the cirrus cloud system. Figure 7 is an example of a GOES visible and infrared image at approximately 2100 UTC. Also shown in Fig. 7 is the VIL scan pattern (cross) as well as the central site location (box). Time series analysis of the GOES imagery, at half-hour time intervals, indicates that the cloud system in northern Wisconsin moves to the south and southeast and arrives over Madison sometime between 2000 and 2100 UTC.

While it is not the intent of this paper to present the type of analysis required to achieve the objectives outlined in section 2, it is, however, useful to present an integrated picture of the various datasets. The first question to address is the capability of the VIL to simulate cloud structure within the field of view (FOV) of the single-point measurements. This is crucial to our first science objective and is best demonstrated by comparing a time series of the observed HSRL backscatter with a simulated time series generated by the VIL observation over and within the HSRL FOV. This comparison is depicted in the top two panels of Fig. 8. There is an excellent correlation

between the VIL-simulated and HSRL time series. The capability of the VIL to simulate the HSRL signals demonstrates that the VIL can be used to characterize temporal and spatial variations within the FOV of the point observations. It also lends confidence in using

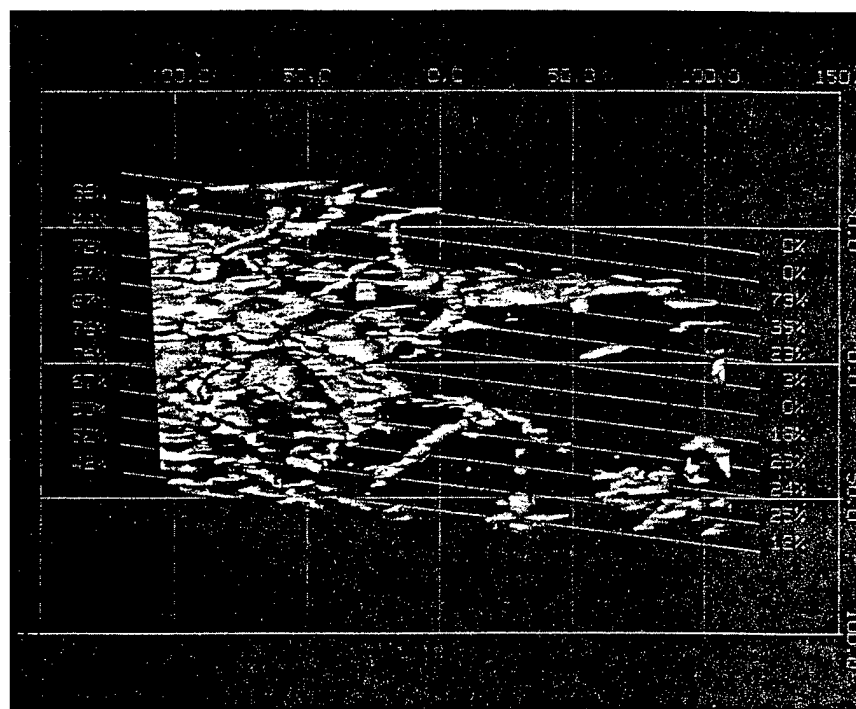


FIG. 6. Top-down view of cirrus clouds constructed from VIL observations. This image presents north-south distance on the vertical axis and observation time along the sloping lines. The rectangular grid squares represent 50 km each. Presented on this figure are the percentages of the time an observer would see cirrus cloud cover at zenith during two separate 1-h time intervals. Cloud cover figures are shown for 12 different observation points placed at 10-km intervals along a north-south line. Cloud cover percentages on the left of the figure are for times between 14:30 and 15:30 CST and the percentages on the right for the times between 13:30 and 14:30 CST.

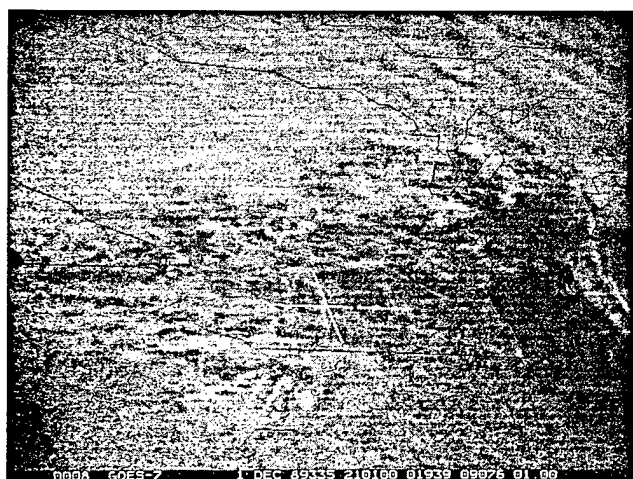


FIG. 7. GOES imagery at 1900 UTC. Also shown is the VIL scan pattern as well as the central site location.

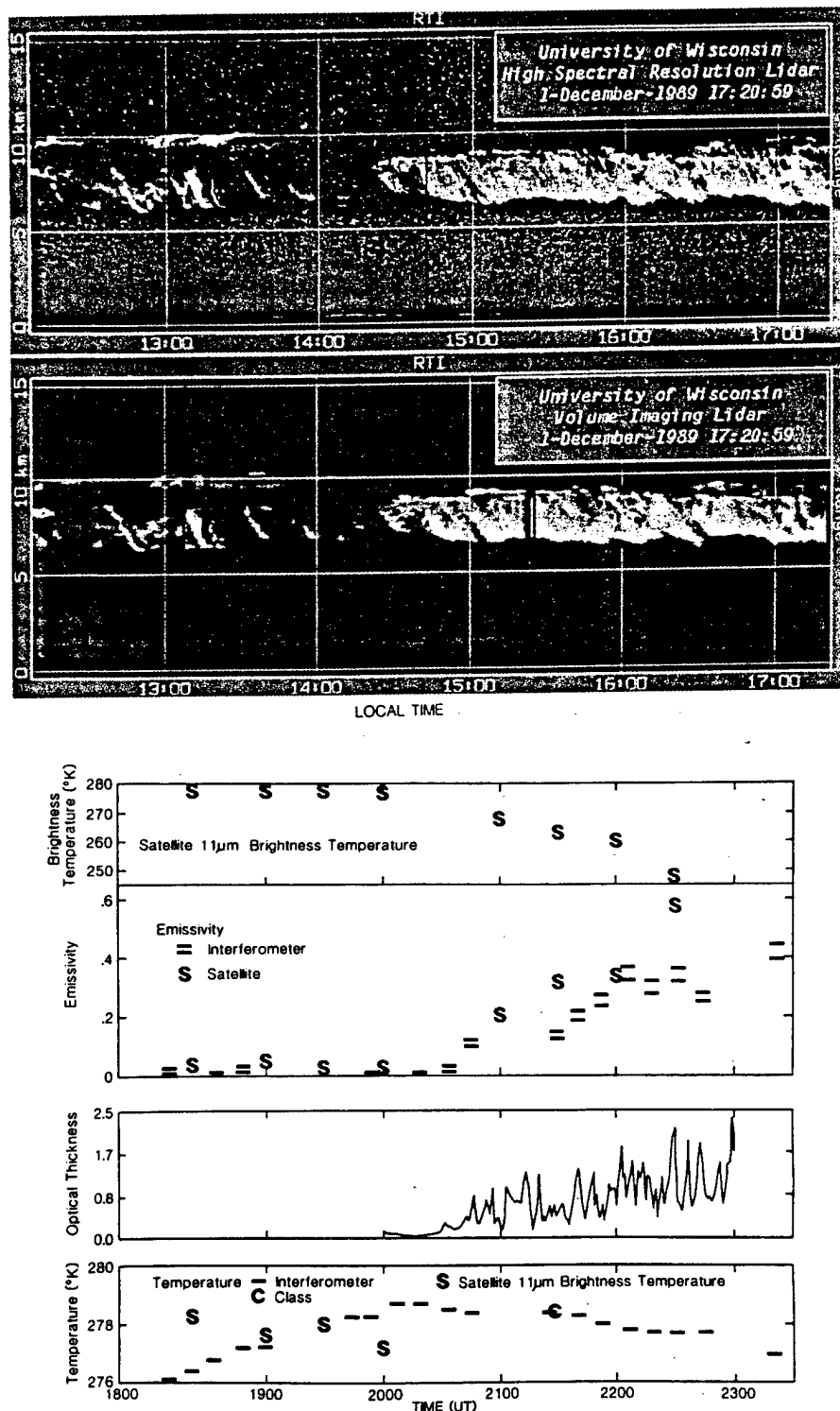


FIG. 8. An integrated depiction of the various datasets. See text for details.

the VIL for statistical descriptions of cirrus spatial scales (objective 4).

Analysis of GOES data is best visualized by animating the satellite imagery. Depicted in the third panel of Fig. 8 is a time series of GOES VISSR $11\text{-}\mu\text{m}$ brightness temperature for the pixel nearest to the central

site. As seen in the satellite animation, decrease in brightness temperature beyond 2030 UTC is due to development of a thick cirrus deck over the central site. The cloud system appeared to be moving from the north-northwest, and therefore its movement was nearly perpendicular to the VIL scan over the central site. The satellite-observed brightness temperature decreases as the observed energy becomes more characteristic of cloud emission rather than surface emission. This can be manifested by an increase in cloud areal coverage within the 8-km satellite footprint, an increase in the cloud opacity, or a combination of both. Again, scanning lidar observations will be used to quantify spatial variability within the satellite pixel FOV and its effect on the satellite retrieval algorithm (objective 3).

Emissivity is often used to parameterize the infrared radiative properties of clouds (objective 2) and is defined as cloud radiance normalized by equivalent radiance of a blackbody at the cloud temperature. The satellite-derived cloud emissivity, derived after the method presented by Wylie and Menzel (1989), is denoted by the "S's" in the fourth panel of Fig. 8. Also shown in this panel are emissivities derived from ground-based interferometer measurements, denoted by two horizontal lines. The interferometer emissivity was derived between absorption lines for the $8\text{--}12\text{-}\mu\text{m}$ region, correcting for the water vapor continuum. The spectral variation of emissivity across this band is denoted by the vertical

15% of the 8–12- μm band mean emissivity. Differences between satellite-derived emissivity and spectral emissivity are due to the different FOV of the two observations.

In parameterizing radiative properties of clouds, it is important to properly couple the shortwave and longwave properties. One such method is a functional relationship between visible optical thickness and window infrared emissivity. A time series plot of the HSRL-observed visible optical thickness is shown in panel 5 of Fig. 8, for 2-min averages. This relationship between the HSRL visible optical thickness and the infrared emissivity will be the basis of the parameterization discussed in objective 2.

The final panel of Fig. 8 depicts the time series of HIS-observed equivalent blackbody temperatures in the 620–700- cm^{-1} spectral band and is representative of the air temperature in the vicinity of the instrument. The “C” represents the corresponding CLASS measurement. The satellite observed 11- μm brightness temperature is also plotted for reference. The agreement between the CLASS and the 620–700- cm^{-1} spectral channel temperatures indicates that this channel can be used to monitor low-level atmospheric temperature changes between CLASS sonde launches. This is important for determining the effects of the lower atmosphere on deriving cloud radiative properties. The coincident CLASS, lidar, and interferometer observations will also be used to improve radiation calculations under clear- and cloudy-sky conditions (objective 5).

5. Summary

An experiment to improve radiative parameterizations of clear and cloudy atmospheres was carried out at the University of Wisconsin in November and December 1989. This experiment consisted of simultaneous observations from a unique complement of instruments, designed to address important issues concerning the parameterization of radiation in global climate models. This paper presented an example of data collected during one day of the experiment. It is clear that a larger dataset needs to be obtained before all science objectives can be fully met. In addition to the observations from CRSPE, these instruments participated in the cirrus FIRE II experiment in November 1992 in Kansas.

Acknowledgments. We gratefully acknowledge Dr. W. Dabberdt for providing partial support of the NCAR CLASS system. We also express our appreciation to R. Dedecker, F. Best, J. Short, T. Dirks, J. Sitzman, B. Howell, and D. Forrest for their support during this

experiment. Partial financial support was provided by the following: Space Science and Engineering Center, NASA Contract NAS1-18272; ONR Grant N00014-91-J-1558, DOE Contract 02182401, and DOE Grant DE-FG02-90ER61058.

References

- Cess, R. D., G. L. Potter, J. -P. Blanchet, G. J. Boer, S. J. Ghan, et al., 1989: Interpretation of cloud–climate feedback as produced by 14 atmospheric general circulation models. *Science*, **245**, 513–516.
- Clough, S. A., R. D. Worsham, W. L. Smith, H. E. Revercomb, R. O. Knuteson, H. W. Woolf, G. P. Anderson, B. L. Hoke, and F. X. Kneizys, 1988: Validation of FASCOD calculations with HIS spectral radiance measurements. *International Radiation Symposium*. Lille, France, 376–379.
- Cox, S. K., D. S. McDougal, D. A. Randall, and R. A. Schiffer, 1987: FIRE—The First ISCCP Regional Experiment. *Bull. Amer. Meteor. Soc.*, **68**, 114–118.
- Elliot, W. P., and D. J. Gaffen, 1991: On the utility of radiosonde humidity archives for climate studies. *Bull. Amer. Meteor. Soc.*, **72**, 1507–1520.
- Finger, F. G., and F. J. Schmidlin, 1991: Upper-Air Measurements and Instrumentation Workshop—Meeting review. *Bull. Amer. Meteor. Soc.*, **72**, 50–55.
- Grund, C. J., and E. W. Eloranta, 1991: The University of Wisconsin High Spectral Resolution Lidar. *Optical Engin.*, **30**, 6–12.
- Johnson, R. W., W. S. Hering, and J. E. Shields, 1989: Automated visibility and cloud cover measurements with a solid state imaging system. Final Report GL-TR-89-0051. Geophysics Laboratory, Hanscom AFB, SIO Ref. 89-7 MPL-U-26/89.
- Ramanathan, V., R. D. Cess, E. F. Harrison, P. Minnis, B. R. Barkstrom, E. Ahmad, and D. Hartmann, 1989: Cloud-radiative forcing and climate: Results from the Earth Radiation Budget Experiment. *Science*, **243**, 57–63.
- Revercomb, H. E., J. Buijs, H. B. Howell, D. D. LaPorte, W. L. Smith, and L. A. Sromovsky, 1988: Radiometric calibration of IR Fourier Transform Spectrometers: Solution to a problem with the High-spectral resolution Interferometer Sounder. *Appl. Optics*, **27**, 3210–3218.
- , W. L. Smith, L. A. Sromovsky, R. O. Knuteson, H. M. Woolf, and H. B. Howell, 1989: Comparisons of FASCOD spectra with HIS observations. *Proc. of the AFGL Annual Review Conference on Atmospheric Transmission Models*. Geophysics Laboratory, Hanscom AFB, 537–573.
- Roeckner, E., U. Schlese, J. Biercampound, and P. Loewe, 1987: Cloud optical depth feedbacks and climate modeling. *Nature*, **329**, 138–149.
- Smith, W. L., H. E. Revercomb, H. B. Howell, H. M. Woolf, R. O. Knuteson, et al., 1990: GAPEX: A ground-based atmospheric Profiling Experiment. *Bull. Amer. Meteor. Soc.*, **71**, 310–318.
- Starr, D. O’C., 1987: A cirrus-cloud experiment: Intensive field observations planned for FIRE. *Bull. Amer. Meteor. Soc.*, **68**, 119–124.
- Stephens, G. L., S. C. Tsay, P. W. Stackhouse, and P. J. Flatau, 1990: The relevance of the microphysical and radiative properties of cirrus clouds to climate and climatic feedback. *J. Atmos. Sci.*, **47**, 1742–1753.
- Suomi, V. E., R. J. Fox, S. S. Limaye, and W. L. Smith, 1983: McIDAS III, A modern interactive data analysis facility. *J. Clim. Appl. Meteor.*, **22**, 766–778.
- Wylie, D. P., and W. P. Menzel, 1989: Two years of cloud cover statistics using VAS. *J. Climate Appl. Meteor.*, **2**, 380–392.

To Ed with thanks

10/25/94

Pami

UNIVERSITY OF JOENSUU
DEPARTMENT OF PHYSICS
VÄISÄLÄ LABORATORY

DISSERTATIONS 6

**A High Spectral Resolution Lidar Based on an Iodine
Absorption Filter**

Päivi Piironen

ACADEMIC DISSERTATION

To be presented, with the permission of the Faculty of Science of
the University of Joensuu, for public criticism in Auditorium P1 of
the University, Tulliportinkatu 1, Joensuu, on October 14th, 1994,
at 12 noon.

JOENSUU 1994

Julkaisija
Publisher Joensuun yliopisto
University of Joensuu

Toimittaja
Editor FT Timo Jääskeläinen

Vaihto
Exchange Joensuun yliopiston kirjasto, vaihdot
PL 107, 80101, JOENSUU
Puh. 973-151 2672, telefax 973-151 2691
Joensuu University Library, exchange
P.O.Box 107, FIN-80101 JOENSUU
Telefax +358 73 151 2691

Myynti
Sale Joensuun yliopiston kirjasto, julkaisujen myynti
PL 107, 80101 JOENSUU
Puh. 973-151 2652, 151 2662, telefax 973-151 2691
Email: lavikainen@joyl.joensuu.fi
Joensuu University Library, sale of publications
P.O. Box 107, FIN-80101 JOENSUU
Telefax +358 73 151 2691
Email: lavikainen@joyl.joensuu.fi

UDK 535.2:551.510.4:551.508
ISSN 1236-4673
ISBN 951-708-268-1

Joensuun yliopiston monistuskampus 1994

Päivi Piironen*; **A high spectral resolution lidar based on an iodine absorption filter** - University of Joensuu. Department of Physics. Väisälä Laboratory. Dissertations; 6, 1994 - 113 p.

ISBN 951-708-268-1

Keywords: High Spectral Resolution Lidar, lidar, iodine absorption, optical parameters of atmosphere, error analysis

*Address: University of Wisconsin-Madison, Space Science and Engineering Center, 1225 West Dayton Street, Madison, WI 53706, USA

Abstract

A High Spectral Resolution Lidar (HSRL) that uses an iodine absorption filter and a tunable, narrow-bandwidth Nd:YAG laser is demonstrated. The iodine absorption filter provides better performance than the Fabry-Perot etalon that it replaces. This study presents an instrument design that can be used as a basis for a design of simple and robust lidar for the measurements of the optical properties of the atmosphere. The HSRL provides calibrated measurements of the optical properties of the atmospheric aerosols. These observations include measurements of aerosol backscatter cross section, optical depth, backscatter phase function, depolarization, and multiple scattering. The errors in the HSRL data are discussed and the effects of different errors on the measured optical parameters are shown.

Preface

This work was carried out in Space Science and Engineering Center of University of Wisconsin (Madison, USA) during years 1991-1994. I would like to thank Dr. Ed Eloranta for serving as my supervisor. Ed's enthusiasm, knowledge, Finnish "sisu", and aim at perfection and honest science will never stop amazing me. Ed's support, criticism, and suggestions during this work are greatly appreciated.

Special thanks go to Dan Forrest for his work on the software development. With his magical touch to the programming Dan helped me on the controlling of the HSRL and his wonderful RTI-displays made possible the real time visualization of the lidar data. Also thanks go to Jim Hedrick for his work on the mechanics and Jim Rose for his work on the electronics.

I would also like to thank Prof. Jyrki Kauppinen (University of Turku, Finland) and Dr. Erkki Kyrölä (Finnish Meteorological Institute, Finland) for their comments on the manuscript. Thanks to Kari Hassinen (University of Joensuu, Finland) for technical help on printing this thesis.

Very special thanks go to my husband Antti for his support during these years. During last years we have shared ideas and sleepless nights while working on our theses. I also wish to thank my parents for all the support and showing me the value of hard work.

The support for my work was provided by the University of Joensuu, Finland. The HSRL was supported by the Naval Research Laboratory, U.S. Department of Navy, under grant N00014-93-1-G013, by National Aeronautics and Space Admin., under grant NAG-1-882, and by Department of Energy, under grant DE-FG02-90ER61058.

Madison, August 1, 1994

Päivi Piironen

Contents

1	Introduction	1
2	Lidar theory of the HSRL	8
3	Instrumentation	13
3.1	Introduction	13
3.1.1	An overview of the high resolution etalon based system	13
3.1.2	A short introduction to the improvements	14
3.2	Transmitter	17
3.2.1	Transmitter laser	17
3.2.2	Optics	20
3.3	Receiver	22
3.3.1	Optics	22
3.3.2	Data system	26
4	Iodine absorption filter	33
5	Calibration and tuning	38
5.1	Calibration theory	38
5.2	The laser wavelength locking into the iodine absorption peak	45
6	Measurements	49
6.1	Depolarization ratio	59
6.2	Measurements of scattering ratio, aerosol backscatter cross section, and optical depth	70
6.3	Measurements of atmospheric temperature	75
7	Error analysis	81
7.1	Error sources	81
7.2	Effects of different errors on the measured optical parameters .	88
8	Conclusions	105

1 Introduction

The climate models used for modeling the transport of the short and longwave radiation in the atmosphere require a knowledge of the aerosol and cloud optical properties. Because the optical properties of cirrus clouds are not well known, the measurements of cloud optical depth, phase function, and particle size provide important information. Clouds affect the radiative balance of the earth and its atmosphere by reflecting incoming solar radiation and trapping outgoing longwave radiation. Cirrus clouds have been found to have an important role on this process^{1,2}. Cirrus clouds consist of large, nonspherical ice crystals and they are generally found between altitudes of 4 and 15 km. Compared to water clouds, cirrus clouds are generally optically thin. Studies based on climate models suggest that presence of cirrus may produce either a heating or cooling effect depending on the cloud optical properties and altitude^{1,2}.

The University of Wisconsin High Spectral Resolution Lidar (HSRL) measures optical properties of the atmosphere by separating the Doppler-broadened molecular backscatter return from the unbroadened aerosol return. The molecular signal is then used as a calibration target which is available at each point in the lidar profile. This calibration allows unambiguous measurements of aerosol scattering cross section, optical depth, and backscatter phase function. Also measurements of depolarization and multiple scattering can be performed. In this study, clear air aerosols, stratospheric aerosols, and cloud particles are all referred to as aerosols. Similar measurements of cloud optical parameters can be made with a Raman-lidar^{3,4}, but because the Raman backscatter cross section is about 1000 times smaller than the Rayleigh backscatter cross section, the HSRL has a significant signal strength advantage over the Raman-technique. Another advantage of the HSRL is that it can provide daytime measurements while sky noise background limits the measurements of the weak Raman signal to night time.

The basic idea of an HSRL was originally presented by Fiocco and DeWolf⁵. They proposed the measurements of atmospheric aerosols by interferometrically separating the backscatter signal. They demonstrated the principle of an HSRL with laboratory measurements of scattering from natural aerosols and artificially produced dense fog. A later experiment with the HSRL technique was performed by Schwiesow

and Lading⁶, who used Michelson interferometers in an attempt to measure atmospheric temperature. Their evaluation showed that a Michelson interferometer based measurements would theoretically produce accurate measurements of atmospheric temperature, but development of a functional system was limited by the quality of available optical components.

An investigation done by Shipley *et al.*⁷ for a shuttle borne lidar experiment to measure global distribution of aerosols and their effects on the atmospheric heat budget started the University of Wisconsin HSRL research. The demonstration of the first University of Wisconsin HSRL was published by Shipley *et al.*⁸. The paper by Sroga *et al.*⁹ presented the first results measured with the same system. The transmitter was based on a dye laser that operated at 476.8 nm wavelength. This laser provided only a 2-4 mW output and it operated at 100 Hz repetition rate. The backscatter signal was collected by a 0.35 telescope with a 320 μ rad receiver field of view. The filtering of the solar background was performed by using an interference filter and three low resolution etalons with a total bandpass of 2 pm. The separation between aerosol and molecular backscatter signals was based on a high resolution etalon with ~ 0.5 pm bandpass. The HSRL was mounted in an aircraft. The system pointed down to ground and it therefore covered only about 2 km measurement range. The range dependence of the receiver spectrometer bandpass due to the angular sensitivity of the etalon transmission complicated the measurements.

The aircraft system was later modified for ground based operations and the changes were reported by Grund¹⁰. The problems due to the range dependence of the spectrometer bandpass were reduced by using a fiber optics scrambler¹². The transmitter laser was changed to a CuCl laser operating at 510.6 nm wavelength. The laser output power was 50 mW at 8 kHz repetition rate. The receiver telescope and the high resolution etalon remained the same, but the number of low resolution etalons was decreased to two providing a 2.5 pm bandpass. This system was capable of measuring cirrus cloud optical parameters up to ~ 12 km altitude. Later, the development of lasers enabled the use of an injection seeded, frequency doubled Nd:YAG-laser (532 nm) as the HSRL transmitter. The new laser provided a 0.7 W output at 4 KHz repetition rate. This change was reported by Grund and Eloranta¹¹.

After all the development in the HSRL, problems with the insufficient calibration accuracy and environmental sensitivity of the system operation remained. The HSRL produced accurate measurements of clear air and thin cirrus, but the measurement accuracy was not sufficient for the cases where the aerosol signal was large compared to the molecular signal. Eventhough the measurement accuracy was not high enough to provide direct measurements of the optical depth profile inside a cloud, the total cloud optical depth was obtained. The cloud optical depth was determined from the decrease in the molecular signal across the cloud. The calculations of optical depth profile inside a cloud were made by assuming a constant backscatter phase function with altitude. The measured molecular profile was fitted with a profile derived from the known molecular backscatter cross section that had been corrected for the atmospheric extinction. The extinction profile was obtained by applying the Bernoulli solution to the aerosol backscatter profile¹². The measured optical depth was used as a constraint.

The accuracy of the HSRL calibration was improved and the sensitivity for environmental changes was reduced in the next University of Wisconsin HSRL (Eloranta and Piironen¹³). In order to make the system operation more stable, the system was moved to a temperature controlled and vibrationally isolated environment. Participation in field experiments was made possible by moving the lidar to a semitrailer. The diameter of the receiver telescope was increased to a 0.5 m and the field of view was decreased to 160 μ rad. A new photon counting data system was designed and extensive computer control of the system operations was implemented. Depolarization and multiple scattering measurement capabilities were added. With the improved system, the measurements of cloud optical properties were performed at altitudes up to ~ 30 km.

During the 18 first years of the University of Wisconsin HSRL, the separation between aerosol and molecular scattering was based on a Fabry-Perot etalon with a 0.5 pm bandpass. With this etalon, the signal was divided into two channels. The signal reflected from the etalon surface was measured with one channel. This channel contained the the wings of the molecular spectrum and the part of the aerosol spectrum that did not pass the high resolution etalon. The other channel was used to measure

the part of the aerosol spectrum and the central part of the molecular spectrum that transmitted through the etalon. The basic idea of the spectral separation of a high resolution etalon based HSRL is presented in Fig 1.

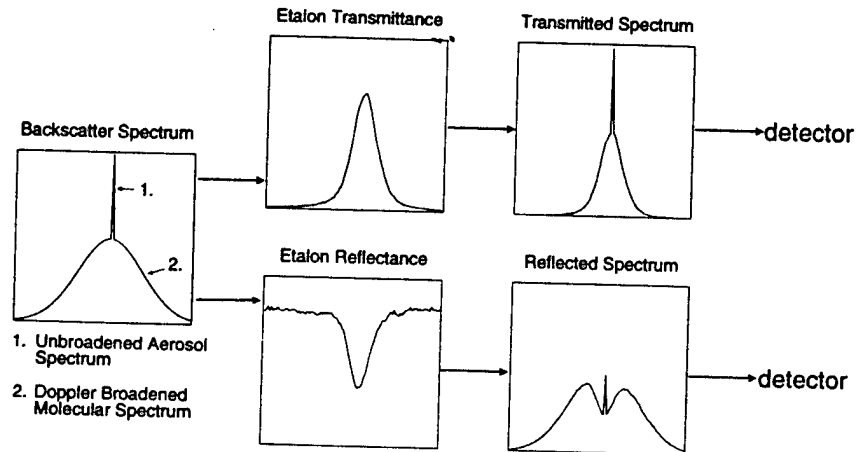


Figure 1. The spectral response of a high resolution etalon based HSRL. The received signal is a combination of the Doppler-broadened molecular backscatter spectrum and the unbroadened aerosol spectrum. The aerosol signal and the center of the molecular signal that transmits through the etalon is detected with one channel. The other channel detects the signal reflected from the etalon.

For the aerosol backscatter signal, only a $\sim 2:1$ separation ratio between aerosol and molecular channel is achieved by an etalon. The Fabry-Perot etalon based HSRL produces accurate measurements of clear air, thin cirrus, and stratospheric aerosols. However, when the system is used to probe dense water clouds, the aerosol signal becomes on the order of 10^3 larger than the molecular return. Therefore, the inversion coefficients used to separate the aerosol and molecular signals must be known with better than 0.01% accuracy or otherwise some of the aerosol return will appear in the separated molecular return. Since the inversion coefficients for the etalon based system are known with only $\sim 0.1\%$ accuracy, the measurements of dense water clouds are subject to error. The performance of a Fabry-Perot etalon is limited by its finesse and the angular distribution of incoming light. The etalon must be operated in pressure and temperature controlled environment, since better than a 0.1 mbar

pressure tuning accuracy and 0.1 °C temperature stability are required to keep the filter performance stable.

Shimizu *et al.*¹⁴ proposed the use of a narrow-band atomic absorption filter in an HSRL and She *et al.*¹⁵ reported high spectral resolution lidar measurements of temperature and aerosol extinction coefficient made by using a barium atomic absorption filter. These studies, and later studies from the same group^{16,17}, have shown, that an absorption filter provides a high rejection against aerosol scattering and therefore it makes the separation between molecular and aerosol scattering easier. Another advantage of an absorption filter is the stability of the absorption characteristics¹⁴. Furthermore, the transmission characteristics of an absorption filter are not dependent on the mechanical alignment of the filter¹⁴ or the angular dependence of the incoming light. Also, a wide dynamic range in rejection against aerosol scattering is achieved by simply changing the vapor pressure¹⁴ or the length of the cell.

This study presents an HSRL employing an iodine absorption filter. The spectrum of the $B^3\Pi_{ou}^+ \rightarrow X^1\Sigma_g^+$ electronic transition in molecular iodine has more than 22 000 absorption lines in the visible wavelengths¹⁸, and 8 of them are easily reached by thermally tuning a frequency doubled Nd:YAG laser output¹⁹. Compared to the barium, the advantage of iodine is that instead of requiring a dye laser, a narrow bandwidth, frequency doubled Nd:YAG laser can be used. Also, a strong absorption is obtained in a short cell at room temperature. Even though iodine has extensive hyperfine structure, the absorption line width is similar to the barium line width, which is broadened by operating at a temperature of ~500 °C.

A large number of iodine absorption lines have been used as reference for Doppler-limited spectroscopy studies and also numerous spectroscopic studies of the line structure and hyperfine structure have been performed. Liao and Gupta²⁰ reported a use of an iodine absorption vapor cell as a narrow band filter for fluorescence spectroscopy. Lately Miles *et al.*²¹ reported the measurements of flow field properties based on an iodine absorption filter and Filtered Rayleigh Scattering technique. The first iodine absorption filter based HSRL is presented here.

The basic idea of an iodine absorption filter based HSRL is presented in Figure 2. The received backscatter signal is divided to two channels. One channel detecting

a sample from the total backscatter spectrum and the other channel the spectrum filtered by the iodine absorption filter. This signal contains information about the wings of the molecular spectrum and a small aerosol cross-talk signal. The first measurements made with the iodine absorption based HSRL were presented by Piironen and Eloranta²².

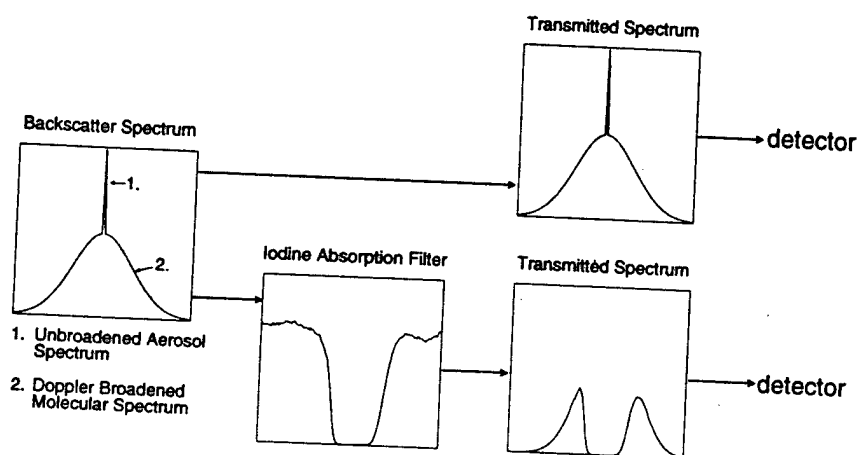


Figure 2. The spectral response of an iodine absorption filter based HSRL. The detected backscatter spectrum is divided to two channels. One containing the information from the total backscatter spectrum and the other the wings of the molecular spectrum and a small aerosol cross-talk.

The work presented in this thesis is organized as follows. A short introduction to the HSRL theory is given in Chapter 2. After that, the instrumentation of the new iodine absorption based HSRL is given in Chapter 3. This chapter also presents the basic principles of the polarization and multiple scattering measurements. A more detailed description of the iodine absorption cell is given in Chapter 4. The system calibration and laser wavelength locking are discussed in Chapter 5. In Chapter 6, examples from the data obtained with the new HSRL are given. This chapter gives a more detailed description of the depolarization measurements and also shows the effects of multiple scattering on the measured depolarization ratio. In addition to the depolarization measurements, the measurements of scattering ratio, aerosol backscatter cross section, and optical depth are discussed. The measurements show, that the

use of an iodine absorption filter enables accurate measurements of cloud optical parameters. Because the cross talk between channels can be accurately corrected and because the $160\ \mu\text{rad}$ field of view of the HSRL effectively suppresses multiple scattering, the optical depth inside a cloud can be measured. This makes future studies of scattering phase function possible. As a final example from the HSRL measurements the Chapter 6 shows an atmospheric temperature profile obtained by the HSRL. The accuracy of the HSRL measurements is discussed in Chapter 7 and the error analysis is presented.

2 Lidar theory of the HSRL

The lidar equation of a monostatic lidar system can be presented in the following form

$$N(R) = \frac{N_o c A}{R^2} \frac{1}{2} \left[\beta_a(R) \frac{P_a(\pi, R)}{4\pi} + \beta_m(R) \frac{P_m(\pi, R)}{4\pi} \right] e^{-2\tau(R)} + M(R) + B, \quad (1)$$

where

$N(R)$	= number of photons incident on the receiver field of view from range R per data bin length,
N_o	= number of transmitted photons,
c	= speed of light,
A	= area of the receiver telescope,
$\beta_a(R), \beta_m(R)$	= aerosol and molecular scattering cross sections per unit volume, respectively,
$\frac{P_a(\pi, R)}{4\pi}, \frac{P_m(\pi, R)}{4\pi}$	= normalized backscatter phase function due to aerosol and molecular scattering, respectively,
$\tau(R)$	= one way optical depth between lidar and backscatter volume at range R, = $\int_0^R \beta_e(r') dr'$, where $\beta_e(R)$ = total extinction cross section per unit volume,
$M(R)$	= multiple scattering contribution incident on the receiver per data bin length,
B	= number of background photons incident on the receiver per data bin length.

Equation (1) demonstrates that the lidar return depends on both the local value of the backscatter cross section and on the optical depth between the lidar and backscattering volume at range R. A conventional single channel lidar provides a single measurement of $N(R)$ at each range, and therefore it does not provide enough information to solve the lidar equation for extinction or backscatter cross section. The knowledge about the relationship between the backscatter cross section and extinction has to

be known or assumed and an estimate of a boundary value has to be given (see for example Klett²³).

In order to make measurements of extinction and backscatter cross section, the HSRL measures two signals which can be processed to present lidar returns from aerosol and molecule backscattering. The separation between the aerosol and molecular scattering is possible, because the signal backscattered from air molecules is Doppler-broadened, while the signal from more massive, slowly moving aerosols remains spectrally unbroadened.

In the case of the HSRL, two separate lidar equations can be written:

1) For aerosols:

$$N_a(R) = F(R) \frac{N_o c A}{2R^2} \beta_a(R) \frac{P_a(\pi, R)}{4\pi} e^{-2 \int_0^R \beta_t(r') dr'} \quad (2)$$

2) For molecules:

$$N_m(R) = F(R) \frac{N_o c A}{2R^2} \beta_m(R) \frac{3}{8\pi} e^{-2 \int_0^R \beta_t(r') dr'}, \quad (3)$$

The molecular backscatter phase function is here replaced with its analytical value $\frac{3}{8\pi}$. The term $F(R)$ is an overlap term, that is a function of receiver and transmitter geometry⁸. Because the molecular scattering cross section is a function of the air density and can be calculated from the Rayleigh scattering theory using an independently measured atmospheric density profile, the equation (3) is well defined and it can be solved for the extinction. The molecular scattering cross section provides a calibration target which is available at each point of the lidar return.

Following optical parameters can be obtained from the separated lidar signals:

1) Aerosol to molecular backscatter ratio (scattering ratio) $SR(R)$

$$SR(R) = \frac{N_a(R)}{N_m(R)}. \quad (4)$$

Notice that, the backscatter ratio measurement is not dependent from the overlap term, and therefore measurements of backscatter ratio for the overlap region can be performed. The same effect can be seen later on the aerosol backscatter cross section and depolarization ratio determination.

2) Aerosol backscatter cross section

The properties of the molecular scattering are well known and therefore, the atmospheric density can be used to compute the molecular scattering cross section per unit volume β_m . From Rayleigh scattering theory²⁴, the molecular scattering cross section per unit volume is

$$\beta_m(R) = \mathcal{N}_m(R) \frac{d\sigma_R(\pi)}{d\Omega}, \quad (5)$$

where

$$\begin{aligned} \mathcal{N}_m &= \text{number of gas molecules per unit volume} \\ \frac{d\sigma_R(\pi)}{d\Omega} &= \text{differential Rayleigh scattering cross section at scattering angle } \pi \\ &\quad \text{per average gas molecule} \end{aligned}$$

For mixture of atmospheric gases below 100 km altitude²⁴,

$$\frac{d\sigma_R(\pi)}{d\Omega} = 5.45 \left[\frac{\lambda(\mu m)}{0.55} \right]^{-4} 10^{-28} \text{ cm}^2 \text{ sr}^{-1}. \quad (6)$$

The number of gas molecules per unit volume can be calculated from the atmospheric pressure $P(R)$ and temperature $T(R)$.

$$\mathcal{N}_m(R) = \frac{P(R)}{T(R)} \frac{N_A}{R_a}, \quad (7)$$

where

$$\begin{aligned} P(R) &= \text{atmospheric pressure at range } R \\ T(R) &= \text{atmospheric temperature at range } R \\ N_A &= \text{Avogadro's number} \\ R_a &= \text{gas constant of dry air} \end{aligned}$$

Thus, by using the previous equations, the molecular scattering cross section per unit volume can be written in the following form.

$$\beta_m = \frac{C_{air} P(R)}{T(R)}, \quad (8)$$

where

$$C_{\text{air}} = 3.786 \times 10^{-6} K h P a^{-1} m^{-1} \text{ at } 532 \text{ nm (from Eq. 5)}$$

$$P(R) = \text{atmospheric pressure}$$

$$T(R) = \text{atmospheric temperature}$$

The aerosol backscatter cross section can be calculated by using the backscatter ratio and the calculated value of β_m

$$\beta_a(R) \frac{P_a(\pi, R)}{4\pi} = SR(R) \beta_m(R) \frac{3}{8\pi}. \quad (9)$$

3) The optical depth of a layer between ranges R_1 and R_2 :

$$\tau(R_2) - \tau(R_1) = \int_{R_1}^{R_2} \beta_e(r') dr' = \frac{1}{2} \ln \left[\frac{\beta_m(R_2) R_1^2 N_m(R_1) F(R_1)}{\beta_m(R_1) R_2^2 N_m(R_2) F(R_2)} \right]. \quad (10)$$

4) Total extinction cross section

The average value of total extinction cross section is a range derivative of the optical depth

$$\langle \beta_e \rangle = \left\langle \frac{\partial \tau(R)}{\partial R} \right\rangle = \frac{\tau(R_2) - \tau(R_1)}{R_2 - R_1}. \quad (11)$$

5) Backscatter phase function

The backscatter phase function, $\frac{P_a(\pi, R)}{4\pi}$, can be calculated from the following equation

$$\frac{P_a(\pi, R)}{4\pi} a(R) = \beta_m(R) \frac{3}{8\pi} \frac{SR(R)}{\beta_e(R)}, \quad (12)$$

where

$$a(R) = \text{single scattering albedo.}$$

For water and ice clouds and most aerosols, the single scattering albedo at the wavelength of 532 nm can be assumed to be unity and therefore the backscatter phase function can be measured.

6) Linear depolarization ratio

The discrimination between water and ice clouds can be made from the depolarization properties of the backscatter signal. The linear depolarization ratio can be given as follows.

$$\delta_{a,m}(R) = N_{(a,m)\perp}(R)/N_{(a,m)\parallel}(R), \quad (13)$$

where N_{\perp} and N_{\parallel} are the number of incident on the receiver perpendicular and parallel to the receiver polarization axis, respectively. In the case of the HSRL, separate depolarizations of aerosol and molecular backscattering can be measured.

7) Cloud particle size

By measuring the signal strength variations as a function of field of view, the size of the cloud particles can be measured. The multiple scattered lidar return is a function of receiver field of view, particle size, range from lidar and the optical depth of the cloud. In the HSRL, the multiple scattering information along with the simultaneous single scattering measurement are used to calculate the cloud particle size. A detailed description of the multiple scattering approximation used for the HSRL measurements is presented by Eloranta^{25,26} and Eloranta and Shipley²⁷.

3 Instrumentation

3.1 Introduction

3.1.1 An overview of the high resolution etalon based system

In the earlier versions of the University of Wisconsin HSRL, the separation between aerosol and molecular backscatter signals was made with a high resolution etalon with ~ 0.5 pm bandpass. The Figure 3 shows the receiver of the etalon based system¹³. The backscattered light was collected by the receiver telescope and directed through a fiber optics scrambler. The fiber optics scrambler was used to reduce the range dependence of the receiver spectrometer bandpass due to the angular sensitivity of the etalon transmission¹². After collimation, the signal was prefiltered with an interference filter and a pair of low resolution etalons. After passing the dual aperture, the light was directed to the high resolution etalon. The high resolution etalon was slightly tilted with respect to the optical axis. This allowed the light that did not pass through the etalon to be reflected back to the dual aperture and to the molecular channel photodetector (PMT1). The light that passed through the high resolution etalon was detected with the aerosol channel photodetector (PMT2). The signal detected with the aerosol channel was a combination of aerosol backscatter spectrum and the center of molecular backscatter spectrum. The signal detected with the molecular channel was a combination of the wings of the molecular spectrum and the part of the aerosol backscatter spectrum that did not pass the high resolution etalon.

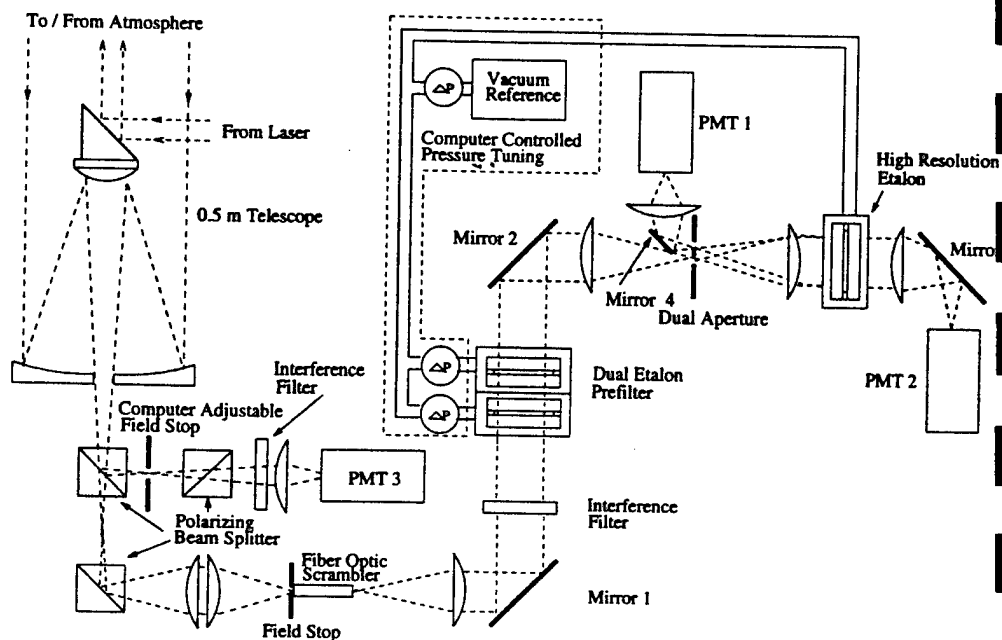


Figure 3. The receiver of the high resolution etalon based system. The backscatter signal is collected with a telescope. The fiber optics scrambler reduces the range dependence of the receiver spectrometer bandpass due to the angular sensitivity of the etalon transmission. The signal is background filtered with a interference filter and a pair of low resolution etalons. The separation between aerosol and molecular backscatter signals is done in the high resolution etalon. The part of the spectrum that transmits the etalon is combination of aerosol backscatter spectrum and the center of molecular backscatter spectrum (PMT2). The signal detected with PMT1 is a combination of the wings of the molecular spectrum and the part of the aerosol backscatter spectrum that did not pass the high resolution etalon.

3.1.2 A short introduction to the improvements

The instrument has been modified to measure polarization and a separate channel has been added to measure both polarization and signal amplitude variations as function of receiver field of view. These modifications allow discrimination between ice and water clouds and measurements of multiple scattering. Along with these modifications, the high resolution etalon, used in the earlier versions of the HSRL, has been

replaced with an iodine absorption filter. Also, the system has been redesigned for use in a semitrailer. Other changes include new data acquisition system, temperature controlled environment for the receiver optics, and improved optical design. The system parameters of the HSRL are summarized in Table 1.

The changes to the HSRL have improved the measurement capabilities of the HSRL. With the new HSRL, the measurements of the optical parameters of the atmosphere below 35 km can be made and therefore, the measurements can cover clouds from water clouds to high altitude cirrus clouds and also measurements of stratospheric aerosol layers can be performed. Clouds with optical depths up to ~ 3 can be measured. This means that most of the cirrus cloud cases can be fully observed and the cloud bases of the thick water clouds can be measured up to 300-500 m inside the cloud. This has been achieved by using a high pulse repetition rate, small pulse energy per laser pulse, and very fast photon counting electronics. Furthermore, the averaging time required for a good signal to noise ratio has been decreased by improving the optical transmission of the system. The use of the iodine filter, the controlling of the pressure of the etalons and the temperature of the optics, and the locking of the laser wavelength to an iodine absorption peak have increased the stability and the reliability of the system. Therefore, the need for frequent calibrations is eliminated and a stable operation can be maintained over a long period of time. The enhanced calibration technique has improved the accuracy of the HSRL calibrations.

Table 1. HSRL specifications (April 26, 1994)

<i>Transmitter</i>	
Wavelength	532 nm
Pulse duration	~ 130 ns
Pulse repetition rate	4 kHz
Average power	~ 0.2 W (seeded)
Frequency stability:	
Without I_2 -locking	≈ 100 MHz/hour (= 0.09 pm/h)
With I_2 -locking	$\lambda \pm 0.052$ pm
<i>Receiver</i>	
Telescope	
Type	Dall-Kirkham
Diameter	0.5 m
Focal length	5.08 m
Wide field of view channel	
Filter bandwidth	1.0 nm
Field of view	computer adjustable 0.21 \rightarrow 4.0 mrad
Polarization rejection	$\sim 1 \times 10^{-3}$
Aerosol+molecular channel	
Filter bandwidth	8 pm
Field of view	0.160 mrad
Polarization rejection	$\sim 1 \times 10^{-3}$
Molecular channel	
Filter bandwidth	1.8 pm
Field of view	0.160 mrad
Polarization rejection	$\sim 1 \times 10^{-3}$
Photon counting data system	
Number of counters	3 (wfov, aerosol+molec., molec.)
Number of data buffers	6 (2 polarizations per channel)
Minimum bin width	100 ns
Number of bins	8192/channel
Max. rate of counters	$\sim 10^9$ Hz, tested to 350 MHz
Embedded computer	Intel i960CA
System control	Sun Sparc II

3.2 Transmitter

3.2.1 Transmitter laser

As a transmitter, the University of Wisconsin HSRL uses a continuously pumped, Q-switched, injection seeded, frequency doubled Nd:YAG laser operating at a 4 kHz pulse repetition rate¹² (Figure 4). The host cavity is based on a Quantronix model 116 laser. The quarter waveplates on either side of the Nd:YAG-rod are used to generate circularly polarized light in the rod in order to eliminate the spatial hole burning. The narrow bandwidth single frequency operation is achieved by injecting the cw-output of a diode pumped monolithic Nd:YAG ring laser (a modified Lightwave model S-100 seedlaser) into the host cavity through a partially transmitting rear mirror. Measurements have shown, that less than 100 MHz/h frequency drift is achieved. The 4 kHz pulse repetition rate is achieved by using an acousto-optic Q-switch.

The output of the laser is externally doubled by a KTP crystal. The frequency doubled output of the laser is tunable over a 124 GHz frequency range by controlling the temperature of the seedlaser diode. The original analog temperature controlling circuit of the seedlaser has been modified and connected to the microprocessor to allow remote control of the seedlaser Nd:YAG crystal temperature.

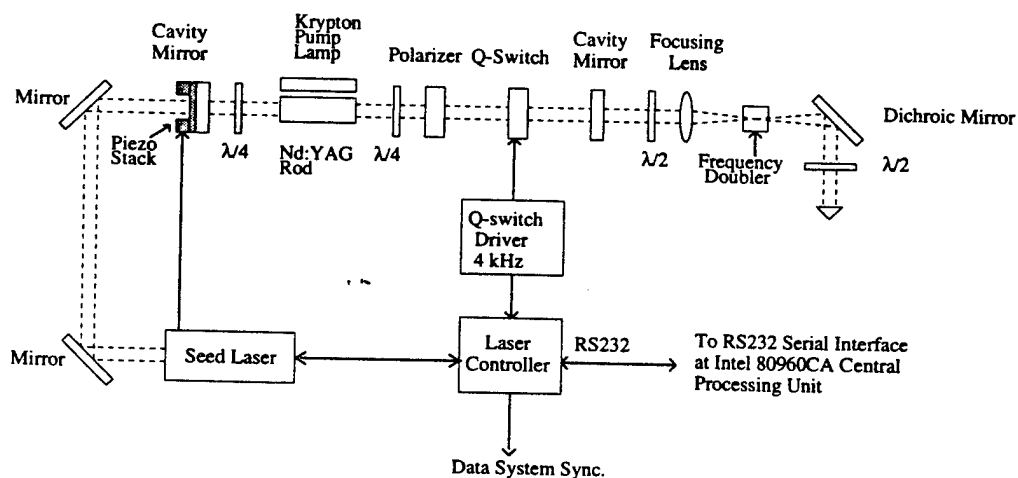


Figure 4. The HSRL transmitter laser.

After frequency doubling, the 532 nm and 1064 nm beams are separated by a harmonic beam separator. Because up to 15% of the residual 1064 nm beam is reflected from the beam separator, a second harmonic beam separator in the laser output (Figure 5) is used to provide more efficient filtering. The remaining 1064 nm beam is cleaned by a spatial filter. The spatial filter also cleans a halo of broader bandpass radiation.

Successful injection seeding requires that overlap between seedlaser resonance frequency and the frequency of a host cavity longitudinal mode is achieved. When the frequency of a host cavity longitudinal mode is locked to the seedlaser resonance frequency, the pulse developing out from the seedlaser signal will saturate the homogeneously broadened gain medium preventing development of any other axial modes from the spontaneous emission. Therefore, because one longitudinal mode is amplified more than any other mode, a spectrally narrow bandwidth pulse is generated. Since the seedlaser emissions used for injection seeding are generally ~ 10 orders of magnitude stronger than the spontaneous emission, the Q-switched pulse builds up sooner out of the seed emission than the spontaneous emission. The frequency locking between seedlaser and host cavity is realized by controlling the host cavity length with a piezoelectric translator.

Because the seeded pulse builds up more rapidly when the host cavity is tuned to the seed laser frequency, the time between the Q-switch opening and the subsequent laser pulse (the Q-switch buildup time) can be used to servo control the tuning of the host cavity²⁸. The spectral purity of the outgoing laser pulse can also be monitored using the Q-switch buildup time. A microcontroller based feedback loop seeks to maintain the cavity length by dithering the rear mirror so that the minimum Q-switch buildup time is obtained. For each laser pulse, a small offset voltage is applied to the piezoelectric translator and the effects to the Q-switch buildup time are simultaneously monitored. Based on the Q-switch buildup time the mirror position is driven towards the minimum time. Statistics on the Q-switch buildup time is collected at 4 kHz rate, but the mirror position is dithered at ~ 140 Hz. The amount of dither is calculated based on the seeding percentage. The observed Q-switch build up time is $\sim 4.5 \mu\text{s}$ and the difference between seeded and unseeded conditions is typically

~ 500 ns. Because the spectral purity of the transmitted laser beam is important for HSRL measurements and because some shots are unseeded, the information from the Q-switch build up time is used to trigger the data system only for seeded shots.

The frequency stability of a single-frequency laser is determined by the seedlaser and the stability of the frequency locking is affected by the environment. The injection seeded operation is easily interrupted by mechanical vibrations transmitted through the support structure or through the cooling water or hoses. The effects of change in the optical length of the cavity due to thermal expansions of the support structure and temperature changes in the laser rod are compensated by the active controlling of the main cavity length. The laser is installed on a Super-Invar breadboard supported by a thick honey comb table that is mounted into a vibration insulated frame. The invar breadboard and the honey comb table are isolated from each other by a rubber pad. The laser was delivered with a Super-Invar table, which is thermally stable, but it is found to be acoustically sensitive. The active controlling of the main cavity length already minimizes the effects of changing environmental temperature so that an acoustically more insensitive table might provide a better performance. The mechanical vibrations coming from the laser cooling pump and transmitted into the cavity by hoses and water are isolated by a pressure dumper in the cooling water line. Because the original pressure dumper did not offer enough isolation, an extra damping system was installed. Also extra long elastic plastic water hoses are used to further attenuate the vibrations coming from the laser cooling pump. Furthermore, the temperature of the surrounding environment is stabilized by controlling the air temperature around the laser. The wavelength locking of the laser output to a iodine absorption line is demonstrated later in Chapter 5.2.

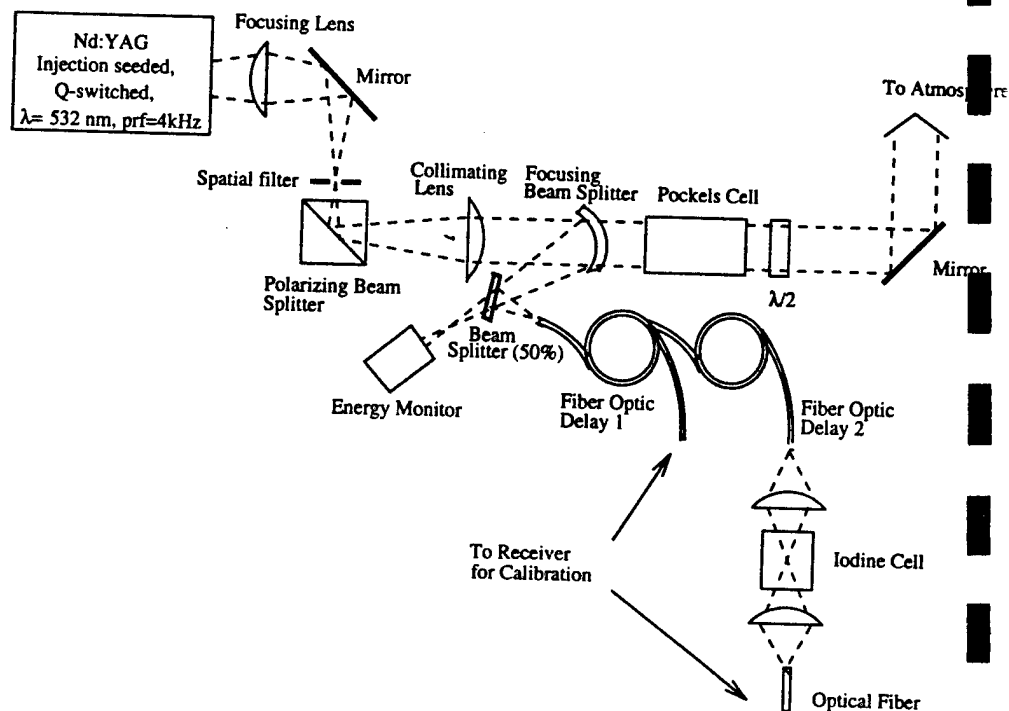


Figure 5. The HSRL transmitter setup. The HSRL transmitter employs an injection seeded, frequency doubled Nd:YAG laser. A Pockels cell in the output is used to rotate the polarization of the outgoing laser beam by 90 degrees for alternative laser pulses. An iodine absorption cell is used for the frequency locking of the laser wavelength. A sample of each laser pulse is directed to a pair of optical fibers, delayed, and injected back to the receiver for system calibrations. The length of the fibers is set so that the time-separated pulses can be recorded into the data profile.

3.2.2 Optics

A small amount ($\sim 2\%$) of each transmitted laser pulse is directed into a pair of 100 m long optical fibers, delayed, and injected back to the receiver for system calibrations (see Figure 5). Since some of the laser shots are unseeded, the delay is necessary so that the measured Q-switch buildup time of each pulse can be used as a quality control to trigger the data system only for seeded shots. The length of the fibers is

set so that the time-separated pulses can be recorded in the data profile. The other ends of the calibration fibers are connected to a diffuse cylinder, which is located at the receiver such that the calibration light signals can be used to monitor system performance during data taking. Another 2 % of the laser light is taken into an energy monitor. The energy normalization of the received signal is realized by storing the energy of each laser pulse into the data record. A 4 cm long iodine cell is used for frequency locking of the laser. This cell provides ~ 50 % absorption when the laser is tuned to the absorption peak. The frequency locking to the iodine peak is described later in Chapter 5.2.

Because the HSRL measures depolarization of the clouds and uses this information to separate between water and ice clouds, the polarization stage of the outgoing laser beam has to be well controlled. The output of the laser is linearly polarized and the orientation of the polarization vector is set perpendicular to the plane of the hypotenuse of the polarization cube. The use of the polarization cube guarantees that the residual cross-polarized component is cleaned out from the outgoing laser beam. In order to be able to use the same receiver optics and the same detector for both polarization components, the polarization of the outgoing laser pulse is rotated by 90 degrees for alternative laser pulses by a Pockels cell. The accuracy of the Pockels cell rotation is measured by observing the light coming from the Pockels cell through a polarizing cube with a photodetector. These calibrations show that the residual cross polarization can be reduced to 0.1 % of the parallel component. The calibration accuracy is limited by the 0.1 % rejection accuracy of the polarizing cube. The timing of the voltage switching between laser pulses is synchronized with the Q-switch signal and the controller electronics assures that the proper Pockels cell voltage is applied in time before the next laser shot. The final alignment between the transmitter and receiver polarization axes is performed by adjusting a half-waveplate and by using the atmosphere as a calibration target.

The use of small receiver field of views is made possible by decreasing the divergence of the outgoing laser beam with a beam expanding telescope (magnification 4x).

3.3 Receiver

3.3.1 Optics

The backscattered light is collected using a 50 cm diameter telescope (see Figure 6). To avoid specular reflection from horizontally oriented ice crystals, the system pointing direction is tilted by 4 degrees from the zenith. The signal polarized parallel to the receiver polarization axis and the signal perpendicular to that are separated by using a polarization cube (see Figure 6). This cube separates the signal to the WFOV-channel (PMT 3) and to the spectrometer-channels (combined aerosol+molecular channel (PMT1) and molecular channel (PMT 2)). An extra polarization cube for both channels is used to clean up the cross polarization component of the received signal down to a level that makes accurate depolarization measurements possible.

The multiple scattering properties can be studied by using the WFOV-channel while simultaneously measuring the single scattering return with the spectrometer channels. A stepper motor driven aperture for the WFOV-channel enables field of view variations between 0.224 and 4 mrad. An interference filter with 1 nm bandpass is used for the background filtering. Because the field of view can be wide and the filter bandpass is broad, the WFOV measurements are currently limited to night time. The field of view of the spectrometer channels is 160 μ rad, which further decreases the background sky noise and multiple scattering effects to the measured signal.

In order to achieve daytime measurements with the spectrometer channels, a low resolution etalon pair and an 1 nm interference filter are used to suppress the background solar radiance. The bandpass of the etalon pair is ~ 9 pm, which is about 3 times the width of the expected Doppler broadened molecular spectrum. The length of the spacers is chosen so that only one common transmission order for the etalon pair occurs inside the interference filter bandpass. The bandpass of the low resolution etalon pair is wider than in earlier systems^{8,12} in order to decrease the system sensitivity for the drift between transmitter wavelength and the etalon transmission maximum. The effects of environmental changes to the etalon performance are eliminated by mounting each etalon into a separate pressure and temperature controlled chamber. A third etalon chamber is used as a pressure reference. The absolute pres-

sure in reference chamber and the differential pressures in each etalon chamber are maintained by a computer controlled servo loop. The etalons are operated near the pressure where the changes in tuning gas density with temperature are cancelled by the thermal expansion of the etalon spacers²⁹. Nitrogen is used as a tuning gas.

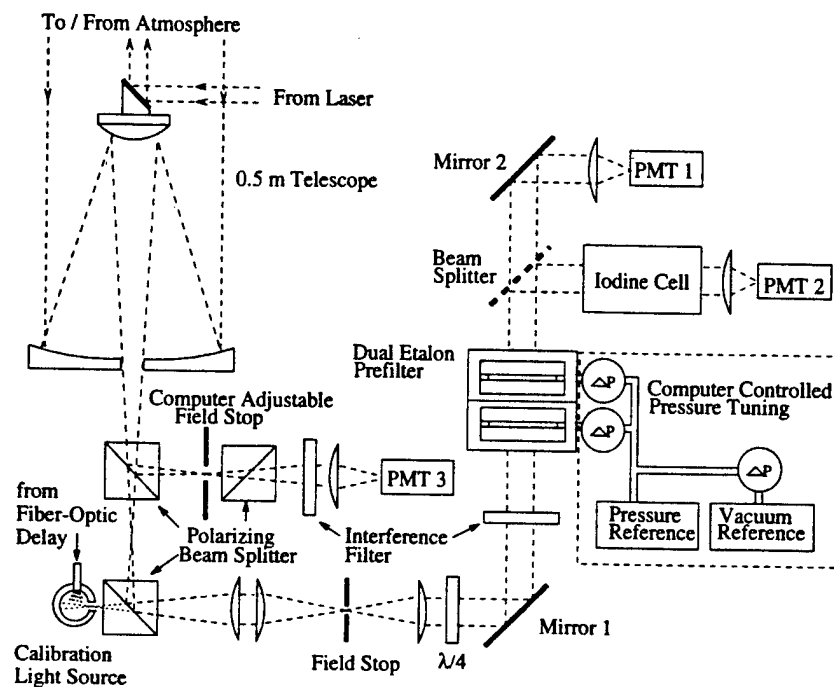


Figure 6. A polarizing prism at the output of the telescope separates the orthogonally polarized signals between wide field of view channel (PMT3) and the spectrometer channels (PMT1 and PMT2). Since the polarization of the transmitted laser pulse is rotated by 90° between laser pulses, each channel alternatively receives perpendicular and parallel components. The received backscatter signal is prefiltered with an interference filter and a low resolution etalon pair before being directed into a beam splitter. The signal detected with PMT1 contains the information about the total aerosol and molecular backscatter signal. The signal directed through the iodine cell and detected by PMT2 is a combination of a amount of aerosol backscatter signal which passes through the absorption cell and the wings of the molecular backscatter signal.

After background filtering, the signal is divided into two channels by a beam splitter. The signal detected with the PMT1 (combined aerosol+molecular channel) contains the information about the total aerosol and molecular backscatter signal. The signal directed through the 43 cm long iodine cell and detected by the PMT2 (molecular channel) is a combination of the small amount of aerosol backscatter signal, which passes through the absorption cell, and the wings of the molecular backscatter signal (see Figure 7). The iodine absorption cell is described in more detail in Chapter 4.

A beamsplitter with a 30/70 (trans./refl.) splitting ratio is used to divide the signal between PMT1 and PMT2. The beam splitting ratio is chosen from the commercially available beamsplitters so that a good photon counting statistics with both channels is achieved when the system is tuned to the iodine absorption peak. Some beamsplitter types have poor transmission and reflection efficiencies and therefore part of the signal is lost in the beamsplitting process. Because good system transmission is important, a beam splitter with a high transmission and reflection efficiencies was chosen.

The beam splitters are highly polarization sensitive elements. When linearly polarized laser beam interacts with atmospheric aerosols and molecules, the backscatter signal consist of two perpendicularly polarized components. Therefore, the polarization sensitivity of the beamsplitter transmission and reflection has to be taken into account. The polarization sensitivity of the beamsplitter performance is noted as a problem in a system described by Krueger *et al.*¹⁷. The advantage of the HSRL is that the received signal is polarization filtered and therefore the light coming from the atmosphere to the beam splitter is always incident with the same polarization. On the contrary, the light from the current calibration light source is polarized orthogonally to the lidar signal and therefore the polarization sensitivity of the beam splitter creates a problem. This problem is solved by generating a circularly polarized light for the beamsplitter with a $\frac{\lambda}{4}$ -waveplate.

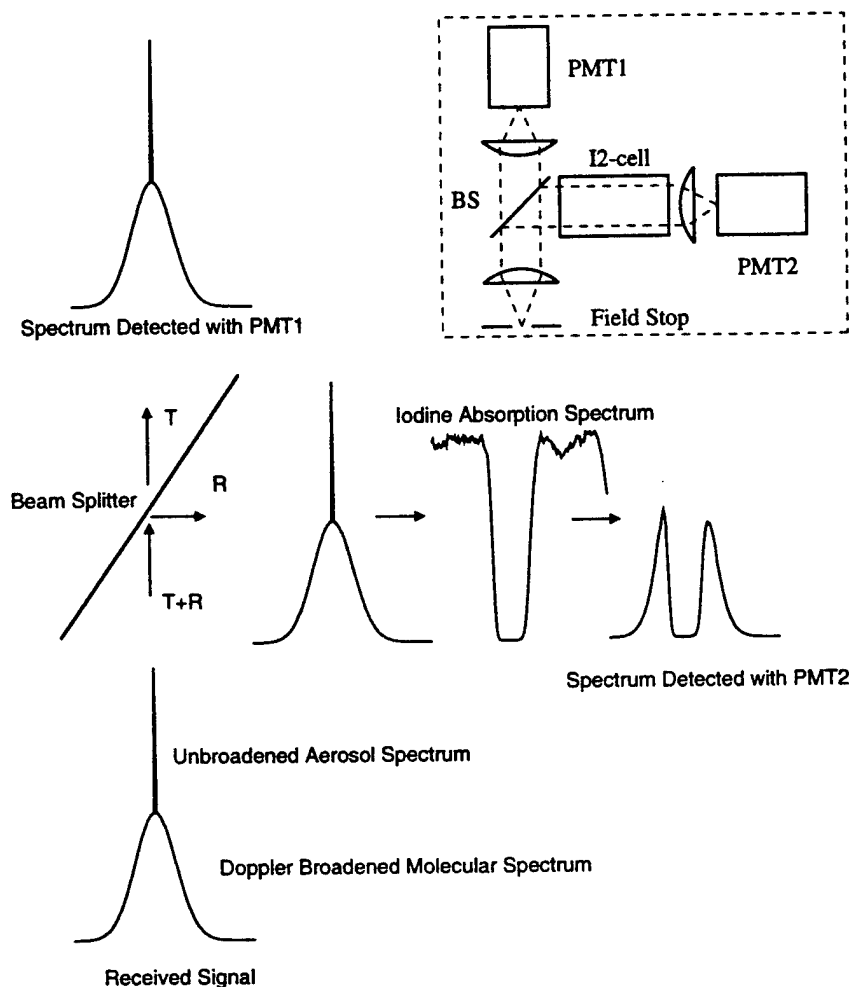


Figure 7. The spectral response of the HSRL receiver. The insert figure at the upper right corner shows a simplified setup of the spectrometer channels. The light that passes the field stop contains information about the Doppler-broadened molecular spectrum and the aerosol backscatter spectrum. The signal is divided into two parts with the beam splitter. The signal, which is transmitted through the beam splitter is detected with PMT1 and it contains information from the total backscatter signal. The signal, that reflects from the beam splitter is directed through an iodine absorption cell. In this process, the aerosol backscatter signal is attenuated in the iodine absorption line. Also the central parts of the molecular spectrum are filtered out and therefore the signal detected with PMT2 is a combination of the wings of the molecular spectrum and that part of the aerosol backscatter signal that passes through the cell.

3.3.2 Data system

In order to increase the dynamical range of the HSRL, new photon counting electronics were designed (Figure 8). The photon counting data system has three counters and each counter has 2 buffers, one for each polarization. Counting rates have been tested up to 350 MHz, but counters are designed to operate up to ~ 1 GHz. The 100 ns bin width enables a 15 m range resolution. The 4 kHz laser repetition rate enables the use of 2333 range bins, which can be used to probe the atmosphere up to 35 km. The limiting factor of the data system is the photomultipliers (EMI 9863B/100), which allow counting only up to 15 MHz without significant pile-up effects. The PMT's are pile-up and afterpulse tested and both corrections are included to the data processing. The corrections are discussed later in this chapter.

Computer control of the system is made by using Intel 80960CA embedded processor. The user interface is realized by using a Sun Sparc Station II. In addition to the data taking and the communication with the Sun, the system processor is used to control HSRL operation including pressure controlling of the etalons, timing of the Pockels cell voltage, controlling of the seedlaser temperature, controlling of the system shutters and relays, and controlling of the WFOV aperture.

Most of the HSRL-operations are computer controllable from a menu interface. System performance can be followed from real time displays. The real time Range Time Indicator (RTI) displays for the raw and/or inverted data are used to display the incoming data so that altitude, variability, thickness and depolarization of the cloud layer can be observed when the clouds move over the lidar site. Similar displays for the cloud optical properties (optical depth, aerosol backscatter cross section, phase function) can be shown.

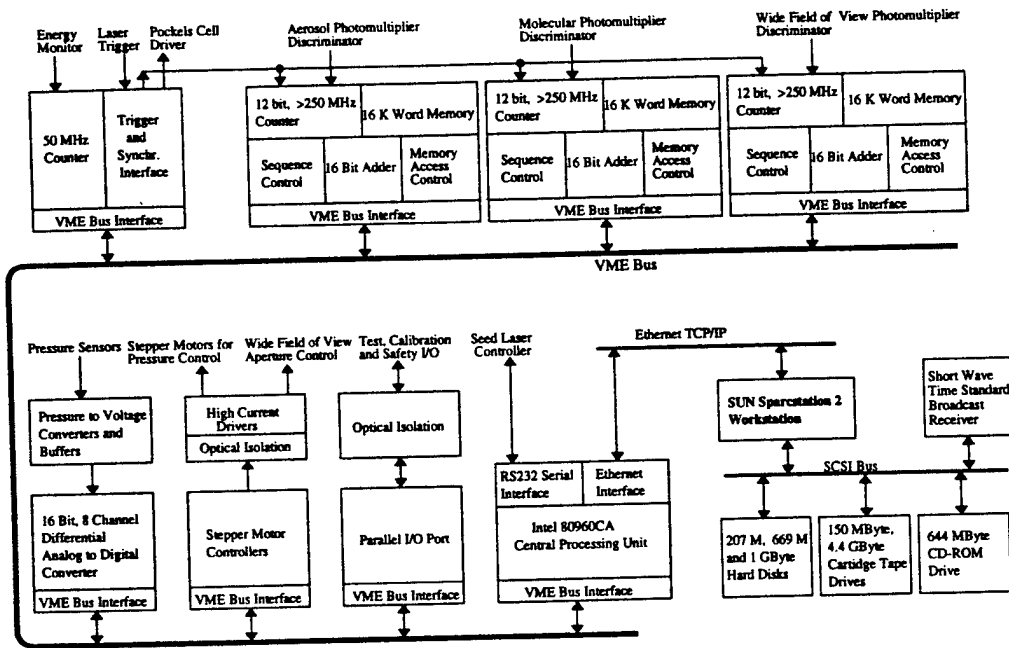


Figure 8. The HSRL data acquisition system.

The new counter design has improved the background light measurement accuracy of the HSRL. Instead of interrupting the data taking every 3.5–7 min for background and calibration checks (as was made with the system described by Grund¹⁰), the new HSRL is capable of measuring the background light simultaneously with the data. The maximum resolution of the data system is increased from 256 to 4096 range bins per channel. In the HSRL, the amount of background light in the measurement is calculated from the measured profile by using the upper altitudes of the lidar profile. The signal together with the background light is saved and therefore different kind of background corrections can be studied. Currently, the measured HSRL profiles are background corrected by assuming the signal above ~33 km to be background. By averaging the upper range bins together, the average amount of background in the measurement is calculated. The disadvantage of the current background correction method is that some of the signal can still be originated from Rayleigh scattering

leading into an overestimate of the amount of background light for altitudes 33 km and higher. A development of a background correction method that removes the Rayleigh scattering contribution from the background is currently in progress.

Photomultiplier afterpulsing can be seen as multiple output counts for a single input photon³⁰. The afterpulsing could be caused by positive electron production in the dynode chain. The afterpulse pulses are time delayed compared to the signal from incident photon and the time delay is proportional to the path length for electron propagation. The signal originated from a short light pulse and measured with the HSRL can be presented in following form

$$\langle S(t) \rangle = \int_0^{t+dt} S(t') \Phi(t-t') dt', \quad (14)$$

where

- $\langle S(t) \rangle$ = signal measured with the HSRL
- $S(t')$ = signal incident on the receiver
- Φ = signal response function, that contains the laser pulse width, datasystem bin width and afterpulsing of the photomultiplier

The afterpulse probability distributions were measured by illuminating the photomultiplier photocathode with a short duration laser light pulse. Pulse counting rates less than one count per 100 ns long data bin per pulse were used. A large number of laser pulses were averaged (~1 hour average). The probability distributions were calculated from the background corrected data. The amount of background light was calculated from the end of data record and the average value was subtracted from data. The measured afterpulse probability distributions of two photomultiplier tubes are presented in Figure 9. The afterpulse probability distribution was found to be different for each tube and therefore a separate correction for each tube had to be implemented to the signal analysis program. With a known afterpulse probability distribution function, the afterpulse contribution can be removed from the measured signal by using deconvolution. The effect of afterpulse correction to the measured signal is presented in Figure 10.

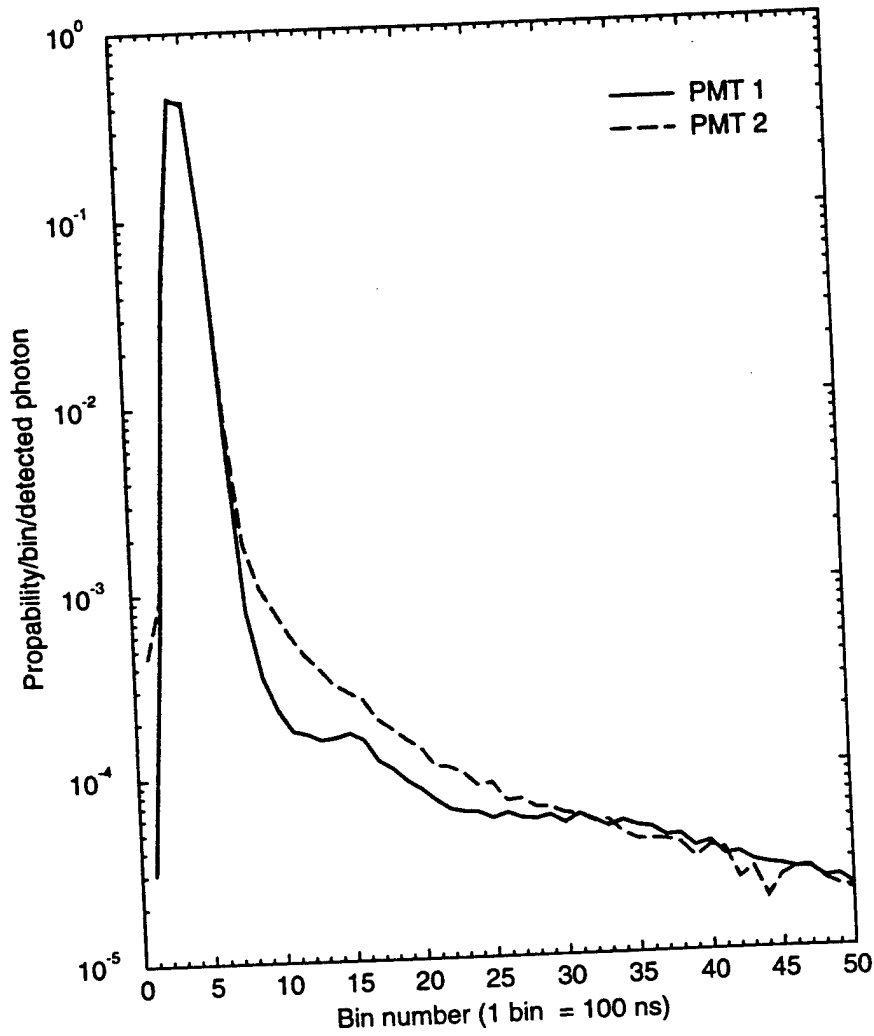


Figure 9. The temporal distributions of two EMI 9863B/100 photomultiplier tubes. The temporal distribution of the measured photons is a convolution of the laser pulse width, bin width of the data system, and the afterpulsing of the photomultiplier. The laser pulse is located in the first bins and the afterpulse can be seen as a decaying tail. The afterpulse distribution of the PMT1 shows better afterpulse behavior than the PMT2.

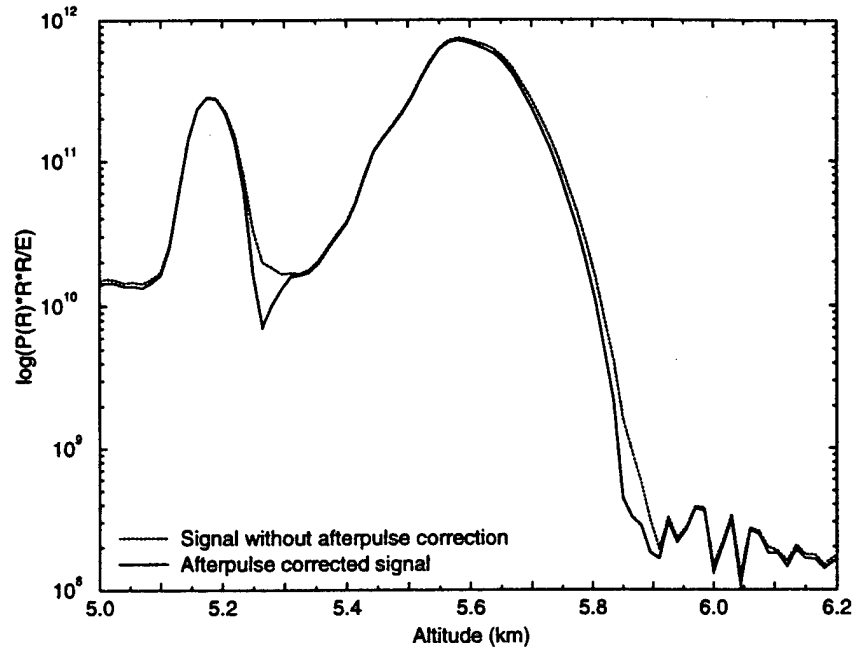


Figure 10. The effect of afterpulse correction to the measured aerosol signal in the case of thick water cloud (at 5.6 km) with an ice crystal precipitation at 5.1 km. The afterpulsing increases the aerosol signal at the end of the cloud, and therefore the geometrical thickness of the clouds is underestimated. The effect of afterpulsing to the molecular signal is similar, and thus a slight overestimate of the optical depth of the cloud is made, if the afterpulse correction is not performed.

The pulse pile-up is seen when all time separated photons are not distinguishable and they overlap. This causes a nonlinear response. In order to be able to separate between counts, a minimum separation time between two pulses is required for them to be distinguished. This time is called resolving time (or dead time). Since the time interval distribution of photons that reach the photomultiplier follow a Poisson distribution, the probability P_o that a pulse overlaps with another pulse inside a certain time interval is given by the following formula³¹

$$P_o = 1 - e^{-Rr} \quad (15)$$

where

τ = resolving time

R = average count rate

In order to obtain the resolving time (dead time) of the photomultipliers, the photomultiplier responses to different count rates were tested. First, light level is set to level which is high enough to generate a pile-up. Then the photomultiplier response to different light levels is measured by changing the light intensity with neutral density filters and recording the signal change. In order to be able to define the resolving time of the photomultiplier, the photon counting was modeled. The pulses coming from the photomultiplier were treated as Poisson distributed signals. The resolving time that produced the best fit between simulated and measured results was used for the pile-up correction. All photomultipliers were found to have ~ 13 ns resolving time. The pile-up correction has to be performed before the afterpulse correction or any other corrections, because the pile-up effect is nonlinear. The pile-up is affected by the signal strength, signal background and afterpulsing and therefore, data has to contain the information from all these factors when the correction for pile-up is performed.

In order to make the pile-up correction for data, the following equation was used

$$N = N_o e^{-R\tau} \quad (16)$$

where

N = measured counts

N_o = actual counts

τ = resolving time

R = average count rate = $\frac{N_o}{dt}$

This equation is solved iteratively for N_o , so that

1. $N_o(1) = N$
2. New $N_o(i+1) = N e^{\frac{N_o(i)}{dt}\tau}$, where dt = bin length [s]

3. Step 2 is repeated until N_0 converges

The effect of pile-up correction to the measured signal is presented in Figure 11.

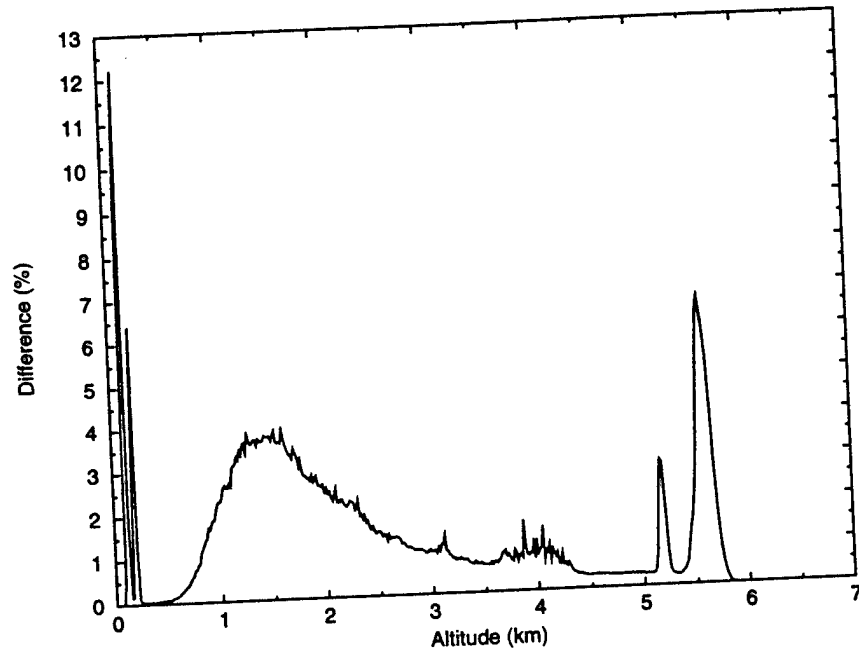


Figure 11. The effect of pile-up correction to the measured aerosol signal in the case of thick water cloud (at 5.6 km) with an ice crystal precipitation at 5.1 km. The calibration fiber signals are shown as spikes at altitudes ~ 0 km. The maximum number of photons measured for the water cloud is 0.68 photons/100 ns bin and after pile-up correction 0.75 photons/100ns bin are observed. Even with this low count rates the effect of pile-up is $\sim 10\%$ and therefore, the pile-up correction is very important when strong returns from clouds are studied.

4 Iodine absorption filter

In order to overcome the limited capability of the high resolution etalon to separate between aerosol and molecular scattering and to increase the system stability and reliability, an iodine absorption filter was constructed. For the first HSRL measurements a 43 cm long cell was made. The cell was made from glass tubing with an attached side arm. Optical quality end windows with anti-reflection coatings were epoxied to the ends. The cell with iodine crystals in a side arm was evacuated and kept at 27 °C. Transferring of the iodine from the absorption cell into the vacuum pump was prevented by evacuating the cell through a cold trap and cooling the side arm with liquid nitrogen. Although the iodine cell can be operated at room temperature, the operating temperature of the cell has to be controlled, because the vapor pressure of iodine is very temperature sensitive³². In the HSRL, the cell temperature is maintained with ± 0.1 °C accuracy by operating the cell in temperature controlled environment.

The iodine spectrum is measured by scanning the laser wavelength by changing the temperature of the seedlaser under computer control. A small amount of laser light is directed into a 100 m long fiber optic delay (Fiber 1 in Figure 4) and sent to the receiver to create a calibration light source. The temperature-wavelength dependence of the scan was determined by using the free spectral range of the high resolution etalon as a reference. This could be made, because the free spectral range of the etalon can be calculated when the length of the etalon spacers is known and the spacing of two (or more) etalon transmission peaks in temperature units can be measured. The calibration was made by simultaneously measuring the transmission spectrum of the high resolution etalon and iodine absorption filter. The simultaneous measurement of the high resolution etalon and iodine absorption filter transmissions was made by measuring the signal reflected from the high resolution etalon (Figure 12) and the signal transmitted through the absorption cell. The pressure in etalon was held constant while the laser wavelength was scanned. The spectrum was normalized by measuring the cell transmittance without the iodine cell.

A part of the measured iodine spectrum is presented in Figure 13. The measured spectrum was compared with a published spectrum¹⁸ and an ~ 0.01 pm wavelength

agreement in relative line positions was observed. The linearity of the temperature scan was confirmed from the free spectral range information of high resolution etalon by performing the scan over more than one free spectral range. Single mode operation between two seedlaser mode hops can be maintained over 20 GHz range (at 1064 nm) and within this range two high resolution etalon free spectral ranges can be covered. During a mode hop the laser frequency jumps back about 10 GHz.

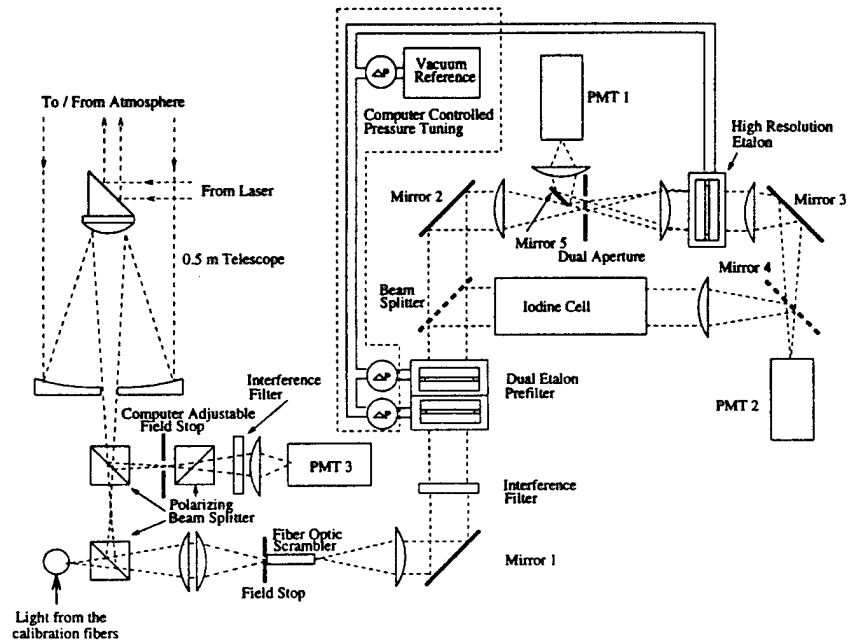


Figure 12. The HSRL receiver used for iodine spectrum calibrations. The same receiver setup was used for the first HSRL measurements with the iodine absorption filter. For data taking the transmission of the high resolution etalon was tuned out from the peak and the etalon was used as a reflector. When the beamsplitter and the mirror 4 are removed from the system, the system returns back to the old HSRL receiver.

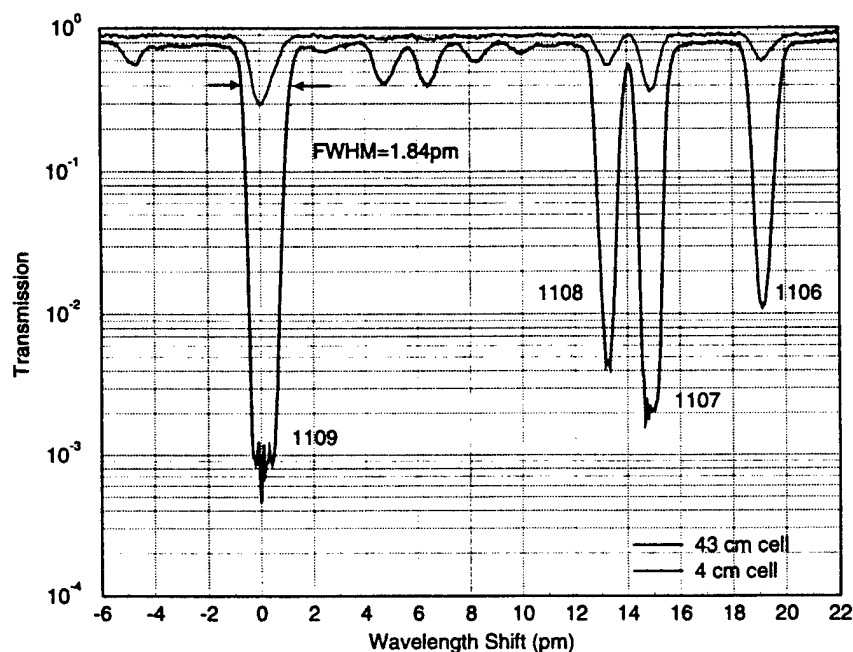


Figure 13. Transmission of a 4 cm and 43 cm iodine cells as a function of wavelength shift. The identification line numbers are from Gerstenkorn and Luc¹⁸.

For initial HSRL measurements the line 1109 (peak wavelength 532.26 nm)¹⁸, which is well isolated from the neighboring lines, was chosen. The full width half maximum width of the line is ~ 1.8 pm and the peak transmission is $\sim 0.08\%$. The hyperfine structure of the peak 1109 defines the asymmetric shape of the absorption peak³³. In fact, the line 1109 is a combination of two rotational vibrational transitions with different hyperfine structures.

The iodine absorption cell provides a robust filter for the HSRL, because it is not dependent on the mechanical alignment of the filter or the angular dependence of the incoming light. Another advantage is the stability of the absorption characteristics. This provides a stable long term operation. The strength of observed absorption line is dependent on the line strength, and the length, temperature, and pressure of the cell. By controlling the operating environment and with a nearly leak proof system, the

current iodine cell is operated for several months without any maintenance. During this time, a small change in absorption strength and line width were observed due to a small leak that was caused by the iodine penetrating through a hose. Also the iodine was found to condense into the walls of the cell, but even during a long period of time, the amount of condensation has been small and $\sim 10\%$ extra absorption is observed. The condensation can be prevented by operating the tip of the side arm couple degrees below the cell temperature. The problems with reactive iodine penetrating through the hoses can be prevented by using a sealed all-glass cell. In a short term operation, the stability of the absorption characteristics has proven to be so good that a system calibration scans from different days can be used for the calculations of the system calibration coefficients. This requires, that the alignment of the receiver optics is stable.

An absorption filter offers a high rejection against aerosol scattering and therefore it makes the separation between aerosol and molecular scattering easier. Also, a wide dynamic range in rejection against aerosol scattering is achieved by simply changing the vapor pressure or the length of the cell. Comparison between high resolution etalon and iodine absorption filter performance is presented in Figure 14. A 2:1 separation between molecular and aerosol scattering by the etalon (Figure 14.b) is measured compared to a 1000:1 separation in the iodine cell when operated at 27°C (Figure 14.a). The molecular transmission in Figure 14.a and Figure 14.b is calculated by using the Doppler-broadened molecular spectrum at -65°C . This temperature is close to the lowest temperature measured at the tropopause and this gives the smallest transmission through the iodine absorption cell. The molecular transmission of the high resolution etalon and the iodine absorption filter are similar (Figure 14.c). Due to wide absorption line width, the molecular transmission of the iodine filter is more dependent on the air temperature than the etalon. The temperature dependence of the cell transmission is modeled by using the table values of iodine vapor pressure³² (Figure 14.d). Calculations show, that by changing the cell temperature from 27°C to 0°C , the online transmission can be tuned from 0.08% to 60%.

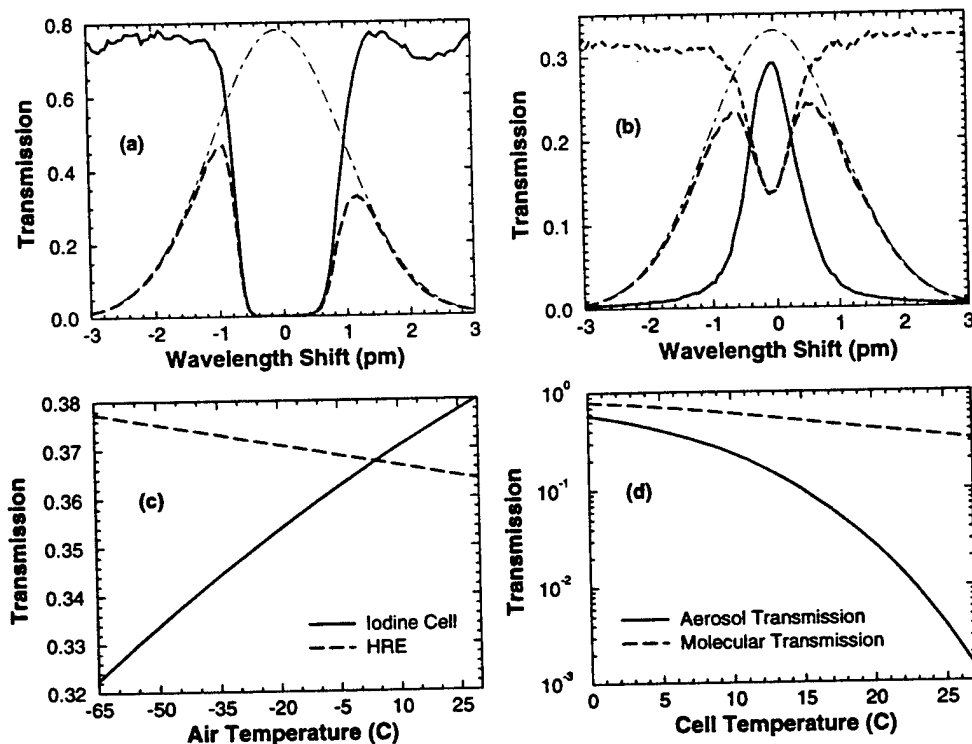


Figure 14. (a) Transmission of 43 cm cell (solid line) together with the molecular transmission (dashed line) at -65 °C air temperature as a function of wavelength shift. Dot-dashed line shows the calculated molecular spectrum at -65 °C. (b) Etalon transmission (solid line) and calculated molecular transmission (dashed line) as a function of wavelength shift. Dot-dashed line shows the calculated molecular spectrum at -65 °C. (c) Comparison of molecular transmission of high resolution etalon and iodine cell as a function of air temperature. (d) Iodine cell aerosol and molecular transmission as a function of cell temperature.

5 Calibration and tuning

5.1 Calibration theory

The HSRL measures optical properties of aerosols by using the backscatter from atmospheric molecules as a calibration target. In the receiver the signal is separated into two separate signals: one proportional to total aerosol and molecular scattering and the other containing the molecular backscattering together with a small aerosol cross talk component. The measured signals are

$$S_{a+m}(R) = \eta[N_a(R) + N_m(R)] \quad (17)$$

$$S_m(R) = \eta[C_{am}N_a(R) + C_{mm}(R)N_m(R)], \quad (18)$$

where

S_{a+m} = signal measured with the combined channel (PMT1 in Figure 6)

S_m = signal measured with molecular channel (PMT 2 in Figure 6)

N_a, N_m = total number of aerosol and molecular backscatter photons
incident on the receiver field of view

C_{am} = aerosol transmission of the molecular channel relative to
the combined channel

C_{mm} = molecular transmission of the molecular channel relative to
the combined channel

η = system efficiency factor that includes the optical transmission
of the combined channel and its photomultiplier quantum efficiency

These two equations can be solved to present the separated aerosol and molecular backscatter signals.

$$N_m(R) = \frac{S_m(R) - C_{am}S_{a+m}(R)}{\eta(C_{mm}(R) - C_{am})} \quad (19)$$

$$N_a(R) = \frac{S_{a+m}(R) - \eta N_m(R)}{\eta} \quad (20)$$

The calibration coefficients C_{am} and C_{mm} are obtained from a system calibration scan. For calibration the system input aperture is uniformly illuminated with a diffuse

light. The receiver spectral transmission function is measured by scanning the laser wavelength over an 11 pm wavelength range around the selected iodine absorption peak and recording the signals (originated from calibration fiber 1 and calibration fiber 2) with both spectrometer channels (PMT1 and PMT2 in Figure 6). A calibration scan is performed before and after each dataset. When system is running for a long period of time (time \sim 3 hours) the system operation is interrupted and a calibration scan is performed. An example from a calibration scan is presented in Figure 15. In addition to the information on the system spectral transmission, the calibration signals contain information on the beamsplitting ratio between channels. Since the signal measured through the iodine cell is flat at the top of the iodine absorption peak, the determination of the wavelength of the absorption maximum is based on the signal from the reference iodine cell (4 cm cell in Figure 5, calibration fiber 2) and measured with the PMT1. Otherwise, the signals from the first calibration fiber are used for the calibration coefficient calculations.

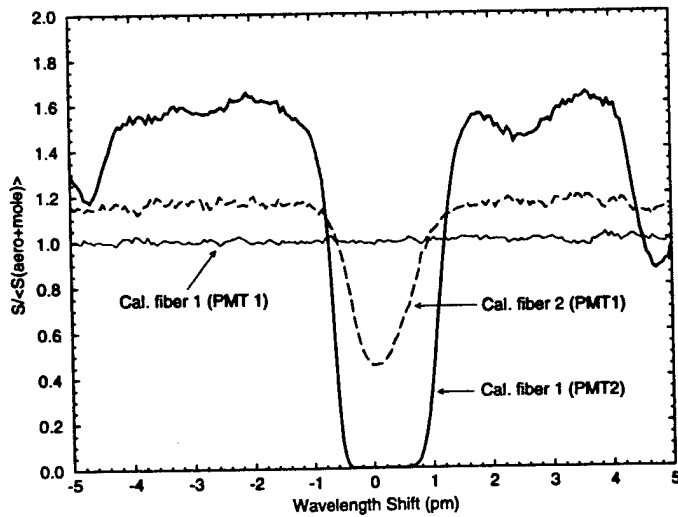


Figure 15. An HSRL calibration scan. The calibration fiber 1 signal that is detected with PMT2 shows the iodine absorption spectrum of the 43 cm long iodine cell. The calibration fiber 2 signal detected with PMT1 presents the absorption spectrum of the 4 cm long reference cell. The signal from calibration fiber 1 and detected with PMT1 is used as a reference.

Since the Doppler-broadening of the aerosol backscatter is negligible, the spectral distribution of the aerosol backscatter can be assumed to be similar to the spectral distribution of the transmitter laser. The measured calibration signals can be presented as a convolution between laser spectral distribution and spectral bandpass of each channel. Therefore, the fraction of the total aerosol backscatter detected by the molecular channel (C_{am}) can be directly obtained from the calibration signals.

$$C_{am} = \frac{S_m(\text{at peak})}{S_{a+m}(\text{at peak})}, \quad (21)$$

where

- S_m = calibration fiber 1 signal detected with the PMT2 at the iodine absorption peak
 S_{am} = calibration fiber 1 signal detected with the PMT1 at the iodine absorption peak.

The fraction of the total molecular backscatter measured by the molecular channel (C_{mm}) is calculated by convoluting the measured filter function with the calculated molecular spectrum.

$$C_{mm} = \frac{\sum_{n=1}^N S_m(\lambda_n) M_{spect}(\lambda_n) \Delta \lambda}{\sum_{n=1}^N S_{a+m}(\lambda_n) M_{spect}(\lambda_n) \Delta \lambda}, \quad (22)$$

where

- S_m = calibration fiber 1 signal detected with the PMT2
 (filter function for molecular channel convoluted with the laser spectrum)
 S_{a+m} = calibration fiber 1 signal detected with the PMT1
 (filter function for aerosol + molecular channel convoluted with the laser spectrum)
 M_{spect} = calculated molecular spectrum
 N = number of points in calibration scan
 λ = wavelength

$\Delta\lambda$ = the wavelength difference between two points in the calibration scan

The divisor on the Eq. 22 is presented as a convolution aerosol and molecular channel. Therefore, the divisor presents the amount of molecular spectrum seen with the combined aerosol and molecular channel. The dividend of the Eq. 22 describes the molecular signal detected through the iodine absorption cell. The molecular spectrum model used in the calculation is presented in a paper by Yip and Nelking³⁴ and it includes the effects of Brillouin scattering as a function of temperature and pressure.

The accuracy of the calibration coefficients is mainly limited by the photon counting statistics. Because the signal transmitted through the absorption peak is small, the error due to photon counting statistics dominates the error in the determination of C_{am} . Therefore, the accuracy of the C_{am} is improved by increasing the photon counting statistics at the absorption peak. Three different ways to increase the photon counting statistics can be considered. First, the signal at the absorption peak can be increased by scaling the light with neutral density filters while scanning. Second, the amount of aerosol backscatter signal can be further decreased into a point where the effects of the photon counting statistics are negligible. Third, longer averaging time can be used.

The disadvantage of using neutral density filters is that the filters have to be well calibrated and the change in the value of neutral density filter has to be recorded into the data so that the signal can be reconstructed back to the absorption spectrum. The disadvantage of the longer absorption cell is that the increased cell length will further decrease the amount of transmitted molecular signal. Also the spectral purity of the laser limits the observable absorption strength. In order to be able to obtain a good photon counting statistics for the signal of the whole absorption peak, a long averaging time is required and therefore the total calibration time would be unreasonable long (~ 1 h) and during this time the laser has time to drift. The drift in the laser output wavelength during the scan effects the width of the measured absorption spectrum.

The current HSRL uses a calibration procedure, where the absorption spectrum is first measured by scanning the laser wavelength so that $\sim 1\%$ photon counting accuracy is achieved for the spectrum around the absorption peak. In order to obtain

a high photon counting statistics in short period of time, the light from the calibration fibers is optimized so that maximum number of photons is detected with small pile-up effects at the detectors. During the scan the location of the peak absorption maximum is detected from the signal through the 4 cm long reference iodine absorption cell. After completing the scan, the seedlaser temperature is set back to the maximum and by using a tuning program (described in more detail in Chapter 5.2) the laser wavelength is kept at the absorption peak until better than 3% photon counting statistics is obtained. With this procedure the effects due to a shift in the laser output wavelength to the width of the absorption spectrum can be minimized and the photon counting errors in the determination of the C_{am} can be reduced from about 20% to 3% within ~ 10 min averaging time.

The atmosphere provides the best reference when the accuracy of the HSRL calibrations is studied. Figure 16 presents an HSRL calibration which is performed simultaneously with data taking. Two different cases are studied. First, a calibration from a thick water cloud is shown. Second, a calibration from clear air is presented. In order to detect the possible range dependence of the calibration, lidar returns from different altitudes are studied. The comparison between calibrations from atmosphere and from the calibration light source also recovers possible misalignments of the system.

The system calibration signal from the iodine absorption spectrum presents a calibration from a pure aerosol target. The agreement between system calibration and atmospheric calibration from a thick water cloud can be seen from Figure 16. Both signals are defined from the ratio of the signal detected through the iodine cell to the signal detected with the combined aerosol+molecular channel. The background corrected, energy normalized signals are used. The data is averaged over a 90 m range. An expected calibration curve from a pure molecular target can be calculated by convoluting the measured iodine absorption spectrum with the calculated molecular spectrum. The calculated molecular calibration together with a measured atmospheric calibration from different altitudes are presented in Figure 16.b-d. The measured absorption spectrum is presented as a reference. For the calculated molecular calibration, the atmospheric temperature, and therefore the width of the Doppler-

broadened molecular spectrum, is calculated by using the temperature values obtained by a radiosonde measurement. The signals from higher altitudes are disturbed by the low photon counting statistics, but otherwise a good agreement between system calibration and atmospheric calibration is obtained and no range dependence in the system calibration is observed. The range dependence of the atmospheric calibration would show up as a noticeable deviation from the system calibration.

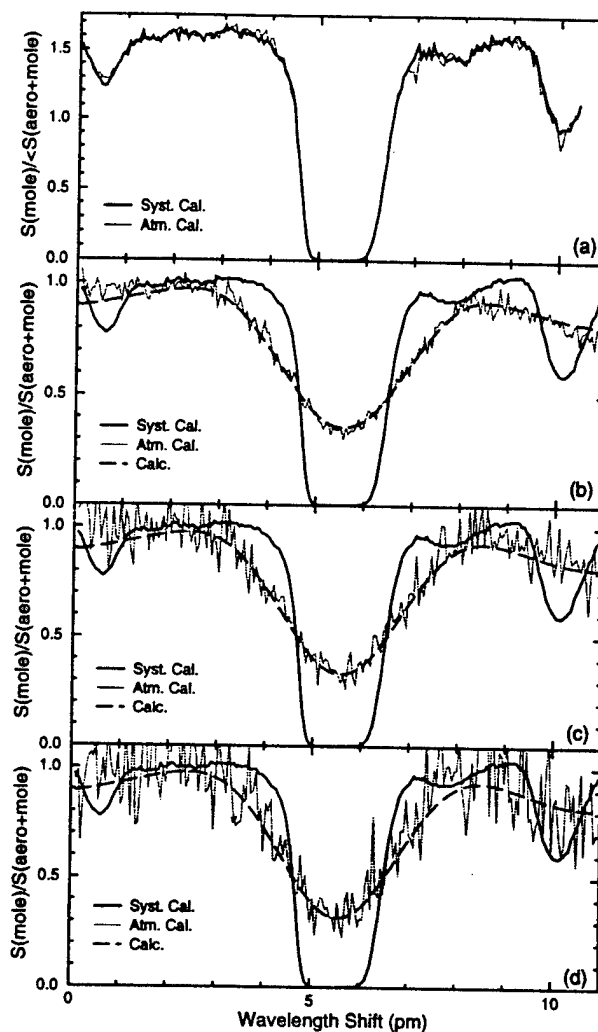


Figure 16. A HSRL calibration scan together with a simultaneous calibration from the atmosphere. Figure (a) shows a calibration from a thick water cloud (thin dashed line) together with a system calibration scan (thick solid line). In figures (c)-(d), the dashed line shows a clear air calibration at 3175 m (b), 5510 m (c), and 7550 m (d). The temperatures at these altitudes were -11°C (b), -32°C (c), and -45°C (d), respectively. The long dashed line presents the expected molecular return. The measured calibration scan is presented as a reference (solid line).

5.2 The laser wavelength locking into the iodine absorption peak

The system calibration is sensitive to the drifts between the transmitter wavelength and the receiver bandpass transmission maximum. The measurements show that the seedlaser drifts at ~ 100 MHz/h rate. In order to achieve a stable long term operation without frequent calibrations, the wavelength of the transmitter laser is locked to the iodine absorption peak. Wavelength locking to the Doppler-broadened iodine absorption line was used because it requires much less power than a locking into a hyperfine structure of the iodine absorption line with Doppler-free technique³³. Compared to the wavelength locking with a high resolution etalon, the advantage of the locking to an iodine absorption peak is that, iodine peak provides an absolute frequency reference. Another technique to lock the laser output wavelength to the Doppler-broadened iodine absorption line was reported by Arie and Byer³⁵. They use Fourier transformation spectroscopy to lock the laser to the center of the Doppler-broadened peak. This method does not require any dither of the laser frequency, but it is more complex.

In the HSRL, the absorption spectrum of the 4 cm long iodine absorption cell is used to provide information about the absorption peak maximum. The absorption peak of the 43 long iodine absorption cell cannot be used as a reference for the wavelength locking because the saturation of the absorption at the peak causes the flat shape of the peak, and because the signal at the peak is small due to the strong absorption. Therefore it does not provide good photon counting statistics for the locking. The length of the reference cell is chosen so that the absorption is $\sim 50\%$. The cell transmission has to be high enough to provide a good photon counting statistics within a short averaging time.

The locking of the laser wavelength to the iodine absorption peak is performed by using an automatic controlling program that works as follows. First, the location of the absorption maximum is detected during a calibration scan. After completing the scan, the program automatically sets the seedlaser temperature to the observed peak. In order to keep the laser wavelength locked to the maximum absorption wavelength, the seedlaser temperature is dithered around the optimum temperature

and information about the ratio of signal from the second calibration fiber to the signal from the first calibration fiber detected with PMT 1 (see Figure 17) is gathered. The seedlaser temperature is kept at temperature that produces the minimum ratio. The basic idea of the tuning program is presented in the following.

The tuning procedure has four steps. First, information about the ratio between calibration fibers is gathered for the seedlaser temperature ($T(\text{peak})$) that was detected to produce the minimum ratio. Then, a temperature $T = T(\text{peak}) + dT$ is applied and the change in the ratio is observed. After gathering enough statistics (~ 30 s), the seedlaser temperature is returned back to the temperature $T(\text{peak})$ and a new value for the ratio at this temperature is measured. After this, the optimum temperature is detected by finding the temperature that produces the minimum ratio. If the temperature $T = T(\text{peak}) + dT$ produced a smaller ratio, then that temperature becomes to the new optimum temperature $T(\text{peak})$. If the ratio for temperature $T = T(\text{peak}) + dT$ was not better, the dithering to temperature $T = T(\text{peak}) - dT$ is performed and the procedure is repeated. The wavelength dither corresponds to temperature change of 0.009°C (0.052 pm). A time history of the dither temperatures for a 9 hour run shows that, the seedlaser temperature is dithered between 3 temperatures under typical operating conditions.

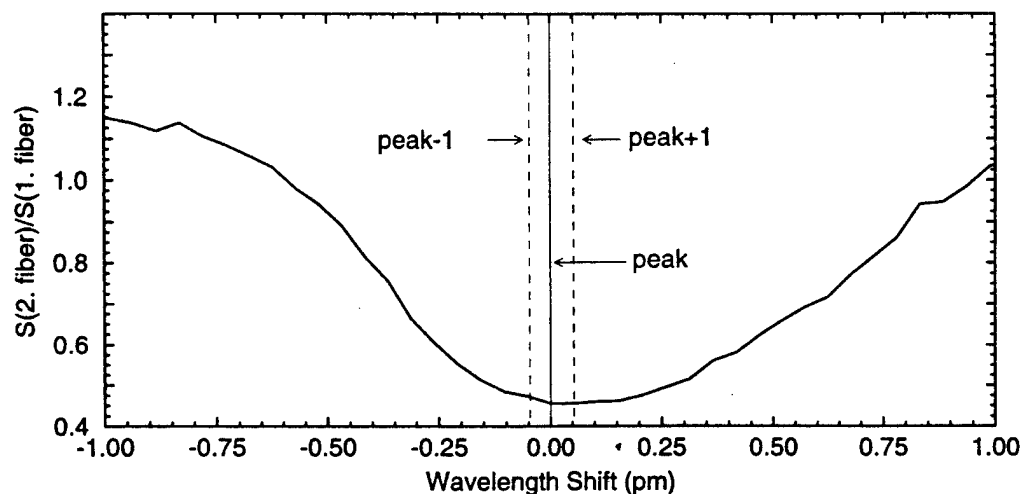


Figure 17. Signal for the frequency locking of the laser. An expanded view from the peak shows that as the temperature is changed in either direction from the detected peak, a change in the ratio is noticed.

Because the absorption peak of the 43 cm long absorption cell is flat around the maximum absorption wavelength, the error due to tuning to the amount of aerosol detected in the molecular channel (C_{am}) is comparable to the photon counting statistics. On the other hand, the error due to dithering to the amount of detected molecular signal in the molecular channel (C_{mm}) is a combination of photon counting statistics and the error between the convoluted signals at different dithering wavelengths. The errors in C_{mm} due to tuning as a function of atmospheric temperature are presented in Figure 18. Figure 18 shows the error in the determination of C_{mm} , when the laser wavelength is tuned off by ± 0.052 pm, but the calculation of C_{mm} is made for the peak wavelength. Also the error due to dithering is shown. The asymmetry of the absorption spectrum makes the errors due to the tuning asymmetric. The total effect of the tuning procedure to the measured profiles has to be calculated as a weighted average of the errors at different dithering wavelengths, because the tuning program is realized so that the laser spends 2/3 of the time at the wavelength that produces

the minimum ratio and 1/3 of the time doing the dithering. Therefore, the total error due to dithering is better than 0.1%, when measurement period is long compared to the dither time. In principle, the error due to wavelength locking can be eliminated by inverting the data by using different calibration coefficients for different dithering wavelengths. This has not been accomplished yet.

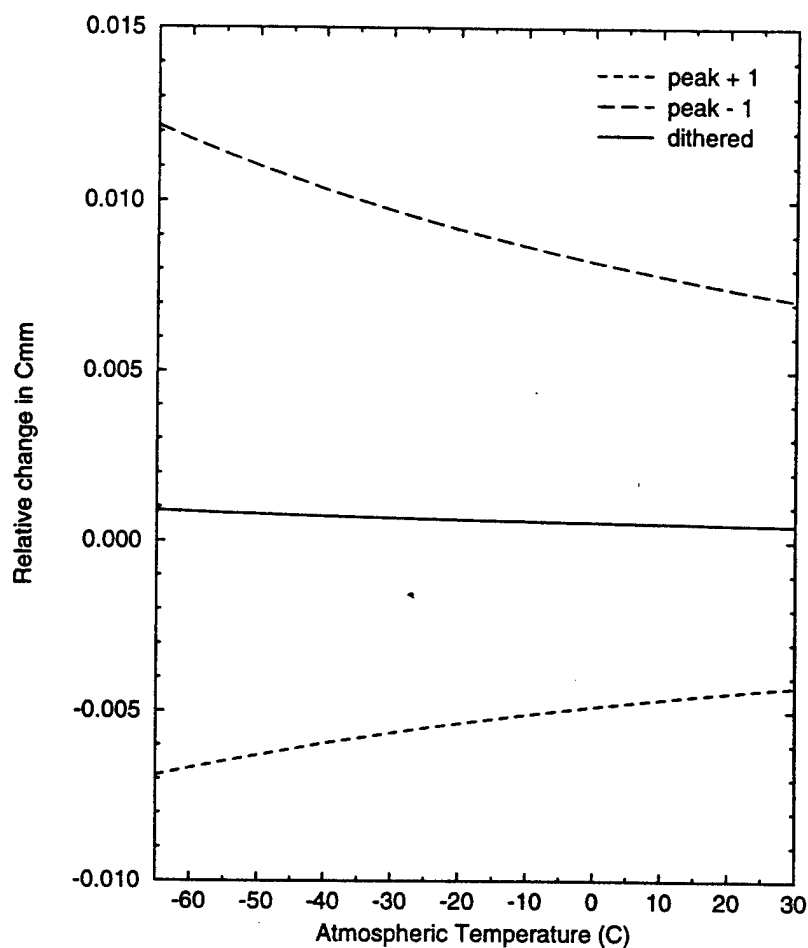


Figure 18. The errors in C_{mm} due to the tuning. Error when the seedlaser temperature is detuned from the optimum temperature by \pm one step (0.009°C) and when the seedlaser temperature is dithered, but the inversion is performed by using the observed peak value.

6 Measurements

Starting from July 1993, the iodine absorption filter based HSRL has been operated at the University of Wisconsin-Madison campus. During this time the HSRL has been routinely operated and the stability and reliability of the system have been tested. As a result, a dataset consisting of ~ 30 different cirrus cloud cases has been obtained with a simultaneous NOAA-11 and/or NOAA-12 satellite overpasses. As an example from the data collected with the HSRL a dataset from November 11, 1993 is shown. This dataset contains a meteorologically interesting case: a cirrus cloud, supercooled water cloud, and ice crystal precipitation together with a strong low level aerosol structure. Figures 19 - 25 present Range Time Indicator (RTI) pictures from the data. Both raw and inverted data are shown along with depolarization and optical depth. The pictures are generated from the background corrected, energy normalized, and range square corrected data.

For the RTI's of the inverted data, the aerosol and molecular signals are separated by using Equations 19 and 20. The optical depth is obtained from the ratio of the inverted molecular profile to the return predicted for the pure molecular scattering (Eq. 10). The color scale shows the signal strength and the white areas are regions where the backscatter signal is larger than the maximum color scale value. The black areas indicate that the signal is smaller than the smallest color scale value.

The Figure 19 shows the raw lidar return detected with the combined aerosol and molecular channel. This profile is similar to the profile obtained with a conventional single channel lidar: the signal from small amounts of aerosol scatterers is dominated by the scattering from molecules, and therefore all aerosol structures are not clearly visible. The ability of the HSRL to separate aerosol and molecular scattering can be seen from the RTI picture of the inverted aerosol signal Figure 20. After inversion, the aerosol structures are more visible and they do not have the decrease with altitude caused by the atmospheric density profile. The ability of the iodine absorption filter to reject aerosol scattering is visible from the RTI of the raw molecular signal (see Figure 21): only a small aerosol cross-talk for the densest parts of the clouds is observed and this is easily removed by the inversion, as can be seen from Figure 22. The phase of the water at different layers can be seen from the depolarization RTI's. Figure

23 shows the raw depolarization observed with the combined aerosol and molecular channel. The inverted aerosol depolarization is shown in the Figure 24. From these pictures, a cirrus cloud at ~ 8 km (depolarization ratio $\sim 40\%$) and a supercooled water cloud at 5 km (depolarization ratio $\sim 1\%$) with ice crystal precipitation can be easily separated. For low level aerosols (0-3.7 km), a two layer polarization structure is seen. The small increase in water cloud depolarization as a function of cloud height is an indicator of multiple scattering. The low molecular depolarization is presented in Figure 25. The low depolarization ratio values with small signal to noise ratio show up in the picture as noise.

The optical depths on the different parts of the data set can be seen from the Figure 26. The optical depth of the cirrus cloud between 7 and 10 km is ~ 0.4 . The water cloud at ~ 5 km has an optical depth of 2.5-3. The extinction through the ice crystal precipitation below the water cloud and the extinction through the water cloud can be seen as a change in the color scale as a function of altitude. The optical depth of the ice crystal precipitation is ~ 0.1 .

A more detailed analysis of the dataset is presented in the following sections. First, the depolarization measurements are discussed in Chapter 7.1. The effects of multiple scattering to the depolarization measurements are shown. The measurements of the cloud particle sizes are not included to this study. The depolarization data from August to November 1993 is analyzed and a summary from the observed depolarizations as a function of atmospheric temperature is given. Second, an example from a measurement of scattering ratio, aerosol backscatter cross section, and optical depth is given together with error estimates for the optical depths (see Chapter 7.2). The temperature dependence of the Doppler-broadened molecular spectrum enables the measurements of the atmospheric temperature by the HSRL. Preliminary results from a temperature measurement are presented in Chapter 7.4.

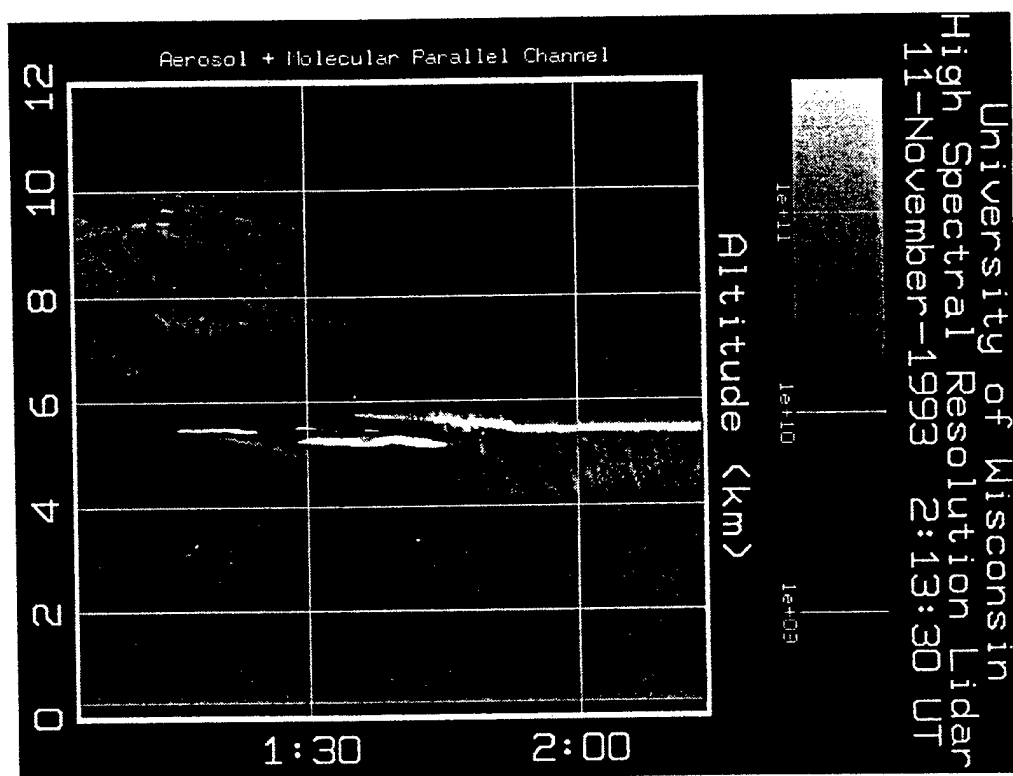


Figure 19. The raw lidar return presenting the combined aerosol and molecular channel return. A water cloud layer with an ice crystal precipitation are seen at 5 km. Above the water cloud, a cirrus cloud can be seen. The low level aerosol structure between 0 and 3.7 km is hardly visible because it is damped by the molecular backscatter signal.

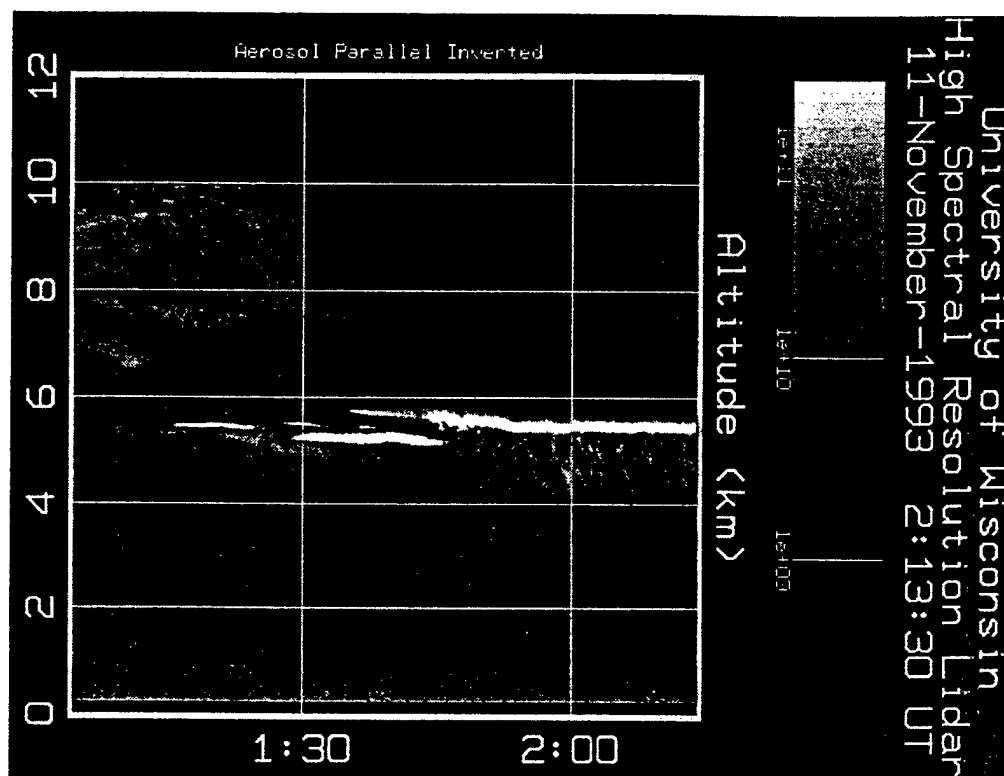


Figure 20. The inverted aerosol profile. After separating the aerosol and molecular backscatter returns, the layers where the aerosol backscatter signal is small compared to the molecular signal are clearly visible. The largest difference is seen for the low level aerosol layer between 0 and 3.7 km.

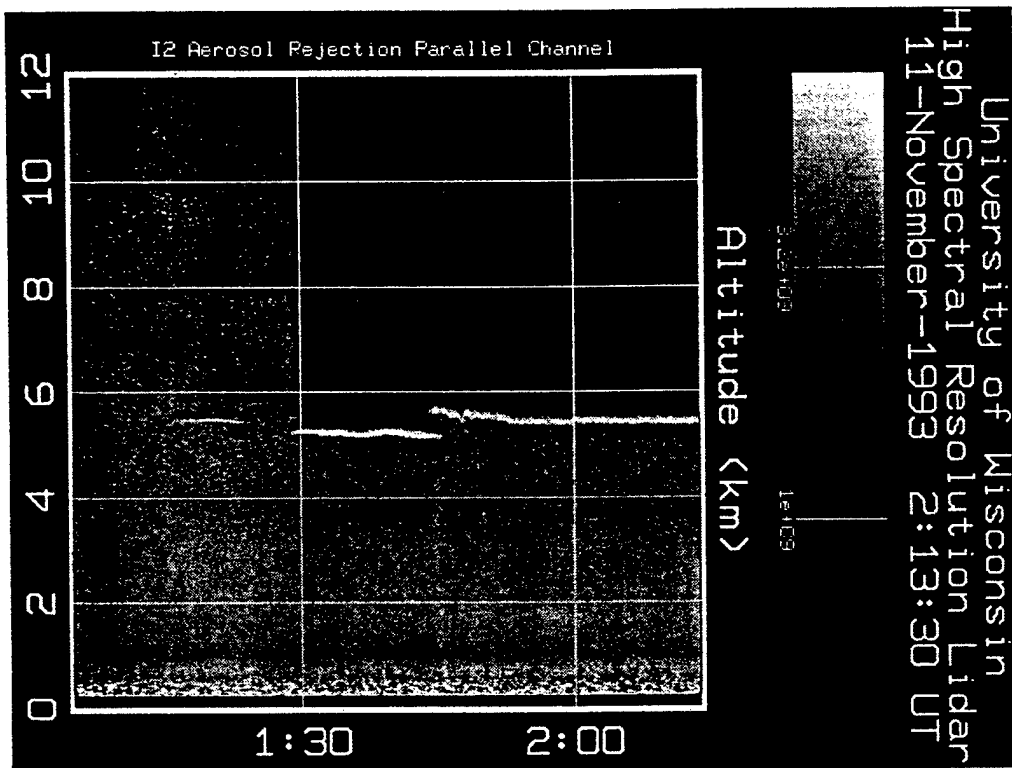


Figure 21. The raw molecular return. A small aerosol cross talk signal is visible for the densest parts of the water cloud at ~ 5.5 km. The dark areas indicate that very little or no return through parts of the water cloud is observed.

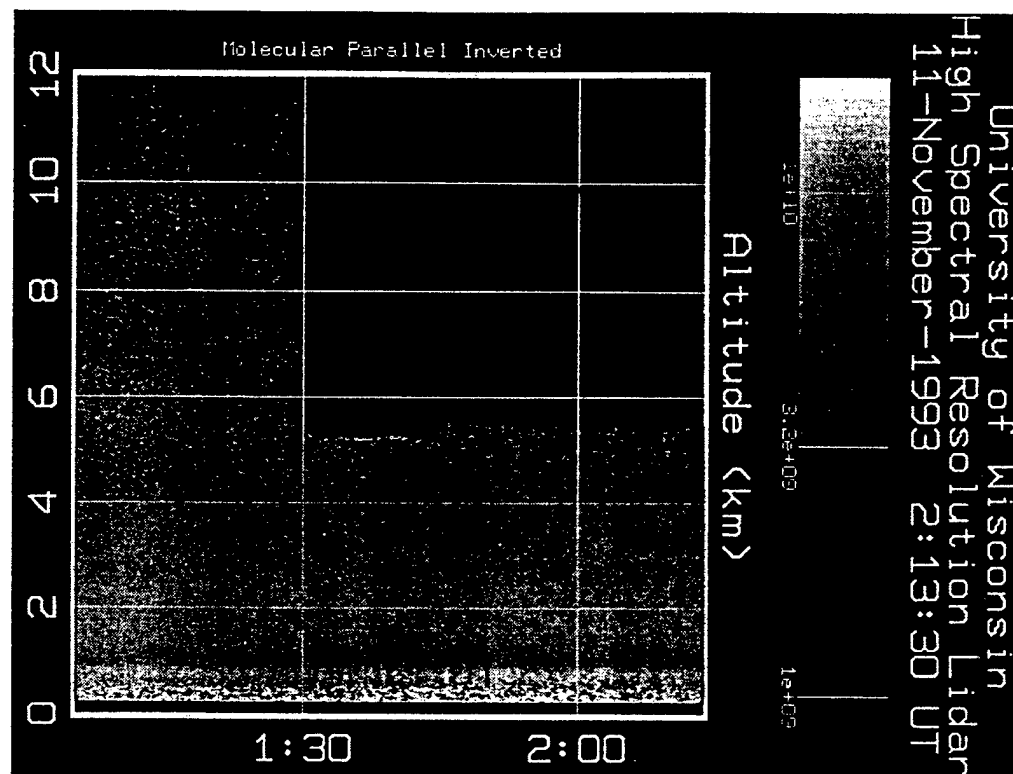


Figure 22. The inverted molecular profile. After the inversion, the cross talk that was visible in Figure 21 cannot be seen and the inverted molecular profile therefore presents the atmospheric extinction at various points of the dataset. The inaccuracy of the overlap correction can be seen as a darker line at ~ 1 km.

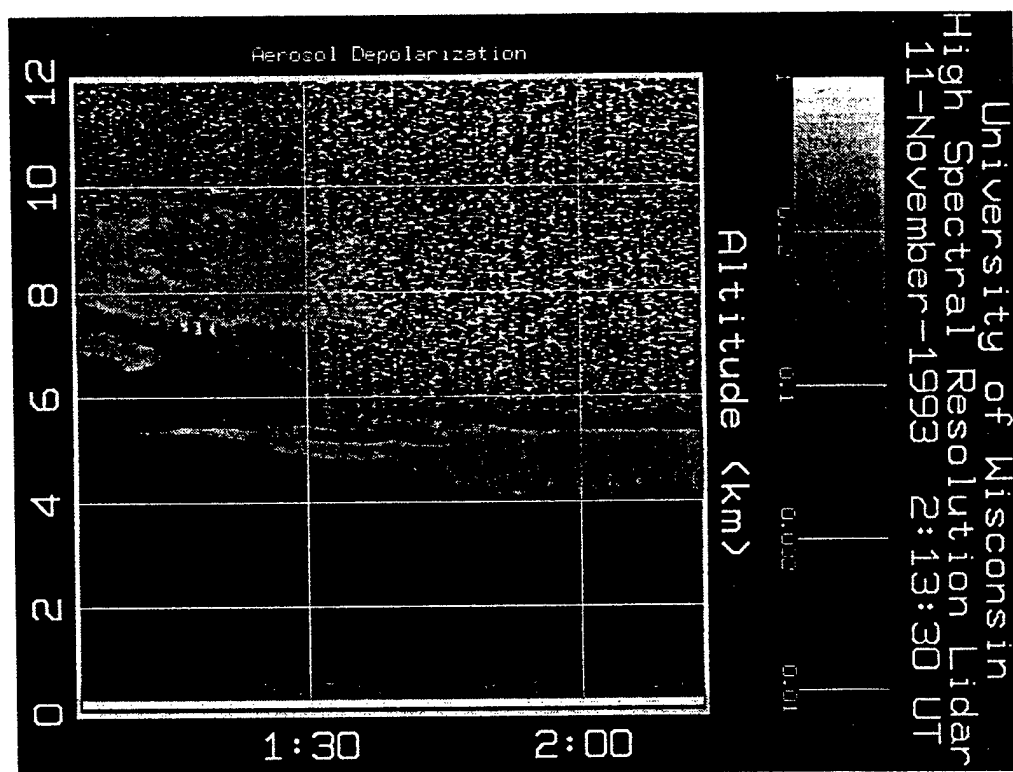


Figure 23. The raw aerosol depolarization combined with the molecular depolarization. The picture shows the depolarization ratio that is seen with a lidar that cannot separate the aerosol and molecular backscatter signals. The depolarizations for altitudes with low aerosol content are dominated by the molecular depolarization. The parts of the cirrus cloud and parts of the ice crystal precipitation between 4 and 5.5 km show depolarization ratios that are $\sim 10\%$, and those layers could be expected to contain mixture of ice and water. Some parts of aerosol layer between 2 and 3.7 km show depolarization of $\sim 3.5\%$. The water cloud at 5.5 km has $\sim 1\%$ depolarization. The increase in the water cloud depolarization as a function of altitude is due to the multiple scattering.

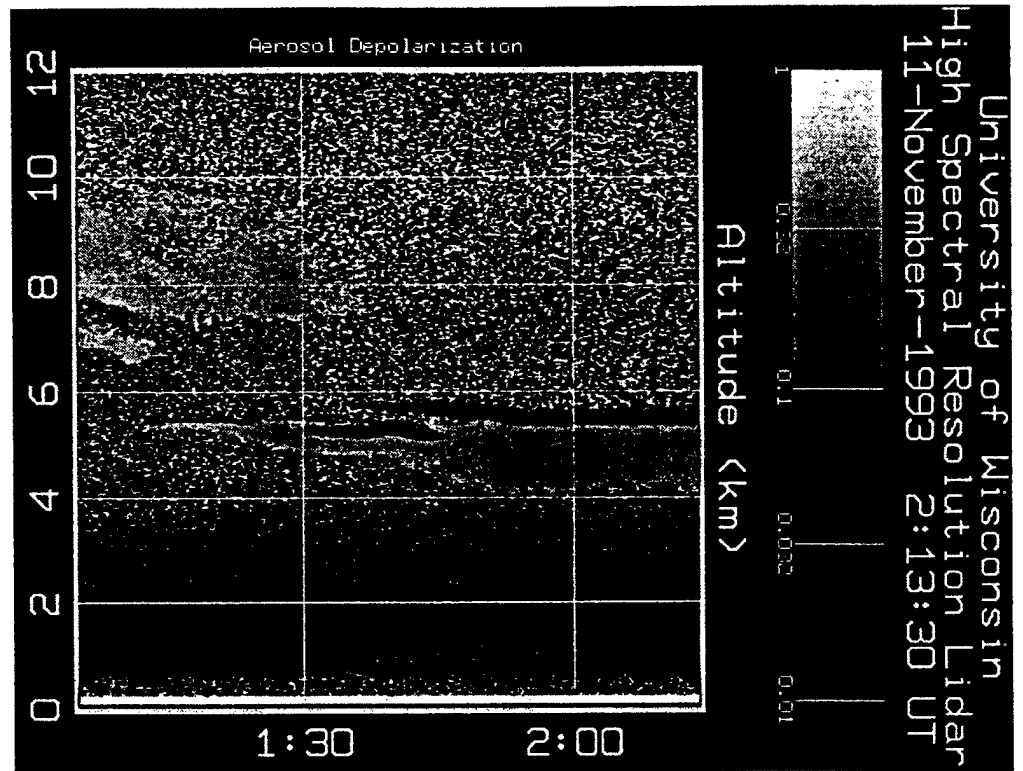


Figure 24. The inverted aerosol depolarization. After inversion, the cirrus cloud depolarization of $\sim 40\%$ indicates pure ice depolarization. The ice crystal precipitation falling out from the water cloud show similar depolarizations values. The low level aerosol structure shows a two layer polarization structure. A $\sim 1\%$ depolarization ratio for the layer between 0.5-2 km is observed indicating nearly spherical particles. The depolarization of the layer between 2 and 3.7 km shows a $\sim 5\%$ depolarization.

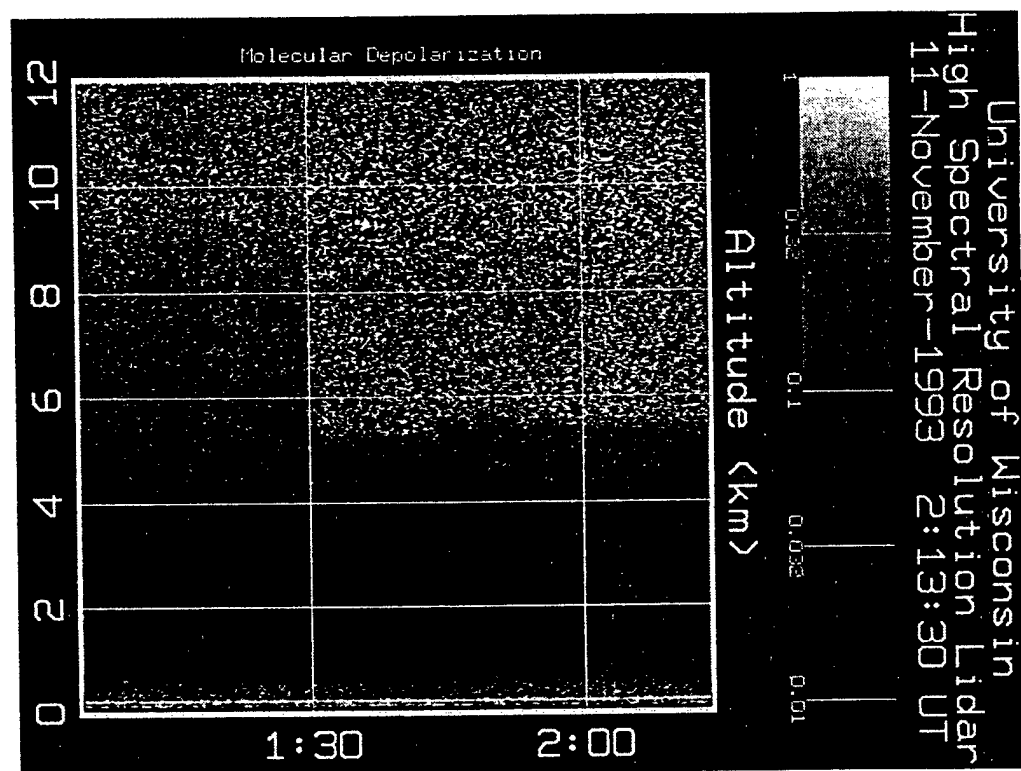


Figure 25. The inverted molecular depolarization. A less than 1% molecular depolarization is observed. The increase in the depolarization variations at the higher altitude is due to the low signal to noise ratio.

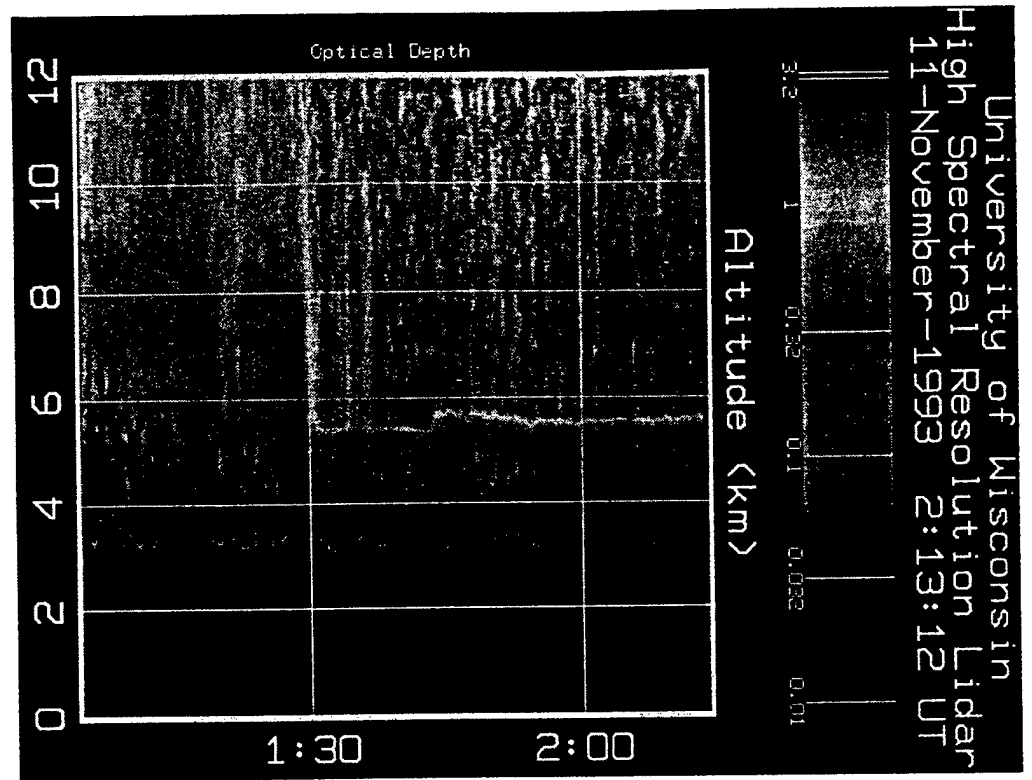


Figure 26. The optical depth. The optical depth above 3 km is shown. The optical depth of the cirrus cloud between 7 and 10 km is ~ 0.4 . The water cloud at ~ 5 km has a optical depth of 2.5-3. The extinction through the ice crystal precipitation below the water cloud and the extinction through the water cloud can be seen as a change in the color scale. The optical depth of the ice crystal precipitation is ~ 0.1 .

6.1 Depolarization ratio

Lidar measurements of atmospheric depolarization can be used to distinguish between liquid and solid phases of water in the atmosphere³⁶⁻³⁸. The quantity to describe the degree of polarization is the linear depolarization ratio δ

$$\delta = \frac{I_{\perp}}{I_{\parallel}}, \quad (23)$$

where I_{\perp} and I_{\parallel} are the measured perpendicular and parallel backscatter intensities in respect to the transmitter polarization axis. The backscatter signal of a linearly polarized laser beam from spherical particles is totally linearly polarized ($\delta = 0$). The particles can be assumed to be spherical in case of wet haze, fog, cloud droplets, and small raindrops. The depolarization of the pure molecular atmosphere is nonzero, because of the anisotropy of the air, and therefore a 0.37–0.4 % depolarization for the Cabannes line is expected^{39,40}. The depolarization of the molecular return that includes the Cabannes line and the rotational Raman lines is $\sim 1.5\%$ ⁴⁰. If particles are nonspherical (as ice crystals, snow flakes or dust particles) or if the backscatter signal has a multiple scattering contribution, the backscattered signal contains a cross-polarized component ($0 < \delta < 1$). A specular reflection from a oriented ice crystal layer provides a small depolarization, which therefore can be misinterpreted as the backscatter signal from a water cloud, but the off vertical pointing direction of the HSRL is expected to prevent this.

Lidar studies of atmospheric polarization have been traditionally based on a technique, where a linearly polarized laser beam is sent to the atmosphere and the received polarization components are separated by a polarization cube and detected by a pair a photomultiplier tubes, one for each polarization component. This method requires a precise calibration of the receiver in order to avoid the problems due to differences between channels in optics, and in photomultiplier sensitivity.

In the new HSRL (see Figs. 5 and 6), the polarization measurements are made by using one transmitter laser and one detector for both polarization components. The transmitted laser beam is linearly polarized, and for polarization measurements the polarization of the transmitted laser beam is rotated by 90 degrees on alternative laser pulses by a Pockels cell. In the receiver, the signal parallel to the transmitter

polarization axis and the signal perpendicular to that are separated and cleaned by a polarization cube pair. Since the polarization of the transmitted laser shot alternates between two subsequent laser shots, the same detector can accurately measure both polarization components and therefore no calibration of the receiver is required. The 250 μs time separation between laser pulses insures, that both depolarization components are measured from the same atmospheric scatterers. The depolarization variations as a function of field of view can be studied with the new WFOV-channel. The effects of specular reflection from a horizontally oriented crystal layer are minimized by tilting the receiver by 4 degrees from the zenith. With the HSRL, separate measurements of aerosol and molecular depolarizations can be made.

Depolarization measurements are affected by presence of multiple scattering when a lidar is used to probe dense clouds. Because the amount of detected multiple scattering is dependent from the cloud particle size, range from the cloud, optical depth of the cloud, and the field of view of the system, typical systems with 1-5 mrad field of views have difficulties separating between water and ice for dense clouds. In order to separate between water and ice for optically thick clouds, the HSRL uses a 160 μrad field of view for the spectrometer channels.

Figure 27 represents an example of the multiple scattering effect on the measured depolarization. Figure 27.a. shows the measured energy and range square corrected signals from a supercooled water cloud with ice precipitation. For the WFOV-channels, 0.22, 0.65, 1.1, and 1.6 mrad field of views are used. The WFOV-channel measurements are then compared to the measurements of the 0.16 mrad field of view channels. The amount of multiple scattering in the signal is calculated from the ratio of the WFOV-signal to the signal simultaneously measured with the narrow field of view channel (see Figure 27.b.). Figure 27.c shows the depolarization ratios for different field of views and the Figure 27.d shows the ratio of the WFOV depolarization to the narrow field of view depolarization. For the optically thin ice crystal precipitation layer, the change in depolarization as a function of field of view is hardly noticeable. The change from ice to water shows up as a drop in the depolarization ratio. All field of views show a low depolarization for the water cloud base but as soon as the signal penetrates deeper into the cloud, an increase in the depolarization

as a function of field of view can be observed. Inside 300 m the multiple scattering effects in the cloud will increase the depolarization of the larger field of views up to the level which is comparable with the observed ice crystal depolarization and therefore, the separation between ice and water becomes impossible. The low values of depolarization observed with the narrow field of view channel and with the smallest WFOV field of view show that the narrow field of view effectively suppresses the effects of multiple scattering. Therefore, the HSRL signals from these field of views can be used to separate between ice and water clouds even for optically thick clouds. On the other hand, information from depolarization and signal strength variations as a function of field of view can be used to verify multiple scattering calculations.

Theoretically, the depolarization of the spherical droplets should be zero, but the depolarization ratios observed for the water cloud at 5.5 km is $\sim 2\%$. In the cases of water clouds with an ice crystal precipitation, the non-zero values of depolarization ratio can be explained by the presence of ice. Because the water cloud is precipitating ice, there has to be some ice mixed with water in the cloud. The scattering from the cloud base is ~ 20 times larger than signal from ice crystal precipitation. Based on this ratio, $\sim 2\%$ ($\sim 1/20 \times$ ice depolarization of 40%) depolarization for the cloud base depolarization can be expected due to the presence of ice crystals with $\sim 40\%$ depolarization.

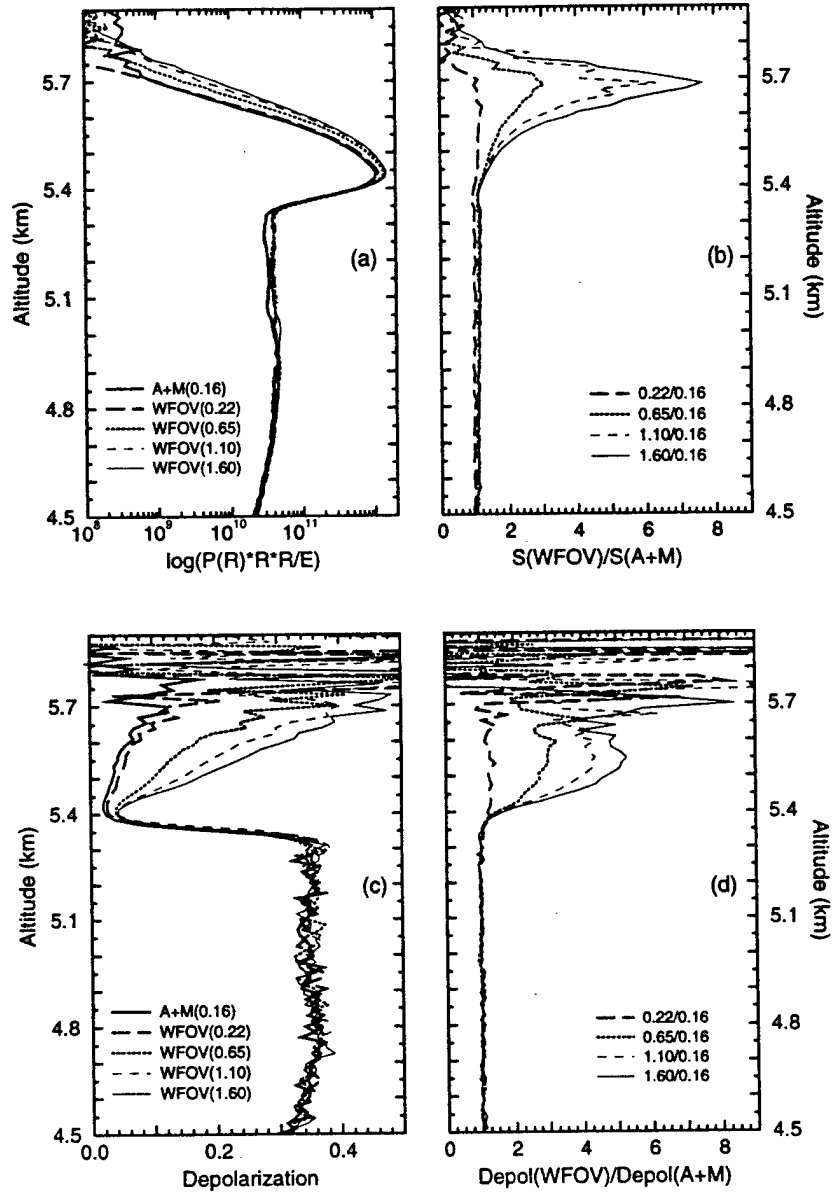


Figure 27. Effects of multiple scattering on depolarization in the backscatter return from a water cloud at 5.5 km with ice crystal precipitation between 4.5 and 5.3 km. Data obtained on November 11, 1993 02:04-02:14 UT. (a) Measured signals. (b) Ratios of measured WFOV signals to 0.16 mrad field of view signal. (c) Measured depolarization ratios. The cloud base depolarization of the smallest field of view at 5.4 km is $\sim 2\%$. (d) Ratios of the measured WFOV depolarizations to the depolarization of the 0.16 mrad field of view channel.

The capability of the HSRL to distinguish between aerosol and molecular scattering allows separate polarization measurements. This is important when layers with a low aerosol content are studied. The effects of the molecular scattering on the observed depolarization can be seen by comparing the raw and inverted aerosol depolarization ratios. For the cases where the amount of aerosol scatterers is small, the signal from molecular scattering dominates the depolarization picture (see Figure 23). Therefore, aerosol depolarizations similar to the molecular depolarization can be seen and also parts of the cirrus cloud and ice crystal precipitation show depolarization ratios which are close to the depolarization of the supercooled water or mixture of ice and water (green areas in the raw aerosol depolarization RTI). After inversion a clear difference in the depolarizations is seen: the depolarization of the low level aerosols is better defined and the depolarization of the cirrus shows that the cloud contains pure ice crystals (Figure 24). Therefore, a clear separation between ice and water can be based to the depolarization ratios calculated from the inverted aerosol profiles. The effect of the inversion to the depolarization ratio is also visible from the Figures 28 - 29.

The profile of the raw aerosol depolarization shows the depolarization of the combined aerosol+molecular channel and therefore, it shows the depolarization ratio which is seen with a conventional single channel lidar. The raw molecular depolarization contains the depolarization component of the aerosol cross talk together with the molecular depolarization. In the same figure, the separated aerosol and molecular signals are shown with the inverted aerosol and molecular depolarizations. Figure 28 shows a two layer water cloud with an ice crystal precipitation. The peaks of the water clouds are observed at 5.2 and 5.6 km and the corresponding low depolarization values are 1-2 %. A small increase in the depolarization with penetration depth is observed. The values of raw depolarization of the ice crystal precipitation are close to those of water and ice mixture, but the inverted depolarization ratios show a clear ice depolarization. After inversion the increase in aerosol depolarization at 2-3.7 km is also very clear. The Figure 29 shows a water cloud layer at 5.4 km with a more dense ice crystal precipitation. With increased backscatter signal from ice, the value of raw depolarization ratio indicates clear ice and therefore the effects of molecular

depolarization do not show up so clearly, even though a change in depolarization ratio is observed after the inversion.

The depolarization observed in the clear air is 0.7–0.8 %, when the observations are made without the low resolution etalons. When the low resolution etalons are used, the depolarization is 0.55–0.6 %. The expected value for the molecular depolarization of the Cabannes line is ~ 0.4 and ~ 1.44 for the Cabannes line^{39,40} and rotational Raman lines⁴⁰. The HSRL observations show a 1.5 % depolarization for the signal from the rotational Raman lines and Cabannes line. Because the system filter bandpass admits a small fraction of the rotational Raman lines (75 % depolarization) and simultaneously blocks part of the Cabannes line, the molecular depolarization value measured by the HSRL is larger than the expected Cabannes line depolarization. The amount of transmitted rotational Raman signal is temperature dependent. A model to calculate the expected depolarization was written. This model includes the rotational Raman spectrum for nitrogen and oxygen, molecular spectrum including effects of Brillouin scattering, and spectral transmissions of different filters. The polarization that correspond to different atmospheric temperatures can be calculated. The ratio of rotational Raman signal to Rayleigh signal is chosen so, that a 1.44 % depolarization for the clear air is observed. These calculations show, that a 0.56 –0.62 % depolarization is expected for the case where no low resolution etalons were used. A 0.402 –0.425 % depolarization is expected, when one or two etalon are used. The depolarization observed with the HSRL are larger than the expected values. The cause of the additional depolarization in the HSRL measurements is currently unknown.

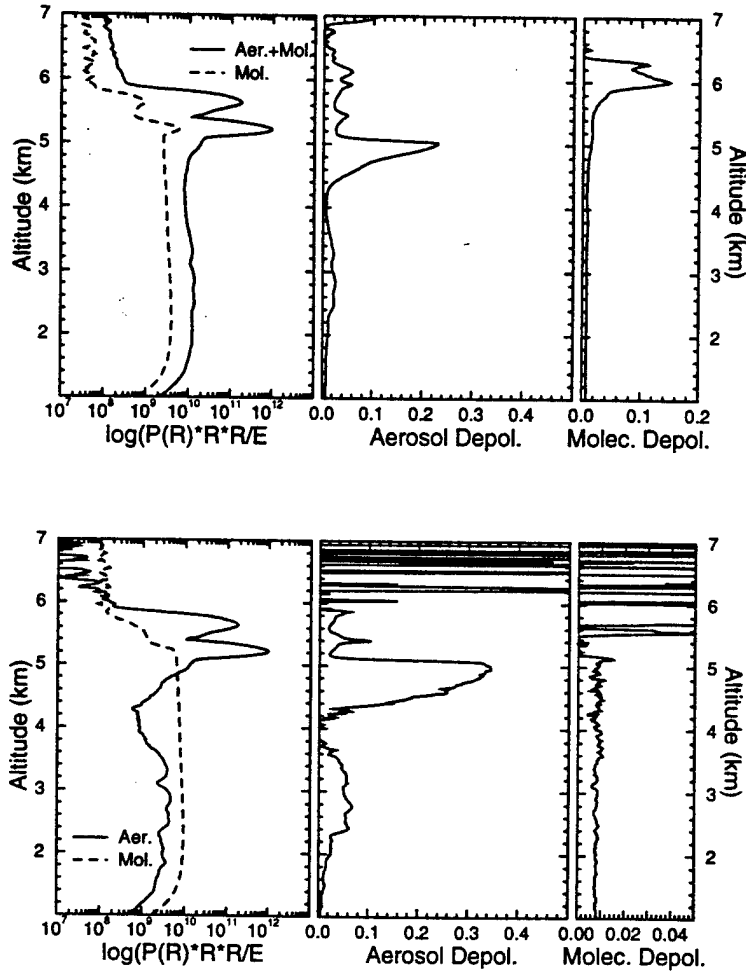


Figure 28. Raw and inverted depolarization ratios of clear atmosphere with ice crystal precipitation and two water cloud layers above it (November 11, 1993 01:35-01:47 UT). The upper set shows the raw aerosol and raw molecular profiles together with the depolarizations. The lower set shows the inverted profiles with the inverted depolarizations. The water clouds are observed at 5.2 and 5.6 km altitudes. The low water cloud depolarization values can be observed from the aerosol depolarization figures. The small increase in water cloud depolarization as a function of penetration depth is due to the multiple scattering. The weak signal from the ice crystal precipitation is visible 4.3-5.1 km. Because of the low ice crystal content, the raw depolarization ratios of the ice crystal precipitation shows values that would indicate mixed phase, but after the inversion a clear ice crystal depolarization is visible. The clear air aerosol depolarization is less than 6%. The observed molecular depolarization is 0.8 %.

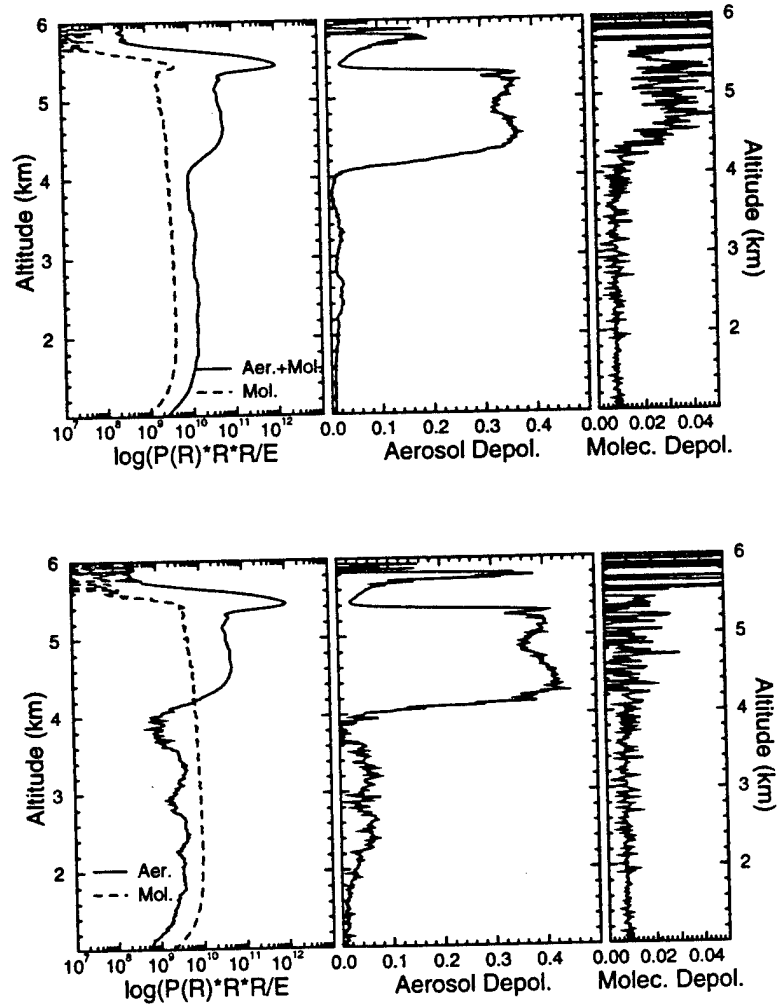


Figure 29. Raw and inverted depolarization ratios of a thin cirrus cloud and a thin water cloud with an ice crystal precipitation (November 11, 1993 01:55-02:01 UT). The upper set shows the raw aerosol and molecular profiles along with the raw depolarization ratios. The lower set shows the inverted profiles with the inverted depolarization ratios. The water cloud at 5.5 km has a low depolarization value $\sim 1.5\%$ at the cloud base and it increases towards the cloud top due to the multiple scattering. The dense ice crystal precipitation is visible between 4 and 5.4 km. Because the ice crystal content of the precipitation is large compared to the molecular backscatter, only small difference between raw and inverted aerosol depolarizations is observed. The raw molecular depolarization shows a small increase for the cloud, but after the inversion a constant 0.8% depolarization is observed.

The depolarization data for cirrus clouds obtained between August and November 1993 have been analyzed. A summary of the observed depolarization ratios as a function of temperature are presented in Figure 30. In this study only clouds with scattering ratios greater than 0.5 were used. This was made in order to fully separate cloud depolarizations from noisy clear air depolarizations. The values of clear air depolarizations are low and affected by the photon counting statistics. Because the HSRL measurements have shown, that the scattering ratios of clear air aerosol and stratospheric aerosols can exceed values 1-3, the use of the scattering ratio of 0.5 does not guarantee a clear separation between clouds and clear air aerosols. On the other hand, the scattering ratios of the cirrus clouds can be below 1. Therefore, a visual separation between cirrus clouds and clear air aerosols is made and only the cloud altitudes are included to the study. In this study, 2 min averaging times for the data were used. By using a short averaging time, the errors due to temporal changes of the atmosphere were minimized. The atmospheric temperatures were obtained from radiosonde measurements and temperature intervals of 5 °C were used. Water clouds at cirrus cloud altitudes were separated from ice clouds based on the depolarization ratio values. Clouds with depolarization ratio values less than 15 % were classified as water clouds.

The high depolarization values of the cirrus clouds are easily separable from the water cloud depolarizations. The average cirrus cloud depolarization varies from 33% to 41% showing an increase towards the colder temperatures. Part of this can be expected to be from different shape, size, and orientation of the ice crystals at different temperatures^{41,42}. The size and shape of the ice crystals have been found to be different at different temperatures and the crystals have been found to have a preferred orientation. A similar increase in cloud depolarization towards colder temperature was observed by Platt *et al.*⁴³. His study was made for midlatitude and tropical cirrus and the depolarization values for temperatures from -30°C to -10 °C were lower, ranging from ~0.15 to ~0.25. The cirrus cloud depolarizations measured with the HSRL do not show any depolarization values below 20% for the temperatures from -30 to -10 °C. The system used by Platt had a 2.5 mrad field of view, and the low depolarization values are possibly caused by multiple scattering from water

clouds. The HSRL measurements have shown that when the depolarization of a water cloud is measured with a system with ~ 1.0 mrad field of view, the effects of multiple scattering are large enough to cause depolarization values of $\sim 20\%$, and therefore the separation between water and ice becomes impossible. Also the HSRL measurements show a substantial probability of observing water at temperatures from -30 to 0°C .

In 45% of the cases simultaneous observations of water cloud layers at the cirrus cloud altitudes were made. The Figure 30 shows, that supercooled water clouds at cirrus cloud altitudes are found at temperatures as low as -35°C . Above 0°C temperature the low depolarization values indicate pure water, and the presence of cirrus disappears. The water cloud depolarizations are below 10 % and they contain the effects of multiple scattering. When the same clouds are studied with a NOAA-11 or NOAA-12 satellite, the simultaneous appearance of the water and ice cannot be noticed. On the satellite measurements, the cloud types are separated by using the information on the temperature. Therefore, if satellite data is used for cirrus optical depth studies, a supercooled water cloud layer mixed with ice cannot be easily separated and water will increase the optical depth value determined for the cirrus cloud. The depolarization ratio knowledge of the cloud measured with a lidar can be used to separate the water from ice and therefore separate optical depth measurements for both constituents can be performed.

The initial measurements have shown that the HSRL is capable of measuring cirrus cloud particle sizes. These measurements together with phase function measurements can be used for further studies of the cloud particle size effects on the depolarization ratio²⁶.

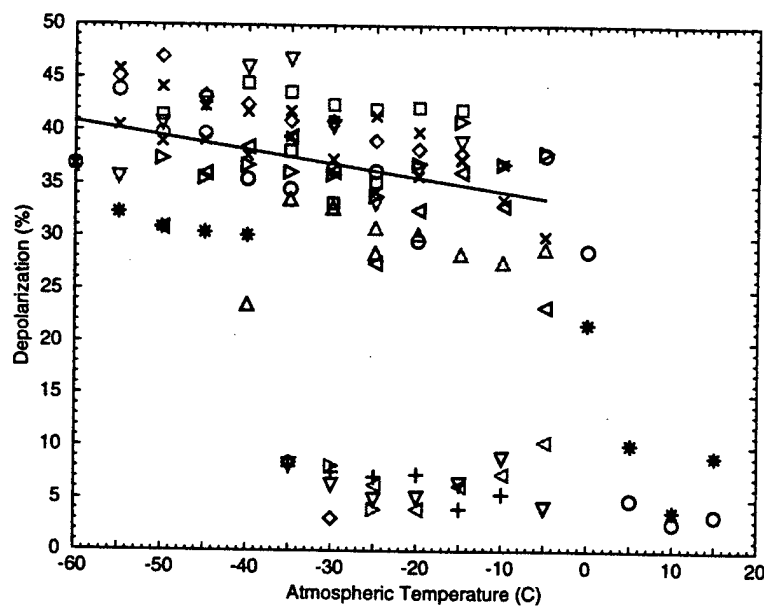


Figure 30. Cirrus cloud and supercooled water cloud depolarization as a function of temperature observed between August 2 and November 11, 1993. The depolarization values below 10% are indication of water clouds and higher depolarization values indicate the presence of ice.

6.2 Measurements of scattering ratio, aerosol backscatter cross section, and optical depth

Two examples from the measured scattering ratio, aerosol backscatter cross section and optical depth profiles for the November 11, 1993 dataset are presented in figures 31 and 32. The cloud altitude and geometrical thickness of the clouds can be seen from the inverted aerosol profile. The inverted molecular signal shows the extinction in the signal through the atmosphere. This can be compared to the predicted Rayleigh return, calculated from the radiosonde data. The unsmoothed profiles are used. The Figure 31 shows a thin cirrus cloud case and the Figure 32 presents a water cloud together with a thin cirrus cloud. The water cloud is seen at 5.2 km altitude and the cirrus cloud can be found ranging from 7 to 9.2 km. The measured signals show the large dynamical range achieved in HSRL measurements: signal strength variations over four decades are seen.

The scattering ratio is calculated from the ratio of inverted aerosol profile to the inverted molecular profile. The measured scattering ratios for the whole dataset vary from $\sim 10^{-3}$ to ~ 1000 . The maximum scattering ratio is 10 for the case presented in Figure 31 and ~ 300 for the water cloud case in Figure 32.

The aerosol backscatter cross section is obtained from the scattering ratio and an estimate for the atmospheric density profile. The values of aerosol backscatter cross section change from $\sim 10^{-6} m^{-1} sr^{-1}$ for cirrus and ice precipitation to $\sim 10^{-4} m^{-1} sr^{-1}$ for water cloud. The observed aerosol backscatter values of the clear air are between 10^{-6} and $10^{-7} m^{-1} sr^{-1}$.

The total optical depths are calculated from the ratio of the inverted molecular signal to the return predicted for the pure molecular scattering. They range from 0.5 to 2.5 for this dataset. The Figure 31 shows a optical depth of 0.5 for the cirrus cloud and a optical depth 1.4 is observed for the case in Figure 32. The water cloud optical depth is 1 and the cirrus cloud gives an optical depth of 0.4. With the laser power used for this measurement, the optical depth of 2.5 is the upper limit of the current system. By increasing the laser output power larger optical depths can be measured. Because the cross talk between channels is small and it can be accurately corrected, and also because the 160 μrad field of view of the HSRL effectively suppresses multiple

scattering, the optical depths inside a cloud can be measured.

The accuracy of the optical depth measurements can be seen from the Figure 33. The leftmost graph shows the error in the optical depth measurement of a thin cirrus cloud and rightmost graph shows the error when a cirrus cloud of optical depth ~ 1 is studied. The errors presented here are root mean square errors and they consist of photon counting, background correction, calibration, and wavelength tuning errors. The signals are spatially averaged with a 150 m filter and the filtering is taken into account in the error analysis. The accuracy of the optical depth measurements is limited by the photon counting statistics. This can be seen from the error bars, which are on the same order as the signal fluctuations. The accuracy of the HSRL measurements can be increased by increasing the signal strength and/or by using a constrained nonlinear fit to the inverted molecular profile.

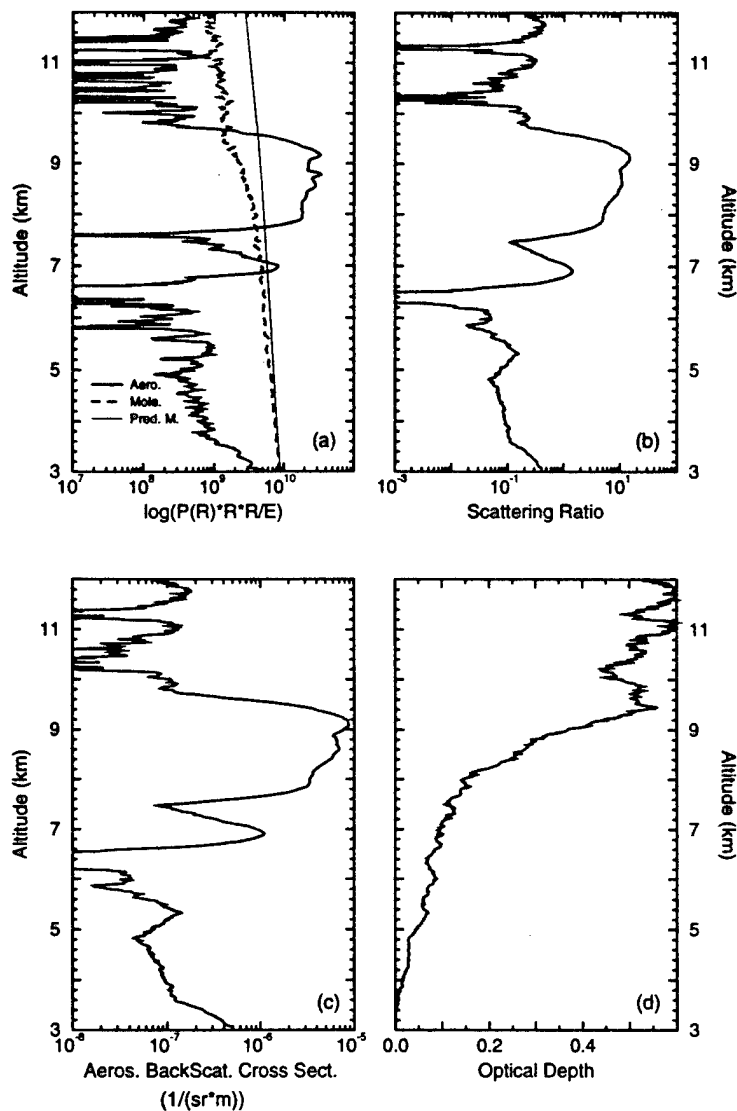


Figure 31. The measured scattering ratio, aerosol backscatter cross section and optical depth profiles of a thin cirrus cloud between 6.5 and 10 km (November 11, 1993 01:05-01:09 UT). (a) The inverted aerosol and molecular profiles along with a calculated molecular profile. The difference between the calculated and measured profiles shows the extinction. (b) The scattering ratio values are ranging from ~ 0.1 (clear air between 3 and 6.5 km) to 10 (cirrus cloud at 10 km). (c) The aerosol backscatter cross section of the cirrus cloud is $\sim 5 \cdot 10^{-6} m^{-1} sr^{-1}$ and $\sim 10^{-7} m^{-1} sr^{-1}$ for the clear air between altitudes 3 and 6.5 km. (d) The optical depth between 3 and 11 km is 0.55. The optical depth of the cirrus cloud is 0.4.

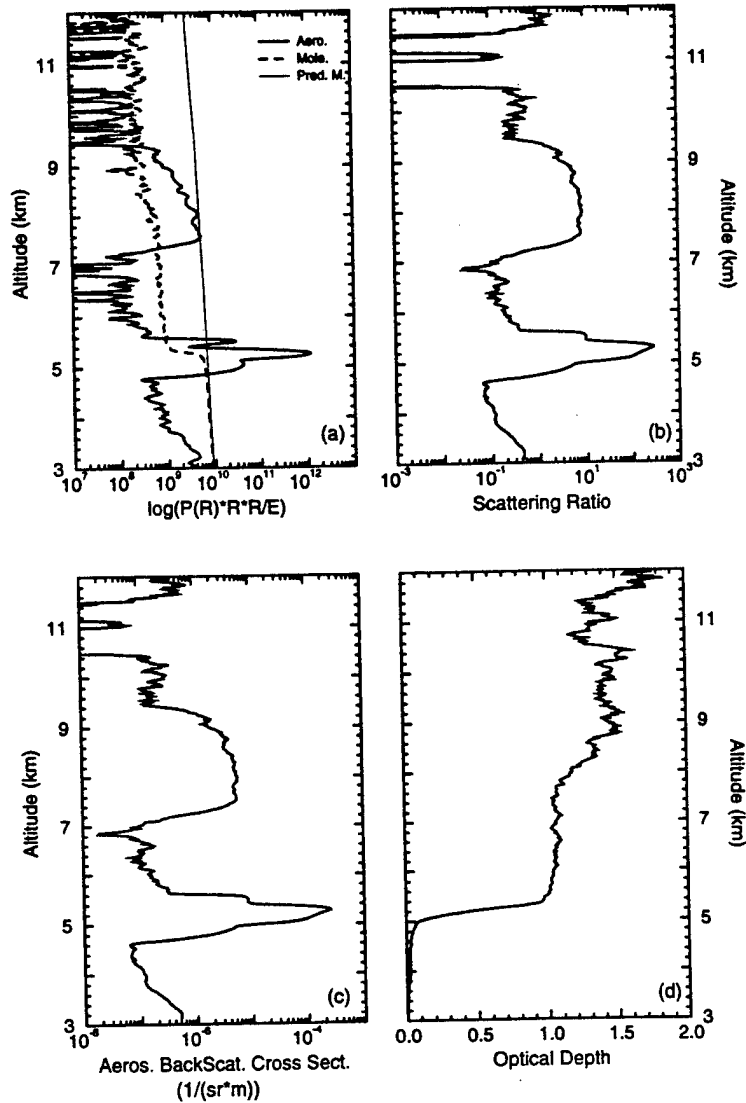


Figure 32. Scattering ratio, aerosol backscatter cross section and optical depth profiles of a thin cirrus cloud between 7 and 9.2 km and a water cloud with an ice crystal precipitation at 5.2 km (November 11, 1993 01:29-01:34 UT). (a) The inverted aerosol and molecular profiles along with the calculated molecular profile of the clear air. (b) Scattering ratio of the water cloud is ~ 300 and 10 for the cirrus cloud. (c) The observed aerosol backscatter cross sections are ranging from $10^{-7} m^{-1} sr^{-1}$ for the clear air to $2 \cdot 10^{-4} m^{-1} sr^{-1}$ for the water cloud. (d) The optical depth is 1 for the water cloud and 0.4 for the cirrus.

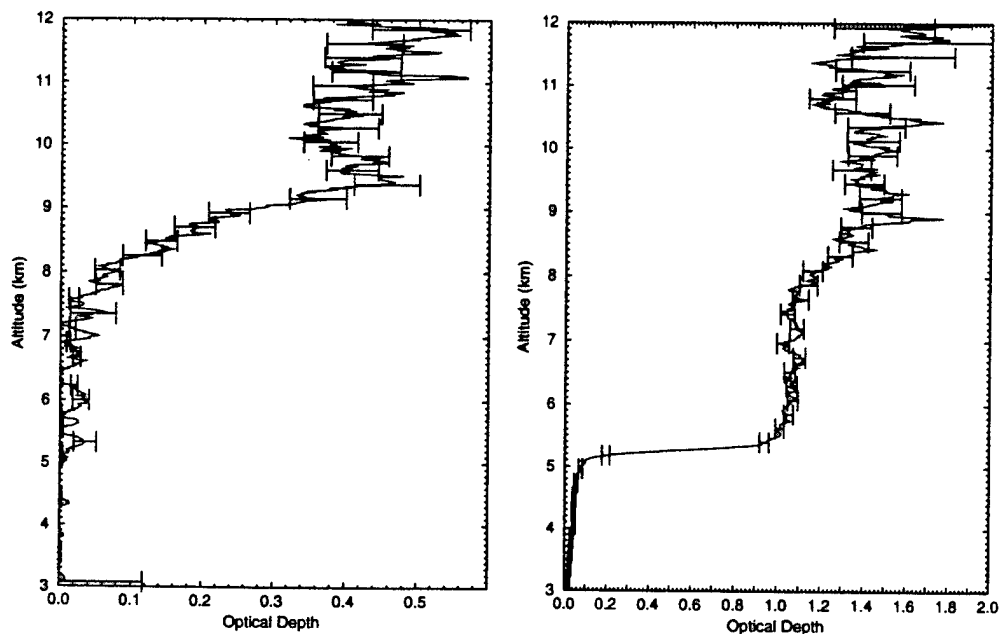


Figure 33. The root mean square errors in the optical depth measurement. A thin cirrus case (November 11, 1993 01:05-01:09 UT) (leftmost graph) and a cloud layer of optical depth of 1.4 (November 11, 1993 01:29-01:34 UT) (rightmost graph). The cases are the same as in Figure 29. The error bars are of the same order as the signal fluctuations indicating that the optical depth measurements are mostly limited by the photon counting statistics.

6.3 Measurements of atmospheric temperature

The temperature dependence of the Doppler-broadened molecular spectrum enables the measurements of the atmospheric temperature by a HSRL. The capability to measure the temperature would eliminate the possible errors due to the difference between the radiosonde reading and the current temperature over the lidar site. For this purpose, the temperature measurement capabilities of the University of Wisconsin HSRL were studied. The presence of clouds and strong layers of clear air aerosols will affect the shape of the molecular spectrum measured with the HSRL. The temperature measurement method presented in the following was used to test the capability of the HSRL to accurately measure the molecular spectrum width for layers with small aerosol content.

Lidars have been used for the measurements of the atmospheric temperature profile by many lidar groups. The technique proposed by Strauch *et al.*⁴⁴ and Cooney⁴⁵ allows calibrated temperature measurements by using the rotational Raman spectrum of nitrogen. With this technique about 1 °C temperature accuracy at low altitudes is achieved. Kalshoven *et al.*⁴⁶ demonstrated a differential absorption lidar method for temperature measurements. They used 2 laser wavelengths and O₂-absorption lines to measure atmospheric temperature up to 1 km altitude with 1 °C accuracy. Later Endemann and Byer⁴⁷ reported simultaneous measurements of atmospheric temperature and humidity with a continuously tunable IR-lidar. They used a three-wavelength differential absorption lidar technique and water vapor absorption lines. With this technique a 2.3 °C absolute accuracy was achieved. In addition to Raman and differential absorption lidar techniques, Keckhut *et al.*⁴⁸ used Rayleigh scattering lidar to measure atmospheric temperature for altitudes 30–70 km.

The temperature measurements made with a high resolution lidar have been reported by Alvarez *et al.*¹⁶. Their temperature measurement is based on the two barium absorption filters with different bandpasses. Because the strength of the signal received through an absorption cell is proportional to the width of the Doppler-broadened spectrum, the information of the signal strength together with a theoretical calculation for the Doppler-broadened Rayleigh-Brillouin spectrum can be used for the determination of the atmospheric temperature. Their latest measurements have

shown that only a 10 °C accuracy is achieved for profiles up to 5 km.

The preliminary measurements of the atmospheric temperature made with the University of Wisconsin HSRL have been based on one iodine absorption filter. For temperature measurements the system transmission spectrum is measured by scanning the laser wavelength over the iodine absorption spectrum, similarly as in the system calibration scan. For one temperature profile, data from 5 calibration scans were averaged. This was done to increase the signal to noise ratio of the measurement. The measured profile was calculated by averaging the signal over a 300 m range with 1 km steps.

The signal from atmosphere and detected through the iodine absorption cell is a convolution of the Doppler-broadened molecular spectrum and the iodine absorption spectrum. The Brillouin modified approximation for the Doppler-broadened spectrum was used to calculate the molecular line shapes at temperatures ranging from -70 to +30 °C with 1°C resolution. The calculated line shapes were convoluted with the measured iodine absorption spectrum. In order to define the atmospheric temperature at certain altitude, a least square fit was used to fit the measured profile to the calculated profile. The temperature that produced the best fit defined the temperature of that altitude. Figure 34 shows an example of the received signal from 8 km altitude observed through the iodine absorption cell normalized by the signal observed with the channel without iodine absorption filter. The iodine absorption spectrum is shown as a reference. The modeled molecular profile is shown for the temperature that produced the best fit. The best fit was found at -47°C temperature.

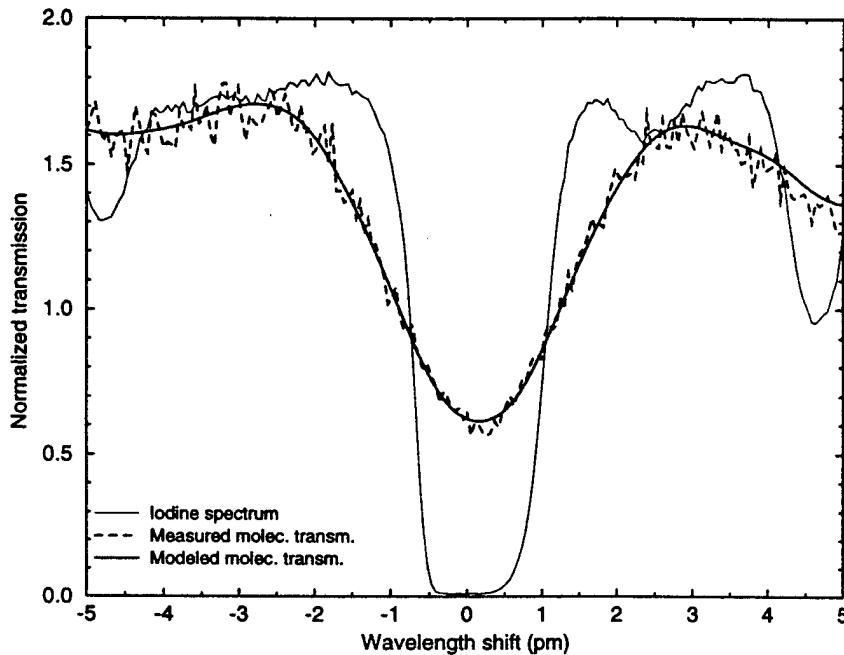


Figure 34. The HSRL signal from 8 km altitude observed through the iodine absorption filter normalized by the signal measured simultaneously without the iodine absorption filter. The iodine absorption spectrum is plotted for reference. The modeled molecular transmission is shown for the temperature that produced the best fit between measured and calculated molecular transmissions. The best fit was obtained at -47°C temperature.

The sensitivity of the molecular transmission of the iodine absorption filter to the width of the molecular spectrum is illustrated in Figure 35. The figure shows the effect of incorrect temperature to the fit. For this figure, the modeled molecular transmissions were subtracted from the modeled molecular transmission at -47°C temperature. The temperature difference of 5°C is displayed. The Figure 35 shows that a clear difference between temperatures is achieved, but because the differences are small, the accurate measurements of atmospheric temperature by the scanning technique are difficult to obtain.

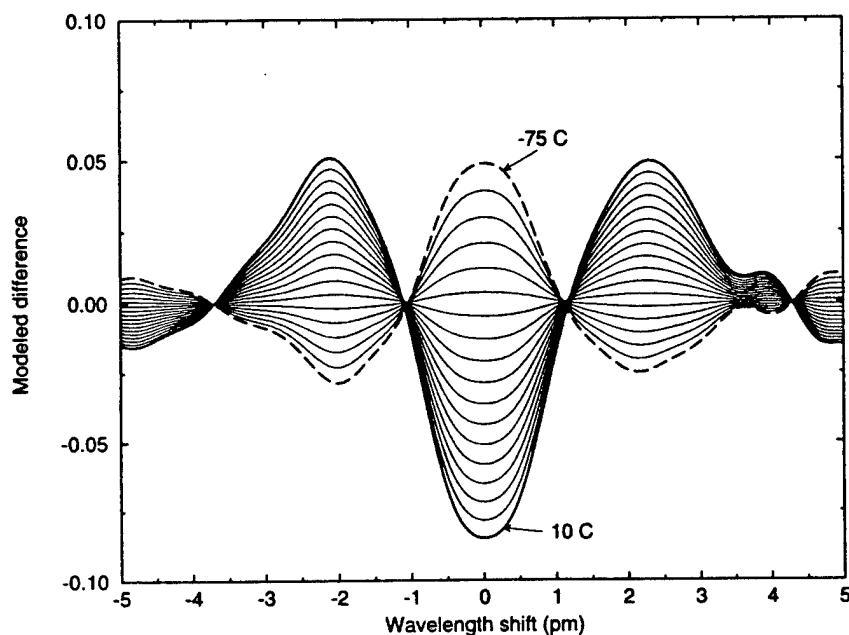


Figure 35. The sensitivity of the molecular transmission to the temperature. The difference in modeled molecular transmission to the molecular transmission at -47°C is shown with 5°C temperature steps.

A temperature profile measured on February 27, 1994, in Madison between 00:00 and 03:00 UT is presented in Figure 36. For the comparison the radiosonde temperature profiles from nearest weather stations are presented. The stations at Green Bay (WI, 180 km northeast from Madison), Peoria (IL, 350 km south from Madison), and St. Cloud (MN, 450 northwest from Madison) provided a radiosonde profile at 00:00 UT. The temperature values measured by the HSRL agree with the temperatures measured with the radiosondes. For the profile between 4 and 8 km the observed rms temperature differences are 2.97, 7.08, and 5.52°C between HSRL and the weather stations. The rms difference between weather stations is 7.06°C . For low altitudes, the largest difference between profiles is observed. This is expected because of the synoptic scale variations in weather conditions between different locations.

For altitudes between 6-8 km, a good agreement between HSRL measurement and the central Minnesota (St. Cloud) radiosonde profile is seen. These altitudes had a low aerosol content providing scattering ratio of ~ 0.02 . The temperatures above 8 km show a big deviation from the radiosonde temperatures. This is due a strong aerosol layer, that disturbs the HSRL temperature measurement. The scattering ratio of the aerosol layer above 8 km was ~ 0.3 . Also the measured temperature values for altitude between 2 and 3.5 km are colder than the radiosonde values. This is due to presence of a low level aerosol layer with scattering ratio of ~ 0.1 . The presence of aerosols deepens the measured spectrum and therefore a fit into this spectrum underestimates the temperature. Therefore, if the temperatures are going to be measured in the presence of aerosols, the effect of the aerosol signal has to be separated from the molecular contribution.

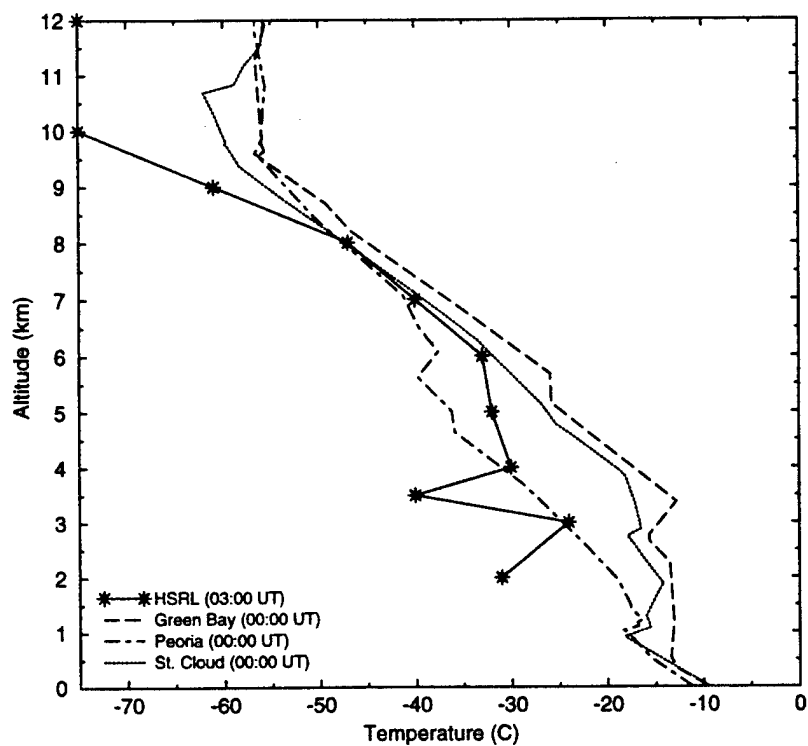


Figure 36. A temperature profile obtained with the HSRL on February 27, 1994. The temperature profile obtained with radiosondes show the atmospheric temperature measured at the closest weather stations. A good agreement between HSRL and radiosonde observations is observed between altitudes of 4 and 8 km. These are altitudes with a low aerosol backscatter content.

7 Error analysis

7.1 Error sources

The signal detected with a photon counting system is a combination of backscatter signal, background light, and internal noise in the photodetector. The lidar equation (Eq. (1)) shows that the amount of received signal is determined by the number of transmitted photons, scattering cross section, backscatter phase function, area of the telescope, transmission of the receiver optics, and the sensitivity of the detectors. On the other hand, the HSRL measurements are dependent on the system calibration coefficients (Eqs. (17) and (18)). The errors in the HSRL measurements can be divided into 5 main categories:

1. errors due to photon counting statistics
2. errors due to changes in system calibration coefficients
3. errors in the background subtraction
4. errors due to a multiple scattering contribution
5. errors in the atmospheric temperature profile used to compute the molecular density

The error in the photon counting process is proportional to the square root of the measured signal. The errors due to photon counting statistics that are induced to the calibration coefficients were discussed in Chapter 5.

The system detection efficiency is a combination of the system transmission and the photomultiplier quantum efficiency. The system detection efficiency affects the amount of detected signal and therefore, it is directly related to the photon counting statistics. A model to calculate the expected system transmission was developed. This model includes the spectral transmission of interference filters, etalons, and iodine absorption cell, transmissions and reflections of optical components (lenses, mirrors, cubes, etalon chamber windows) and photomultiplier quantum efficiencies.

The transmittance and reflectance values of different optical components were confirmed with measurements. The calculated transmission efficiencies were compared with the measured values. For this study, a clear air case was chosen. Because the properties of molecular scattering are well known, the lidar equation for molecular scattering (Eq. 3) can be solved for the number of photons expected for the pure molecular return.

In order to predict the expected molecular return, the calculated system transmission was convoluted with the calculated molecular spectrum at a 5 km reference altitude. The temperature for the Doppler-broadened molecular spectrum calculation was taken from a radiosonde profile. By calculating the ratio of measured to expected number of photons given by the lidar equation, the actual system transmission was estimated. The two way extinction between lidar and the backscatter volume was assumed to ~ 1 . The comparison between expected and measured detection efficiency values is given in Table 2. This comparison was made without using the low resolution etalons. Each etalon decreases the transmission by a factor of ~ 2 .

Table 2. HSRL detection efficiency

Channel	Calculated (%)	Measured (%)
Aerosol+Molecular	0.78	0.6
Molecular	0.44	0.36
WFOV	4.4	3.4

The transmission efficiency values show $\sim 25\%$ difference between calculated and measured values. A $\sim 10\%$ error can be made by assuming the extinction between lidar to 1. Also the uncertainty on the transmission and reflectance values of optical components affect the calculation. The largest uncertainty is the quantum efficiency of the photomultipliers. The value 0.12 is taken from the manufacturers specification, but only a 0.03 change in the quantum efficiency would correct the difference. The transmissions and reflectances of the receiver components that affect to the detection efficiency are listed in Table 3. The transmission and reflection numbers of some components are confirmed with a measurement and rest of the values are obtained from the manufacturers specifications.

Table 3. Transmission / Reflection losses in HSRL components. The source for the transmission and reflection values is manufacturers specification (spec.) or a measurement (meas.).

Channel	Component	R or T (%)	Source	Total(%)
ALL				
	Telescope mirrors (2)	R = 90.0	meas.	R= 81.0
	Interference filter (1)	T= 50.0	meas.	T=50.0
	Polarizing cubes (2/channel)	T=99.0	spec.	T=99.0
		R=93.0	spec.	R=93.0
	PMT quantum efficiency	QE= 12.0	spec.	QE= 12.0
A+M, M				
	Etalon chamber windows (3)	T= 90.0	meas.	T= 73.0
	Mirrors (2 /channel)	T= 90.0	meas.	T= 81.0
	Lenses (3 / channel)	T=99.4	spec.	T=98.2
A+M				
	Beam splitter	T=30.0	meas.	T=30.0
M				
	Beam splitter	R=70.0	meas.	R=70.0
	Iodine absorption cell	T(cell)=80.0	meas.	T=80.0
		T(mol.)~30.0	calc.	T=30.0
WFOV				
	Lens	T=99.4	spec.	T = 99.4
Total eff.				
	Aerosol+Molecular Channel			0.78
	Molecular Channel			0.44
	WFOV Channel			4.4

The reflectivity of the telescope mirrors is limited by the reflectivity of the aluminum coating. The poor transmission values of the etalon chamber windows and the mirrors have a big effect on the detection efficiency, because they lose $\sim 41\%$ of the received signal. These components are taken from the old system and they are not optimized for the current operating wavelength. In order to increase the system performance, these components are going to be replaced in near future.

The errors due to change in the system calibration coefficients are mainly caused by change in the transmission-receiver wavelength tuning and change in the system alignment. These errors can be calculated by a partial differentiation.

A change in atmospheric temperature and pressure affects the amount of detected molecular signal. Therefore, if the radiosonde profile is not valid for the measure-

ment conditions, an error is generated in the calculated molecular signal. The width of the Doppler-broadened spectrum directly affects the calibration coefficient C_{mm} . This affects to the amount of molecular signal subtracted from the signal detected with the combined aerosol+molecular channel. In Brillouin spectrum and molecular backscatter cross section calculations, the effects of changing atmospheric conditions are minimized by using the current radiosonde data from the nearest weather stations. By comparing temperature and pressure readings from the closest radiosonde stations, an $\sim 1-5\%$ difference between stations is observed. This due to the geographic separation between weather stations. Because the lidar is located between these stations, the error is expected to be smaller.

In addition to the atmospheric temperature and pressure changes, the effects of the wind on the measurement has to be considered because the high wind velocities can shift the Doppler-broadened spectrum with respect to the laser wavelength. A bulk shift in respect to the radiated spectrum is an indicator of wind, while the line broadening is associated with the random thermal motions of the molecules (and aerosols). If the line center of the Doppler-broadened spectrum is shifted in respect to the transmitted wavelength, the system calibration will be in error. The Doppler-shift for the backscatter signal can be calculated from

$$\frac{\Delta\nu}{2\nu_o} = \frac{v}{c}, \quad (24)$$

where

- $\Delta\nu$ = wavenumber shift
- $2\nu_o$ = wavenumber of the laser line center
- v = molecular velocity
- c = velocity of light

The wind velocities measured by a radiosonde can be used as an estimate for the horizontal wind. The maximum horizontal wind velocities are generally smaller than 70 m/s at cirrus cloud altitudes, and the maximum vertical winds are normally below 1 m/s in troposphere. Therefore, the maximum wind to the lidar pointing direction θ ($\theta = 4$ degrees from the zenith) is $v_l = v_x \sin\theta + v_y \cos\theta$, which corresponds to a

velocity of 5.9 m/s. The shift in the spectrum is 19.8 fm, which is much smaller than the current 0.052 pm detection accuracy of the molecular spectrum. Also the horizontal wind speeds are generally much lower⁴⁹, and therefore, the effects due to wind to the HSRL measurements are negligible, but caution is required if larger zenith angles of the pointing direction are considered.

The uncertainty in transmitter-receiver peak transmission tuning can be seen as a shift in the transmitter wavelength in respect to the spectral transmission maximum of the receiver. This effects the amount of detected molecular signal, but if the drift is large, a change in the amount of detected aerosol is observed. The drift also affects the system transmission. In the current HSRL, the effects of a drift between transmitter and receiver wavelengths are minimized by locking the transmitter laser wavelength to the iodine absorption peak (see Chapter 5.2). The effects of the wavelength locking to the measured signal were also discussed in Chapter 5.2.

In addition to the previous errors, the system calibration is affected by all misalignments of the system. The error due to a system misalignment can be divided into three different categories:

1. alignment error in the receiver optics
2. alignment error between transmitter and receiver pointing direction
3. an error in the compensation for the beamsplitter polarization dependence

A small alignment error (off focus, off axis or misalignment in system pointing direction) can lead situations, where part of the backscattered light is lost in the optics, detector, or atmosphere. This can easily lead into a range dependence of the received signal. This affects the inversion and furthermore, the measured optical depth. A misalignment also affects the total system transmittance and the signal to noise ratio of the measured signal. System pointing instabilities make the overlap correction of the received signal difficult. The overlap region is the close distance range where the overlap of the receiver field of view and the transmitted beam is incomplete. The effect of misalignment between transmitter end receiver pointing directions is largest for the overlap region. The effects vary daily depending from

the accuracy of the alignment between transmitter and receiver pointing direction. Large receiver field of views are less critical for the alignment errors. The signal measured with the large field of views of the WFOV channel can be used to align the small field of view channels. In the HSRL, the alignment between transmitter and receiver pointing directions is performed as follows. A corner cube is used to direct the outgoing laser beam to the receiver. The beam is aligned to the center of the receiver aperture by adjusting the turning mirror on the top of the telescope secondary mirror. Then the corner cube is removed and the signal from the atmosphere is used to verify the alignment. The signal of the large field of view of the WFOV-channel is compared to signal of the combined channel. If the channels are properly aligned and if the transmitter and receiver pointing directions are the same, the slopes of the signals are similar for the altitudes above the overlap region and therefore, the ratio between WFOV-channel signal to the spectrometer channel signal is constant. The alignment of the smallest WFOV channel aperture can be verified similarly by comparing the signal from the larger aperture to the signal from the smallest WFOV aperture. The effects of alignment errors on the system measurement accuracy are not included to the error analysis, because with a careful alignment the errors can be minimized.

The accuracy of the background correction is mostly affected by the photon counting statistics. The effects of photon counting on the measured background are decreased by summing at least 66 range bins together. The background correction method used in HSRL measurements was described earlier in Chapter 3.2.2. In addition to the photon counting statistics, the accuracy of the background correction is affected by the slight tendency to overestimate the number of background counts for altitudes close to 33 km. Eventhough atmospheric density, and therefore the amount of Rayleigh scattering, decreases rapidly with the range, some of the signal that is measured into the upper range bins of the HSRL can still be due to Rayleigh scattering. Therefore, when those range bins are used to calculate the number of background counts, the background is slightly overestimated due to the Rayleigh signal.

The effects of the multiple scattering on the received lidar signal are usually neglected and the received signal is assumed to be single scattered. A lidar return from

water and thick cirrus clouds usually encounters large optical depths within a short distance of the cloud boundary and therefore, many of the received photons are likely to be from multiple scattering. The effect of multiple scattering to the lidar signal is dependent from the receiver field of view, cloud particle size, range from the lidar, and the optical depth of the cloud. The effect of multiple scattering can be seen in the lidar profile as a reduction in the rate of attenuation of the signal. In depolarization, the effect of multiple scattering will show up as an increase in the depolarization ratio towards the cloud top. The HSRL measurements have shown, that the effect of multiple scattering on the smallest field of view signals is small, because the depolarization ratio values observed for the water clouds are low.

The current HSRL profiles are not corrected for multiple scattering contributions. An inversion program that accounts multiple scattering effects is currently in progress. The magnitude of the error caused by assuming the signal to be originated from single scattering depends from the field of view of the receiver, optical thickness of the cloud, size of the cloud particles, and penetration depth. The clear air aerosols and thin cirrus layers have a small or no multiple scattering effect. Because of the large particle size of ice crystals, the signal from thick cirrus clouds contains a multiple scattering contribution even for the small field of views. The multiple scattering from water cloud droplets is distributed to the larger field of views. The amount of multiple scattering on the measured signal can be estimated from the paper by Eloranta and Shipley²⁷.

7.2 Effects of different errors on the measured optical parameters

The effects of different errors on the inverted aerosol and molecular return and to the measured optical parameters were calculated by partially differentiating Equations (19), (20), and (4)–(13). The error analysis is made for the data obtained on November 11, 1993. A section of the data for a thin two-layer cirrus cloud structure is analyzed. The case is the same as shown in Figure 31. The thin cirrus cloud case is chosen for this study for two reasons. First, the backscatter signal from thin high altitude cirrus is small. Therefore, an error analysis made for the thin cirrus tests the measurement sensitivity of the system. Second, if accurate measurements of thin cirrus clouds can be made within short averaging time, then the HSRL can be considered for studies of contrail formed cirrus. The short averaging time is important for the contrail studies, because they drift rapidly with the wind and only a limited number of samples from one contrail can be obtained.

Information from cloud optical properties can be obtained by comparing the HSRL measurements with satellite observations. Thus, the averaging time of the HSRL data has to be close to the time resolution of a satellite image. The use of the short averaging times also prevents the smoothing of the the lidar signal so that the rapid changes in cloud structure in both time and altitude remain in the data. For this study, the 3 min averaging time was chosen to study the errors in the inverted aerosol and molecular returns, inverted aerosol and molecular depolarization ratios, backscatter ratio, optical depth, and aerosol backscatter cross section. Because the measurement of the backscatter phase function is difficult due to uncertainty in the extinction cross section determination, the 6 min averaging time was used for error analysis of the phase function measurement.

The error analysis presented here shows the total errors together with the partial errors. All errors are calculated as mean square errors (see Equations 26-35) and presented as fractional root mean square errors (see Figures 37- 44). The partial errors in Figures 37- 44 present the effects of errors on the photon counting of the combined channel and the molecular channel, error in the molecular backscatter cross section per unit volume due to the uncertainty in temperature and pressure profiles,

and errors in the calibration coefficient determination. The error estimate calculations include the photon counting error, error in the background correction, error due to the uncertainty in the temperature and pressure profiles measured with a radiosonde, and errors due to the tuning of the laser wavelength. The errors due to system alignment and the error due to multiple scattering effects are not included to this error analysis. Also the error in the determination of the range R is negligible.

The errors in background correction are assumed to be from photon counting statistics. The uncertainty of 2 % for the temperature profiles is used. The error in pressure profile is estimated to 1 mbar of the radiosonde pressure reading at each altitude. The error is due to the geographic separation between closest weather stations. This is estimated from the radiosonde measurements from the closest weather stations. The uncertainty on the molecular spectrum calculation is estimated with the 2% uncertainty on the atmospheric temperature. The error on the calibration coefficient C_{mm} determination is a combination of the photon counting error, uncertainty of the molecular spectrum, and the error caused by tuning of the laser wavelength. The accuracy of the calibration coefficient C_{am} determination is limited by the photon counting statistics. The error in the molecular backscatter cross section per unit volume measurement depends on the errors in the atmospheric temperature and pressure.

The error in the molecular profile can be given as

$$\begin{aligned}
 (\Delta N_m(R))^2 = & \left(\frac{\partial N_m(R)}{\partial S_m(R)} \right)^2 (\Delta S_m(R))^2 + \left(\frac{\partial N_m(R)}{\partial S_{a+m}(R)} \right)^2 (\Delta S_{a+m}(R))^2 + \\
 & \left(\frac{\partial N_m(R)}{\partial C_{mm}(R)} \right)^2 (\Delta C_{mm}(R))^2 + \left(\frac{\partial N_m(R)}{\partial C_{am}} \right)^2 (\Delta C_{am})^2 + \\
 & \left(\frac{\partial N_m(R)}{\partial B_{a+m}} \right)^2 (\Delta B_{a+m})^2 + \left(\frac{\partial N_m(R)}{\partial B_m} \right)^2 (\Delta B_m)^2, \quad (25)
 \end{aligned}$$

which leads to equation

$$\left(\frac{\Delta N_m(R)}{N_m(R)}\right)^2 = \frac{C_{am}(R)^2 \Delta S_{a+m}(R)^2}{(S_m(R) - B_m(R) - C_{am}(R)(S_{a+m}(R) - B_{a+m}(R)))^2} + \frac{\Delta S_m(R)^2}{(S_m(R) - B_m(R) - C_{am}(R)(S_{a+m}(R) - B_{a+m}(R)))^2} + \frac{\Delta C_{am}(R)^2}{(C_{mm}(R) - C_{am}(R))^2} + \frac{\Delta C_{mm}(R)^2}{(C_{mm}(R) - C_{am}(R))^2} + \frac{C_{am}(R)^2 \Delta B_{a+m}(R)^2}{(S_m(R) - B_m(R) - C_{am}(R)(S_{a+m}(R) - B_{a+m}(R)))^2} + \frac{\Delta B_m(R)^2}{(S_m(R) - B_m(R) - C_{am}(R)(S_{a+m}(R) - B_{a+m}(R)))^2} \quad (26)$$

$\Delta S_m(R)$ and $\Delta S_{a+m}(R)$ are the photon counting errors. $\Delta C_{am}(R)$ and $\Delta C_{mm}(R)$ are the errors in the calibration coefficient determination. The background correction errors are given by $\Delta B_m(R)$ and $\Delta B_{a+m}(R)$. The error analysis made for the calibration coefficients show that C_{mm} can be determined with better than 5 % accuracy and C_{am} with a better than 2 % accuracy.

The effects of different errors on the inverted molecular return are shown in Figure 37. The errors in inverted molecular return are dominated by the photon counting statistics and the determination of the calibration coefficient C_{mm} . The error due to the measurement accuracy of the aerosol signal is negligible. The errors in the C_{am} determination have only a small effect on the inverted molecular return.

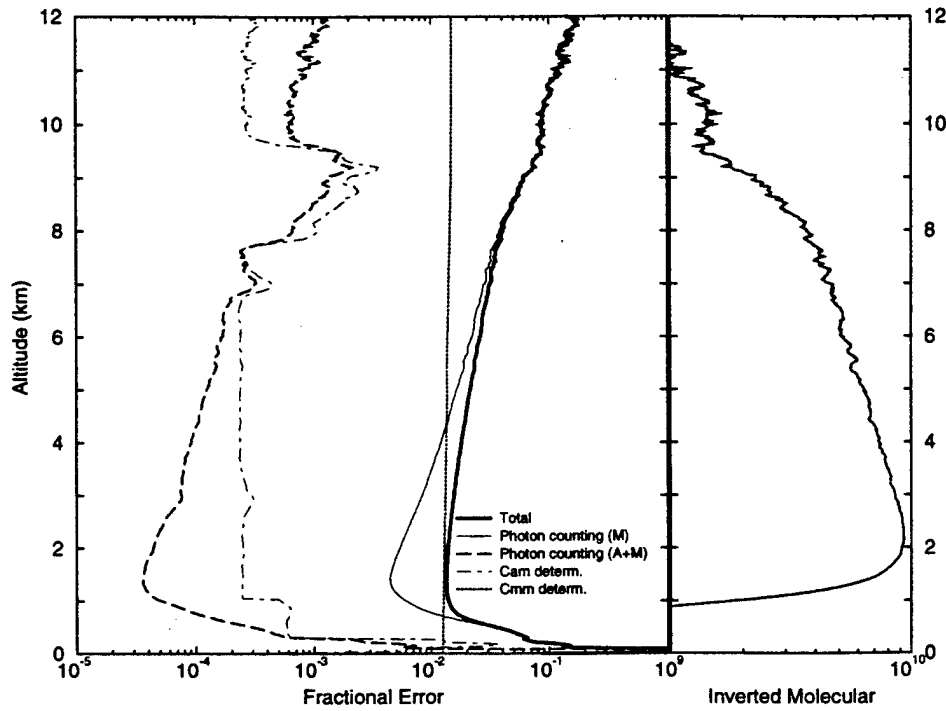


Figure 37. The effects of different errors on the inverted molecular profile (November 11, 1993, 01:05-01:08 UT). Data from a thin cirrus cloud is analyzed by using a 3 min. averaging time. The measured molecular profile (rightmost graph) presents the signal variations as a function of altitude. The extinction due to the thin cirrus cloud is observed between 6.5 and 10 km. The accuracy of the inverted molecular return determination is mostly limited by the photon counting statistics and the determination accuracy of the calibration coefficient C_{mm} (leftmost graph). The large errors shown in the overlap region below 2 km are due to a focus error and incomplete overlap of the receiver field of view and transmitted laser beam.

The error in the measured aerosol profile can be derived similarly to the molecular profile

$$\begin{aligned}
 (\Delta N_a(R))^2 = & \left(\frac{\partial N_a(R)}{\partial S_m(R)} \right)^2 (\Delta S_m(R))^2 + \left(\frac{\partial N_a(R)}{\partial S_{a+m}(R)} \right)^2 (\Delta S_{a+m}(R))^2 + \\
 & \left(\frac{\partial N_a(R)}{\partial C_{mm}(R)} \right)^2 (\Delta C_{mm}(R))^2 + \left(\frac{\partial N_a(R)}{\partial C_{am}(R)} \right)^2 (\Delta C_{am}(R))^2 + \\
 & \left(\frac{\partial N_a(R)}{\partial B_{a+m}(R)} \right)^2 (\Delta B_{a+m}(R))^2 + \left(\frac{\partial N_a(R)}{\partial B_m(R)} \right)^2 (\Delta B_m(R))^2 \quad (27)
 \end{aligned}$$

This differential equation can be expanded to following form:

$$\begin{aligned}
 \left(\frac{\Delta N_a(R)}{N_a(R)} \right)^2 = & \frac{C_{mm}(R)^2 \Delta S_{a+m}(R)^2}{(S_m(R) - B_m(R) - C_{mm}(R)(S_{a+m}(R) - B_{a+m}(R)))^2} + \\
 & \frac{\Delta S_m(R)^2}{(S_m(R) - B_m(R) - C_{mm}(R)(S_{a+m}(R) - B_{a+m}(R)))^2} + \\
 & \frac{\Delta C_{am}(R)^2}{(C_{am}(R) - C_{mm}(R))^2} + \frac{\Delta C_{mm}(R)^2}{(C_{am}(R) - C_{mm}(R))^2} + \\
 & \frac{C_{mm}(R)^2 \Delta B_{a+m}(R)^2}{(S_m(R) - B_m(R) - C_{mm}(R)(S_{a+m}(R) - B_{a+m}(R)))^2} + \\
 & \frac{\Delta B_m(R)^2}{(S_m(R) - B_m(R) - C_{mm}(R)(S_{a+m}(R) - B_{a+m}(R)))^2} \quad (28)
 \end{aligned}$$

The accuracy of the inverted aerosol return is mostly affected by the determination accuracy of the inverted molecular return (photon counting statistics and C_{mm} determination accuracy) and the photon counting statistics of the combined aerosol and molecular channel (see Figure 38). For the cases of small aerosol backscatter content, large errors in the determination of the aerosol return are made when short averaging times are used. The errors are caused by subtracting a large amount of molecular signal from the combined channel signal that contains the strong molecular signal together with a small aerosol contribution. Therefore, the statistics of the molecular signal dominates the aerosol backscatter signal determination. The determination of clear air aerosols requires longer averaging times in order to achieve reliable results. On the other hand, the measurements of cloud aerosols can be done with $\sim 1.0\%$ accuracy (7-10 km).

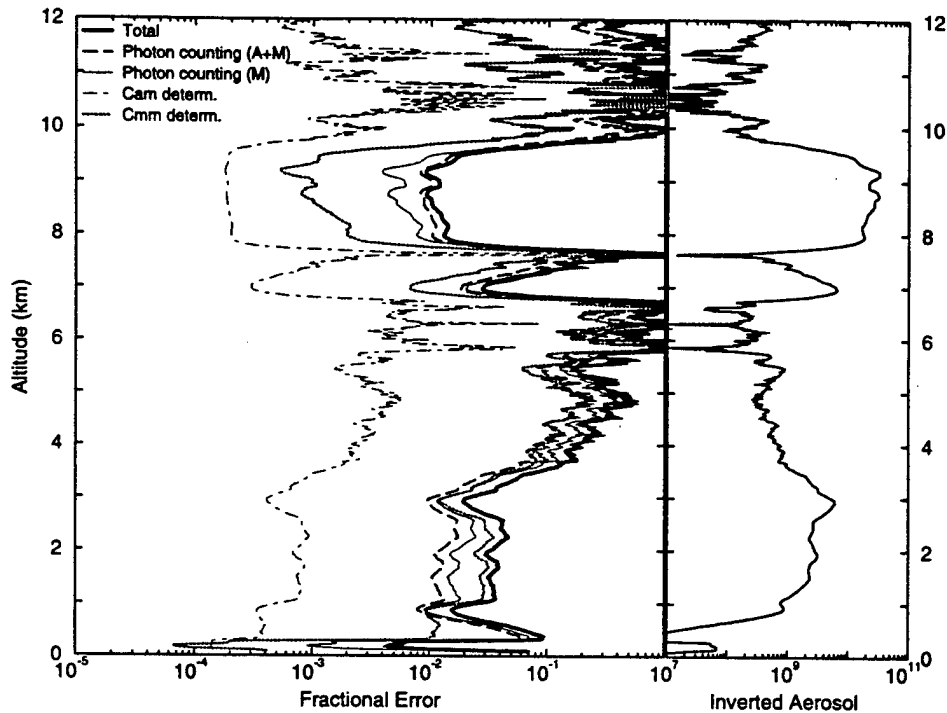


Figure 38. The effects of different errors on the inverted aerosol profile in case of a thin cirrus cloud (November 11, 1993, 01:05-01:08 UT). Averaging time of the data is 3 min. The measured aerosol profile (rightmost graph) shows the signal variation as function of altitude. The thin cirrus layer is observed between 6.5 and 10 km and a strong aerosol layer is seen between 0 and 3.5 km. The measurements of the aerosols are limited by the accuracy of the molecular profile measurements (leftmost graph). The 3 min averaging time provides 1-5% accuracy for thin cirrus cloud and strong aerosol layer measurements, but a longer averaging time is required for the measurements of the clear air aerosols.

Using the calculated errors for the measured aerosol and molecular profiles, the errors in the determination of the optical parameters (see Chapter 2) can be calculated as follows.

The errors in the determination of inverted aerosol and molecular returns have a direct effect on the accuracy of the backscatter ratio (or scattering ratio) determination (Figure 39). Therefore, the error in the backscatter ratio is

$$(\Delta SR(R))^2 = \left(\frac{\partial SR(R)}{\partial N_a(R)} \right)^2 (\Delta N_a(R))^2 + \left(\frac{\partial SR(R)}{\partial N_m(R)} \right)^2 (\Delta N_m(R))^2, \quad (29)$$

The effects of errors on photon counting, background correction, and calibration can be derived by combining the previous equation with the equations (26) and (28). Similar derivations of the differential errors can be made for the optical parameters given in following.

For the cases of a low aerosol backscatter content, the errors in the backscatter ratio are dominated by the errors in the aerosol return determination. For a stronger aerosol backscatter return from a cloud, the errors due to molecular return determination are on the same order or higher than the errors due to aerosol return determination. The backscatter ratios of the thin cirrus and strong aerosol layers can be determined with better than 10% accuracy, but measurements of the clear air require longer averaging times.

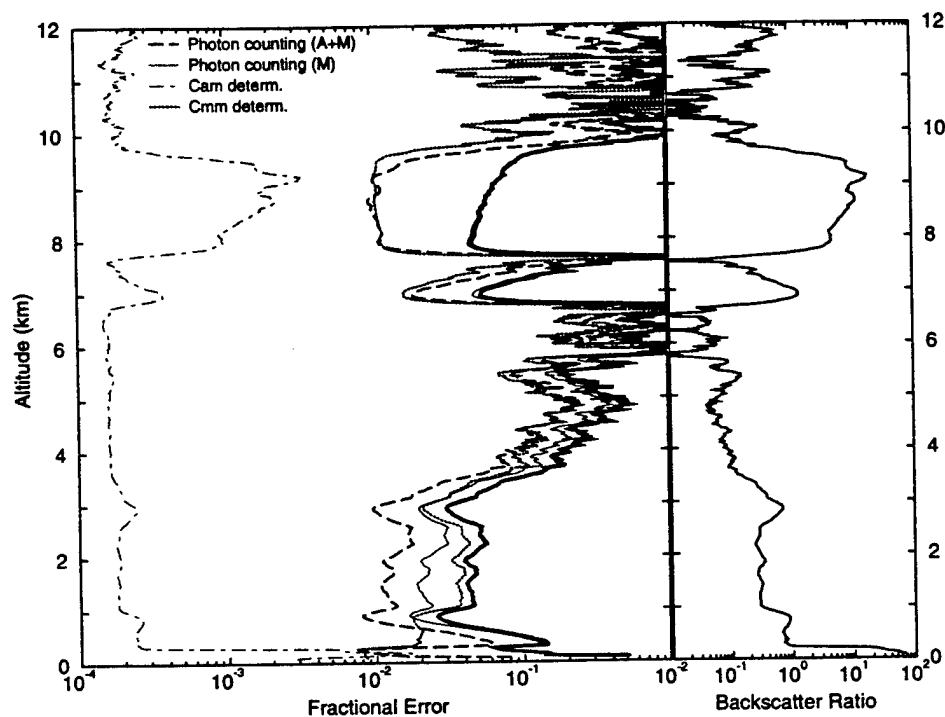


Figure 39. The effects of different errors on the backscatter ratio in case of a thin cirrus cloud (November 11, 1993, 01:05-01:08 UT). Averaging time of the data is 3 min. The backscatter ratio profile (rightmost graph) shows the ratio of the aerosol return to the molecular return as a function of altitude. Backscatter ratios ~ 0.1 to 20 are observed. The errors in the backscatter ratio measurement (leftmost graph) are determined by the accuracy of the aerosol and molecular return measurements. For the altitudes with a low aerosol content, the error in backscatter ratio is limited by the accuracy of the aerosol backscatter return measurement. For the cirrus cloud the accuracy depends on the goodness of the molecular backscatter profile measurement.

The error in optical depth can be approximated as sum of error in the molecular scattering cross section per unit volume and error in the molecular return determination.

$$(\Delta\tau(R))^2 \approx 2 \left(\frac{\partial\tau(R)}{\partial\beta_m(R)} \right)^2 (\Delta\beta_m(R))^2 + 2 \left(\frac{\partial\tau(R)}{\partial N_m(R)} \right)^2 (\Delta N_m)^2 \quad (30)$$

Error in the molecular scattering cross section per unit volume $\Delta\beta_m(R)$ is determined by the uncertainties in the radiosonde based measurement of the atmospheric temperature and pressure.

$$(\Delta\beta_m(R))^2 = \left(\frac{\partial\beta_m(R)}{\partial T(R)} \right)^2 (\Delta T(R))^2 + \left(\frac{\partial\beta_m(R)}{\partial P(R)} \right)^2 (\Delta P(R))^2 \quad (31)$$

Error in optical depth measurement is dominated by the error in the determination of the molecular return and the uncertainty on the density profile measured by a radiosonde (see Figure 40). For this study, a 2% error in the temperature profiles is assumed. The closest radiosonde measurement site is Green Bay (WI), which is ~ 180 km northeast from the lidar. Because the weather conditions can vary between the lidar site and the closest weather station, larger errors in the temperature profile are possible. The effects of errors on the atmospheric density profile can be minimized by making radiosonde measurements on the lidar site.

The figure shows, that with 3 min averaging time the cloud optical depths can be detected with ~ 10 % accuracy. This accuracy is sufficient when clouds with optical depths greater than 1 are measured. For situations where optical depth is less than 1, a longer averaging time is required.

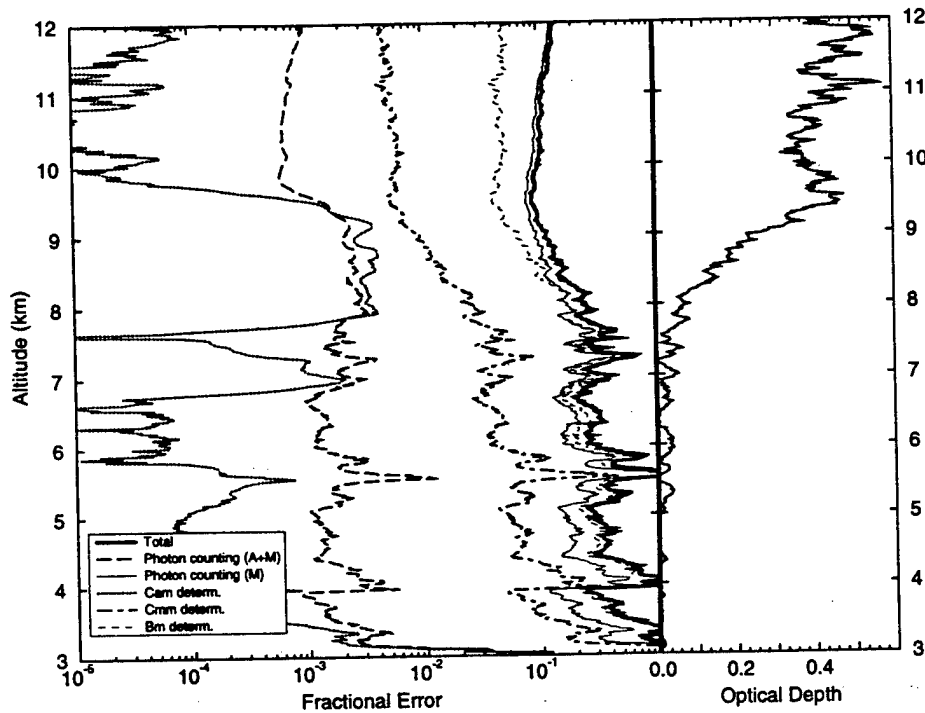


Figure 40. The effects of different errors to the optical depth in case of a thin cirrus cloud (November 11, 1993, 01:05-01:08 UT). Averaging time of the data is 3 min. The optical depth profile (rightmost graph) shows the variation of the optical depth as a function of altitude. Optical depth of 0.5 is measured for the range from 3 to 12 km and optical depth of 0.4 is observed for the cirrus cloud between 6.5 and 10 km. The errors in the measurement of the optical depth below 6.5 km are dominated by the inaccuracy of the radiosonde profile (leftmost graph) and the photon counting statistics of the molecular channel. The error in the calibration coefficient C_{mm} determination also has a significant effect on the total error. The optical depth of the thin cirrus cloud can be measured with $\sim 10\%$ accuracy.

The accuracy of the aerosol backscatter cross section measurement is limited by the accuracy of the molecular backscatter cross section per unit volume determination and the accuracy of the backscatter ratio.

$$\left(\Delta \beta_a(R) \frac{P_a(\pi, R)}{4\pi} \right)^2 = \left(\frac{\partial \beta_a(R) \frac{P_a(\pi, R)}{4\pi}}{\partial \beta_m(R, T, P)} \right)^2 (\Delta \beta_m(R, T, P))^2 + \left(\frac{\partial \beta_a(R) \frac{P_a(\pi, R)}{4\pi}}{\partial SR(R)} \right)^2 (\Delta SR(R))^2 \quad (32)$$

The effects of different errors on the aerosol backscatter cross section are shown in Figure 41. This figure shows, that the measurements are mostly limited by the photon counting statistics, but also the uncertainty on the $\beta_m(R)$ determination has a significant effect. The aerosol backscatter cross sections of clouds and strong aerosol layers can be observed with better than 10 % accuracy, but the measurements of clear air aerosol backscatter cross sections require longer averaging time.

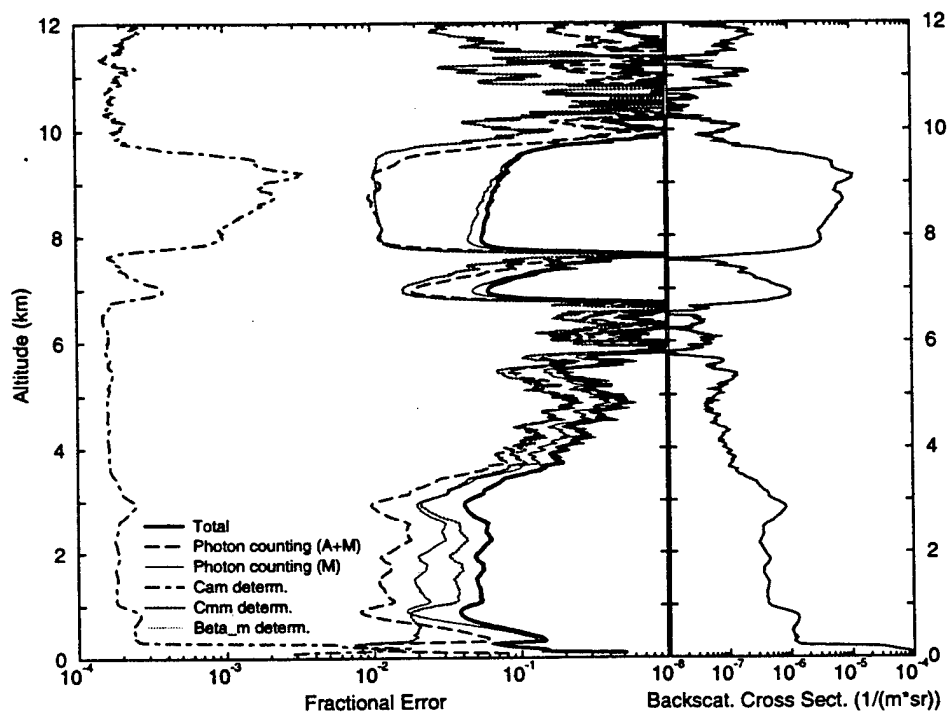


Figure 41. The effects of different errors to the aerosol backscatter cross section in case of a thin cirrus cloud (November 11, 1993, 01:05-01:08 UT). Averaging time of the data is 3 min. The aerosol backscatter profile is presented as a function of altitude (rightmost graph) and the backscatter cross section values range from $\sim 10^{-7}$ to $10^{-5} 1/m$. The aerosol backscatter cross section of the cirrus cloud (6-10 km) and the strong aerosol layer between 1 and 3.7 km can be determined with 4-10 % accuracy, but the measurements of the aerosol backscatter cross section of the clear air require a longer averaging time (leftmost graph).

The error in the phase function is affected by the errors on determinations of the molecular scattering cross section per unit volume, the aerosol and molecular profile, and the extinction cross section. These errors can be further divided to the photon counting errors, errors in the calibration coefficient determination, and errors in the background subtraction.

$$\left(\Delta \frac{P_a(\pi, R)}{4\pi}\right)^2 = \left(\frac{\partial \frac{P_a(\pi, R)}{4\pi}}{\partial \beta_m(R)}\right)^2 (\Delta \beta_m(R))^2 + \left(\frac{\partial \frac{P_a(\pi, R)}{4\pi}}{\partial SR(R)}\right)^2 (\Delta SR(R))^2 + \left(\frac{\partial \frac{P_a(\pi, R)}{4\pi}}{\partial \beta_e(R)}\right)^2 (\Delta \beta_e(R))^2 \quad (33)$$

Because the extinction section is a range derivative of the optical depth, the determination accuracy of the molecular profile limits the phase function measurements. For this study, the accuracy of the phase function determination is estimated for a 6 min section of the thin two-layer cirrus cloud. The statistics obtained within 3 min averaging time is not sufficient for the measurements of phase function profiles.

The accuracy of the phase function value determination can be seen from Figure 42. The cloud phase function can be observed with 10-20% accuracy when 6 min averaging time is used. By increasing the averaging time or the signal strength, accurate measurements of cloud phase function profiles can be made.

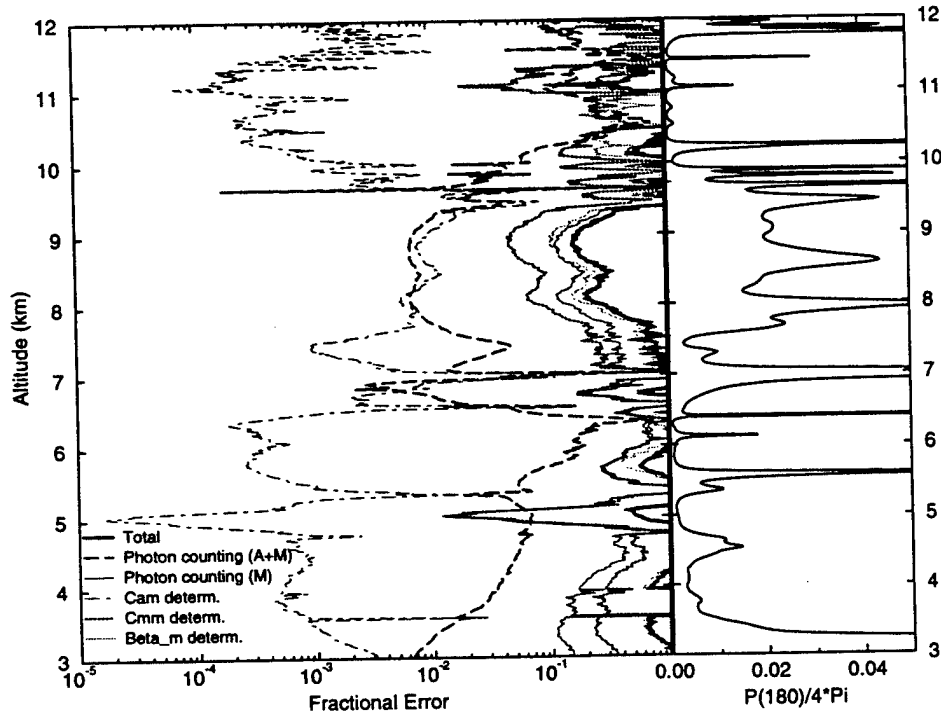


Figure 42. The effects of different errors on the phase function in case of a thin cirrus cloud (November 11, 1993, 01:05-01:11 UT). The 6 min averaging time is used. The phase function profile is presented as a function of altitude and the average phase function of the cirrus cloud layer between 7.5 and 10 km is 0.02 (rightmost graph). The accuracy of the phase function measurements is determined by the photon counting statistics, determination accuracy of the calibration coefficients, and accuracy of the molecular scattering cross section per unit volume (leftmost graph). The accuracy achieved within 6 min averaging provides phase function measurements with $\sim 20\%$ accuracy for the cloud layer.

Error in the inverted depolarization ratio can be presented as a sum of errors in the parallel channel and the perpendicular channel signals.

$$(\Delta\delta_{a,m}(R))^2 = \left(\frac{\partial\delta_{a,m}}{\partial N_{a,m\perp}}\right)^2 (\Delta N_{a,m\perp})^2 + \left(\frac{\partial\delta_{a,m}}{\partial N_{a,m\parallel}}\right)^2 (\Delta N_{a,m\parallel})^2 \quad (34)$$

The Fig 43 shows that the accuracy of the depolarization measurements is mostly limited by the accuracy of the perpendicular channel signal. The errors in the perpendicular channel signal determination are dominated by the photon counting statistics. The Figure 43 shows that short averaging times provide accurate measurements of cloud depolarization, and therefore reliable separation between water and ice clouds can be based on the depolarization measurements of the HSRL. Also reliable depolarization measurements of strong aerosol layers can be performed.

Figure 44 presents the errors in the molecular depolarization ratio. The measurements of molecular depolarization ratio can be performed with better than 10 % accuracy for the altitudes between 0.8 and 4 km. Reliable measurements of molecular depolarization for higher altitudes require longer averaging times. By using long averaging times the effects of atmospheric temperature on the measured depolarization can be studied.

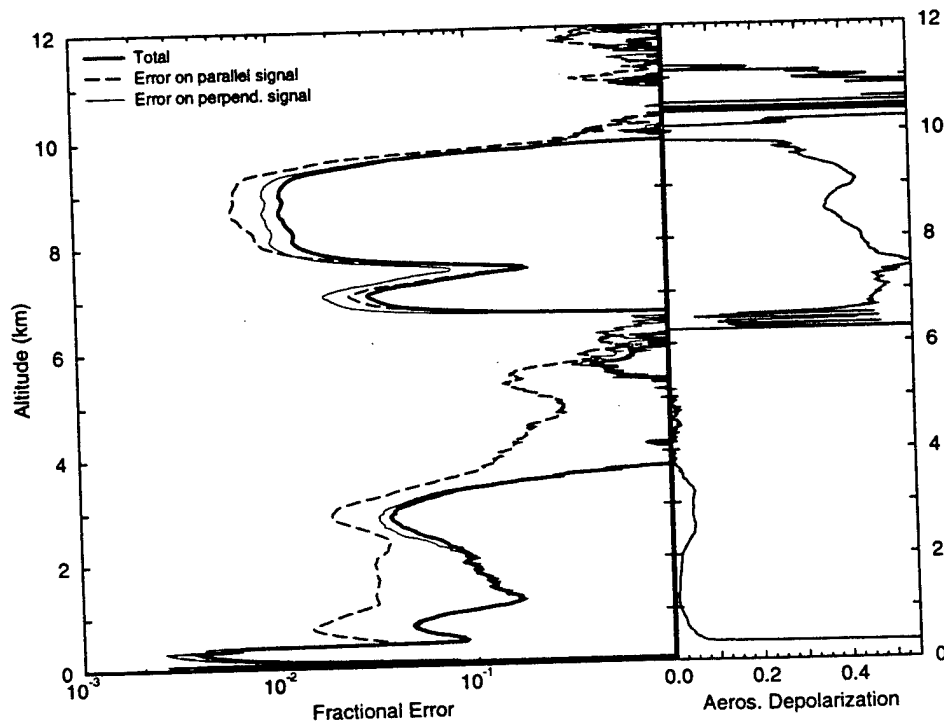


Figure 43. The effects of different errors to the inverted aerosol depolarization ratio in case of a thin cirrus cloud (November 11, 1993, 01:05-01:08 UT). Averaging time of the data is 3 min. The depolarization profile shows the variations of the inverted aerosol depolarization as a function of altitude (rightmost graph). A $\sim 40\%$ cirrus cloud depolarization is observed (6.5 - 10 km) and the depolarization of the strong aerosol layer is $\sim 5\%$. The measurements of the inverted aerosol depolarization ratio are limited by the accuracy of the perpendicular signal (leftmost graph). The depolarizations of clouds can be measured with $\sim 1\%$ accuracy. The depolarizations of strong aerosol layers are obtained with better than 10% accuracy.

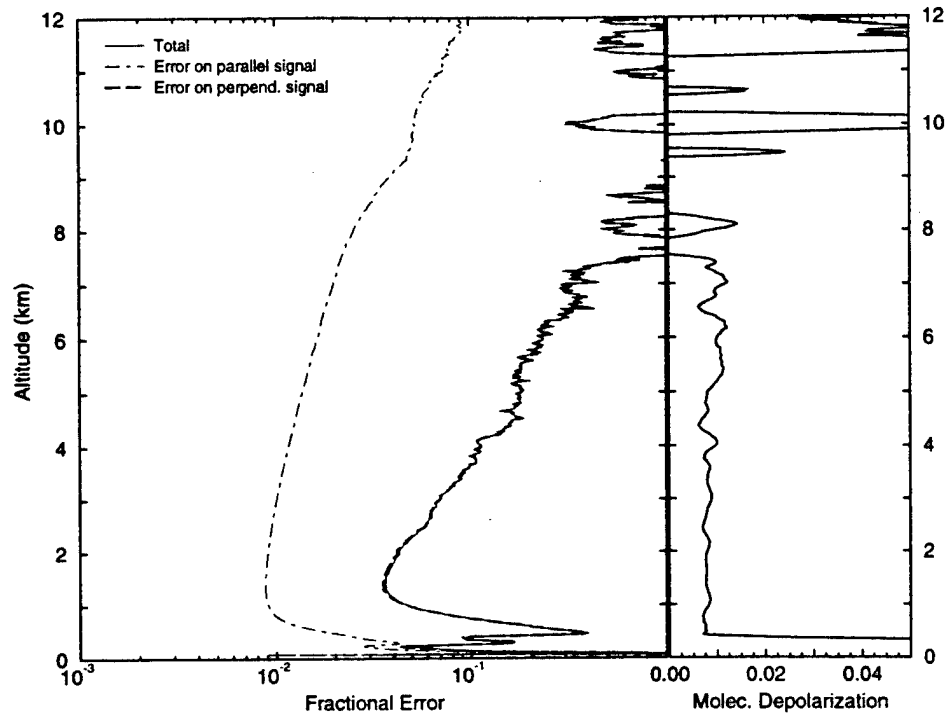


Figure 44. The effects of different errors on the inverted molecular depolarization ratio in case of a thin cirrus cloud (November 11, 1993, 01:05-01:08 UT). Averaging time of the data is 3 min. The depolarization profile shows the variations of the inverted molecular depolarization as a function of altitude (rightmost graph). A 0.8 % depolarization is observed from 0.5 to 7 km. The measurements of the molecular depolarization are limited by the accuracy of the perpendicular signal measurement (leftmost graph). For altitude between 0.8 and 4 km better than 10% accuracy is achieved. Measurements molecular depolarization for the higher altitudes require longer averaging times.

8 Conclusions

The work presented in this thesis has shown that the installation of the iodine absorption filter has substantially improved the performance of the University of the Wisconsin-Madison High Spectral Resolution lidar (HSRL). The new system design that includes the iodine absorption filter, polarization, and multiple scattering measurement capabilities is shown. The high resolution etalon, that was used in the earlier system to separate between aerosol and molecular scattering, provided only 1:2 separation for the aerosol backscatter signal between channels. The iodine absorption filter has been shown to suppress the aerosol backscatter signal on molecular channel down to 0.08% and therefore the aerosol cross talk signal on the molecular signal can be easily removed even for optically thick clouds. In the etalon based system, the determination of the system calibration terms was sufficient to provide accurate inversions only for the clear air aerosols and thin cirrus clouds. The use of the iodine absorption filter has also improved the robustness of the HSRL, reduced the complexity of the system, and increased the optical transmission of the system, so that accurate measurements of the optical depth, backscatter cross section and phase function can be made. Also the simultaneous measurements of depolarization and multiple scattering are performed. The HSRL implementation shows a depolarization measurement technique that uses the one transmitter laser and one detector to measure both polarization components. Therefore, no calibration of the receiver is required. The multiple scattering measurements are realized with a separate channel that allows measurements of signal strength variations as function of field of view simultaneously with the measurements of the narrow field of view channels.

The iodine absorption filter provides an absolute wavelength reference for the HSRL measurements. The iodine absorption line observed through a cell with 50% transmission on the line center is used for the wavelength locking of the HSRL transmitter laser. This provides stable operation over a long period of time without a need for frequent calibrations. Measurements have shown that the laser wavelength is maintained within ± 0.052 pm.

The stability and reliability of the system have been tested by operating the iodine absorption based HSRL at the University of Wisconsin-Madison campus. Start-

ing from July 1993, the HSRL has been routinely operated and data from different atmospheric conditions have been recorded. This dataset contains ~ 30 cirrus cloud cases. The measurements show that accurate measurements of optical properties of the atmosphere can be performed. The improved measurement accuracy has made possible to measure optical depth profiles inside the clouds. The current HSRL can be used to probe clouds that have optical depths up to ~ 3 . This means that most of the cirrus cloud cases can be fully observed and the bases of thick water clouds can be measured up to 300–500 m inside the cloud. This has been achieved by using the iodine absorption filter, high laser pulse repetition rate, small pulse energy per laser pulse, and very fast photon counting data system. The measurement accuracy of the HSRL is high enough to provide accurate measurements of optical parameters of clouds and strong clear air aerosol layers within 3 min averaging time, but the accurate measurements of clear air optical parameters require longer averaging times. The clear air optical parameters can be measured up to 35 km. The error analysis shows that accuracy of the HSRL measurements is mostly limited by the photon counting statistics. The system performance can be increased by increasing the system detection efficiency or/and increasing the transmitted laser power. The greatest improvement would be a photodetector with higher quantum efficiency and faster count rate capability.

The depolarization data obtained by the HSRL shows the ability of the HSRL to distinguish between water and ice clouds. It is shown, that the $160\mu\text{rad}$ field of view of the spectrometer channels effectively suppresses the multiple scattering effects on the measured depolarization ratio. Therefore, a reliable separation between water and ice clouds is possible. The HSRL measurements have shown, that traditional systems with 1–5 mrad field of views cannot reliably separate between water and ice, because the depolarization observed with a 1 mrad field of view is comparable to the ice depolarization within a small penetration depth from the water cloud base due to the multiple scattering. The error analysis shows, that the depolarization of the clear air aerosol layers can be observed with better than 10 % accuracy. The accuracy of the cloud depolarization measurements is better than 1 %. The measurements of depolarizations of weak aerosol layers and molecular backscatterer are limited by the

photon counting statistics.

The study of the cloud depolarizations between August 2 and November 11, 1993 shows that in 45 % of cirrus cloud cases simultaneous observations of supercooled water at cirrus cloud altitudes were made. The average cirrus cloud depolarization is shown to increase from 33% at -5°C temperature to 41% at -60°C . The observed behavior is different than observed by Platt *et al.*⁴³. The depolarization observed by Platt *et al.* ranged from $\sim 15\%$ to $\sim 40\%$ between temperatures from -10 to -60°C . The largest difference between the HSRL measurements and Platt's measurements is observed for the temperature range from -30 to -10°C , where Platt observed low cirrus cloud depolarizations. The low values of depolarization in Platt's measurement are most probably caused by multiple scattering from supercooled water droplets, because the system used for this measurement had a 2.5 mrad field of view. The HSRL measurements show that supercooled water clouds have been found at temperatures as low as -40°C and pure water clouds have been found at temperatures above 0°C . No water has been found at temperatures below -40°C and the presence of cirrus disappears at temperatures above 0°C . In the HSRL measurements, the cirrus cloud depolarization ratios for all temperatures are close to the values observed for the temperatures without supercooled water clouds. The small difference in the observed depolarization as a function of temperature may be a result of different shapes, sizes, and orientations of the ice crystals at different temperatures.

The depolarization of the molecular backscatter is $\sim 0.7\text{--}0.8\%$, when measured without the low resolution etalons. When the low resolution etalons are used, a $\sim 0.55\text{--}0.6\%$ depolarization is measured. The depolarization measured for the signal from the Cabannes line and the rotational Raman lines is 1.5% without any spectral filters. The measured molecular depolarization value is larger than the expected 0.4% depolarization of Cabannes line. The system filter bandpass admits a small fraction of the rotational Raman lines and blocks part of the Cabannes line and therefore an increase on the depolarization ratio is observed due to the presence of the highly depolarized rotational Raman lines. The model calculation for the depolarization transmission of the system show, that a $0.56\text{--}0.62\%$ depolarization is expected for the case where no low resolution etalons were used. A $0.402\text{--}0.425\%$ depolarization

is expected, when one or two etalon are used. The depolarization observed with the HSRL are larger than the expected values. The cause of the small difference between expected and measured depolarization values is currently unknown. The further analysis of the depolarization measurement accuracy of the HSRL requires an advanced study of effects of the iodine spectrum and rotational Raman lines to the depolarization.

The HSRL measurements require a knowledge of the atmospheric temperature profile. The atmospheric temperature profile measured with the HSRL shows that the HSRL can be used to measure temperature with a high enough accuracy so that the measured temperature profiles can be used for the analysis of the HSRL data. Therefore, the requirement for radiosonde measurements of atmospheric temperature could be eliminated. Before the temperature measurements with the HSRL can be routinely performed, the effects of aerosol backscatter signal to the molecular transmission of the iodine absorption filter have to be removed.

This study has provided an instrument basis for a design of a simple and robust lidar for the measurements of the optical properties of the atmosphere. The University of Wisconsin HSRL provides a unique instrument for the measurements of the cloud optical properties and the data measured with the HSRL provides useful information that can be used for the climate models that study the effects of clouds to the earth's atmosphere.

References

- [1] Stephens, G. L. and P. J. Webster, "Clouds and climate: Sensitivity of simple systems," *J. Atm. Sci.*, **39**, 235-247, 1981.
- [2] Liou, K.-N., "Influence of cirrus clouds on weather and climate processes: A global perspective," *Monthly Weather Review*, **114**, 1167-1192, 1986.
- [3] Ansmann, A., U. Wandinger, M. Riebesell, C. Weitkamp, and W. Michaelis, "Independent measurements of extinction and backscatter profiles in cirrus clouds by using a combined Raman elastic-backscatter lidar," *Appl. Opt.*, **31**, 7113-7131, 1992.
- [4] Whiteman, D. N., S. H. Melfi, and R. A. Ferrare, "Raman lidar system for the measurements of water vapor and aerosols in the Earth's atmosphere," *Appl. Opt.*, **31**, 3068-3082, 1992.
- [5] Fiocco, G. and J. B. DeWolf, "Frequency spectrum of laser echoes from atmospheric constituents and determination of aerosol content of air," *J. Atm. Sci.*, **25**, 488-496, 1968.
- [6] Schwiesow, R. L. and L. Lading, "Temperature profiling by Rayleigh-scattering lidar," *Appl. Opt.*, **20**, 1972-1979, 1972.
- [7] Shipley, S. T., J. H. Joseph, J. T. Trauger, P. J. Guetter, E. W. Eloranta, J. E. Lawler, W. J. Wiscombe, A. P. Odell, F. L. Roesler, J. A. Weinman, "The evaluation of a shuttle borne lidar experiment to measure the global distribution of aerosols and their effect on the atmospheric heat budget," Final report on NASA grant NSG 1057, 1975 pp. 150.
- [8] Shipley, S. T., D.H. Tracy, E. W. Eloranta, J. T. Trauger, J. T. Sroga, F. L. Roesler, and J. A. Weinman, "High resolution lidar to measure optical scattering properties of atmospheric aerosols. 1: Theory and instrumentation," *Appl. Opt.*, **22**, 3716-3724, 1983.

- [9] Sroga, J. T., E. W. Eloranta, S. T. Shipley, "F. L. Roesler, and P. J. Tryon, High spectral resolution lidar to measure optical scattering properties of atmospheric aerosols. 2: Calibration and data analysis," *Appl. Opt.* , 22, 3725-3732, 1983.
- [10] Grund, C. J., "Measurement of cirrus cloud optical properties by high spectral resolution lidar," Ph.D. Thesis, Department of Meteorology, University of Wisconsin-Madison, 1987.
- [11] Grund, C. J., E. W. Eloranta, "Fiber-optics scrambler reduces the bandpass range dependence of Fabry-Perot etalons used for spectral analysis of lidar backscatterer," *Appl. Opt.* 30, 2668, 1991.
- [12] Grund, C. J. and E. W. Eloranta, "University of Wisconsin High Spectral Resolution Lidar," *Optical Engineering*, 30, 6-12, 1991.
- [13] Eloranta, E. W. and P. K. Piironen, "Adaptation of the University of Wisconsin High Resolution Lidar for polarization and multiple scattering measurements," Sixteenth International Laser Radar Conference, Cambridge, Massachusetts, July 20-24, 1992, NASA Conference Publication 3158, 353-356, 1992.
- [14] Shimizu, H., S. A. Lee, and C. Y. She, "High spectral resolution lidar system with atomic blocking filters for measuring atmospheric parameters," *Appl. Opt.* 22, 1373-1391, 1983.
- [15] She, C. Y., R. J. Alvarez II, L. M. Caldwell, and D. A. Krueger, "High-spectral-resolution Rayleigh-Mie lidar measurements of aerosol and atmospheric profiles," *Opt. Lett.* 17, 541-543, 1992.
- [16] Alvarez, R. J. II, L. M. Caldwell, P. G. Wolyn, D. A. Krueger, T. B. McKee, and C. Y. She, "Profiling temperature, pressure, and aerosol properties using a high spectral resolution lidar employing atomic blocking filters," *J. Atm. Ocean. Techn.* 10, 546-556, 1993.

- [17] Krueger, D. A., L. M. Caldwell, R. J. Alvarez II, and C. Y. She, "Self-consistent method of determining vertical profiles of aerosol and atmospheric properties using a high spectral resolution Rayleigh-Mie lidar," *J. Atm. Ocean. Techn.* **10**, 533-545, 1993.
- [18] Gerstenkorn, S. and P. Luc, *Atlas du spectre d'absorption de la molecule d'iode* (Centre National de la Recherche Scientifique, Paris, 1978).
- [19] Harrison, J. A., M. Zahedi, and J. W. Nibler, "Use of seeded Nd:YAG lasers for high-resolution spectroscopy," *Opt. Lett.* **18**, 149-151, 1993.
- [20] Liao, K. H. and R. Gupta, " I_2 vapor cell as narrow band optical filter," *Rev. Sci. Instr.*, **49**, 867-869, 1978.
- [21] Miles, R. B., J. N. Forkey, and W. R. Lempert, "Filtered Rayleigh Scattering measurements of supersonic/hypersonic facilities," AIAA 17th Aerospace Ground Testing Conference, July 6-8, 1992, Nashville, TN (USA).
- [22] Piironen, P. and E. W. Eloranta, "Demonstration of a high spectral resolution lidar based on an iodine absorption filter," *Opt. Lett.* **19**, 234-236, 1994.
- [23] Klett, J. D., "Stable analytical inversion solution for processing lidar returns," *Appl. Opt.* **20**, 211-220, 1981.
- [24] Hinkley, E. D. (editor), "Laser Monitoring of the Atmosphere," Springer-Verlag, New York, 1976.
- [25] Eloranta, E. W. "Calculation of doubly scattered lidar returns," Ph. D. Thesis, Department of Meteorology, University of Wisconsin, 1972.
- [26] Eloranta, E. W., "A practical model for the calculation of multiply scattered lidar returns," Optical Society of America, Remote Sensing of the Atmosphere, Topical Meeting, Salt Lake City, Utah, March 8-12, 1993, pp. ThE20-1.
- [27] Eloranta, E. W. and S. T. Shipley, "A solution for multiple scattering," in *Atmospheric Aerosols: Their Formation, Optical Properties, and Effects*, Spectrum Press, Hampton, Virginia, 1982.

- [28] *Model S100 Injection Seeding System*, Lightwave Electronics Corporation, California, USA, 1989.
- [29] Grund, C. J., F. L. Roesler, and E. W. Eloranta, "Thermally induced spectral drift cancellation in pressure-tuned Fabry-Perot etalons," *Appl. Opt.* , **27**, 662-663, 1988.
- [30] Sroga, J. F., "Remote measurements of aerosol scattering properties by an airborne high spectral resolution lidar," Ph. D. Thesis, University of Wisconsin-Madison, 1983.
- [31] *How to perform photon counting using photomultiplier tubes*, Hamamatsu, Technical Information, No. ET-06/Feb 1990.
- [32] *TRC thermodynamic tables (Non-hydrocarbons)*, (College Station, Tex. : Thermodynamics Research Center, Texas A & M University, 1986), pp. k-190, ka-190.
- [33] Arie, A. and R. L. Byer, "Laser heterodyne spectroscopy of $^{127}\text{I}_2$ hyperfine structure near 532 nm," *J. Opt. Soc. Am. B.*, **10**, 1990-1997, 1993.
- [34] Yip, S. and M. Nelking, "Application of kinetic model to time-dependent density correlations in fluids," *Physical Review*, **135**, A1241-A1247, 1964.
- [35] Arie, A. and R. L. Byer, "Frequency stabilization of the 1064-nm Nd:YAG lasers to Doppler-broadened lines of iodine," *Appl. Opt.* , **32**, 7382-7386, 1993.
- [36] Scotland, R. M., K. Sassen, and R. Stone, "Observations by lidar of linear depolarizations of hydrometeors," *J. Appl. Meteor.*, **10**, 1011-1017, 1971.
- [37] Sassen, K. "The polarization lidar technique for cloud research: a review and current assessment," *Bull. Am. Meteor. Soc.*, **72**, 1848-1866, 1991.
- [38] Pal, S. R. and A. I. Carswell, "Polarization properties of lidar backscattering from clouds," *Appl. Opt.* , **12**, 1530-1535, 1973.
- [39] Rowell, R. L. and G. M. Aval, "Rayleigh-Raman depolarization of laser light scattered by gases," *J. Chem. Phys.*, **54**, 1960-1964, 1971.

- [40] Young, A. T., "Rayleigh scattering," *Physics Today*, January 1982, 42-48, 1982.
- [41] Liou, K.-N. and H. Lahore, "Laser sensing of cloud composition: a backscatter depolarization technique," *J. Appl. Meteor.*, **13** 257-263, 1974.
- [42] Kumai, M., "Formation of ice crystals and dissipation of supercooled fog by artificial nucleation, and variations of crystal habit at early growth stages," *J. Appl. Meteor.*, **21**, 579-587, 1982.
- [43] Platt, C. M. R., J. C. Scott, and A. C. Dilley, "Remote sensing of high clouds. Part VI: Optical properties of midlatitude and tropical cirrus," *J. Atm. Sci.* **44**, 729-747, 1987.
- [44] Strauch, R. G., V. E. Derr, and R. E. Cupp, "Atmospheric temperature measurement using Raman backscatter," *Appl. Opt.* , **10**, 2665-2669, 1971.
- [45] Cooney, J., "Measurements of atmospheric temperature profiles by Raman backscatter" *J. of Appl. Meteor.*, **11**, 108-112, 1972.
- [46] Kalshoven, J. E., Jr., C. L. Korb, G. K. Schemmer, and M. Dombrowski, "Laser remote sensing of atmospheric temperature by observing resonant absorption of oxygen," *Appl. Opt.* , **20**, 1967-1971, 1981.
- [47] Endemann, M. and R. L. Byer, "Simultaneous measurements of atmospheric temperature and humidity using a continuously tunable IR lidar," *Appl. Opt.* , **20**, 3211-3217, 1981.
- [48] P. Keckhut, A. Hauchecorne, and M. L. Chanin, "A critical review of the database acquired for the long-term surveillance of the middle atmosphere of the French Rayleigh lidars," *J. Atm. Ocean. Techn.*, **10**, 850-867, 1993.
- [49] Heymsfield, A. J., "Precipitation development in stratiform ice clouds: A microphysical and dynamical study," *J. Atm. Sci.*, **34**, 367-381, 1977.

**ANALYSIS OF VISIBLE AND INFRARED
CIRRUS CLOUD OPTICAL PROPERTIES
USING HIGH SPECTRAL RESOLUTION
REMOTE SENSING**

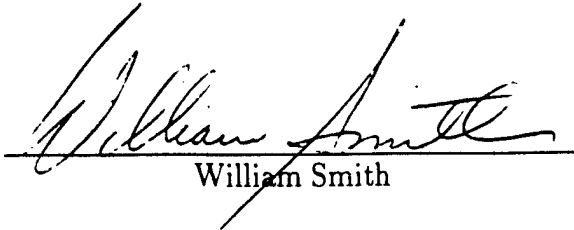
By
Daniel H. DeSlover

A THESIS SUBMITTED IN PARTIAL FULFILLMENT OF THE
REQUIREMENTS FOR THE DEGREE OF

Master of Science
(Atmospheric and Oceanic Sciences)

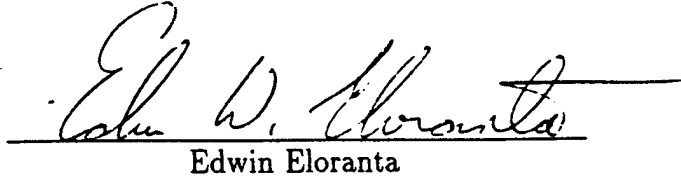
at the
UNIVERSITY OF WISCONSIN – MADISON
1996

Approved by:


William Smith

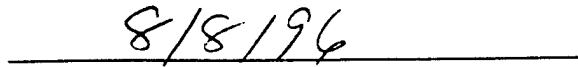
Professor, Atmospheric and Oceanic Sciences

Approved by:


Edwin Eloranta

Senior Scientist, Atmospheric and Oceanic Sciences

Date:


8/8/96

Abstract

Infrared and visible cirrus cloud optical properties were measured using ground-based high spectral resolution remote sensing data. The optical properties include: downwelling atmospheric radiance at infrared wavelengths and atmospheric aerosol backscatter cross-section and depolarization at a visible wavelength. Data was acquired at the University of Wisconsin-Madison, during a 3 month case study from October through early December, 1995. The instrument suite included: a High Spectral Resolution Lidar (HSRL), an Atmospheric Emitted Radiance Interferometer (AERI), and a Cross-chain Loran Atmospheric Sounding System (CLASS).

The high spectral resolution AERI allowed data analysis in 19 spectral intervals between water vapor lines in the infrared atmospheric window located between 770 and 1200 cm^{-1} . AERI measured downwelling atmospheric radiance provided the downwelling brightness temperature. AERI radiance combined with radiosonde data, HSRL measured cloud boundaries, and Fast Atmospheric Signature Code (FASCOD3P) allowed inversion of infrared cloud optical depth at each of these spectral regions. The infrared results were compared against 0.532 μm HSRL measured optical depth and derived brightness temperatures. HSRL derived brightness temperatures were determined using visible optical depth data, radiosonde data, and FASCOD3P model simulated clear sky radiance and transmission below the cloud. A comparison of visible to infrared optical depths demonstrated a spectral dependence in the data. Mie theory applied to ice spheres suggested a spectral particle size sensitivity that was apparent in the data and consistent with 35 to 50 μm radius particles. Optical depth and brightness temperature results are presented for various cases which demonstrate close agreement between the instruments. Combining the data from each instrument yields a weighted cloud extinction cross-section which improved the results relative to Mie theory.

An estimation of the expected error is also given, where the primary error sources were water vapor continuum uncertainties in the FASCOD3P model derived values and instrument field of view and temporal averaging differences. Brightness temperature errors, associated with FASCOD3P uncertainties, approached 4 K for a boundary layer relative humidity of less than 70 percent. Instrumental field of view and dwell-time characteristics exhibited large differences in the results for non-uniform cloud conditions. Field of view differences were shown to account for an 80 percent difference in measured optical depth, while instrumental dwell-times were shown to account for a several-fold difference in optical depth. Both examples were for the extreme case of broken cirrus.

Acknowledgments

I would like to thank my advisors, Dr. Edwin Eloranta and Prof. William Smith, who provided me with the opportunity to perform research under their supervision with a pair of phenomenal instruments. The data used for this thesis would not have been possible without their support.

The time taken by Dr. Edwin Eloranta and Professors Steve Ackerman, Matt Hitchman, and William Smith to review this thesis was appreciated. The comments and suggestions were helpful in bringing the ideas forward more clearly.

Many kudos to the entire UW lidar group. A huge thanks to Päivi Piironen for helping out with the HSRL data acquisition and analysis, and making sure I was awake to take data! Also, for taking the time to read over my first draft and providing helpful suggestions for improvement. Dan Forrest, Antti Piironen, and Walter Wolf were always helpful in pointing out better methods of approach on computer and other related issues.

Thanks to Andrew Collard for useful discussions regarding AERI measurements and data analysis and for feedback on my results. Also, for getting me going with the adding-doubling model, which was needed to derive cirrus reflectance of upwelling radiance.

Acquisition and analysis of the AERI data would not have occurred without the assistance of Bob Knuteson, Hank Revercomb, Ralph Dedecker, Tim Dirks, and Ray Garcia. I appreciate the opportunity granted in the use of the instrument and that 'extra' time needed to finish the case study. Also, to John Short for helping out with the CLASS system and maintaining a steady supply of radiosondes and LN_2 .

Finally, I would like to express my gratitude to the Wisconsin Space Grant Consortium for partially funding my involvement in this research. Additional funding and instrument operations were supported under the following grants: NSF, ATM-9321330; NASA, NAG-1-882; Lockheed, SK30G4160F; USAFGL, F19628-91-K-0007; DOE, DR-FG02-90ER61057; and NOAA, NA47EC0057.

Contents

Abstract	i
Acknowledgements	iii
List of Tables	vi
List of Figures	vii
1 Introduction	1
2 Theory	5
2.1 Infrared Spectrum	5
2.1.1 IR Radiative Transfer	8
2.1.2 FASCOD3P Model	11
2.1.3 IR Scattering from Mie Model	17
2.1.4 IR Optical Depth Inversion	19
2.1.5 IR Optical Depth using Ozone Attenuation	21
2.2 Visible Spectrum	22
2.2.1 General Lidar Equation	22
2.2.2 Two-Channel Lidar	24
2.2.3 Visible Optical Properties	26
2.2.4 HSRL Derived Brightness Temperature	28
3 Instrumentation	30
3.1 AERI	30
3.1.1 Hardware	31
3.1.2 Characteristics	33
3.1.3 Calibration and Acquisition	33
3.2 HSRL	34
3.2.1 Transmitter	34

List of Tables

1	AERI Specifications	33
2	Väisälä Radiosonde Specifications	37
3	AERI/HSRL Data Cases at UW - Madison	38
4	HSRL:AERI Derived $\alpha(\nu)$ for Uniform Cloud	50
5	HSRL:AERI Derived $\alpha(\nu)$ for Weighted Cloud	70
6	AERI Microwindow Regions	79
7	FASCOD3P Input File: Row 2	86
8	FASCOD3P Input File: Row 5	87
9	Reflectance Fit Coefficients	89

List of Figures

1	Example illustration of atmospheric downwelling radiance.	7
2	Radiosonde temperature and dewpoint temperature data for Madison, WI on 17 November 1994, 00:00 UTC.	12
3	AERI measured and FASCOD3P calculated clear sky atmospheric column radiance for data acquired at Madison, WI on 17 November 1994, 00:00 UTC.	13
4	Gamma spectrum for AERI measured clear sky and FASCOD3P calculated radiance difference shown in Figure 3.	15
5	Downwelling fractional radiance difference for altitudes 9 through 15 km.	17
6	HSRL two-channel technique, where molecular and aerosol backscatter signal is separated with an iodine absorption filter.	25
7	Upper plot illustrates HSRL measured column integrated visible optical depth relative to inverted aerosol and molecular backscatter returns shown in the lower plot.	27
8	Photograph of AERI-00 prototype.	31
9	Schematic diagram of Michelson interferometer technique.	32
10	HSRL inverted aerosol backscatter signal for 17 November 1994. The abscissa indicates time in UTC format.	40
11	HSRL inverted aerosol depolarization signal for 17 November 1994. The abscissa indicates time in UTC format.	41
12	HSRL inverted aerosol backscatter signal for 10 November 1995. The abscissa indicates time in UTC format.	42
13	HSRL inverted aerosol depolarization signal for 10 November 1995. The abscissa indicates time in UTC format.	43
14	HSRL visible and AERI infrared optical depth as a function of time on 17 November 1994.	45

15	HSRL visible and AERI infrared optical depth as a function of time on 9-10 November 1995.	48
16	Infrared optical depth as a function of cloud radiance.	49
17	Comparison of HSRL visible and AERI 862 cm^{-1} microwindow infrared optical depth for the cirrus cases listed in Table 3.	50
18	HSRL backscatter cross-section as a function of altitude for data taken between 23:55 and 00:03 UTC 9-10 November 1995.	52
19	Comparison of temperature and dewpoint temperature data for radiosondes launched from the UW at 00:00 and 03:00 UTC on 17 November 1994.	54
20	Expected radiance error due to atmospheric changes over a 3 hour period and expected uncertainties in the radiosonde measurements.	55
21	AERI measured optical depth uncertainty for data acquired 17 November 1994.	56
22	Spectral comparison of experimentally derived $\alpha(\nu)$ against Mie theory for various particle size distributions.	58
23	HSRL derived brightness temperature relative to AERI measured values for 811 cm^{-1} and 820 cm^{-1} microwindows on 17 November 1994.	60
24	HSRL derived brightness temperature relative to AERI measured values for 934 cm^{-1} and 1096 microwindows on 17 November 1994.	61
25	HSRL derived brightness temperature as a function of time at 934 cm^{-1} relative to AERI measured values on 9-10 November 1995 at Madison. Also illustrated is the HSRL measured visible column optical depth.	62
26	AERI and HSRL derived brightness temperature data for the cirrus cases given in Table 3 for the 934 cm^{-1} microwindow.	64
27	Visible to infrared optical depth ratio, $\alpha(\nu)$, comprising all spectral microwindows for the data cases listed in Table 3.	65

28	Visible to infrared optical depth ratio, $\alpha(\nu)$, as a function of time, relative to the visible optical depth, at 934 cm^{-1} for 17 November 1994 data.	66
29	Spectral visible to infrared optical depth data for individual data cases listed in Table 3.	67
30	Similar to Figure 22, but updated with $\alpha(\nu)$ using weighted data from all cases.	69
31	Effects of Gamma correction on HSRL derived brightness temperature for 17 November 1994 data.	71
32	Comparison of measured and derived radiances for 9–10 November 1995.	73
33	Upper figure shows HSRL derived brightness temperature and maximum expected brightness temperature, given the radiance errors illustrated in Figure 20, for data acquired on 17 November 1994. .	74
34	A visualization of AERI microwindow regions listed in Table 6, 760 through 910 cm^{-1}	80
35	Spectral continuation of Figure 34, 910 through 1090 cm^{-1}	81
36	Spectral continuation of Figure 34, 1090 through 1250 cm^{-1}	82
37	A comparison of broadband brightness temperature using parameterized Planck function linear in temperature and standard Planck function.	84
38	Portion of a typical FASCOD3P 'TAPE5' data file.	85
39	Reflectance as a function of IR optical depth and a sixth-order polynomial fit for the microwindow region centered at 722 cm^{-1}	88

1 Introduction

The climatic importance of atmospheric anthropogenic gases such as carbon dioxide and methane, in addition to the state of the ozone layer, is currently a major scientific and political issue (Schneider, 1990; Chappelaz et al., 1993; Genthon et al., 1987). However, cirrus clouds have a similar climatic role as these 'greenhouse gases,' where a one percent increase in cirrus cloud cover is comparable to a four percent increase in carbon dioxide. This is based on cloud cover results published by Rossow and Lacis (1990). An effort directed toward the study of cirrus clouds should be similar to the level and scope of greenhouse gas research.

Analysis of cirrus cloud optical properties is necessary to develop an understanding of the earth's radiative budget. The radiative transfer mechanism drives the atmospheric temperature cycle; where incident solar (shortwave or visible) radiation is imbalanced with upwelling terrestrial (longwave or infrared) radiation. A change in the mean global coverage of cirrus clouds could have a sustained repercussion to the thermally driven global climate. Clouds which consist of ice particles, with a typical altitude range of 4 to 15 km, are referred to as cirrus in this thesis.

Absorption and scattering of radiation are processes which determine the atmospheric column optical thickness. Optically thin cirrus is more transparent to downwelling visible light than to upwelling radiation due to absorption by ice in the infrared (IR). Thus, heating of the lower atmosphere occurs with the presence of thin cirrus. As the cirrus becomes optically thick, it begins to scatter a greater amount of solar radiation back to space, while trapping a greater amount of upwelling IR radiation. The magnitude of radiative forcing is dependent upon the cloud altitude and particle size distribution. High altitude clouds offer greater ability to trap upwelling IR radiation. Cloud particle size affects the amount of solar radiation that reaches the surface. Simultaneous visible and infrared measurement of the cloud optical depth is critical in developing model simulations that will properly account for the presence of cirrus in radiative transfer calculations.

Interest in cirrus clouds and their effect on the radiation budget has increased within the last few decades. Radiative transfer modeling, given various particle sizes and shapes (Deirmendjian, 1969; Plass and Kattawar, 1971; Stephens, 1980; Hess and Wiegner, 1994), have been useful to gauge the importance of cirrus to radiative transfer. Recent technological advancement has demonstrated the feasibility of visible and infrared observations using both ground-based and space-borne instrumentation incorporating active and passive techniques (Stone et al., 1990; Platt, 1973; Piironen and Eloranta, 1994; Smith et al., 1993).

Platt (1973) monitors simultaneous visible and infrared properties using a single-channel ground-based lidar and broadband radiometer. A single channel lidar cannot determine the cloud optical depth, due to the inherent coupling of the extinction cross-section to the aerosol and molecular backscatter cross-sections. Therefore, radiometer measurements are required to derive the visible cirrus cloud optical depth. However, the approach makes several assumptions to infer the cirrus optical properties. This includes the assumption that the visible to infrared extinction coefficient is constant, which is used to convert the measured broadband infrared optical depth to a visible value derived from simultaneous infrared and visible measurements (Platt, 1979; Platt and Dilley, 1979). This results in visible optical properties that are dependent upon the infrared measurements. This technique also requires a large data set to extract the backscatter-to-extinction ratio. Cloud radiance is determined by removing a model calculated clear sky radiance from the surface to cloud base; and is often contaminated with atmospheric water vapor. Finally, temporal and spatial differences due to instrument characteristics also affect the data. The use of high spectral resolution instruments to measure visible and infrared properties reduces these problems. Furthermore, it provides the opportunity to spectrally validate the models.

This thesis encompasses my research conducted on cirrus cloud optical properties, incorporating data from two high spectral resolution remote sensing instruments developed at the University of Wisconsin - Madison (UW). The first instrument, the Atmospheric Emitted Radiance Interferometer (AERI), is a passive

sensor that measures the emitted spectral radiance from an atmospheric column. The second instrument, the High Spectral Resolution Lidar (HSRL), is an active sensor which emits visible light and measures the aerosol backscattered signal and depolarization as a function of altitude. Each instrument monitors a vertical atmospheric column that is advected into the instrument's respective field of view in the zenith direction. Atmospheric state information is necessary to invert the data collected by these instruments. It is acquired through the use of a local radiosonde launch using the Cross-chain Loran Atmospheric Sounding System (CLASS). Recent theses by Piironen (1994) and Feltz (1994) provide an additional detailed description of the HSRL and AERI, respectively.

AERI measured downwelling radiance, vertical atmospheric temperature and dewpoint temperature profiles, and HSRL measured cloud boundaries will allow inversion of the IR radiative transfer equation for a cloudy atmosphere to yield the cloud infrared optical depth. The high spectral resolution AERI measurements will provide IR optical depths in a number of regions between water vapor absorption lines within the infrared atmospheric window located between 770 and 1200 cm^{-1} . The HSRL provides a 532 nm optical depth, which can be compared to the IR measured values.

This analysis will reveal an experimental relationship of the visible to infrared optical depth for each spectral region by two different techniques: a direct comparison of the measured visible to derived infrared optical depth; and iteration of the ratio using a forward solution of the radiative transfer equation, based on the HSRL measured visible optical depth, to derive the downwelling column radiance relative to AERI measured data at the given wavenumber regions. In the former approach, the visible to infrared optical depth ratio will be used to determine the downwelling column radiance. The latter approach will yield the infrared optical depth. Overall, both techniques will produce the same optical properties. However, the latter should achieve better results given the effective cloud weighting inherent to the HSRL data and coupling of the visible and IR data.

Particle size, shape, number density, and phase are additional parameters which affect the radiative transfer mechanism. Particles that are much smaller than the incident wavelength will scatter the light according to Rayleigh theory, whereas particle size on the order of the wavelength will scatter according to Mie theory assuming spherical ice particles. Although ice particles are not spherical, a Mie theory model will be utilized to compare the spectral optical depth measurements with theory.

A brief overview of the AERI, HSRL, and CLASS systems will describe each instrument. The goal is to detail the individual instrument characteristics that allow solution of the problem at hand. This should provide the reader with a fundamental background to complement the theoretical derivations and experimental results that will be presented.

Data was collected during a three-month case study at the UW, which occurred from October through early December, 1995. Additional data sets were acquired at the UW, prior to this experiment, when both the AERI and HSRL were available for simultaneous operation. This provided a fair sample of cirrus events with a few mixed-phase and water cloud cases. Data acquisition in a winter climate also reduced background atmospheric emission due to boundary layer humidity, which increases during the summer season.

2 Theory

The atmosphere consists of molecules and aerosols. An aerosol constitutes anything other than a molecule suspended in the atmosphere, typically within a size range between 10^{-2} to 10^4 μm (Measures, 1992). This includes wind blown dust and pollen, various forms of pollution (e.g., ash, sulfites) which may change through photochemical processes, and all varieties of clouds. Together these particles scatter, absorb, and emit radiation from the ultraviolet through infrared.

The presence of an equator to pole gradient of incident solar radiation, coupled with infrared radiative cooling, induces a thermally driven global circulation. Spectral characteristics due to thermal differences between solar and terrestrial emission allow independent observation of this radiative imbalance; where the visible and infrared Planck emission curves exhibit negligible overlap. The following sections will detail and differentiate the radiative principles required to analyze remotely sensed observations in the infrared and visible domains.

2.1 Infrared Spectrum

Atmospheric constituents, primarily carbon dioxide, water vapor, and ozone (CO_2 , H_2O , and O_3 , respectively), provide the medium for radiative interaction due to absorption of upwelling terrestrial radiation. Subsequently, the energy is isotropically re-emitted at the wavelengths where the absorption occurred. Airborne aerosols also contribute to the radiative transfer mechanism and should not be neglected.

Optical depth, in a given spectral band, depends on the absorption line strength and the vertical distribution of atmospheric gases. CO_2 is well-mixed and is often treated as a permanent species, although its overall concentration changes slowly with time. H_2O and O_3 concentrations have significant spatial and temporal variation. Atmospheric water vapor content determines the current synoptic situation, where advection of moist or dry air will dictate the local moisture profile. O_3

concentration peaks in the stratosphere, between 15 and 30 km, and is produced by photochemical processes. O_3 concentration also varies with the synoptic situation, where stratospheric air is often ingested into the troposphere during a cold frontal passage. O_3 is often produced from combustion engine exhaust in the lower atmosphere by photochemical reactions.

Figure 1 illustrates downwelling spectral radiance as a function of wavenumber. The dominant species are CO_2 (600 to 800 cm^{-1} , 15 μm), O_3 (1000 to 1060 cm^{-1} , 9.6 μm), and H_2O . The H_2O absorption signature is of particular interest due to its spectral distribution. The atmospheric window (800 to 1200 cm^{-1}) is the most transparent region in the spectrum. Measurements between water vapor lines within the atmospheric window (referred to as 'microwindows' and tabulated in Appendix A) yield observations with the least atmospheric contamination. The H_2O absorption lines present an additional problem because the far 'wings' of individual H_2O lines combine to form the water vapor continuum. Thus, even the microwindows are not completely transparent.

An overlay of Planck radiance, for several temperature values (200 through 280 K, in 20 K increments), is shown in Figure 1 for comparison to the downwelling radiance. Note the contrast between the atmospheric window and regions of strong absorption, where the atmosphere becomes opaque over a short distance. These values correlate well with a surface measured temperature of 277 K. The spikes in the observed spectrum between 1400 and 1800 cm^{-1} are artifacts of water vapor absorption lines which become opaque within the instrument, causing the system responsivity to approach zero. This results in an increase in calibrated radiance noise due to the small instrumental noise in these opaque spectral regions.

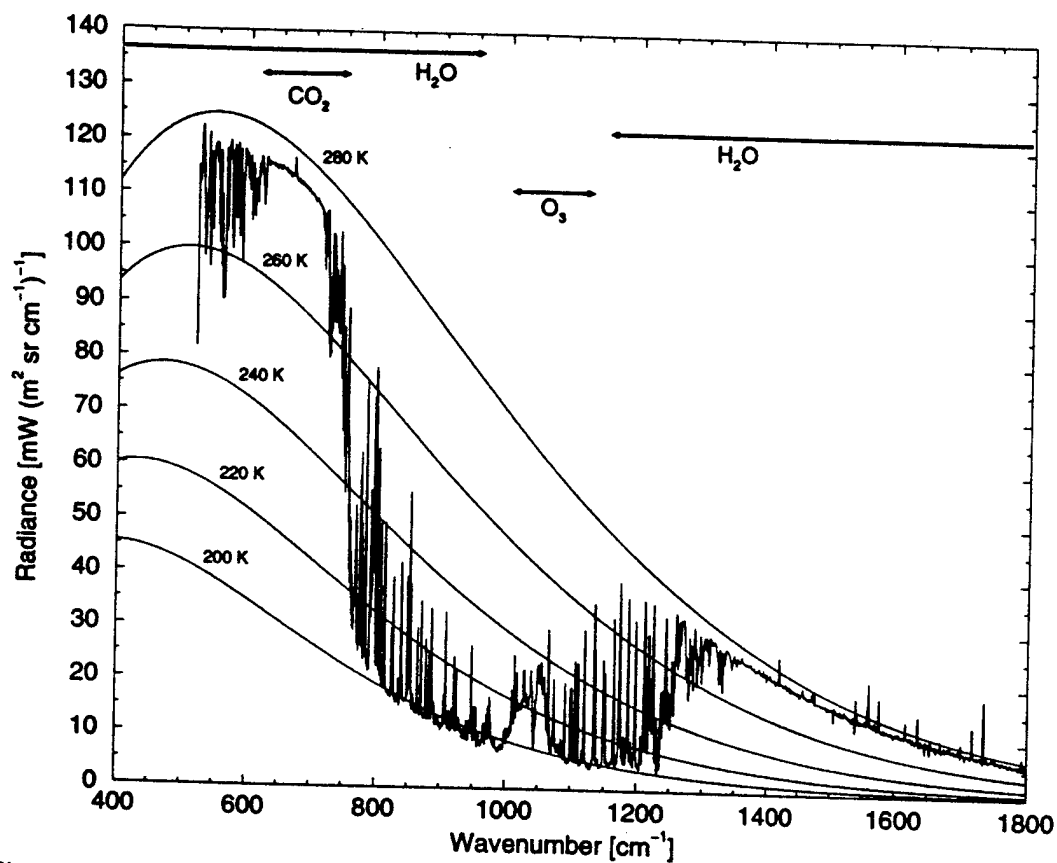


Figure 1: Illustration of atmospheric downwelling radiance relative to values derived from the Planck function for various temperatures. Also noted are the absorption regions for various atmospheric constituents. The spikes in the measured radiance, between 1400 and 1800 cm⁻¹, are a result of water vapor absorption lines which become opaque within the instrument.

2.1.1 IR Radiative Transfer

Given a temperature profile and vertical distribution of gaseous constituents in a clear atmosphere, one can derive the radiance if the spectroscopic properties of the gas are also known. For monochromatic radiation, the differential transmissivity through the atmosphere is determined by

$$d\tau(\nu, p_a, p) = -\tau(\nu, p_a, p) \left(\sum_x k_x(\nu) g^{-1} r_x dp \right); \quad (1)$$

where

- $\tau(\nu, p_a, p)$ = atmospheric transmission from p_a to p ;
- $k_x(\nu)$ = absorption of atmospheric constituent x , $\text{m}^2 \text{kg}^{-1}$;
- ν = wavenumber, cm^{-1} ;
- g = gravitational acceleration, m s^{-2} ;
- r_x = mixing ratio of constituent x , g kg^{-1} ; and
- p = pressure at given level, hPa.

Atmospheric pressure units are often expressed in mb, and are equivalent to hPa.

The general radiative transfer equation (RTE) for downwelling spectral radiance in a clear atmosphere is described by the relation

$$R(\nu) \downarrow = \int_0^{p_s} B(\nu, T(p)) d\tau(\nu, p_s, p); \quad (2)$$

where

$$B(\nu, T(p)) = \frac{2hc^2\nu^3}{\exp\left[\frac{hc\nu}{kT(p)}\right] - 1} \quad (3)$$

represents the Planck radiance, $\text{mW (m}^2 \text{sr cm}^{-1})^{-1}$;

$$d\tau(\nu, p_s, p) = \frac{\partial\tau(\nu)}{\partial p} dp$$

is the differential transmission over the pressure layers;

- $R(\nu) \downarrow$ = AERI measured downwelling column radiance,
 $\text{mW (m}^2 \text{ sr cm}^{-1})^{-1}$;
 $T(p)$ = temperature at pressure level p , K;
 h = Planck's constant, J s;
 c = speed of light, m s^{-2} ;
 k = Boltzmann's constant, J K^{-1} ;

and the integral limits, p_s and 0, specify surface layer and top of atmosphere, respectively.

The radiance is often described in terms of a temperature because it removes the spectral dependence, normalizing the data with respect to the Planck curve. This 'effective temperature' is referred to as the brightness temperature, T_b , and is the solution of Equation 3 for $T(p)$, in terms of the measured radiance,

$$T_b(\nu) = \frac{h\nu}{k \ln \left[\frac{2hc^2\nu^3}{R(\nu)\downarrow} + 1 \right]}; \quad (4)$$

where the measured downwelling column radiance, $R(\nu) \downarrow$, has been substituted for the Planck radiance, $B(\nu, T(p))$.

Equation 4 will yield small errors when used for a spectral bandpass rather than a single wavenumber; where the bandpass would be represented by the mean wavenumber, ν_c . A correction, based on a least-squares fit of the measured radiance in a given bandpass over a typical temperature domain, can be applied to Equation 4, such that

$$T'_b(\nu_c) = \frac{1}{b} \left[\frac{h\nu_c}{k \ln \left[\frac{2hc^2\nu_c^3}{R(\nu)\downarrow} + 1 \right]} - a \right]; \quad (5)$$

where a and b are the least-squares fit y-intercept and slope, respectively. Appendix B summarizes this approach and illustrates the associated errors.

Additional absorption and radiative feedback must be accounted for if a cloud is introduced to the atmosphere. When this occurs, the atmosphere can be partitioned into layers: clear sky below the cloud, cloud layer, and clear sky above the

cloud; assuming a single cloud layer. Equation 2, the clear sky RTE, would be adjusted as

$$\begin{aligned}
 R(\nu) \downarrow \approx & \int_{p_b}^{p_s} B(\nu, T(p)) d\tau(\nu, p, p_s) \\
 & + \tau(\nu, p_b, p_s) \int_{p_t}^{p_b} B(\nu, T(p)) d[\tau(\nu, p, p_b) \tau_{cld}(\nu, p, p_b)] \\
 & + \tau(\nu, p_b, p_s) \tau(\nu, p_t, p_b) \tau_{cld}(\nu, p_t, p_b) \int_0^{p_t} B(\nu, T(p)) d\tau(\nu, p, p_t) \\
 & + \tau(\nu, \tau_{cld}) \tau(\nu, p_b, p_s) \left[B(\nu, T_s) \tau(\nu, p_b, p_s) + \int_{p_s}^{p_b} B(\nu, T(p)) d\tau(\nu, p, p_s) \right],
 \end{aligned} \tag{6}$$

where

- $\tau_{cld}(\nu, p, p_b)$ = cloud transmissivity, from cloud base to p ;
- $r(\nu, \tau_{cld})$ = angular integrated cloud reflectivity;
- p_b = cloud base pressure, hPa; and
- p_t = cloud top pressure, hPa.

The first three terms of Equation 6 are an expansion of Equation 2, whereas the last term accounts for the reflection of upwelling terrestrial and atmospheric radiation from below the cloud. A cloud particle size distribution outside the 50 μm radius reflectance parameterization yields a very small (see Appendix D) change in the radiance. This accounts for the approximation in Equation 6.

The following sections discuss the individual terms of the cloudy RTE, where: an atmospheric transmission model is used to calculate the clear sky values; an evaluation of cloud optical properties will lead to a cloud reflectivity term; and the RTE can be inverted to derive an optical depth for the cloud. The final section describes a technique to determine an estimate of the optical depth using the 9.6 μm ozone band.

2.1.2 FASCOD3P Model

An atmospheric radiative transfer model is required to determine the downwelling clear sky radiance,

$$R_{clr}^{fasc}(\nu, p_s, p_b) \downarrow = \int_{p_b}^{p_s} B(\nu, T(p)) d\tau(\nu, p, p_s),$$

upwelling clear sky radiance, including terrestrial contribution,

$$R_{clr}^{fasc}(\nu, p_s, p_b) \uparrow = B(\nu, T_s) \tau(\nu, p_b, p_s) + \int_{p_s}^{p_b} B(\nu, T(p)) d\tau(\nu, p, p_b),$$

and transmission,

$$\tau_{clr}^{fasc}(\nu, p_s, p_b) = \tau(\nu, p_b, p_s),$$

below the cloud base. The Air Force Philips laboratory line-by-line transmission model, Fast Atmospheric Signature Code (FASCOD3P) (Clough et al., 1986), is used for this purpose. Knowledge of the clear sky radiance and transmission effectively projects the ground-based downwelling measured radiance to cloud base.

The model utilizes the Air Force Geophysics Laboratory HITRAN database (Rothman et al., 1987) of atmospheric transmission lines and a local radiosonde profile to calculate radiance and transmission of the atmosphere. The radiosonde is used to obtain temperature and moisture profiles. A number of additional parameters (e.g., spectral information, additional atmospheric data, path characteristics, and output format) are also required in the FASCOD3P input file. Appendix C shows a typical FASCOD3P input file and provides an explanation of the individual parameters.

Figure 2 illustrates data for a radiosonde launched on 17 November 1994, 00:00 UTC (16 November, 18:00 CST) in Madison, WI during an evening of scattered cirrus. Temperature and dewpoint temperature are shown as a function of altitude. The individual data points indicate levels that were used in the FASCOD3P calculations. These points were chosen to preserve the measured vertical structure

with a reduced number of levels, to satisfy model constraints. Also given are the lidar measured cloud boundaries, which agree with the low dewpoint depression in the radiosonde measurements.

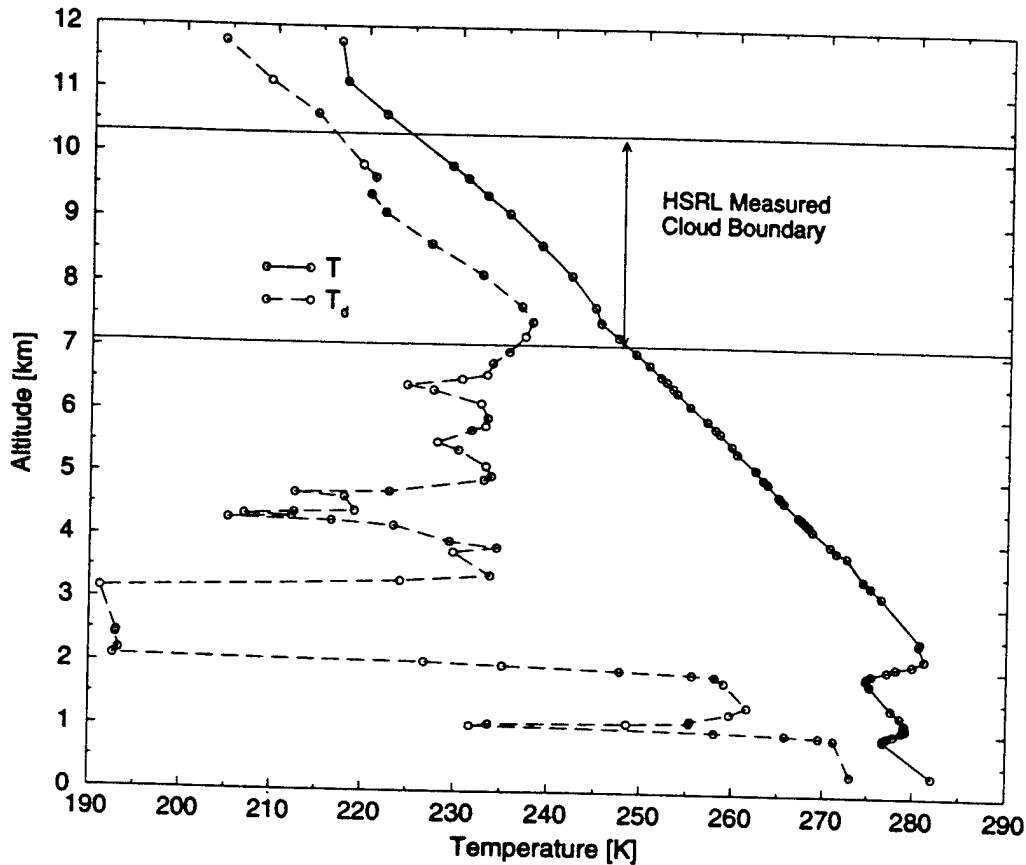


Figure 2: Radiosonde data for Madison, WI on 17 November 1994, 00:00 UTC. Points indicate FASCOD3P levels, where the solid line indicates temperature and the dashed line dewpoint temperature.

The application of FASCOD3P in the present context results in two primary limitations. The first is the proper representation of the water vapor continuum (Grant, 1990; Cachorro et al., 1987; Clough, 1995; Thériault et al., 1994). The second is the ability to account for the presence of lower level aerosols (Volz, 1973). As a result, the FASCOD3P radiance prediction may differ by as much as 40 percent from the AERI measured values. Figure 3 provides an example which shows radiance differences which correspond to brightness temperature differences of up

to 15 K. A correction, referred to as the Gamma technique (Smith et al., 1993), can be applied to the FASCOD3P calculated transmittance until the radiance values agree with clear sky AERI measurements. A simultaneous lidar observation ensures the AERI observation is indeed clear.

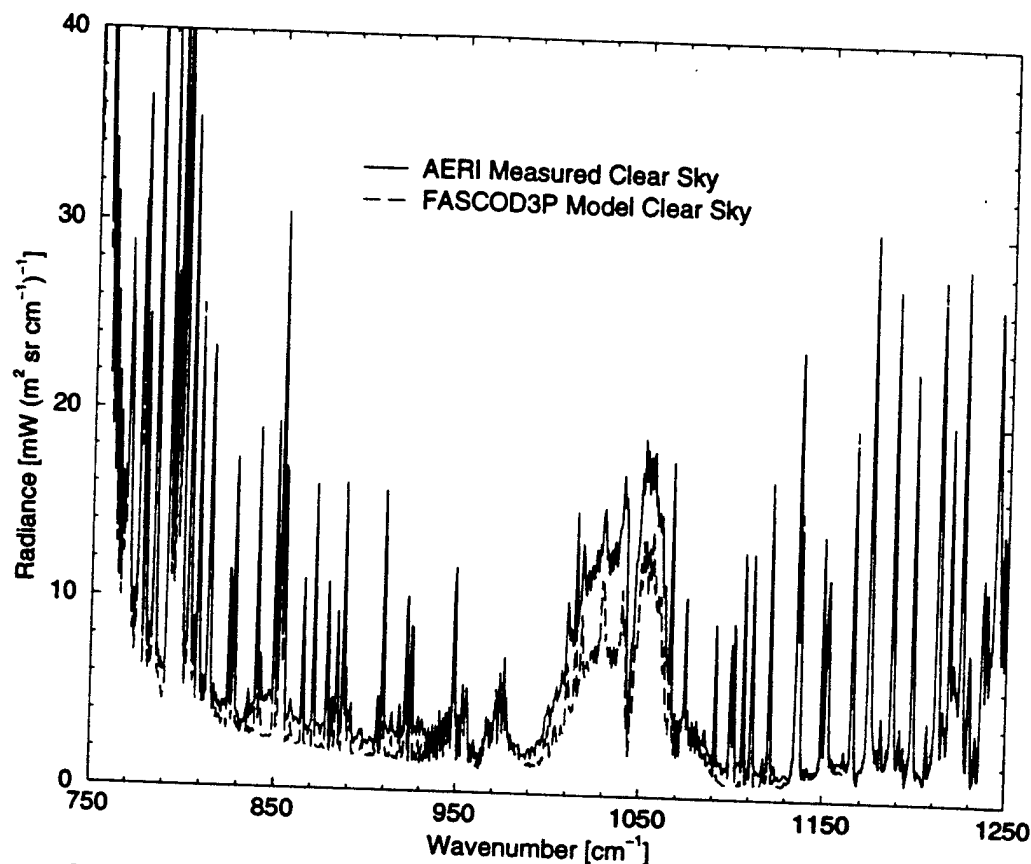


Figure 3: AERI measured and FASCOD3P calculated clear sky atmospheric column radiance for data acquired at Madison, WI on 17 November 1994, 00:00 UTC. The upper solid-line represents AERI data while the lower dashed-line is the model calculated radiance.

Cases which lack a clear sky observation present an additional shortcoming to this technique. Gamma values from another case must be used when this occurs, similar to the case in question. One approach would be to obtain a database of measurements based on atmospheric conditions and season, which could be applied to this situation. Fortunately, this predicament is not a factor in the data

to be presented in this thesis. Furthermore, the AERI is typically operated in an environment which allows continuous data acquisition, given acceptable weather conditions. This would increase the likelihood of observing a clear sky data point near the time of interest.

AERI measured column radiance, $R_m(\nu)$, differs from the FASCOD3P calculation by

$$R_m(\nu) = R_{clr}^{fasc}(\nu) + \Delta(\nu), \quad (7)$$

where $\Delta(\nu)$ is the FASCOD3P derived radiance error. Although a correction is applied to adjust the model radiance to match the measured radiance, knowledge of $\Delta(\nu)$ is required to correct for the model determined radiance from the surface to cloud base. Equation 7 relates to the total column radiance, however it is assumed that the $\Delta(\nu)$ contribution occurs in the lower atmosphere. Therefore, the same bias is applied to the model derived radiance from surface to cloud base,

$$R_{clr}^{cor}(\nu, p_t, p_b) = R_{clr}^{fasc}(\nu, p_t, p_b) + \Delta(\nu); \quad (8)$$

where $R_{clr}^{cor}(\nu, p_t, p_b)$ represents the corrected model radiance.

The Gamma correction is achieved by linearly scaling the FASCOD3P derived optical depth as a function of wavenumber,

$$\delta^*(\nu, p_s, p) = \gamma(\nu) \delta(\nu, p_s, p), \quad (9)$$

where $\gamma(\nu)$ is the scaling factor, $\delta(\nu, p_s, p)$ is the uncorrected spectral optical depth, and $\delta^*(\nu, p_s, p)$ is the corrected spectral optical depth.

A forward iteration in $\gamma(\nu)$ is executed until $|\gamma_n(\nu) - \gamma_{n-1}(\nu)| \leq 0.01$, using the following method (Smith et al., 1993):

$$\gamma_n(\nu) = \gamma_{n-1}(\nu) + \frac{\partial \gamma_{n-1}}{\partial R_c(\nu)} [R_m(\nu) - R_c(\nu)] \quad (10)$$

where

$$\frac{\partial \gamma_{n-1}}{\partial R_c(\nu)} = \frac{\gamma_{n-1}(\nu) - \gamma_{n-2}(\nu)}{R_c(\gamma_{n-1}) - R_c(\gamma_{n-2})}, \quad n \geq 2, \quad (11)$$

and $R_c(\nu)$ is the corrected radiance based on the current γ corrected transmittance. The iteration is seeded with an initial γ value of either 0.95 or 1.05, dependent upon the sign of the original difference between the measured and calculated radiance. Figure 4 illustrates the resultant γ spectrum for the radiance difference specified in Figure 3.

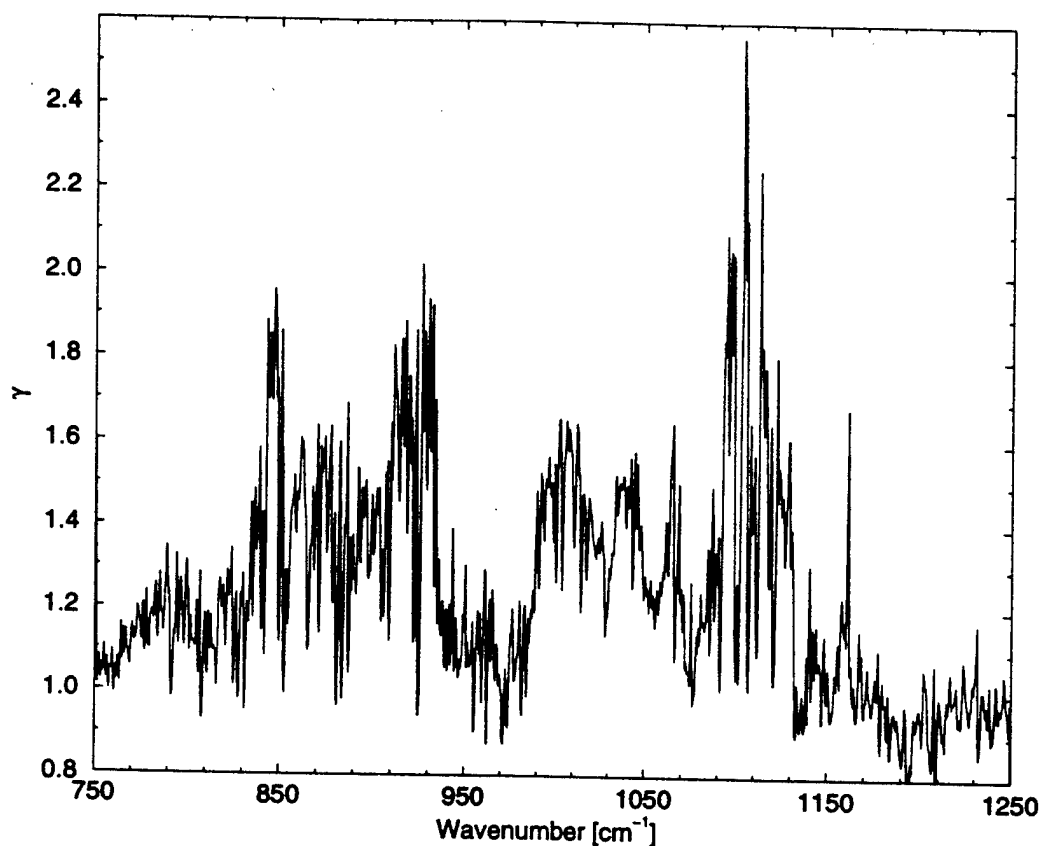


Figure 4: Gamma spectrum for AERI measured clear sky and FASCOD3P calculated radiance difference shown in Figure 3. The spectral Gamma values scale the FASCOD3P infrared optical depth to account for the model radiance difference.

The Gamma technique provides a means for correcting the atmospheric transmission through radiance observations. However, the approach adjusts the column

transmissivity based on spectral selectivity and does not account for vertical differences in atmospheric constituents. This becomes a problem when vertical resolution is significant to the calculations; but should not be a factor in these calculations, which require a single transmissivity.

The downwelling radiance from the region above the cloud is assumed to be small in all calculations. FASCOD3P can be utilized to show that the radiance contribution is negligible for the atmosphere above cirrus level clouds. This is accomplished by comparing the FASCOD3P calculated downwelling radiance from the earth surface to an altitude of 9 km against a similar calculation to 15 km. It should be noted that this comparison will represent a maximum difference, because the model does not include the effects of cirrus which would further attenuate the upper atmospheric source while increasing the total radiance measured by the instrument.

Figure 5 shows the fractional difference in FASCOD3P calculated downwelling radiance using an upper limit of 15 km versus 9 km, which yields the percent radiance reaching the surface from an atmospheric layer between 9 and 15 km. The upper limit of 15 km was chosen based on cirrus cloud top altitude. A radiance contribution due to ozone, between 950 and 1060 μm , occurs beyond this altitude, but it not a factor when using data within the chosen microwindows. Calculations are based on local radiosonde data at Madison, WI on 17 November 1994, 00:00 UTC, shown in Figure 2. H_2O and O_3 are the primary features, while the remainder of the spectral region contributes a negligible radiance.

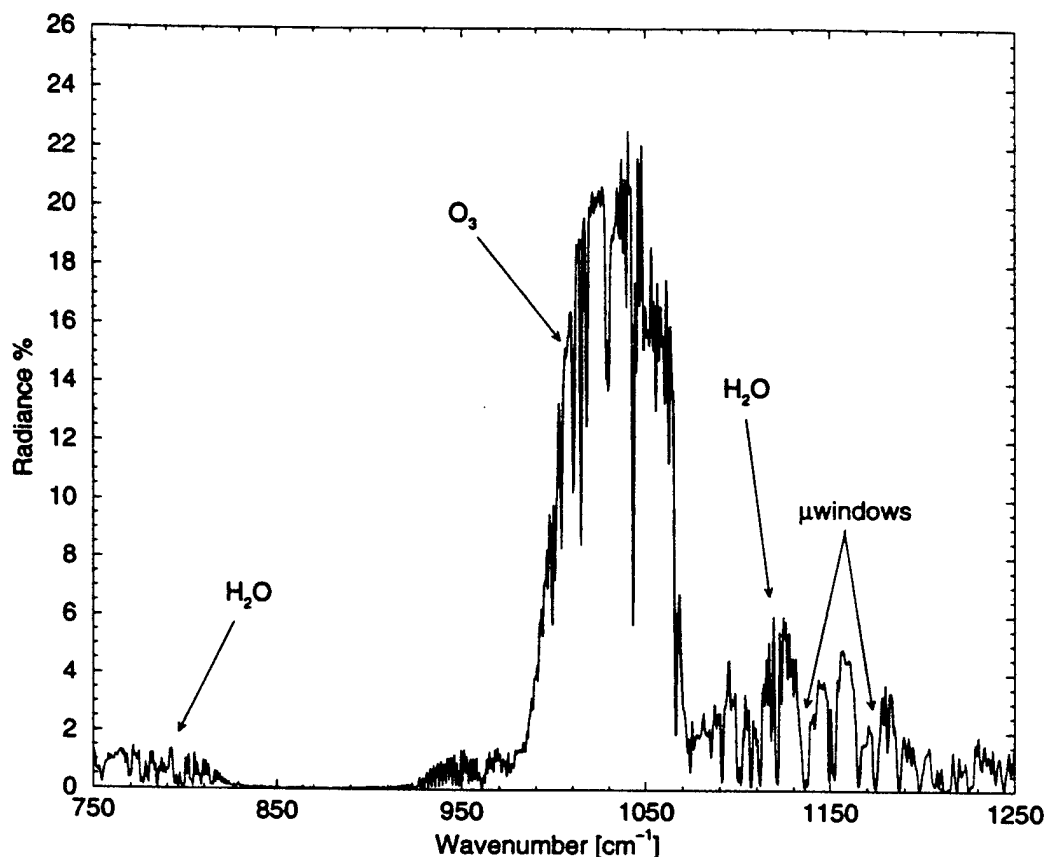


Figure 5: Downwelling fractional radiance difference for altitudes 9 through 15 km signifies a negligible atmospheric radiance contribution above cloud top for spectral regions outside absorption lines; based on FASCOD3P model simulations.

2.1.3 IR Scattering from Mie Model

The infrared scattering cross-section for molecules is much smaller than the absorption cross-section; and extinction in the IR is dominated by absorption such that scattering can be neglected. However, ice crystals and water droplets found in clouds are of similar magnitude or greater in size than wavelengths associated with IR radiation. Although extinction by absorption continues to dominate, scattering of upwelling terrestrial and atmospheric emission from below the cloud will provide a small contribution to the downwelling measured radiance.

Model simulations using Mie theory and an adding-doubling model (Collard et al., 1995) suggest that the cirrus scattered signal received at the surface is at least an order of magnitude smaller than cloud emission. Up to this point, each term in the RTE can be determined using atmospheric state measurements. Invocation of Mie theory requires knowledge of cloud particle size to determine the phase function, such that a size distribution (Hansen, 1971) must be assumed,

$$n(r) dr = c r^{(1-3b)/b} \exp(-r/(r_{eff} b)) dr; \quad (12)$$

where $n(r)$ is the number of particles of radius r and c is a normalization constant. The calculations use an effective radius, r_{eff} , of $50 \mu\text{m}$ and effective variance, b , of 0.25. A $50 \mu\text{m}$ r_{eff} is consistent with measured values for cirrus (Poellot and Henderson, 1994).

The resultant phase function derived from the Mie calculations is a function of the particle size distribution and the index of refraction. The spectral reflectance has an angular dependence described by the phase function and has a magnitude that is dependent on the concentration of particles. This implies that the reflectance will vary for each microwindow and depend upon the cloud infrared transmissivity, which cannot be inverted from the RTE until the reflectance is known. Therefore, an iterative solution is necessary, which requires parameterization of the reflectance as a function of cloud transmissivity, $r(\nu, \tau_{cl})$. The reflectance is determined with the adding-doubling model by monitoring the ratio of upwelling relative to downwelling radiant flux at the cloud base.

This approach is feasible if a particle size distribution is assumed and an independent parameterization is determined for each microwindow region. The latter constraint is necessary due to the frequency dependent index of refraction for ice. This technique is outlined for a sample AERI microwindow wavenumber, and the polynomial fit coefficients are tabulated, in Appendix D.

2.1.4 IR Optical Depth Inversion

The radiative transfer solution for a cloudy atmosphere, Equation 6, was derived earlier. A solution for the optical depth of the cloud can now be obtained by inverting Equation 6 for τ_{cld} in terms of the variables discussed in the previous sections,

$$R \downarrow \approx R_{clr}^{fasc}(p_s, p_b) \downarrow + r(\tau_{cld}) \tau_{clr}^{fasc}(p_s, p_b) R_{clr}^{fasc}(p_s, p_b) \uparrow + \tau_{clr}^{fasc}(p_s, p_b) \int_{p_t}^{p_b} B(\nu, T(p)) d[\tau_{clr}(p, p_b) \tau_{cld}(p, p_b)]; \quad (13)$$

where the radiance contribution above the cloud was shown to be negligible by the FASCOD3P model, the upwelling model radiance includes the terrestrial contribution, the model derived radiances are corrected based on Equation 8, and the spectral dependence is implied. Rearranging terms results in a radiance value that effectively projects the instrument to cloud base:

$$R \downarrow - R_{clr}^{fasc}(p_s, p_b) \downarrow - r(\tau_{cld}) \tau_{clr}^{fasc}(p_s, p_b) R_{clr}^{fasc}(p_s, p_b) \uparrow \approx \tau_{clr}^{fasc}(p_s, p_b) \int_{p_t}^{p_b} B(T(p)) d[\tau_{clr}(p, p_b) \tau_{cld}(p, p_b)]. \quad (14)$$

Integration by parts transforms the right hand side, such that

$$\int_{p_t}^{p_b} B(T(p)) d[\tau_{clr}(p, p_b) \tau_{cld}(p, p_b)] \approx [B(T(p)) \tau_{clr}(p, p_b) \tau_{cld}(p, p_b)] \Big|_{p_t}^{p_b} - \int_{p_t}^{p_b} \tau_{clr}(p, p_b) \tau_{cld}(p, p_b) dB(T(p)).$$

The Trapezoid Rule is applied to the remaining integral at the endpoints to obtain a final solution for the cloud transmissivity

$$\tau_{cld}(p_t, p_b) \approx \frac{1}{\tau_{clr}^{fasc}(p_t, p_b)} \left[1 - \frac{R_{cld}(\tau_{cld}, p_s, p_b, p_t) \downarrow}{\tau_{clr}^{fasc}(p_s, p_b) B_{mid_cld}} \right]; \quad (15)$$

where

$$R_{cld}(\tau_{cld}, p_s, p_b, p_t) \downarrow = R \downarrow - R_{clr}^{fasc}(p_s, p_b) \downarrow \\ - r(\tau_{cld}) \tau_{clr}^{fasc}(p_t, p_b) R_{clr}^{fasc}(p_s, p_b) \uparrow$$

is the downwelling cloud radiance; and

$$B_{mid_cld} = \frac{B(T(p_b)) + B(T(p_t))}{2}$$

is the average Planck radiance of the cloud determined from local radiosonde data and lidar derived cloud boundaries, and the clear sky transmissivity within the cloud, $\tau(\nu, p_t, p_b)$, is obtained from FASCOD3P. The solution is iterated for τ_{cld} in the reflectance term until a solution converges to within 0.001 (Ackerman et al., 1990).

The algorithm takes into consideration the fact that the cloud may be opaque. This reduces the effective cloud top altitude, while increasing the effective cloud top temperature. Equation 15 would yield an unphysical solution based on true cloud base and top temperatures. Therefore, a direct solution of Equation 15 is not attempted because the measured radiance for an opaque cloud will be larger than the mid-cloud radiance determined from radiosonde measurements. The result is a $R_{cld} \downarrow : B_{mid_cld}$ ratio that becomes larger than unity, yielding a negative, unphysical solution of Equation 15.

Instead, the cloud is broken into vertical layers defined by the radiosonde temperature profile, where the cloud transmittance is calculated from the cloud base to a given altitude layer. If the transmittance becomes negative, the cloud is labeled as opaque at the previous altitude. Otherwise, the process continues until the cloud top is reached, where the solution is taken to be the cloud infrared transmittance. It will be shown that a cloud transmittance less than 0.05 (infrared optical depth > 3) is the minimum resolvable value.

2.1.5 IR Optical Depth using Ozone Attenuation

A second technique for determining IR optical depth from downwelling atmospheric radiance utilizes the 9.6 μm ozone band. For this approach, Grund and Eloranta (1994) suggested that ozone could be treated as a source term above the cloud level whose surface measured radiance is attenuated by the presence of cirrus. Thus, a clear sky measurement of the ozone column radiance is necessary at some point during the data acquisition. It is further assumed that changes in the ozone distribution over a several hour period are negligible.

Although the ozone concentration peaks in the stratosphere, the radiance contribution from the troposphere is not negligible due to the increased temperature near the earth's surface. Tropospheric radiance can be minimized by choosing a spectral region whose weighting function peaks at a maximum altitude (van Delst, 1996).

The atmospheric window baseline radiance, $R_{base}(\nu) \downarrow$, must be separated from the measured radiance, $R(\nu) \downarrow$, in the spectral region of interest to yield the contribution due to ozone, $R_{oz}(\nu) \downarrow$,

$$R_{oz}(\nu) \downarrow = R(\nu) \downarrow - R_{base}(\nu) \downarrow. \quad (16)$$

Microwindow radiance, centered at 1080 cm^{-1} , is converted to a brightness temperature, which represents the baseline window value. $R_{base}(\nu) \downarrow$ is then calculated from the derived brightness temperature at the ozone wavenumber; which is chosen in the 9.6 μm wings, 1063 cm^{-1} , to represent upper atmospheric emission.

Given $R_{oz}(\nu) \downarrow$ at each time interval in the data set and a clear sky reference value, $R_{oz_ref}(\nu)$, one can use Beer's Law (neglecting cloud reflectance of surface emission) to determine the cloud optical depth, δ_{cld} ,

$$R_{oz}(\nu) \downarrow = R_{oz_ref}(\nu) \downarrow e^{-\delta_{cld}}. \quad (17)$$

The error associated with this approach is obvious when the reference radiance is specified in layers,

$$R_{oz_ref} \downarrow = R_{oz_below} \downarrow + R_{oz_above} \downarrow, \quad (18)$$

such that

$$R_{oz} \downarrow = R_{oz_below} \downarrow + R_{oz_above} \downarrow e^{-\delta_{cld}}; \quad (19)$$

where $R_{oz_above} \downarrow$ and $R_{oz_below} \downarrow$ represent ozone radiance above and below the cloud, respectively, and the spectral dependence is implied. A further assumption requires that the ozone emitted radiance within the cloud and atmospheric transmissivity below the cloud are negligible. Substitution of Equation 18 into Equation 19 produces

$$\delta_{cld} = -\ln \left[\frac{R_{oz} \downarrow - R_{oz_below} \downarrow}{R_{oz_ref} \downarrow - R_{oz_below} \downarrow} \right]. \quad (20)$$

Therefore, knowledge of the ozone radiance below the cloud is necessary to properly determine the optical depth using this technique. This results in an underestimated optical depth measurement. Application of FASCOD3P data below the cloud base is utilized to determine R_{oz_below} . Unfortunately, a local ozone profile is not available and a mid-latitude standard model is assumed. Nonetheless, this provides a first order correction to the measured cloud radiance.

2.2 Visible Spectrum

The interaction of incident solar energy with the earth's atmosphere is similar to the infrared RTE, however absorption is very weak and scattering dominates for both molecular and aerosol interaction. For lidar operation, a wavelength is chosen such that absorption is minimal and extinction of the laser pulse can be attributed to scattering. As a result, the formalism that was used to derive optical depth in the infrared is not valid for visible data.

2.2.1 General Lidar Equation

The range resolved lidar power can be represented as (Piironen, 1994),

$$P(r) = E_0 \frac{cA}{2r^2} \left[\frac{3}{8\pi} \beta_m(r) + \frac{\varphi(\pi, r)}{4\pi} \beta_a(r) \right] e^{-2 \int_0^r \beta_t(r') dr'} + M(r) + b, \quad (21)$$

where

- $P(r)$ = lidar power incident on receiver from range r , W;
- E_o = laser pulse energy, J;
- c = speed of light, m s^{-1} ;
- A = area of the receiver, m^2 ;
- $\beta_a(r)$ = aerosol scattering cross-section per unit volume from range r , m^{-1} ;
- $\beta_m(r)$ = molecular scattering cross-section per unit volume from range r , m^{-1} ;
- $\beta_e(r')$ = extinction cross-section per unit volume from range r , m^{-1} ;
- $\frac{3}{8\pi}$ = analytical molecular backscatter phase function, sr^{-1} ;
- $\frac{p(\pi, r)}{4\pi}$ = aerosol backscatter phase function from range r , sr^{-1} ;
- $M(r)$ = multiply-scattered return from range r , W;
- b = background signal, W;

and the range is determined relative to the time, t , following the transmitted pulse, such that

$$r = \frac{c t}{2}.$$

Multiple scatter is reduced by limiting the system field of view. However, it is an important feature in the measurement and is a topic under investigation (Eloranta and Piironen, 1992). System optical characteristics and measurement of the background signal are determined through calibration. Nonetheless, there remain four unknowns in Equation 21: aerosol and molecular cross-sections per unit volume, aerosol backscatter phase function, and extinction cross-section. The column optical depth, $\delta(r)$, is related to the extinction cross-section as

$$\delta(r) = \int_0^r \beta_e(r') dr'. \quad (22)$$

Measurement of individual optical properties is not possible with a single channel lidar due to the inherent coupling of extinction cross-section with the aerosol

and molecular backscatter cross-sections. However, it can be accomplished with the separation of Equation 21 into individual molecular and aerosol equations,

$$P_m(r) = E_0 \frac{cA}{2r^2} \frac{3}{8\pi} \beta_m(r) e^{-2\delta(r)} \quad (23)$$

and

$$P_a(r) = E_0 \frac{cA}{2r^2} \frac{\varphi(\pi, r)}{4\pi} \beta_a(r) e^{-2\delta(r)}, \quad (24)$$

respectively; where multiple scattering and the background contribution have been assumed to be negligible.

2.2.2 Two-Channel Lidar

The decoupling of Equation 21 is possible because the spectral response of a scattered photon is dependent upon particle velocity. Molecules, mostly N_2 and O_2 , move with a mean velocity proportional to \sqrt{T} whose distribution is represented by Maxwellian statistics; where T is the temperature at a given range. Photons scattered from a molecule will have their energy shifted, resulting in a symmetric Doppler pulse broadening of the original beam after a number of scattered photons return in a given range bin. However, much larger, slower moving aerosols have a velocity similar to the mean wind at a given range. Therefore, aerosol backscatter exhibits negligible broadening with respect to the original pulse due to the small vertical wind velocity for a pulse propagating in the zenith direction.

Figure 6 illustrates the spectral response difference between molecular and aerosol backscatter, and the technique utilized to separate the combined signals. The outgoing lidar pulse has a narrow linewidth. Aerosol backscatter is spectrally similar to the laser linewidth, whereas thermal broadening occurs with molecular scatter. An iodine absorption filter (Piironen, 1994) provides the bandpass necessary to spectrally filter the aerosol signal from the backscattered return.

Using this approach, an ensemble of molecular backscattered photons can be differentiated from the aerosol return by a two-channel HSRL through spectral

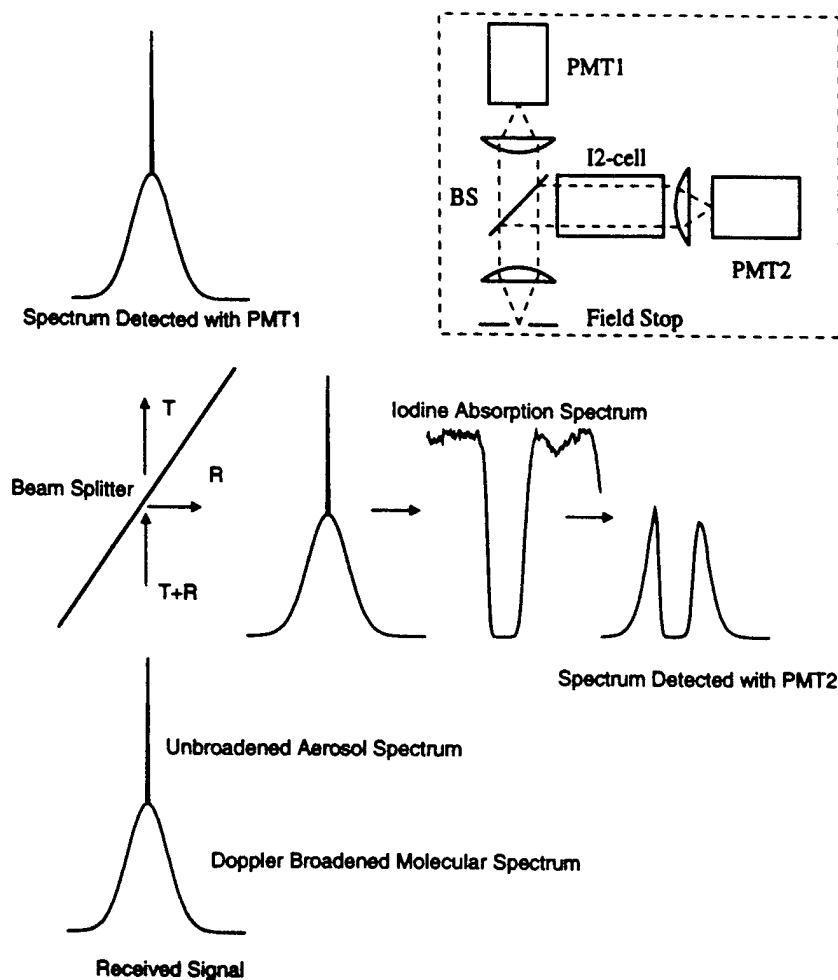


Figure 6: HSRL two-channel technique, where molecular and aerosol backscatter signal is separated with an iodine absorption filter. A beam splitter transmits a portion of the return signal to one channel, while the reflected portion is directed through the iodine absorption filter and measured with a second channel. A spectral calibration of the absorption filter allows direct measurement of the individual aerosol and molecular backscatter signals. The insert illustrates a schematic diagram of the HSRL instrumentation. Figure used with permission (Piironen, 1994).

separation of the backscattered signal. One channel measurement represents a majority of the molecular signal, where the aerosol and a portion of the molecular signal has been effectively filtered from the detected signal. A separate channel simultaneously monitors the unfiltered backscatter, due to the combination of molecular and aerosol photons. The iodine spectrum is measured before data acquisition to deconvolve the data. A schematic diagram of the instrument is illustrated as an insert in Figure 6.

2.2.3 Visible Optical Properties

Separation of Equation 21 into Equations 23 and 24 allows solution of various atmospheric properties. Given a well mixed atmosphere, one can deduce the molecular backscatter cross-section per unit volume, $\frac{3}{8\pi} \beta_m(r)$, (Piironen, 1994)

$$\frac{3}{8\pi} \beta_m(r) = 3.78 \times 10^{-6} \frac{p(r)}{T(r)} \quad (25)$$

at the laser wavelength of 532 nm. A local radiosonde yields the vertical temperature and pressure profiles. Knowledge of the molecular backscatter cross-section per unit volume as a function of range thus provides a calibration target for the lidar.

Substitution of $\beta_m(r)$ into Equation 23 for two atmospheric levels, r_1 and r_2 , yields the optical depth of that layer at the lidar wavelength,

$$\delta(r_2) - \delta(r_1) = \frac{1}{2} \ln \left[\frac{P_m(r_1) r_1^2 \beta_m(r_2)}{P_m(r_2) r_2^2 \beta_m(r_1)} \right]. \quad (26)$$

The scattering ratio, aerosol to molecular signal, is defined as

$$SR(r) = \frac{P_a(r)}{P_m(r)}. \quad (27)$$

Using this definition and taking the ratio of Equation 24 to Equation 23, the aerosol backscatter cross-section can be written as

$$\frac{\varphi(\pi, r)}{4\pi} \beta_a(r) = \frac{3}{8\pi} \beta_m(r) SR(r). \quad (28)$$

Figure 7 illustrates the HSRL measured aerosol and molecular backscattered return as a function of altitude (lower plot). The column integrated visible optical depth (upper plot) is due to aerosol attenuation of the molecular signal, determined from Equation 26. Aerosol backscatter, represented by the dashed curve, increases with cloudcover (5.5 to 7.5 km) and haze (3.5 to 5 km).

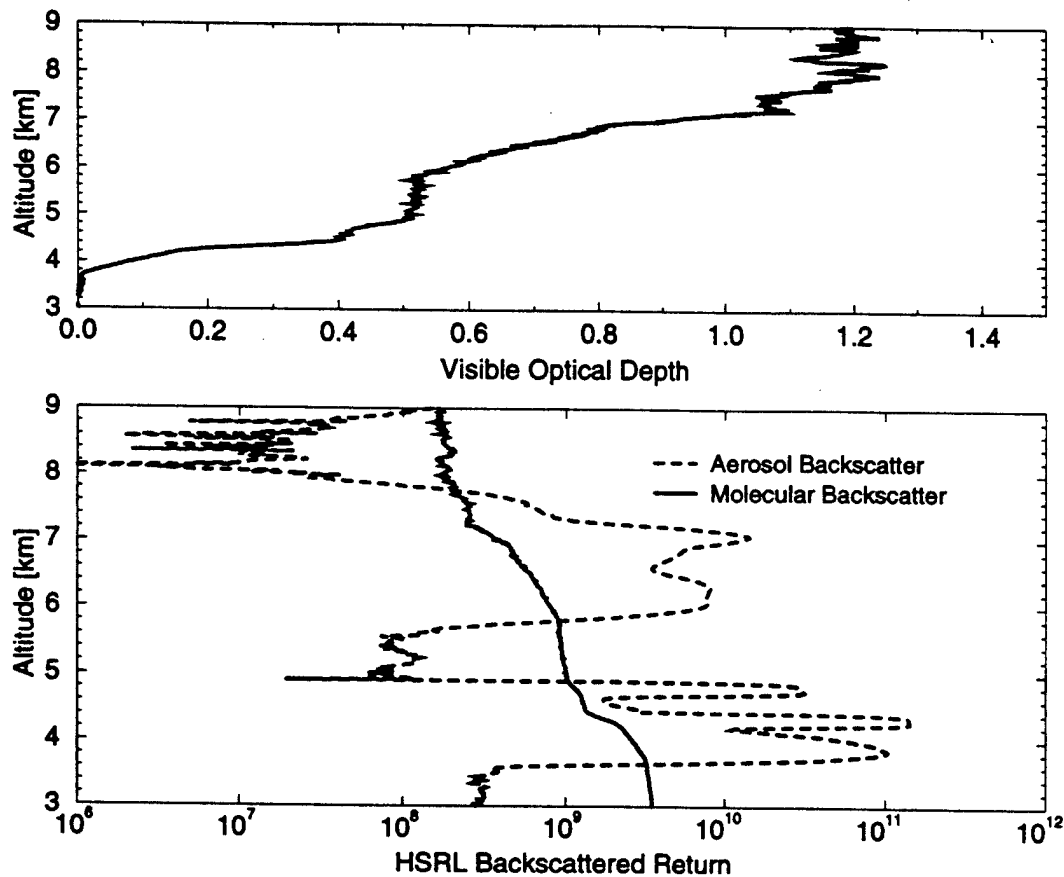


Figure 7: Upper plot illustrates HSRL measured column integrated visible optical depth relative to inverted aerosol (dashed line) and molecular (solid line) backscatter returns shown in the lower plot.

Backscatter depolarization is monitored to discriminate between spherical and non-spherical particles. Spherical particles (e.g., liquid, water-vapor laden solids) backscatter photons with a small change in the polarization. However, non-spherical particles (e.g., ice crystals, dust) backscatter light with a large change in

polarization. Range resolved depolarization provides analysis of cloud phase and discriminates between spherical and non-spherical aerosols.

2.2.4 HSRL Derived Brightness Temperature

HSRL measured visible optical depth can be utilized to derive infrared radiance, converted to a brightness temperature, and compared to AERI measured values. Simultaneous visible and infrared optical depth measurements using the HSRL and AERI, respectively, yields the relationship between the visible and infrared optical depth at each spectral region,

$$\alpha(\nu) = \frac{\delta(532 \text{ nm})}{\delta_{IR}(\nu)}; \quad (29)$$

where $\alpha(\nu)$ represents the ratio of visible to infrared optical depths. Here, the 'visible' optical depth is assumed to be represented by the HSRL measured 532 nm optical depth. This is a valid assumption because the visible extinction cross-section is due to scattering rather than absorption. The infrared cloud transmissivity, as a function of infrared cloud optical depth, can then be described in terms of the HSRL measured visible cloud optical depth,

$$\tau_{cld}(\nu, p, p_b) = e^{-\delta_{IR}(\nu, p, p_b)} = e^{-\delta(532 \text{ nm}, p, p_b)/\alpha(\nu)}. \quad (30)$$

Using this information, the HSRL integrated column optical depth can be transformed into an infrared value. This approach uses the cloudy RTE solution, Equation 6, in a forward calculation to derive the IR radiance,

$$\begin{aligned} R(\nu) \downarrow &\approx R_{clr}^{fasc}(\nu, p_s, p_b) \downarrow \\ &+ \tau_{clr}(\nu, p_s, p_b) \int_{p_t}^{p_b} B(\nu, T(p)) d[\tau_{clr}(\nu, p, p_b) \tau_{cld}(\nu, p, p_b)] \\ &+ r(\nu, \tau_{cld}) \tau_{clr}(\nu, p_b, p_s) \\ &\times \left[B(\nu, T_s) \tau_{clr}(\nu, p_b, p_s) + \int_{p_s}^{p_b} B(\nu, T(p)) d\tau_{clr}(\nu, p, p_s) \right], \end{aligned} \quad (31)$$

where

$R(\nu) \downarrow$ = HSRL derived column integrated downwelling
radiance, $\text{mW (m}^2 \text{ sr cm}^{-1})^{-1}$;

$B(\nu, T(p))$ = radiosonde determined Planck radiance,
 $\text{mW (m}^2 \text{ sr cm}^{-1})^{-1}$; and

$d\tau_{cl}(\nu, p, p_b)$ = HSRL differential visible cloud transmissivity.

The first term in Equation 31 represents clear sky radiance below the cloud, calculated using the FASCOD3P atmospheric transmission model for a given radiosonde profile. The second term is the cloud contribution, attenuated by the clear sky transmittance below the cloud, τ_{clr} , which is also determined by the model. The last term is the cloud reflected upwelling terrestrial and clear sky radiance from below the cloud. The radiance contribution from above the cloud was previously shown to be negligible. Multiple-scattering effects are also neglected for visible scattering.

The previous technique utilizes independent observations of AERI derived infrared and HSRL measured visible optical depth to determine a spectral optical depth ratio and HSRL derived downwelling brightness temperature. Equation 30 suggests an alternative method, where the HSRL measured visible optical depth is used to determine the column radiance. This is accomplished by iterating $\alpha(\nu)$ until the value agrees with the AERI measured value. The infrared cloud optical depth follows immediately from Equation 30 after $\alpha(\nu)$ is determined. It is expected that the iteration of $\alpha(\nu)$ will yield better results because the cloud is effectively weighted by the HSRL measured visible optical depth. The former solution assumes a uniform cloud, governed by HSRL measured cloud boundaries, to determine the infrared optical depth and optical depth ratio.

3 Instrumentation

Atmospheric data was collected at the University of Wisconsin - Madison using two high spectral resolution instruments: an active remote sensor in the visible, the High Spectral Resolution Lidar (HSRL); and a passive sensor in the infrared, the Atmospheric Emitted Radiance Interferometer (AERI). These instruments simultaneously measure a vertical atmospheric column that is advected into the instrument's field of view. A description of their data acquisition techniques and capabilities will be described in the following subsections. The Cross-chain Loran Atmospheric Sounding System (CLASS) was utilized to track locally-launched radiosondes, which provide atmospheric state information required to invert the AERI and HSRL data.

Radiosondes were released from the Atmospheric and Oceanic Sciences (AOS) rooftop, where the AERI and CLASS reside during local data acquisition. The HSRL is located adjacent to the AOS building in the loading dock. Approximately 40 m separates the HSRL from the AERI.

3.1 AERI

Atmospheric emission spectra, see Figure 1, were obtained with the zenith viewing AERI (Revercomb et al., 1993), which was derived from the HIS aircraft instrument (Smith et al., 1993). The AERI is based on an infrared atmospheric spectrometer developed at the UW utilizing a commercial BOMEM Inc. (Quebec, Canada) M100 Michelson interferometer. A pair of blackbody sources, ambient and hot, serve as calibration references. Data acquisition and system control is achieved with a dedicated PC, which transfers raw data to a second PC for processing and storage. The system is set in a thermally isolated environment to facilitate data acquisition over an extreme atmospheric temperature range. Figure 8 is a photograph of the AERI system.

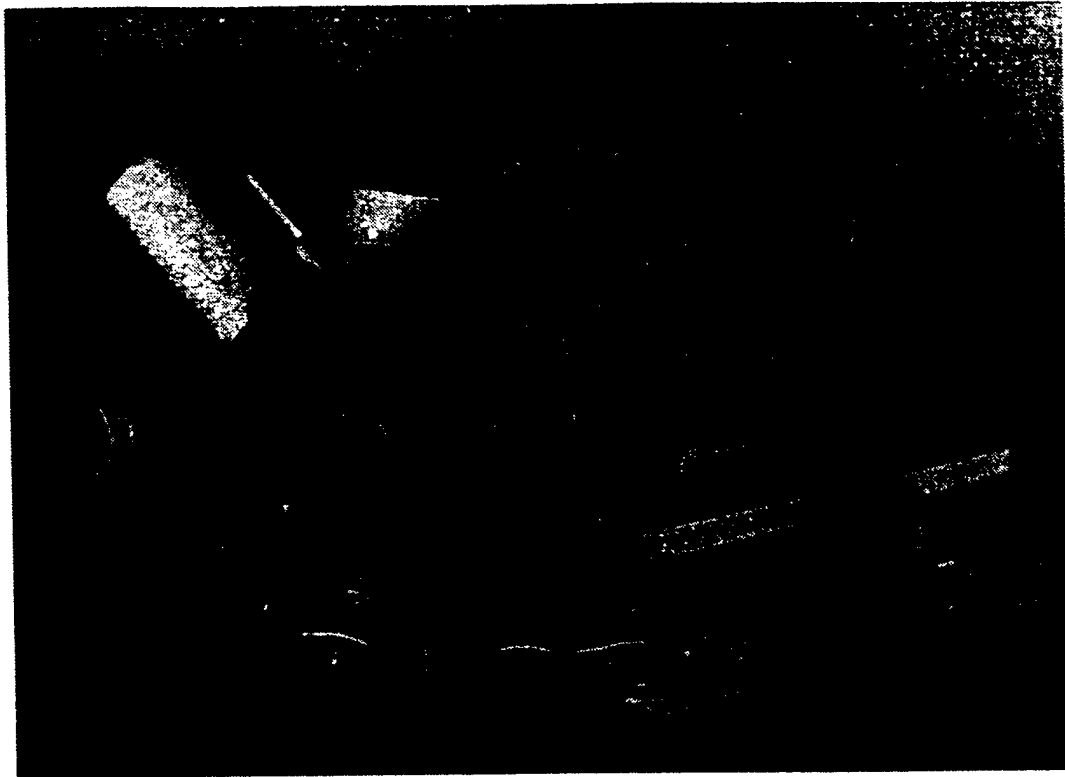


Figure 8: AERI-00 prototype: where the cylindrical objects are the hot and ambient blackbodies, and the motor to the left moves the scanning mirror. The box labeled 'Bomem' is the commercial Michelson interferometer. A PC controlled data acquisition system resides in the enclosure beneath the instrument. Data is transferred to a second PC for processing and storage after each radiance measurement.

3.1.1 Hardware

The Michelson interferometer produces an interferogram, the spectral summation of all interference patterns, which represents the Fourier transform of the atmospheric emission spectra. A schematic diagram of the Michelson interferometer is illustrated in Figure 9. The interferogram is produced by changing the phase of the incoming signal and combining this signal with a reference, stationary-phase, signal. This is accomplished by splitting the incident beam with a 50 percent

reflective mirror into two paths. The first path utilizes a fixed mirror to return the signal to the splitter and serves as the phase reference. The second path has a mirror which is scanned continuously back and forth in two second intervals, changing the path length (and phase) of the beam, relative to the first. The two signals are recombined at the splitter to produce the interferogram.

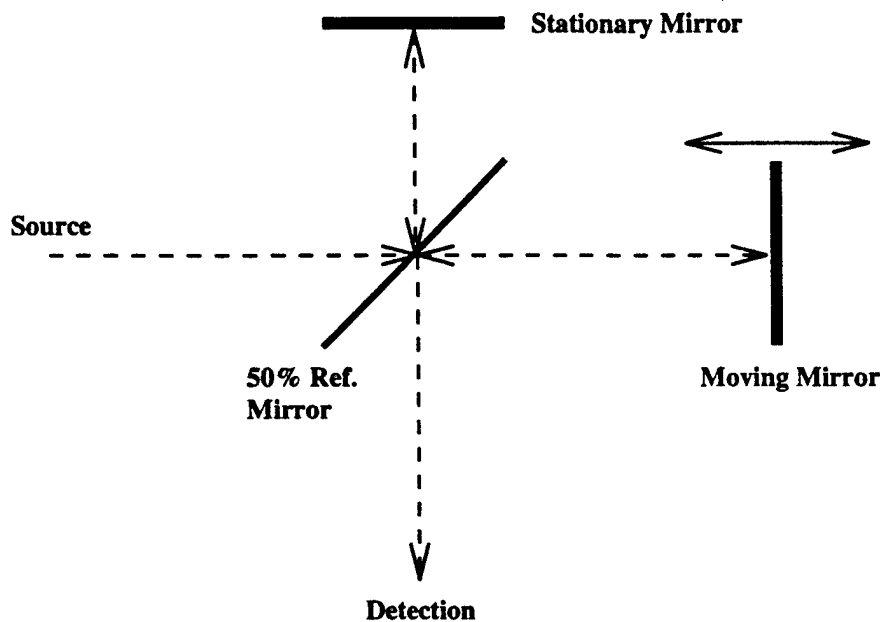


Figure 9: Schematic diagram of Michelson interferometer technique. It produces an interferogram which yields an atmospheric emission spectrum following Fourier transformation of the data. The radiation path is represented by the dashed lines.

The interferogram is monitored with a two-channel detection scheme, which uses a shortwave sensitive layer of indium antimonide (InSb) stacked in front of longwave sensitive mercury cadmium telluride (HgCdTe), cooled to 77 K with liquid nitrogen. This experiment utilized a liquid nitrogen dewar, which required refilling in 6-hour periods. An alternative option allows the use of a self-contained, mechanical Stirling cooler. This allows unassisted, continuous operation of the system under fair atmospheric conditions (Revercomb et al., 1996).

3.1.2 Characteristics

After combining data from each detector channel, a broad spectral coverage exists from 520 to 3020 cm^{-1} (3.3 to 19.2 μm). These consist of two bands, with band 1 in the region 520 through 1800 cm^{-1} (5.6 to 19.2 μm) and band 2 from 1800 to 3020 cm^{-1} (3.3 to 5.6 μm). Instrument spectral resolution is 0.5 cm^{-1} , increasing to 1.0 cm^{-1} after apodization of the data. Table 1 summarizes the AERI specifications.

Table 1: AERI Specifications

Spectral Range	520 to 3020 cm^{-1} (3.3 to 19.2 μm)
Band 1	520 to 1800 cm^{-1} (5.6 to 19.2 μm)
Band 2	1800 to 3020 cm^{-1} (3.3 to 5.6 μm)
Field of View (FOV)	32 mrad full-angle
Temporal Resolution	7 min
HBB1 (Ambient)	1.5 min
HBB2 (334 K)	1.5 min
Scene	3 min
Transfer of Data	1 min

3.1.3 Calibration and Acquisition

The system alternates between three viewing modes directed by a rotating plane mirror, with an uncoated gold surface, which is set at a 45° angle to the source. Observation modes include an ambient blackbody calibration source (dwell time average of 1.5 minutes), hot reference blackbody calibration source (1.5 minutes) maintained at 334 K, and zenith atmosphere view (3 minutes). This combines to yield a data sample rate of approximately 7 minutes after adding data transfer time. The scan time for each mode was reduced by one-third, relative to standard operation in the field, to obtain a greater temporal resolution for the instrument. This facilitates comparison to HSRL data. The blackbody calibrations are required to interpolate the atmospheric observation from a pair of spectrally characterized targets.

The blackbody references are high emissivity cavities developed at the UW, consisting of copper with a diffuse black overcoat. They are thermally monitored with high precision thermistors and controlled with a feedback servo (Revercomb et al., 1993). A third blackbody source, maintained at 77 K, is used to periodically monitor the stability of the hot and ambient calibration, and to adjust for nonlinear effects.

A data system of two networked IBM PC computers handle data acquisition, system control, and data analysis. The first computer, located with the interferometer system, controls timing of the viewing modes and storage of the raw interferometric data. This raw data is transferred, following each view mode, to a second computer; where the data is processed, stored, and displayed.

3.2 HSRL

The HSRL, one of two lidar systems that operates at the UW, consists of the following subsystems: transmitter, receiver, and data acquisition. These systems are integrated together in a semi-trailer to facilitate portable, remote measurements of atmospheric optical properties. Atmospheric particulates (i.e., aerosol and molecules) scatter the light away from the beam path. The backscatter component is subsequently collected by the detection system for analysis. This ability, coupled with a unique filter and detection design, offers the capability to measure aerosol and molecular backscatter and depolarization, and gauge the magnitude of particle sizes by measuring multiply-scattered events. A brief overview of the HSRL instrumentation follows, a detailed description can be found in the literature (Piironen, 1994; Piironen and Eloranta, 1994).

3.2.1 Transmitter

The HSRL incorporates a continuously-pumped, injection-seeded, Q-switched, frequency doubled Nd:YAG laser, operating at 4 kHz, to direct pulse of coherent light in the near-zenith direction. The beam is offset 4 degrees from the vertical

to prevent specular reflection from preferentially oriented crystals in cirrus ice clouds. A Pockels cell rotates successive pulses by 90 degrees for polarization measurements.

The output frequency is locked to an iodine absorption line, which helps to prevent seed-laser drift and provides an output pulse that is spectrally tuned to the bandpass of the detection system. The pulse energy is monitored on a shot-to-shot basis to normalize the return signal.

Proper alignment is required to ensure that the transmitter and receiver field of views are coincident. A pair of servo-motors in the surface plane control the transmitted pulse direction, such that the transmitter and receiver are properly aligned before data acquisition. This is achieved by maximizing the return signal as a function of transmitter direction in the x- and y-planes.

3.2.2 Receiver

Light that is backscattered is collected with a 0.5 m telescope and monitored as a function of time to determine a vertical distribution of the backscattered energy. This results in the measurement of the aerosol and molecular backscatter cross-sections, aerosol and molecular depolarization, and particle size.

The signal collected by the telescope is directed to a series of detectors. The aerosol and molecular return is measured with a pair of photomultiplier tubes. A 0.3 nm bandwidth interference filter is used to reduce background signal in both channels. A Fabry-Perot étalon is placed in the optical path for additional background filtering during daytime operation. A 1.8 pm bandwidth iodine absorption filter is placed in the path of one channel to spectrally remove the aerosol scattered component (refer to Figure 6). The other channel observes the combined molecular and aerosol return. The seed laser is temperature tuned to determine the spectral signature of the iodine absorption cell. This allows deconvolution of the two-channel data into individual molecular and aerosol components. Depolarization for each channel is determined by monitoring the ratio of the return signal of successive pulses, which are transmitted with orthogonal polarization.

Data collected by a variable aperture detector, following an 1 nm bandpass interference filter to reduce background signal, is utilized to measure multiple scattering events (Eloranta and Piironen, 1992). Cycling through a series of aperture sizes (0.21 through 4.0 mrad, for evening operation) adjusts the effective detector FOV, where an increased FOV allows a greater reception of multiply-scattered photons. This feature is limited during daytime operation with a maximum aperture size of 0.5 mrad.

3.2.3 Electronics and Computer

Photomultiplier tubes in photon counting mode detect the backscatter signal. Data is time resolved in 100 ns bin widths, resulting in 15 m vertical resolution over 2333 data bins. A total of 8192 data bins are available for data acquisition among the various detector channels. System functions are maintained by an embedded Intel i960CA processor.

The system is monitored by a Sun Sparc II workstation which also stores and displays the raw data. Data points are displayed for a given polarization in a 4000 shot average, which allow real-time observation of the atmosphere as it is advected over the instrument.

3.3 CLASS

The CLASS was developed by the National Center for Atmospheric Research (NCAR) and licensed to the Radian Corporation. Cross-chain Loran refers to the triangulation procedure used to specify the radiosonde position required to determine the vertical wind profile; where a 'chain' of three to five Loran stations track the radiosonde instrument package.

Temporal resolution of the radiosonde is 10 seconds; yielding a vertical spatial resolution of 30 to 50 m for a 200 g balloon, dependent upon balloon ascent rate. A Väisälä radiosonde instrument package was used for all retrievals. Table 2 indicates the specifications for the Väisälä sonde.

Table 2: Väisälä Radiosonde Specifications

Variable	Range	Uncertainty	Resolution
Pressure	3 to 1060 mb	0.5 mb	0.1 mb
Temperature	-90 to 60 K	0.2 K	0.1 K
Dewpoint Temperature		2 K	1 K
Relative Humidity	0 to 96 %		

4 Results

Data was acquired at UW - Madison (96 N, 32 W) during simultaneous operation of HSRL and AERI systems; where each case includes a local CLASS radio-sonde launch, see Table 3 for summary. HSRL data sets were typically scheduled to coincide with a satellite measurement (Landsat, NOAA-11 overpass, or GOES-8 scan). It should be noted that the UW Volume Imaging Lidar (VIL) (Piironen and Eloranta, 1995) was also in operation on various days.

Table 3: AERI/HSRL Data Cases at UW - Madison

Date Time (UTC)	Cloud Description
17 Nov 1994 00:00-05:15	Scattered cirrus, 7.5 to 12 km.
25-26 Oct 1995 22:00-02:00	Mostly clear, some thin scattered cirrus, 9-11 km.
26 Oct 1995 14:15-19:00	Thick ice cloud with base at 2 km, turning to mixed phase at 4 km, then back to ice.
9-10 Nov 1995 23:30-03:00	Moderate cirrus, increasing in optical thickness with decreasing cloud base.
16-17 Nov 1995 22:00-02:45	Clear skies turning cloudy with non-uniform cirrus above a thin layer of water.
2 Dec 1995 18:15-19:15	4 km water cloud with very uniform base. Broken cirrus noted at 6 to 8 km.
4 Dec 1995 15:15-20:00	Broken cirrus, some water, very non-uniform cloud.
6 Dec 1995 16:15-23:00	Broken, thin cirrus at 6-10 km, becoming clear.

Derived results for each instrument are classified into two categories: optical depth and brightness temperature. Optical depth calculations yield a visible to infrared optical depth ratio, $\alpha(\nu)$, that is based on a uniform infrared cloud extinction cross-section. Brightness temperature measurements utilize a weighted

visible cloud extinction cross-section to derive $\alpha(\nu)$. The goal is to demonstrate the improvement gained in using the latter approach. This will illustrate agreement between the instruments, while taking care to differentiate inconsistencies due to errors associated with instrument properties and measurements, atmospheric conditions, and assumptions inherent in the incorporation of FASCOD3P and Mie model simulations.

In an effort to avoid confusion from multiple data sets, emphasis will be placed on results from two cases. Data from these days is useful in that the data acquisition period extended for several hours; and the observations were comprised of cirrus over a range of optical thickness and cloud base altitudes. Figures 10 through 13 illustrate the inverted HSRL aerosol backscatter and depolarization for these cases.

Figures 10 and 11 are inverted aerosol backscatter and depolarization, respectively, for data taken on 17 November 1994. Times are given in Universal Coordinated Time (UTC). Data is displayed in range-time-indicator (RTI) format, where the backscatter intensity scale is given in the color bar to the right of the image. Broken cirrus exists between 7 and 12 km, which provides a variable case for comparison against the AERI data. The feature within the bottom 2 km of the RTI is the planetary boundary layer. Large depolarization values, Figure 11, shows the clouds to consist entirely of ice particles. Depolarization remains near zero for spherical particles, which are seen within the humid boundary layer. This agrees with the radiosonde data which was previously shown in Figure 2.

Figures 12 and 13 are inverted aerosol RTIs for 9–10 November 1995. Two features make this an interesting case for study: the cloud base continues to decrease, nearly monotonically, over a 4 km range in a period of 2 hours; and the optical depth increases until it becomes opaque, with respect to the lidar, near 01:30 UTC. The moderate, boundary level aerosol layer depolarization near 1 km, Figure 13, indicates a transformation from spherical to non-spherical particles between 01:00 to 02:00 UTC.

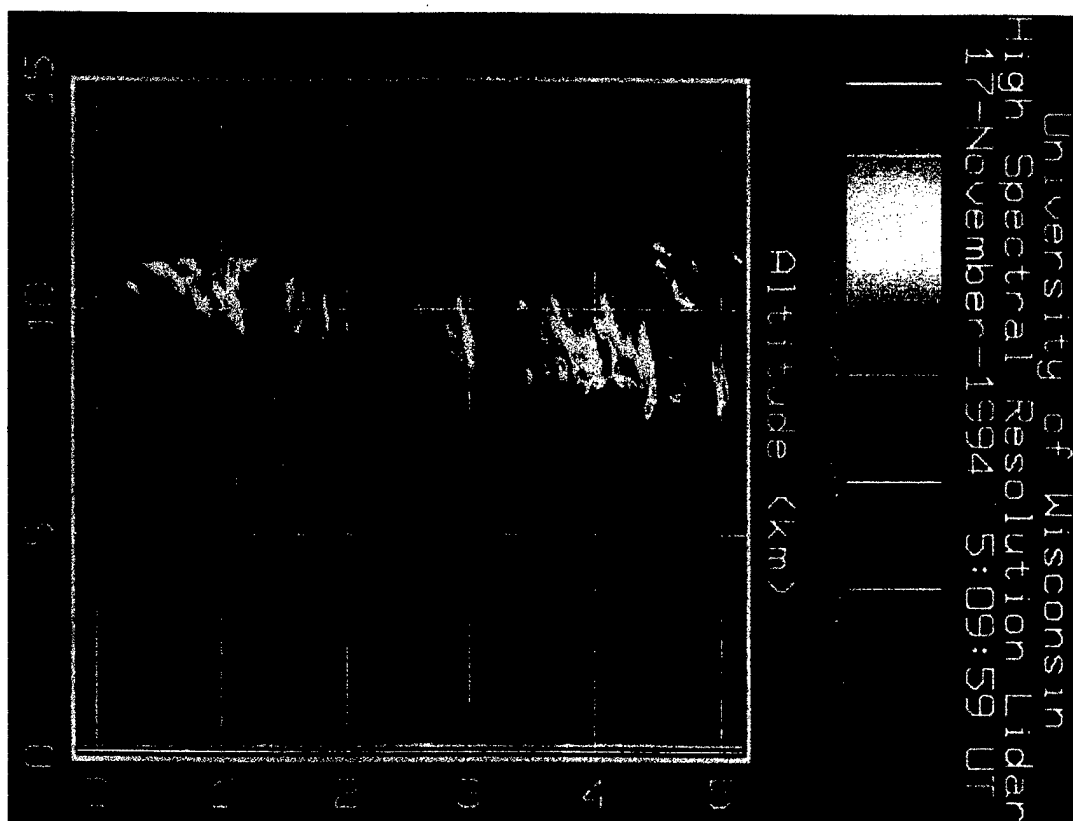


Figure 10: HSRL inverted aerosol backscatter signal for 17 November 1994. The abscissa indicates time in UTC format.

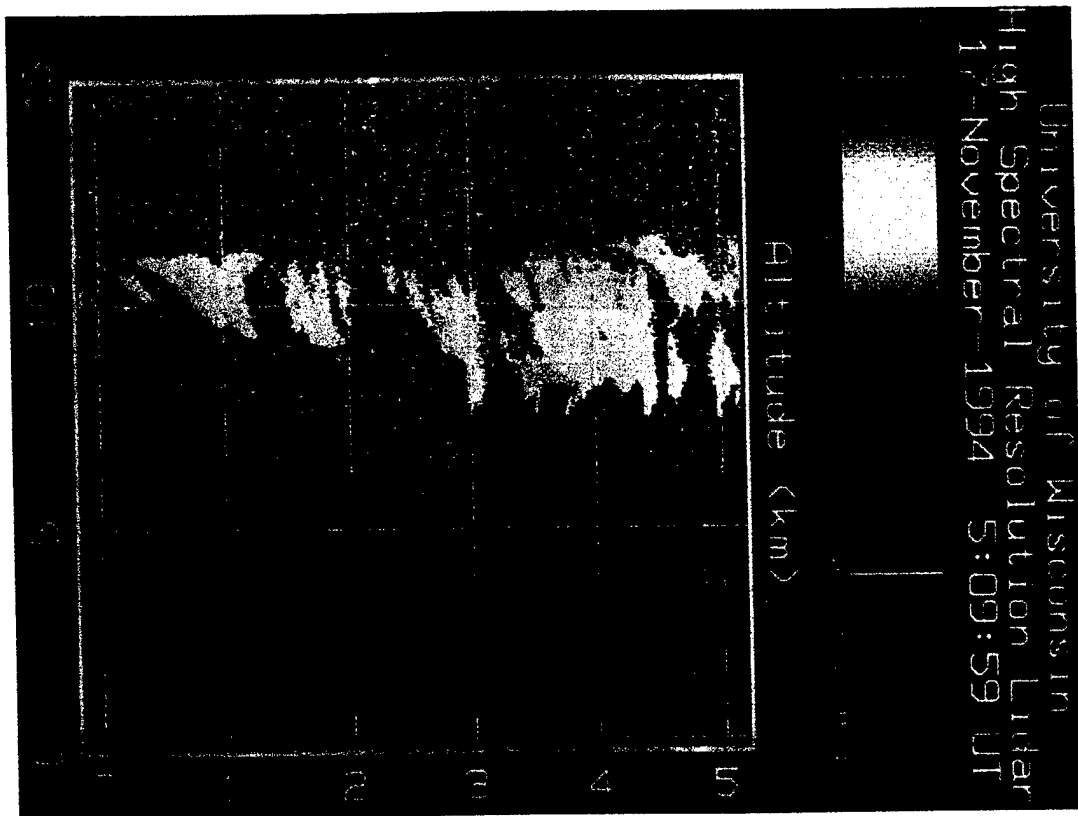


Figure 11: HSRL inverted aerosol depolarization signal for 17 November 1994.
The abscissa indicates time in UTC format.

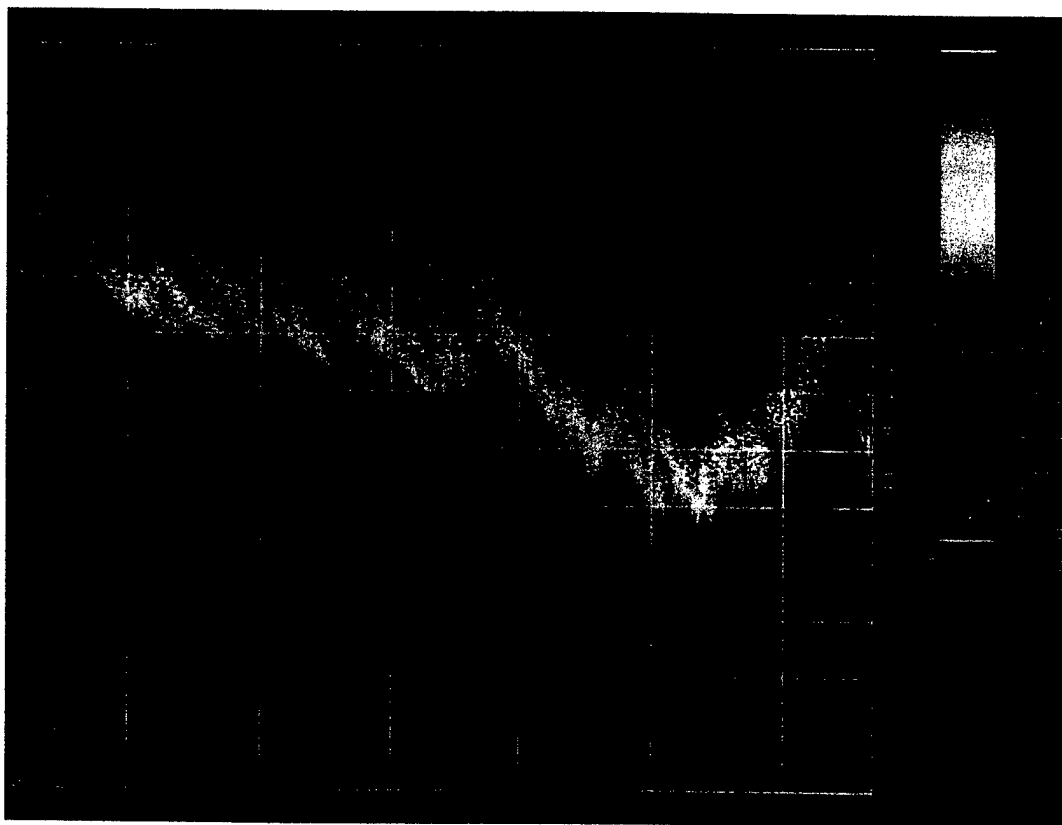


Figure 12: HSRL inverted aerosol backscatter signal for 10 November 1995. The abscissa indicates time in UTC format.

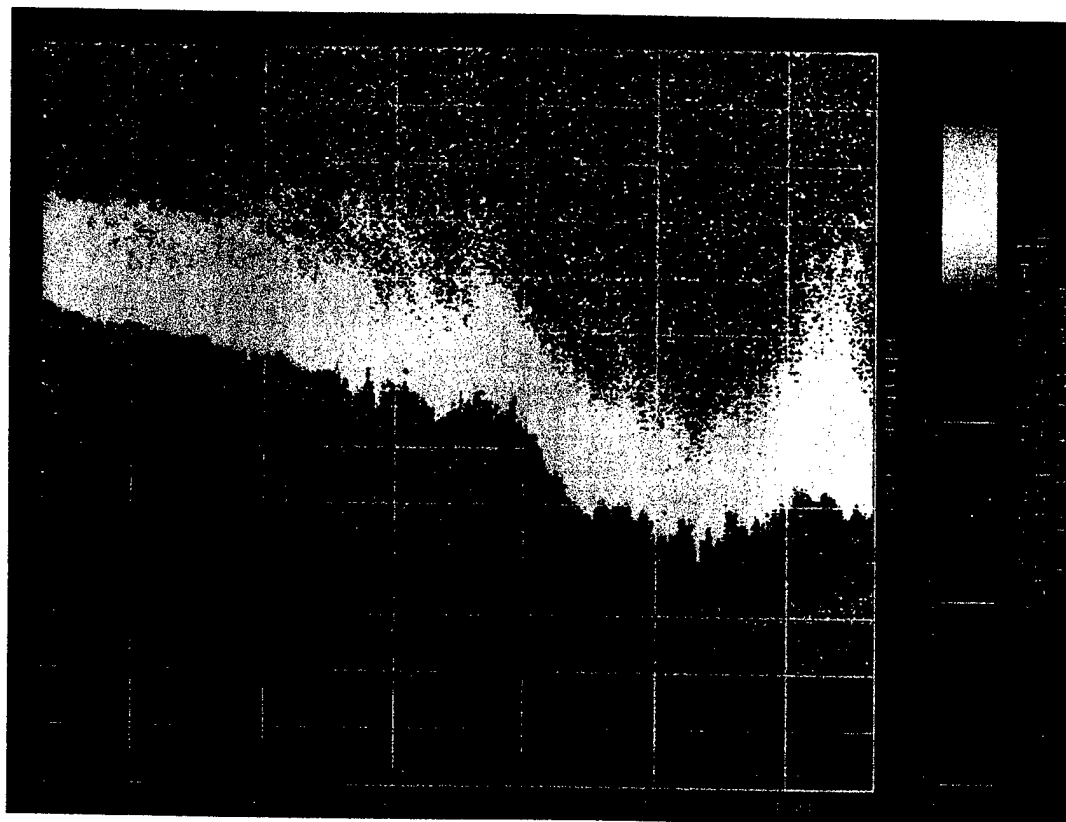


Figure 13: HSRL inverted aerosol depolarization signal for 10 November 1995. The abscissa indicates time in UTC format.

4.1 AERI and HSRL Derived Optical Depth

HSRL measurements give the backscatter cross-section at 15 m resolution, which provides a single visible optical depth at the operational wavelength of 532 nm for each data point. This represents the total cloud column integrated optical depth. AERI data yields an infrared optical depth for each microwindow region and the single ozone calculation; based on the data inversions given in Sections 2.1.4 and 2.1.5, respectively. The data is presented in two forms: temporal results for a given case; and as a scatter plot comprising the entire cirrus data set for a given microwindow. The latter comparison produces visible to infrared measurements which can be compared to Mie theory.

Figure 14 illustrates HSRL and AERI optical depth measurements at Madison, WI on 17 November 1994. All derived optical depth values are shown on the graph: the solid black line represents HSRL visible optical depth; the thin, gray lines are the AERI microwindow infrared optical depths; and the dashed, black line is infrared optical depth derived from attenuation of ozone radiance due to cirrus. Calculations based on ozone attenuation are shown for completeness. A local ozone profile is not available and requires the use of the mid-latitude standard model employed by FASCOD3P. Model calculations overestimate the column ozone radiance for Madison, WI. Local data implies that scaling the FASCOD3P derived column ozone radiance below the cloud to 70 percent of the original value yields an infrared optical depth consistent with microwindow values. The proper approach requires scaling the ozone concentration rather than the radiance. Nonetheless, this approach is feasible for the optically thin ozone transmittance below the cloud base.

The HSRL and AERI microwindow optical depth data agree well in Figure 14; aside from a few points which will be discussed next. The nearly 2:1 ratio between visible and infrared optical depths is expected from theory. This occurs because the scattering cross-section is roughly two-fold larger than the absorption cross-section. The spread in AERI microwindow data as the optical depth increases is

due to the index of refraction of ice spectral dependence, and will be compared to Mie theory for the statistical ensemble of points for the cases listed in Table 3.

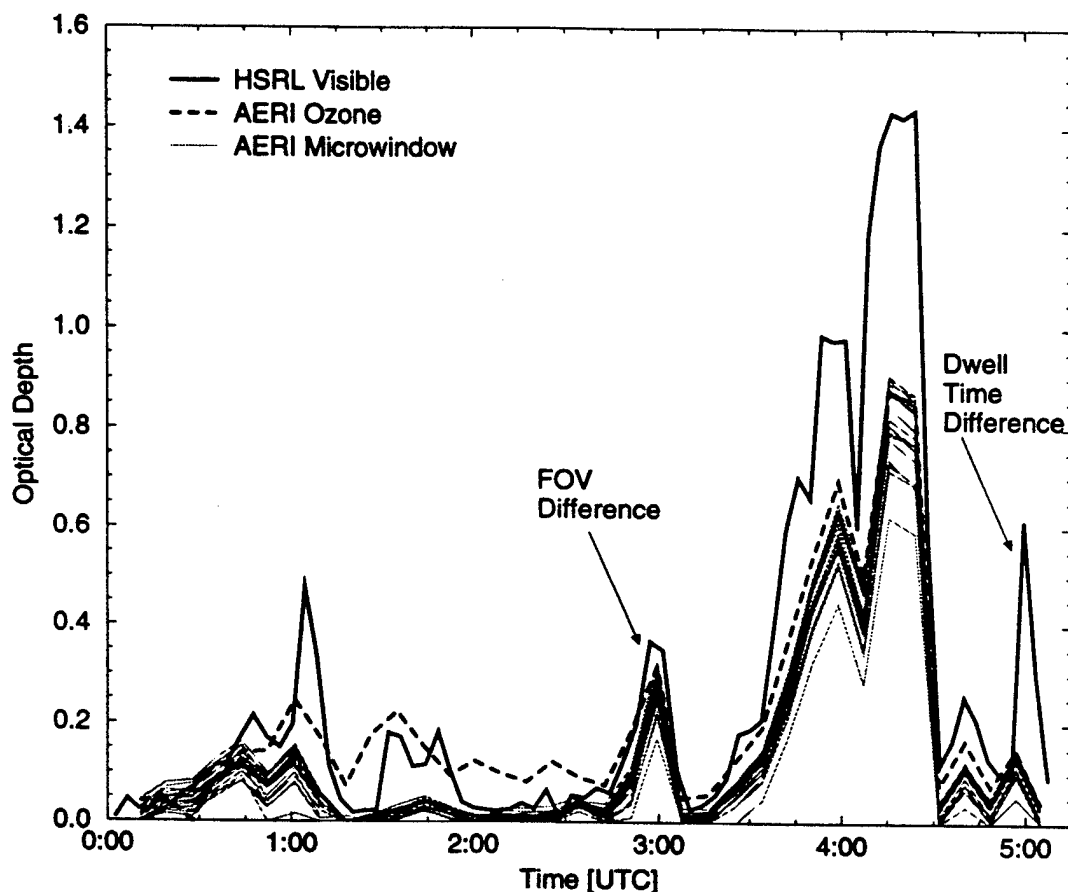


Figure 14: HSRL visible and AERI infrared optical depth as a function of time on 17 November 1994. The numerous thin, gray lines represent the various AERI microwindow regions. Note the spread in the microwindow lines as a result of the optical depth spectral dependence. Inconsistencies in the data near 03:00 and 05:00 UTC are a result of HSRL and AERI field of view and averaging differences.

Cirrus clouds are structured bodies that exhibit change as they are advected within the instrument's respective field of views; and is apparent in the HSRL data given in Figures 10 through 13. This provides several problems in the data inversion process: changes in cloud base and top altitude as a function of time; temporal averaging errors and dwell time differences between the instruments; and spatial

averaging errors due to field of view differences between the instruments. The magnitude of these errors is determined by comparing differences in observations with model calculations and is detailed in the following paragraphs.

The AERI data inversion relies on FASCOD3P model simulations to provide the clear sky radiance and transmissivity from the surface to cloud base. The model simulated clear sky calculations must be modified according to the HSRL measured cloud base altitude changes, where the cloud base altitude can easily shift by 3 to 5 km in a period of two hours. A table of cloud base heights, based on HSRL data, is generated for each AERI data point such that the proper model output is used at the given time. However, this approach creates a secondary problem inherent to the Gamma correction that is applied to the model.

Recall that the Gamma correction provides a spectral modification to the model clear sky transmissivity. This corrects for differences relative to AERI measured clear sky radiance, primarily due to errors in the model water vapor continuum. The transmissivity correction, which is scaled by the spectral Gamma values, is not affected by the presence of clouds. However, the radiance correction is based upon a single value that represents the total clear sky column radiance, and is not Gamma corrected for a portion of the total column when clouds are present. Section 2.1.2 discussed a correction, where it was assumed that the radiance difference is due to lower atmospheric emission. The spectral bias between measured and calculated total column radiance is applied to the FASCOD3P calculated values from surface to cloud base. This accounts for the FASCOD3P radiance bias in cloudy cases where only a portion of the total atmospheric column radiance is clear. Therefore, the Gamma correction can also be applied to the clear sky radiance in an atmospheric column below the cloud.

HSRL data points are obtained roughly every 3 seconds and are averaged over 3 to 5 minute intervals to determine the optical depth. AERI data is acquired over a 3 minute dwell time, but has a nearly 4 minute dark period due to system calibration and data transfer. One obvious error results when a sudden change in the cloud optical depth occurs over a short time period, and is apparent in Figure

14. The AERI is in calibration mode at 05:00 UTC and does not observe a large change in optical depth, which is measured by the HSRL.

Discrepancies between the instruments due to data point sampling, such as the previous example, are apparent in the data. However, less obvious are the errors inherent to the averaging process for the given instrument. Spatial and temporal averaging are coupled, because the atmosphere is advected through the instrument's field of view. The effect is largest for broken clouds, where a portion of optically thick cloud would be dominated by a portion of clear sky. Structural features, such as spikes in the data due to contrails, become less identifiable in the data set as the time average is increased.

A similar effect occurs due to field of view differences, $160\ \mu\text{rad}$ for the HSRL compared to $32\ \text{mrad}$ for the AERI. This corresponds to an AERI observed area that is more than four orders of magnitude larger than the HSRL. The difference becomes significant for several conditions: the HSRL is observing the edge of a cloud that is within the AERI FOV; a small break in cloud cover occurs in the HSRL FOV, but is not detectable within the larger AERI FOV; or the HSRL FOV is clear, but a small band of clouds is clipping the edge of the AERI FOV. Each of these cases would yield an AERI measured optical depth that is larger than expected based on HSRL observations. Figure 14 illustrates a possible occurrence of this effect near 03:00 UTC. Although the field of views were not monitored by video at this time, one would expect this feature during a case of broken cirrus. A similar feature is not apparent in Figure 15, where the cloud cover was noted as uniform.

An additional factor regarding data acquisition which should be noted is the observation direction of each instrument. The HSRL is tilted 4 degrees from zenith to prevent specular reflection in the return signal. This corresponds to a $60\ \text{mrad}$ offset from zenith, which is greater than the $32\ \text{mrad}$ field of view of the AERI. Thus, each instrument will observe completely different scenes unless care is taken to properly align the systems. The instruments were only roughly aligned for the given case study.

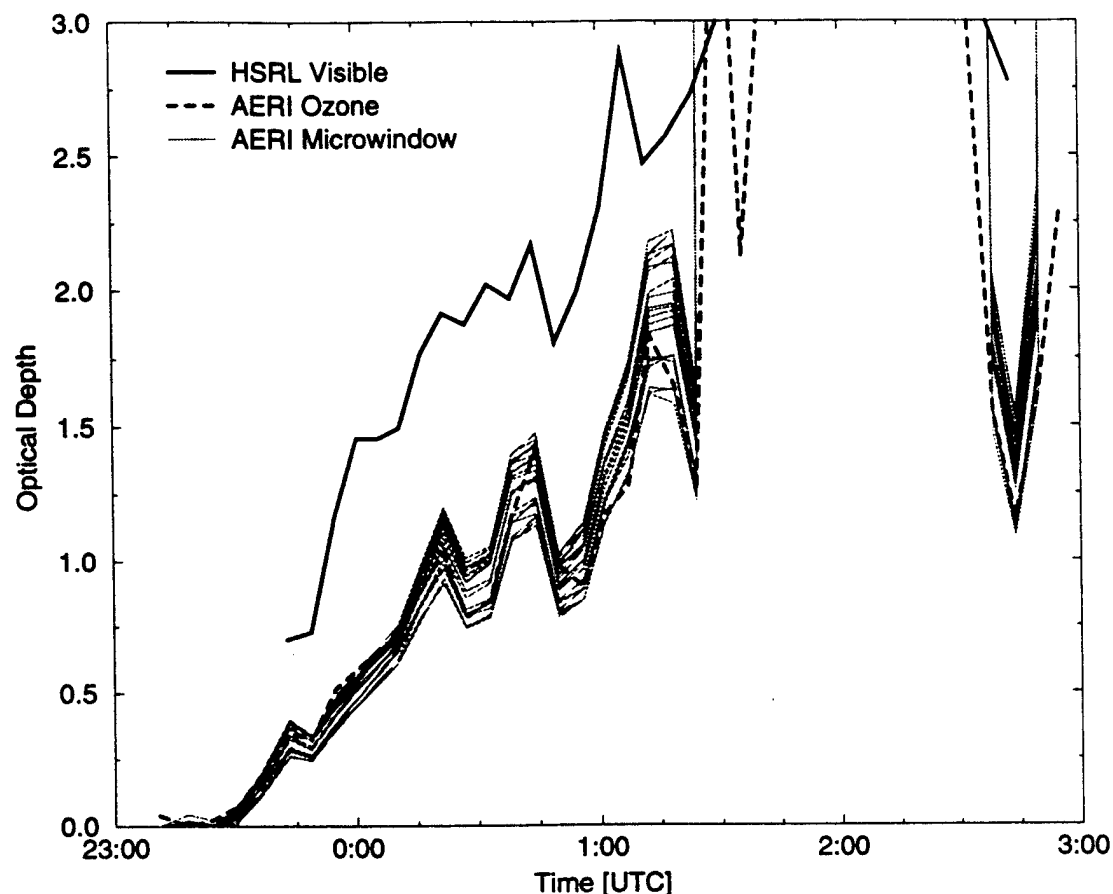


Figure 15: HSRL visible and AERI infrared optical depth as a function of time on 9-10 November 1995. The cloud becomes opaque between 01:30 and 02:30 UTC, signified by an optical depth greater than 3.0.

Optical depth data for the cirrus cases listed in Table 3 were combined and compared against HSRL measured values. This was performed for each microwindow and interpreted with a Least-Squares fit. HSRL averaged data was extrapolated to be similar with AERI times to account for differences in sampling. Values were also limited to optical depths of less than 2 in the visible, which falls well below the HSRL upper limit of 3. Infrared optical depths were limited to 1.6. Figure 16 illustrates the infrared optical depth as a function of cirrus cloud radiance. The IR optical depth gradually increases to a value of 1.6, where it doubles to 3.0 with an additional 25 percent increase in cloud radiance. Above this value, a 5 percent

increase in cloud radiance yields a large increase in the optical depth. These calculations suggest that OD values above 3.0 are very uncertain, thus these clouds are assumed to be opaque.

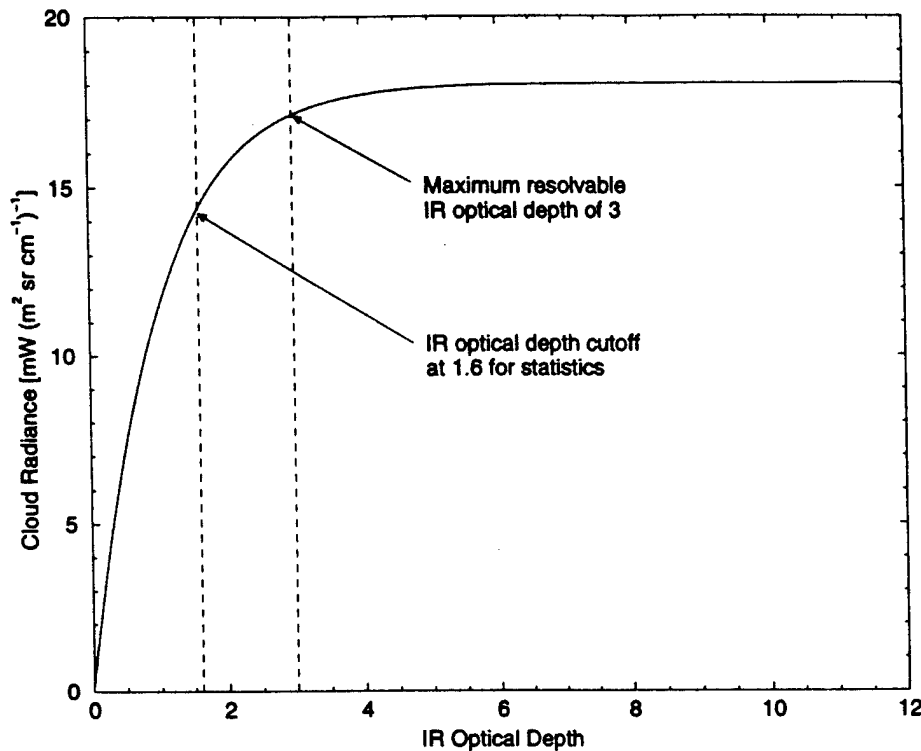


Figure 16: Infrared optical depth as a function of cloud radiance. An AERI IR optical depth cut-off value of 1.6 was used when comparing against HSRL visible data. Small changes in cloud radiance yield a large increase in the cloud optical depth for IR optical depths greater than 3, and the cloud is considered opaque.

Figure 17 shows the results of this technique for the microwindow located at 862 cm^{-1} . The slope is representative of the visible to infrared optical depth ratio, $\alpha(\nu)$, and was determined to be 1.790 given roughly 70 data points. Figure 17 comprises data from the entire cirrus case study, however the scatter about the Least-Squares fit remains large. This eliminates the ability to determine similar results for a single case. Table 4 lists $\alpha(\nu)$ for the remainder of the microwindow regions using this approach. Results from the other technique detailed in the last portion of Section 2.2.4, which iterates a solution for $\alpha(\nu)$, are given in Section 4.2.

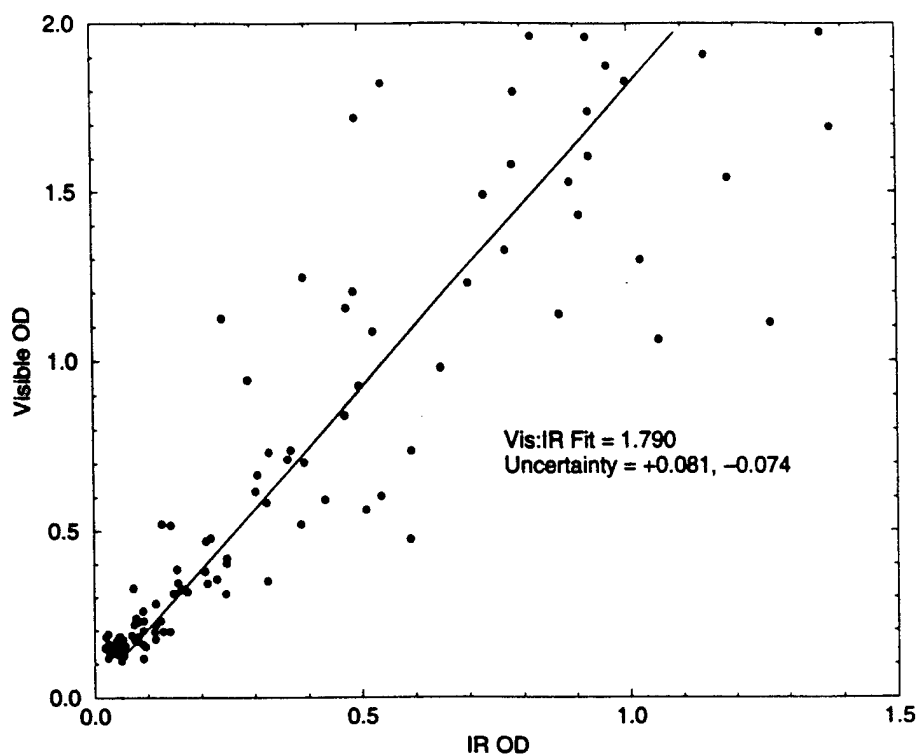


Figure 17: Comparison of HSRL visible and AERI 862 cm^{-1} microwindow infrared optical depth for the cirrus cases listed in Table 3. Least-squares fit slope yields visible to IR optical depth ratio of 1.790, with greater than 4 percent uncertainty.

Table 4: HSRL:AERI Derived $\alpha(\nu)$ for Uniform Cloud

Microwindow ν [cm^{-1}]	$\alpha(\nu)$	Microwindow ν [cm^{-1}]	$\alpha(\nu)$
773.12	1.8523	934.88	1.8528
788.55	1.7602	962.37	1.9176
811.21	1.8264	991.78	2.0572
820.13	1.7300	1080.97	2.1313
831.70	1.7433	1095.68	2.0944
845.69	1.8828	1115.21	2.0344
862.32	1.7897	1128.71	2.0226
875.10	1.7895	1145.34	1.9964
894.14	1.7510	1159.56	2.0005
902.10	1.7570		

A number of additional errors, not related to the instrumental data acquisition characteristics described previously, can contribute to the scatter plot shown in Figure 17. The primary source of error in the visible is due to multiple scattering; whereas uncertainties in radiosonde measurements and misrepresentation in the model simulated water vapor continuum are the largest factors in the infrared. Of course, instrumental spatial and temporal differences are always a significant factor. Application of the Gamma correction, Section 2.1.2, reduces the errors associated with the water vapor continuum.

A significant portion of the HSRL backscattered signal can be attributed to multiple scattering, despite the narrow HSRL field of view. Multiple scatter data on 9–10 November 1995 suggests that as much as 20% of the aerosol signal is due to multiply-scattered return, while using the $160\ \mu\text{rad}$ FOV (Eloranta and Piironen, 1996). This effect is a function of optical depth; and it depends on the particle size, where the forward scatter diffraction peak narrows as the particle size increases. A portion of the forward diffraction peak is narrow enough to remain within the HSRL field of view. Thus, although the photon has experienced extinction through diffraction about the particle, it remains with the original pulse and may contribute to the return signal if backscattered by a second particle. This effect yields a larger than expected return signal, corresponding to a smaller than expected optical depth near cloud base. This is shown in Figure 18 as a function of the backscatter cross-section, relative to the observed molecular signal, for both the corrected and uncorrected cases.

Figure 18 illustrates the molecular density profile, determined from radiosonde measurements, relative to the molecular backscatter cross-section measured by the HSRL (dashed line) for data taken between 23:55 and 00:03 UTC on 9–10 November 1995. Also shown is the corrected backscatter cross-section profile based on a constant phase function fit using diffraction theory to match the top of cloud measurements (Eloranta and Piironen, 1996). The difference between the HSRL measured data and constant phase function corrected data is assumed to be due to multiple scattering. Application of the multiple scattering model (Eloranta and

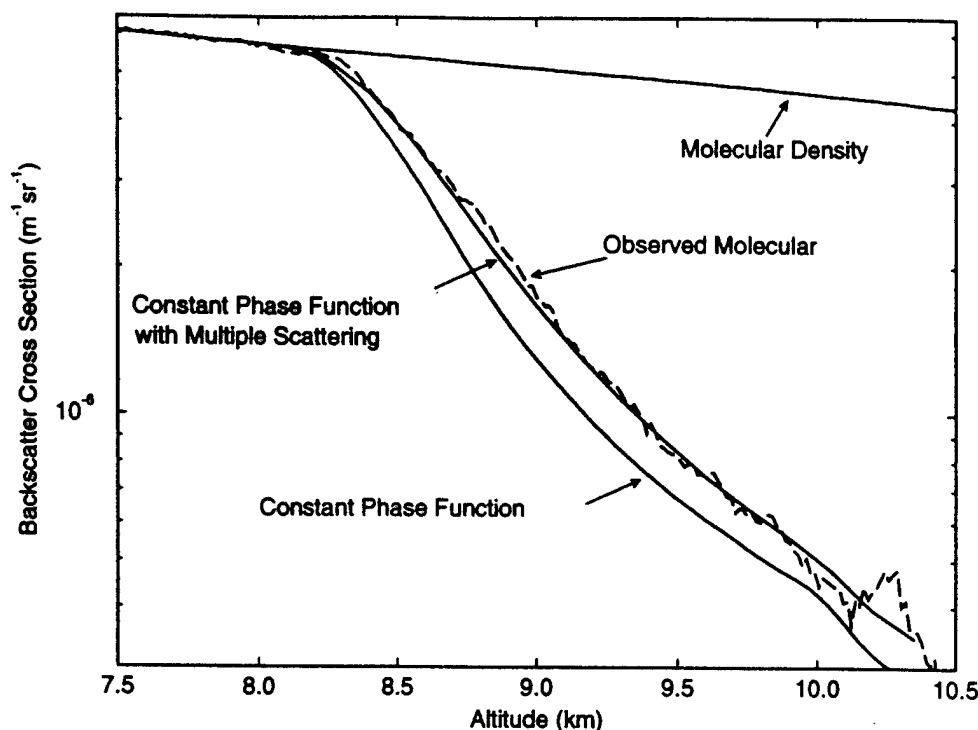


Figure 18: HSRL backscatter cross-section as a function of altitude for data taken between 23:55 and 00:03 UTC 9–10 November 1995. Shown are the observed molecular backscatter cross-section, dashed line; corrected backscatter cross-section based on a constant phase function, lowest line; the adjusted backscatter cross-section based on a constant phase function and multiple scatter model, solid line near dashed line; and the observed molecular density profile.

Shipley, 1982; Eloranta, 1993) to the data indicates the difference to be a result of multiple scattering from $56\text{ }\mu\text{m}$ radius spheres, with similar cross-sectional area as ice crystals. It will be shown that this size is consistent with Mie theory for the set of cirrus data cases given in Table 3.

The maximum expected uncertainty in the radiosonde measurements were given in Table 2: 0.2 K and 2 K for temperature and dewpoint temperature, respectively. However, additional radiosonde errors occur as a result of spatial differences

between the AERI and the radiosonde, and from changes in the atmospheric temperature structure as a function of time. These uncertainties translate into errors in the FASCOD3P calculated radiance.

The radiosonde drifts with the mean wind as it rises, reaching upwards of 200 km from the UW launch point. However, it was already shown that the radiance contribution above 9 km is negligible. This implies that the spatial drift is a concern only during the first 9 km of ascent. Furthermore, the lowest 3 km of the atmospheric column contributes over 80 percent of the measured radiance within the microwindows. A radiosonde ascent rate of 4.5 m per second would reach this altitude within 15 minutes, traveling less than 10 km from the launch point during normal wind conditions. Therefore, discrepancies caused by spatial errors are small compared to the instrument uncertainties. A frontal passage would be an exception to this argument, where a strong contrast in temperature and dewpoint temperature exists over a similar range. This is not a factor for the cirrus cases used in this thesis.

AERI data acquisition may continue for several hours after the release of a radiosonde, measuring the column radiance from an atmosphere with a modified temperature structure with respect to the radiosonde profile. A pair of radiosondes were released within 3 hours, 00:00 and 03:00 UTC, from the UW on 17 November 1994 to determine the effect of atmospheric changes over a typical data acquisition period. The temperature and dewpoint temperature profiles for each radiosonde are given in Figure 19. Both cases illustrate the constrained dewpoint temperature profile lower bounds, which are a result of very dry conditions. This occurs because a measured relative humidity of exactly zero is set to a small value above zero to avoid a singularity. The radiosonde release times of 00:00 and 03:00 UTC occurred after sunset. The data suggests a decrease in the boundary layer thickness and decrease in surface temperature, which is consistent with subsidence above the boundary layer after sunset. FASCOD3P calculations were performed to determine the change in atmospheric column radiance for each case. Assuming the differences can be attributed to advection and atmospheric heating rates, the

changes in radiance caused by this effect can be added to the expected radiative error due to radiosonde instrument uncertainty.

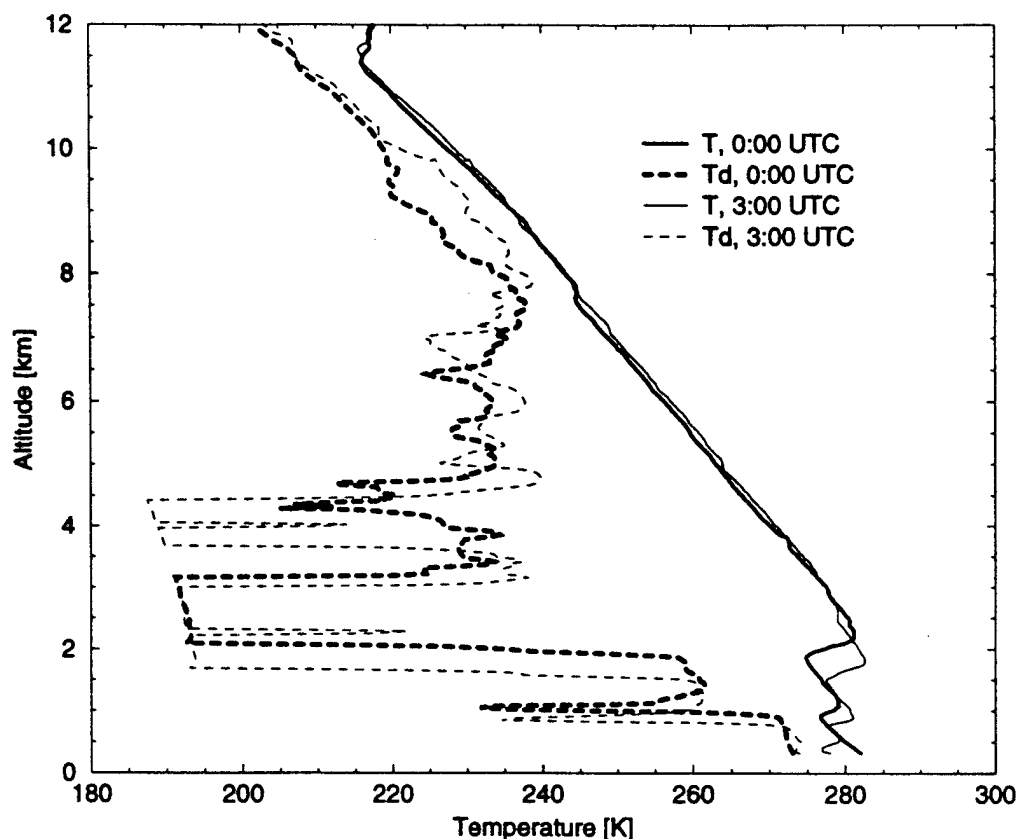


Figure 19: Comparison of temperature (solid lines) and dewpoint temperature (dashed lines) data for radiosondes launched from the UW at 00:00 (heavy lines) and 03:00 (thin lines) UTC on 17 November 1994. Note the decrease in surface temperature and decrease in boundary layer thickness that occurs between 00:00 to 03:00 UTC.

Radiance errors associated with instrumental and atmospheric uncertainties in the radiosonde measurements are given in Figure 20. The upper portion of Figure 20 illustrates the FASCOD3P radiance difference due to changes in the atmospheric temperature and dewpoint temperature structures indicated in Figure 19 (lower line), and due to uncertainties in the radiosonde measurements (middle line). The total error (upper line) is the combined contribution. The lower portion of Figure 20 gives the percent error in cloud radiance, derived from the AERI data

on 17 November 1994, for a measured IR optical depth of 0.5, based on these discrepancies. Note the advantage of high spectral resolution measurements, where the radiance errors are smaller in the microwindow regions than on an absorption line.

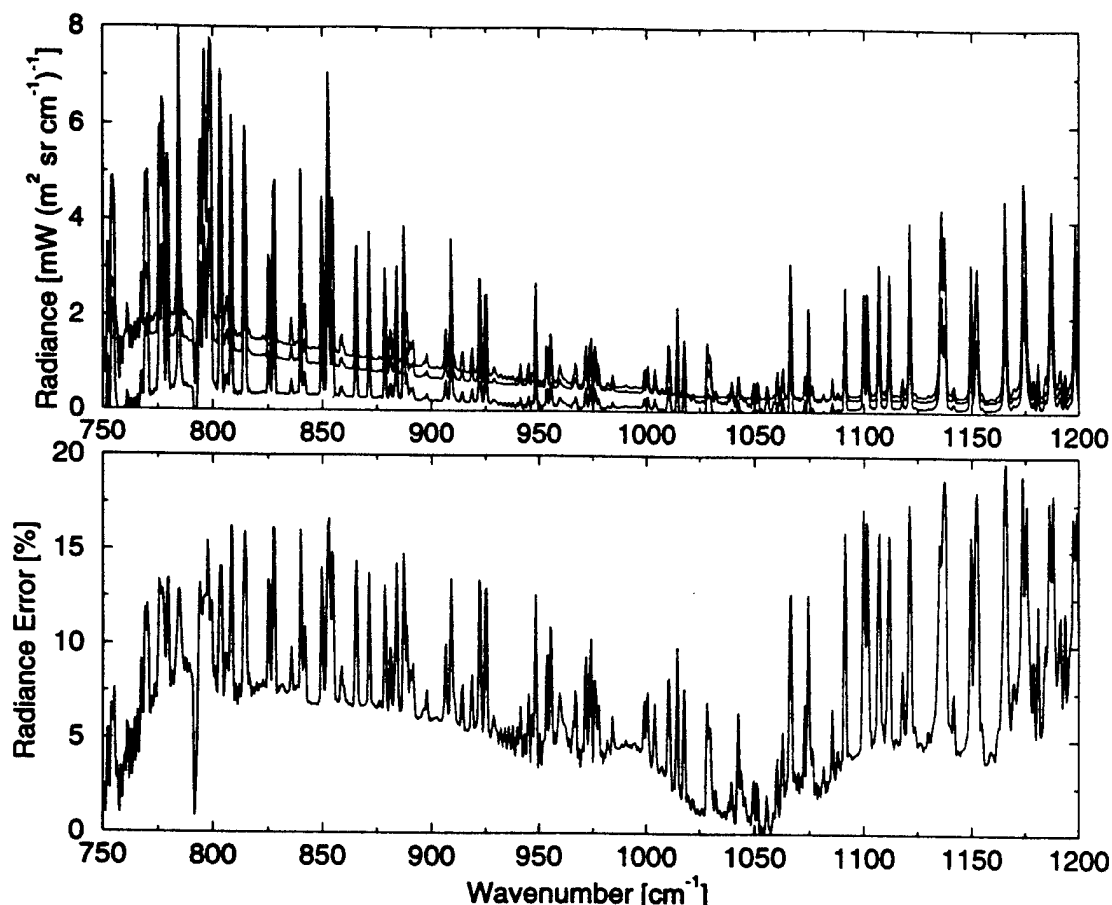


Figure 20: Upper figure shows expected radiance error due to atmospheric changes over a 3 hour period (lower line), refer to Figure 19; error due to expected uncertainties in the radiosonde measurements (middle line), refer to Table 2; and combined radiance error assuming both circumstances (upper line). The lower figure illustrates the percent deviation in cloud radiance, given the above data, for AERI data on 17 November 1994; where the resultant error is calculated for an AERI measured IR optical depth of 0.5

The spectral radiance errors shown in Figure 20 can be used to determine the uncertainties in AERI derived infrared optical depths. Data from 17 November

1994 was inverted using the radiance uncertainty limits to calculate bounds on the infrared optical depths. Figure 21 illustrates the results for a pair of microwindow regions for this data case. The upper figure shows the 1080 cm^{-1} microwindow, representing the most transparent microwindow; whereas the lower figure gives the 810 cm^{-1} results, representing the most opaque microwindow. Error bounds are given by the dotted lines, such that the shaded portion yields the optical depth uncertainty. The bold, solid line indicates the measured infrared optical depth.

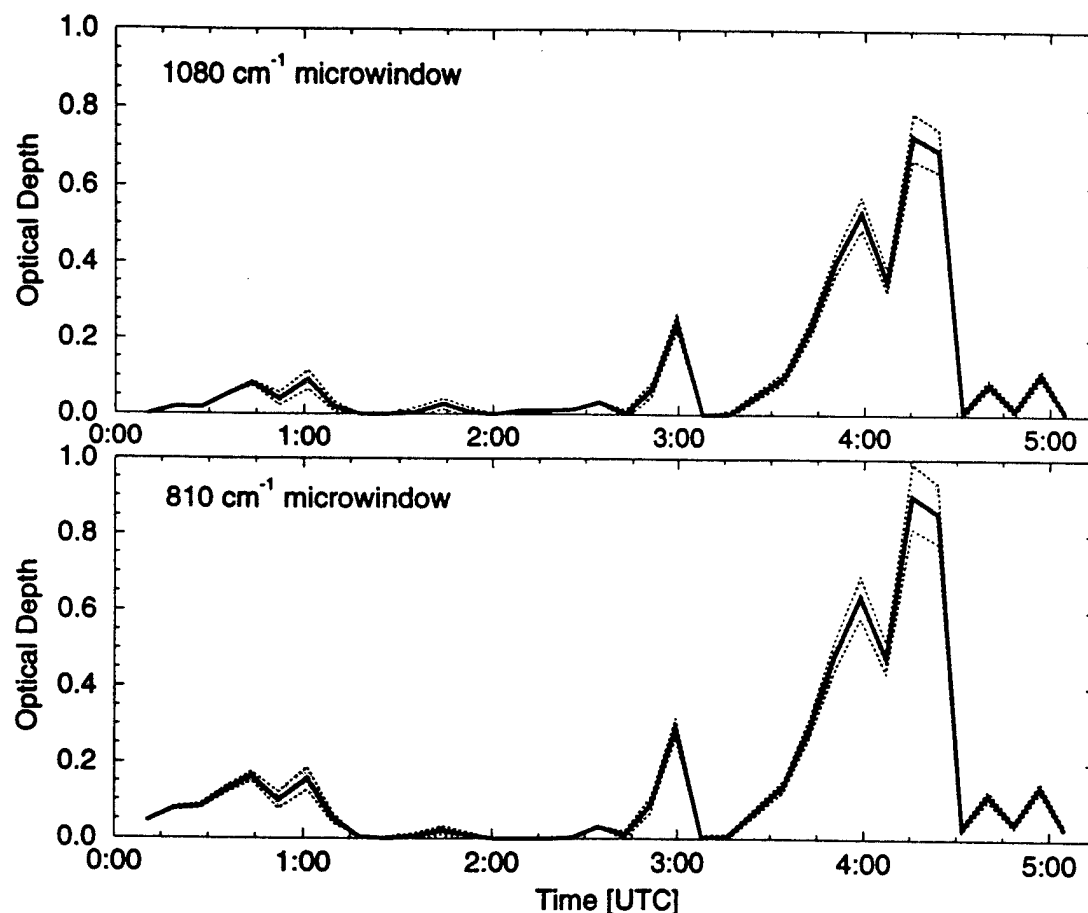


Figure 21: AERI measured optical depth uncertainty for data acquired 17 November 1994. Upper figure indicates 1080 cm^{-1} measured optical depth (bold, solid line) and its uncertainty (shaded region) given radiosonde radiance error illustrated in Figure 20. Lower figure shows 810 cm^{-1} microwindow data. These regions were chosen because they represent the microwindow optical depth extrema.

Data given in Table 4 was spectrally compared to Mie theory, assuming spherical ice particles, where the index of refraction for ice was taken from Warren (1984). Calculations are based on a Hansen distribution, Equation 12, using an effective radius of 25, 50, and 100 μm . The results and imaginary index of refraction are illustrated in Figure 22. The theoretical results compare the scattering efficiency, Q_{scat} , near the lidar wavelength relative to the absorption efficiency, Q_{abs} , for a series of spectral regions in the infrared. The experimentally derived results exhibit a trend similar to the Mie calculations near a 50 μm effective radius. This is consistent with multiple scattering measurements on 9–10 November 1995, Figure 18, where a diffraction theory fit to the data estimated particles with an area equivalent to 56 μm radius spheres (Eloranta and Piironen, 1996). It will be shown in Section 4.2 that the experimental results improve when using an HSRL weighted cloud extinction cross-section.

An interesting feature of Figure 22 occurs near 920 cm^{-1} , where the Mie theory lines overlap. This is the transition point from strong to weak absorption, with increasing wavenumber. Data outside this region is more sensitive to particle size. Figure 22 suggests that a visible to infrared ratio near 1.9, representing 920 cm^{-1} data, would be least dependent on changes in particle size.

As the imaginary index of refraction increases, the particle becomes an efficient absorber; such that the ratio of visible to infrared optical depths approaches a limit as the particle size increases and becomes opaque. In the realm of weak absorption, the particle is not opaque and produces extinction that is proportional to the product of the absorption coefficient and particle volume (Liou et al., 1990); where the absorption coefficient is proportional to the product of the imaginary index of refraction and the wavenumber. For strong absorption, the extinction is dependent on the particle area. The change in the imaginary index of refraction of ice, shown in Figure 22, is large enough across the AERI microwindow range to visualize this effect. Wavenumbers between 1000 and 1150 cm^{-1} are in the realm of weak absorption and exhibit a large dependence on particle size. As the absorption increases, 800 to 900 cm^{-1} , the lines are closer together.

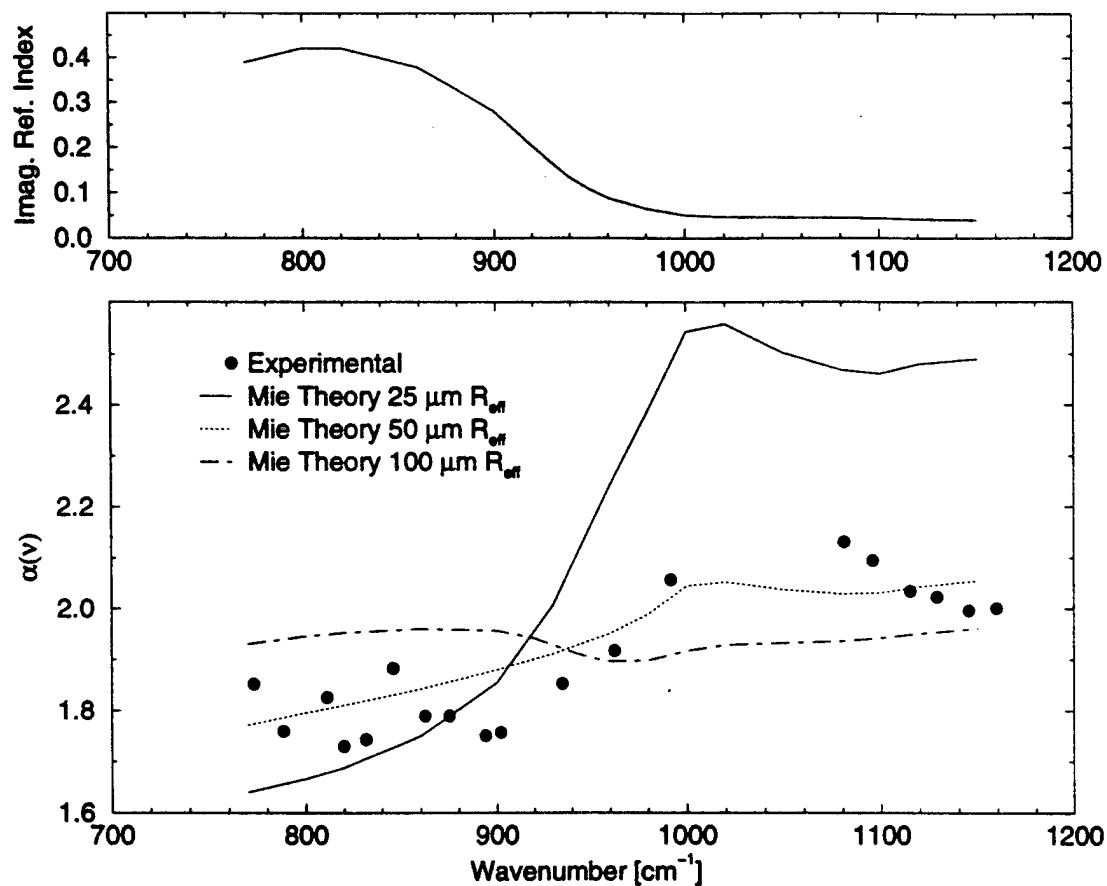


Figure 22: Spectral comparison of experimentally derived $\alpha(\nu)$ against Mie theory for various particle size distributions. Upper plot illustrates imaginary index of refraction used in Mie calculations, taken from Warren (1984). The cross-over point, near 920 cm^{-1} , in the Mie theory curves suggests that this spectral region is least sensitive to particle size.

4.2 AERI and HSRL Derived Brightness Temperature

AERI measured atmospheric column radiance is converted to brightness temperature at each microwindow using Equation 4. This data serves as a reference for HSRL calculated brightness temperature, derived using the visible column optical depth. The HSRL vertical optical depth profile can be converted to an infrared value based on either the ratio data given in Table 4 or the theoretical values derived from Mie theory. A radiosonde profile provides the vertical temperature structure necessary to calculate the Planck radiance at each atmospheric layer. Clear sky radiance and transmissivity calculated with FASCOD3P for the optical depth inversion is used to determine the molecular radiance contribution; which is added to the product of the clear sky transmissivity and the HSRL derived cloud radiance to determine the total column radiance at the given wavenumber. The model derived radiance is adjusted using the Gamma correction to account for errors in the water vapor continuum. This column radiance is then converted to brightness temperature for a spectral comparison with the AERI. The results will be presented in a form similar to the last section: data for a single case and as a scatter plot comprising the entire cirrus data set.

Data given in Figure 22 showed that the least particle size dependent microwindow, for ice spheres, is near 920 cm^{-1} . Therefore, one would expect HSRL derived brightness temperatures to agree with AERI measured values near this region, and exhibit a decrease in correlation away from this region. This should be more apparent within the microwindows located above 1000 cm^{-1} , where the absorption is weak and more sensitive to particle size. Four microwindows have been chosen for this comparison: a pair of strong absorption regions at 811 and 820 cm^{-1} ; the cross-over point at 934 cm^{-1} ; and a weak absorption region at 1096 cm^{-1} .

Figure 23 illustrates the HSRL derived brightness temperature (dashed lines) relative to AERI data (solid lines) for the strong absorption regions located at 811 cm^{-1} (upper) and 820 cm^{-1} (lower) on 17 November 1994. The results are based on the Mie calculated optical depth ratios in Figure 22. The shaded region within

the dashed lines accounts for the difference between 25 and 100 μm particles. The HSRL derived 820 cm^{-1} microwindow shows similar agreement with AERI measurements as the 811 cm^{-1} microwindow, while demonstrating an opposite bias from the baseline temperature. Figure 22 shows similar disagreement between the 811 and 820 cm^{-1} visible to infrared OD ratios, where the 811 cm^{-1} experimental results appear to disagree with the trend demonstrated by the other data.

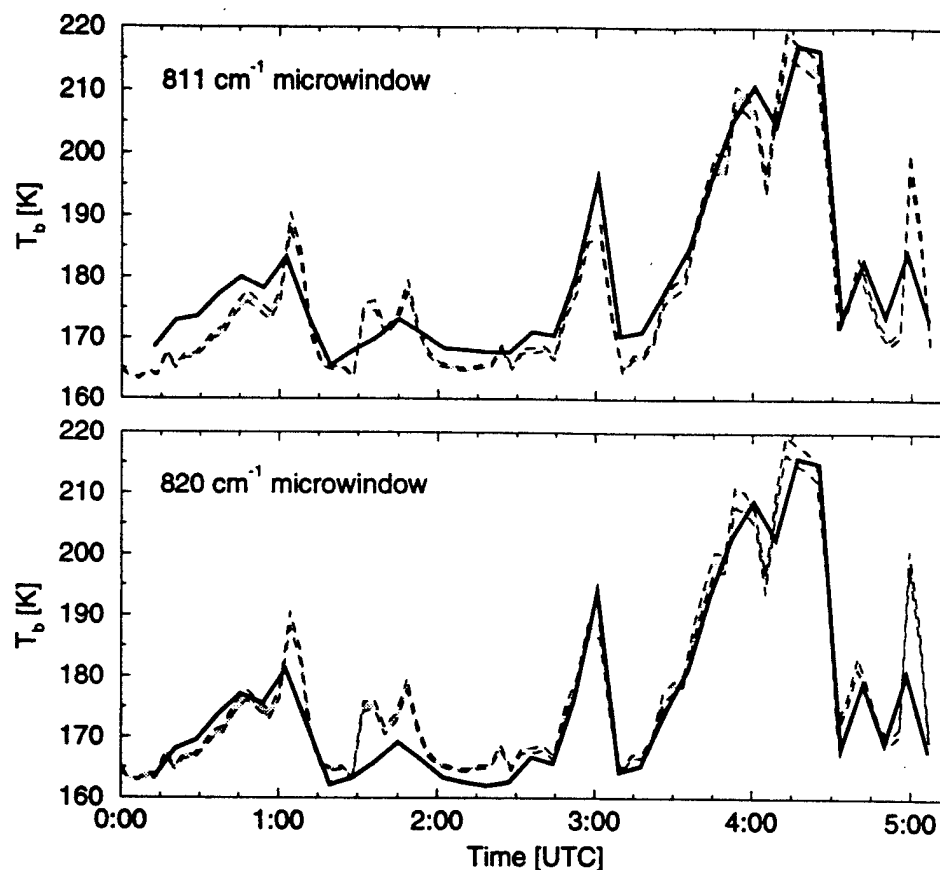


Figure 23: HSRL derived brightness temperature (dashed lines) relative to AERI measured values (solid lines) for 811 cm^{-1} (upper) and 820 cm^{-1} (lower) microwindows on 17 November 1994, Madison. The shaded regions between the dashed lines represents the shift in derived brightness temperature due to a change from 25 to 100 μm particle sizes.

Figure 24 is similar to Figure 23 but illustrates results for the 934 cm^{-1} (upper) and 1096 cm^{-1} (lower) microwindows on 17 November 1994. The deviation in

expected brightness temperature is minimal at 934 cm^{-1} , whereas the 1096 cm^{-1} microwindow exhibits a large dependence on particle size. This is consistent with the Mie calculations shown in Figure 22. HSRL derived brightness temperatures are also in close agreement within these microwindows. The largest discrepancies in the data (near 01:45, 03:00 and 05:00 UTC) are due to the instrumental characteristics discussed in Section 4.1. This particular case was favorable because the clouds never become opaque.

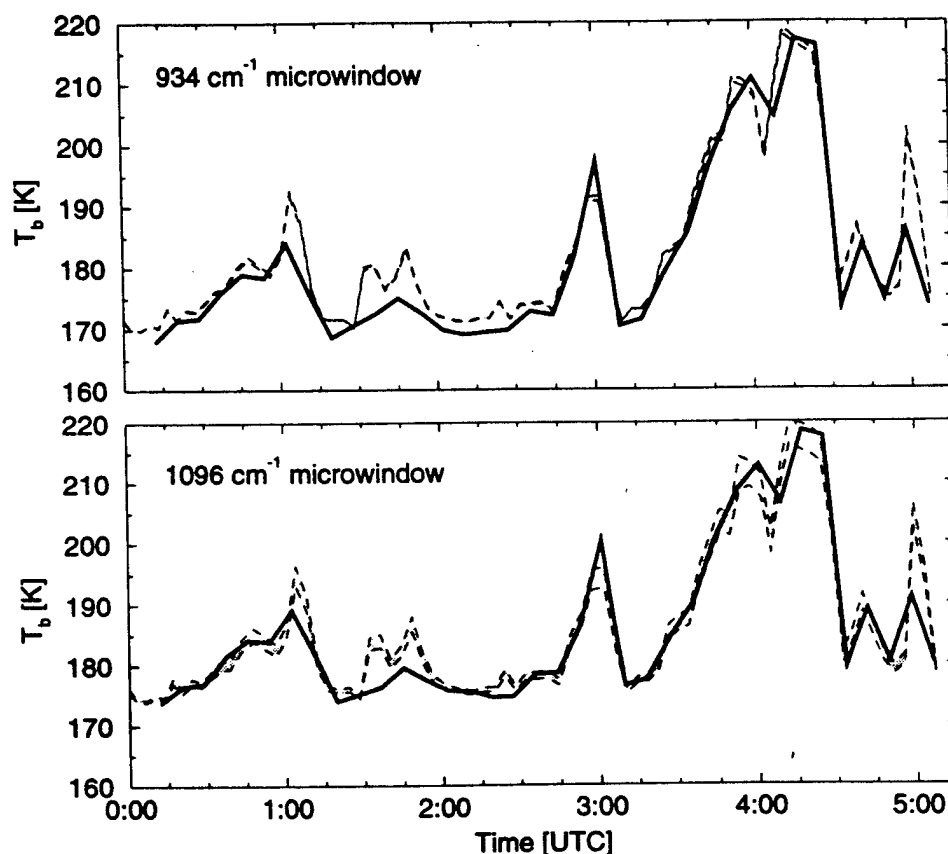


Figure 24: HSRL derived brightness temperature (dashed lines) relative to AERI measured values (solid lines) for 934 cm^{-1} (upper) and 1096 (lower) microwindows on 17 November 1994, Madison. The shaded regions between the dashed lines represents the shift in derived brightness temperature due to a change from 25 to $100\text{ }\mu\text{m}$ particle sizes. Both regions compare well with AERI measured results. Note the reduced uncertainty in the 934 cm^{-1} microwindow as a function of particle size. This is consistent with the analysis of Figure 22.

The case of 9–10 November 1995 did become opaque, between 2:30 and 3:30 UTC. This is apparent in Figures 12 and 15. Brightness temperature data for the 934 cm^{-1} microwindow is given in Figure 25, shown relative to the HSRL measured optical depth (bottom). The two instruments exhibit good correlation until 2:30 UTC, where the cirrus becomes opaque (shaded region).

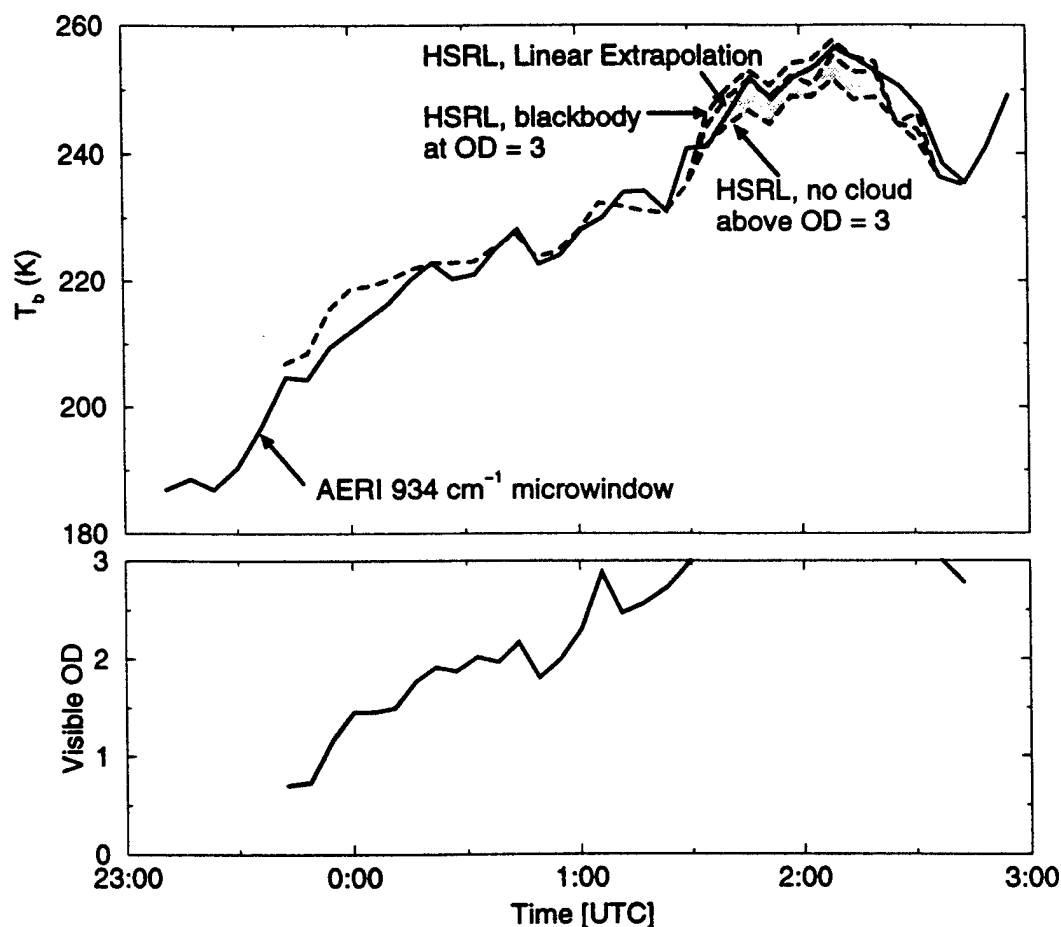


Figure 25: Upper figure shows HSRL derived brightness temperature as a function of time at 934 cm^{-1} (dashed line) relative to AERI measured values (solid) on 9–10 November 1995 at Madison. Shaded portion of figure represents an HSRL observed opaque cloud. Lower figure illustrates HSRL measured visible column optical depth.

Calculation of vertically integrated radiance is performed until the cloud becomes opaque. The visible optical depth above this altitude must be approximated to continue calculation of the column integrated radiance. Three values are determined for this region: a minimum radiance, assuming the cloud terminates where it becomes opaque; a linearly extrapolated value, continuing the calculation based on the change in optical depth over the last 1 km; and a maximum radiance, assuming a blackbody emitter above the opaque point. The AERI measured data shows better agreement when the data is extrapolated, Figure 25.

HSRL and AERI brightness temperature calculations show good correlation over a 100 K temperature range. Figure 26 illustrates data from all cirrus cases for the 934 cm^{-1} microwindow, where HSRL data was interpolated to coincide with AERI times. The dashed lines represent a 5 K deviation from perfect correlation between the instruments. All data points are shown, including those that required extrapolation due to opaque cloud cover. The upward trend in the data is a result of the linear extrapolation of HSRL optical depth when the cloud becomes opaque, which tends to underestimate the optical depth and, therefore, the derived brightness temperature relative to the AERI measured values.

HSRL derived radiance can be utilized to determine a weighted visible to infrared optical depth ratio, $\alpha(\nu)$. This is accomplished by iterating $\alpha(\nu)$, Section 2.2.4, until the HSRL derived radiance agrees with AERI measured values to within $0.001\text{ mW (m}^2\text{ sr cm}^{-1})^{-1}$, rather than using $\alpha(\nu)$ derived in Section 4.1. This should yield an improvement relative to the results determined in Section 4.1, which were based on a direct ratio of HSRL measured visible to AERI derived infrared optical depth. The previous approach assumes a uniform cloud extinction cross-section to determine the IR optical depth. This method inherently weights the cloud extinction cross-section, given the HSRL vertical resolution. Figure 27 illustrates the values of $\alpha(\nu)$ derived for all spectral microwindow regions for the data cases given in Table 3.

Errors in determining $\alpha(\nu)$ are reduced by constraining the data. An upper limit of 15.0 is placed on the $\alpha(\nu)$ iteration, due to inconsistencies between the

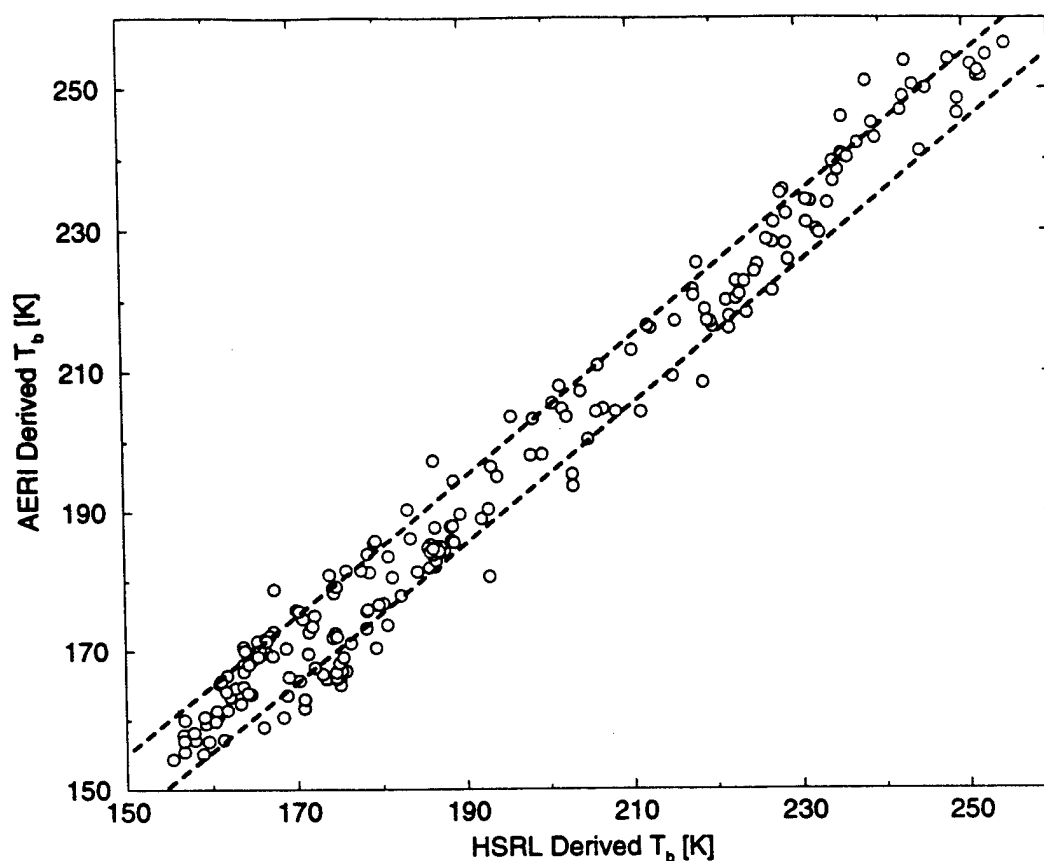


Figure 26: AERI and HSRL derived brightness temperature data for the cirrus cases given in Table 3 for the 934 cm^{-1} microwindow. Dashed lines represent 5 K deviation from perfectly correlated instrument data.

instruments for small optical depths. Data with a visible optical depth less than 0.5 are removed from the analysis, shown by the dashed line in Figure 27. Instrument field of view differences also yield discrepancies in some of the data. This is apparent when the cloud cover within the field of view is not uniform, Figure 28, resulting in the spatial averaging problems discussed in Section 4.1. When this occurs the HSRL derived column radiance does not correlate with AERI data, resulting in a non-physical visible to infrared optical depth ratio. Small breaks in near-uniform cloud cover often underestimate $\alpha(\nu)$; whereas spatially-small, optically-thick clouds in an otherwise clear sky overestimate $\alpha(\nu)$. This is a result of the large AERI field of view relative to the HSRL.

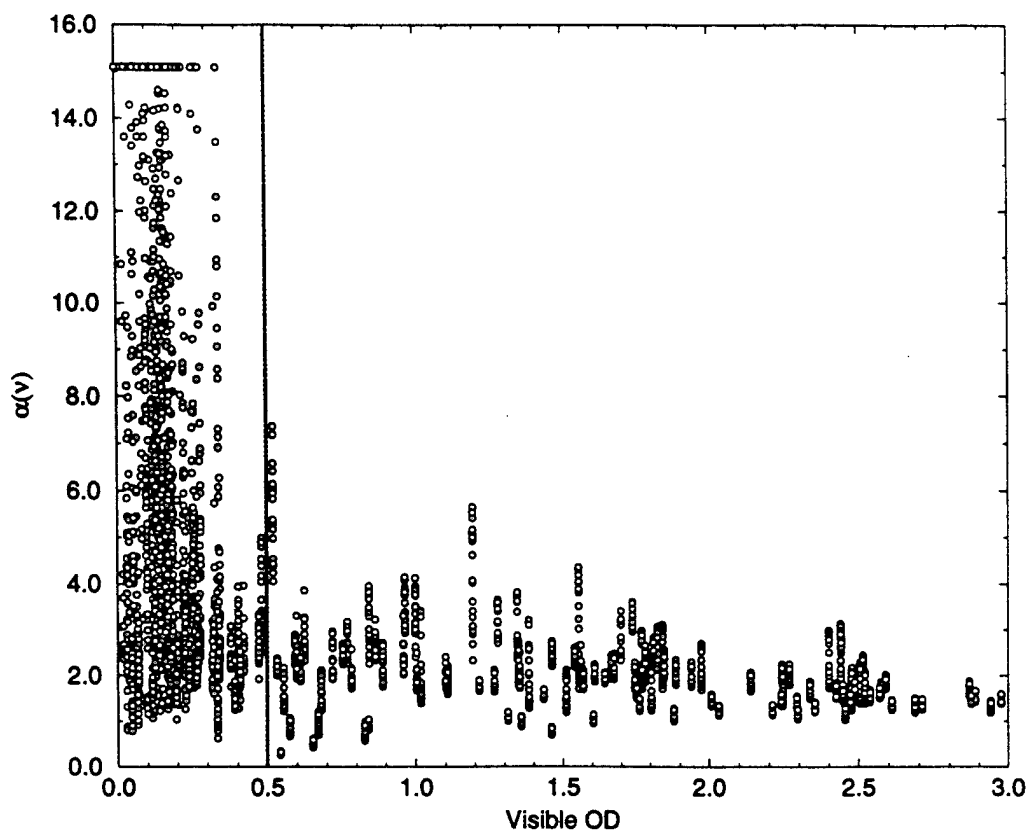


Figure 27: Visible to infrared optical depth ratio, $\alpha(\nu)$, comprising all spectral microwindows for the data cases listed in Table 3. Regions of small optical depth (visible OD < 0.5) yield large uncertainties in $\alpha(\nu)$ due to ill conditioned solutions. Additional errors result from instrument field of view differences. The dashed line represents a constraint on the data which was used to derive the final value of $\alpha(\nu)$.

Figure 28 shows the variation in $\alpha(934 \text{ cm}^{-1})$ as a function of time for data acquired on 17 November 1994. The lower figure illustrates the HSRL measured visible optical depth which was used to derive the values in the upper figure. The regions of increased slope in the lower figure represent temporal changes within the HSRL field of view. The larger AERI field of view and increased dwell time yield radiance measurements that will differ from HSRL derived values. Cases with increased spatial uniformity (e.g., 10 November 1995) will produce reduced scatter in the data, increasing the number of available data points for an improvement in

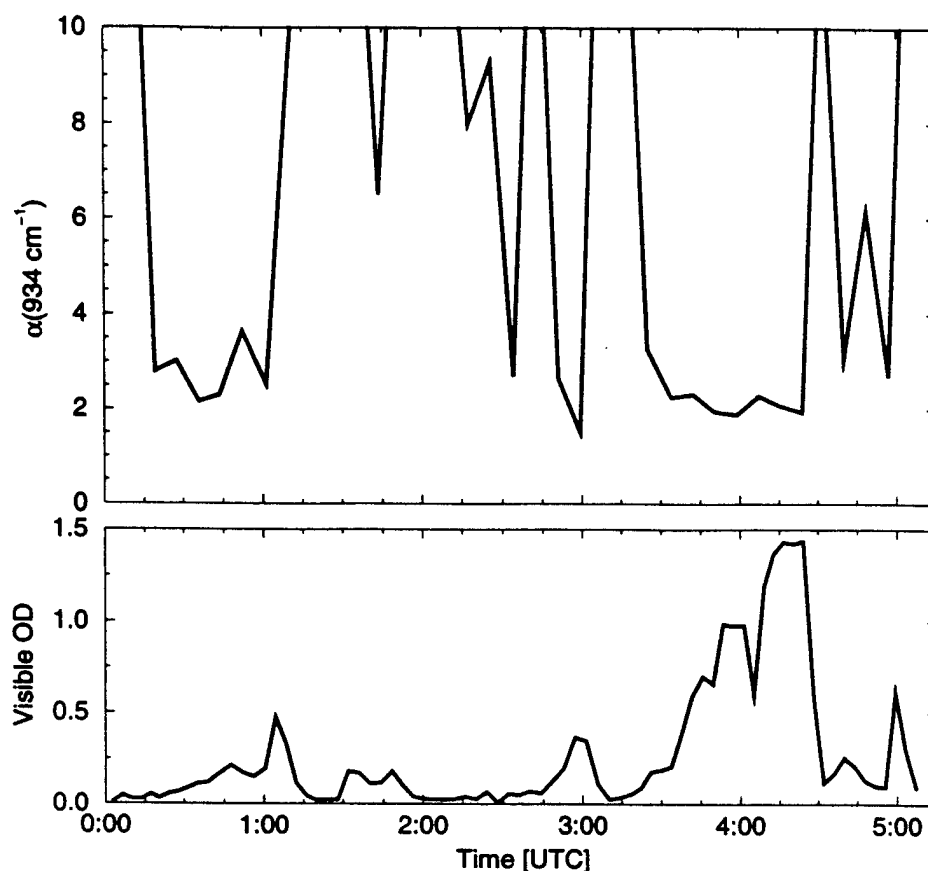


Figure 28: Visible to infrared optical depth ratio, $\alpha(\nu)$, (upper curve) as a function of time, relative to the visible optical depth (lower curve), at 934 cm^{-1} for 17 November 1994 data.

the final statistical analysis. This is evident in Figure 29, which contrasts the results of 17 November 1994 against the other cases.

A spectral comparison of $\alpha(\nu)$ data for individual cases is given in Figure 29 relative to Mie theory. Three of the eight cases listed in Table 3 are not shown because data did not include visible optical depths greater than 0.5 during the data acquisition period. The results from 17 November 1994 (green circles) in Figure 29, exhibited the largest scatter of the cases shown. This was expected given the non-uniformity in cloud cover, and optical depth, indicated in Figure 28. The anomalous 26 October 1995 data (open squares), where $\alpha(\nu)$ appears to be underestimated between 750 and 900 cm^{-1} , is likely due to the HSRL telescope

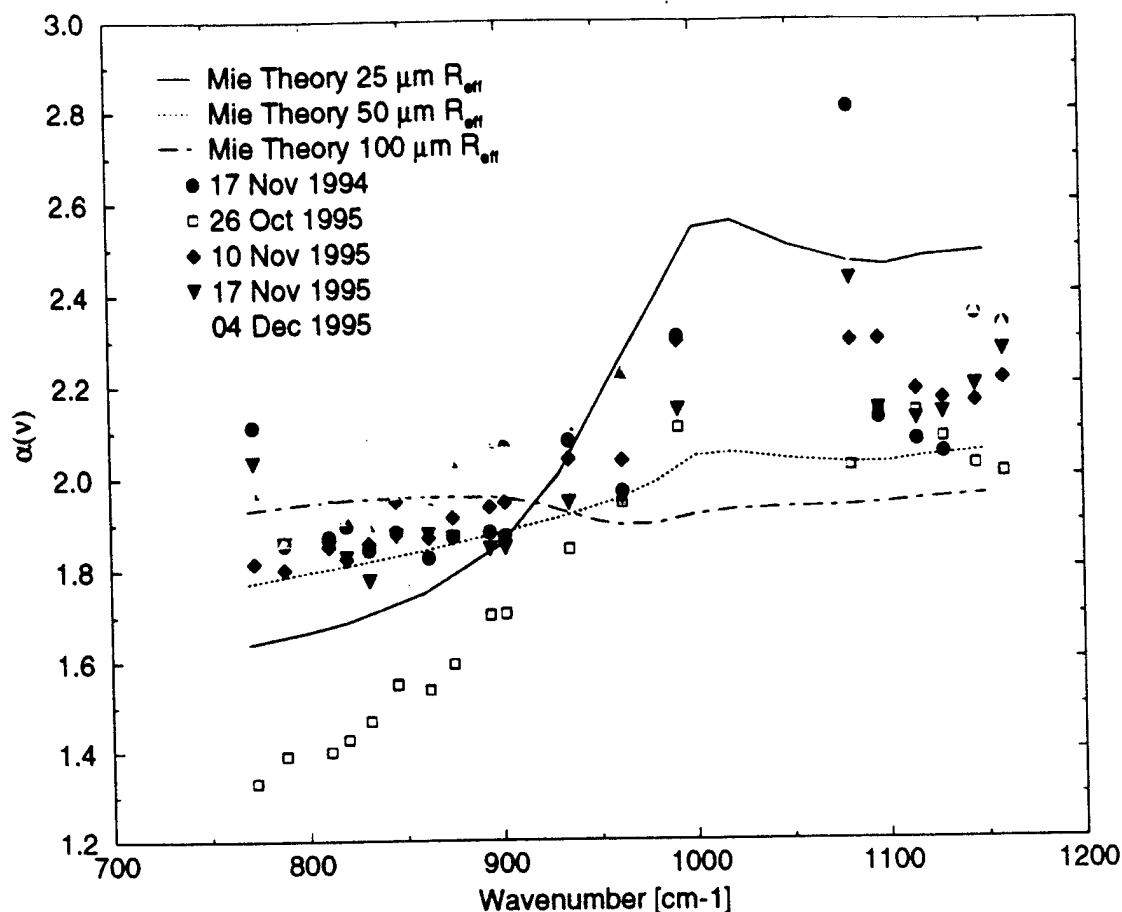


Figure 29: Spectral visible to infrared optical depth data for individual data cases listed in Table 3. The cases that are not shown did not have data within the constraints given in Figure 27. Data from 26 October 1995 appears to be underestimated due to the presence of opaque, low-altitude mixed phase clouds.

configuration which has its focus at infinity. This yields an overlap region between the transmitter and receiver for the first 2.5 km from the surface. The 26 October 1995 case consisted of optically thick ice and mixed phase clouds (shown by HSRL), with a cloud base altitude that varied between 2 and 4 km, which became opaque to the HSRL. This resulted in a visible optical depth measurement that was less than expected, which underestimated the visible to optical depth ratio. The HSRL is capable of such measurements if a refocusing lens is placed in the telescope. This will effectively reduce the receiver and transmitter overlap region. The remaining

cases show good agreement relative to one another. Note that the least scatter in the data among all spectral regions occurs at 934 cm^{-1} . However, all spectral regions exhibiting strong absorption (below 1000 cm^{-1}) show minimal scatter, aside from the anomalous 04 December 1995 case.

Figure 29 illustrates that experimental values of $\alpha(\nu)$ for the individual data cases are consistent with Mie theory for 50 to 100 μm radius particles for wavenumbers smaller than 900 cm^{-1} , but consistent with 25 to 50 μm radius particles for wavenumbers larger than 900 cm^{-1} . This suggests that the entire experimental curve is biased toward larger values of $\alpha(\nu)$. Analysis of Equation 31 indicates that there are five possible explanations for the apparent bias: HSRL measured cloud visible optical depth was overestimated; FASCOD3P calculated clear sky radiance was overestimated; AERI measured downwelling column radiance was overestimated; field of view differences between the instruments yield uncorrelated observations; or limitations of Mie assumptions. The last factor is expected to be negligible in all but specific cases (e.g., a given orientation of ice crystals).

The first three possibilities are inconsistent with instrumental characteristics and measured results. Figure 18 demonstrated HSRL measurement errors due to multiply-scattered return within the HSRL field of view. However, this effect would yield a larger than expected return signal, which corresponds to an underestimate in the measured visible optical depth. FASCOD3P calculations within the microwindow regions also underestimate the radiance relative to AERI measured values, and the Gamma correction minimizes the model errors. The small uncertainty in the AERI measurements eliminates the third possibility.

The bias in the $\alpha(\nu)$ results was likely due to AERI and HSRL instrumental differences. Field of view differences between the instruments were shown to account for large errors during non-uniform cloud cover cases. One would expect the field of view differences to average over a large data set. However, this is not possible given the data analysis constraint imposed on data with a visible optical depth less than 0.5. For cases where the HSRL field of view is full and the AERI FOV is partially clear, $\alpha(\nu)$ is overestimated because the AERI measured radiance

is less than the HSRL derived radiance. Cases where the HSRL FOV observes a clear data point while the AERI FOV is partially clear would be ignored because the visible optical depth value is less than 0.5. The spectral bias in $\alpha(\nu)$ is quite apparent when combining all data points, Figure 30.

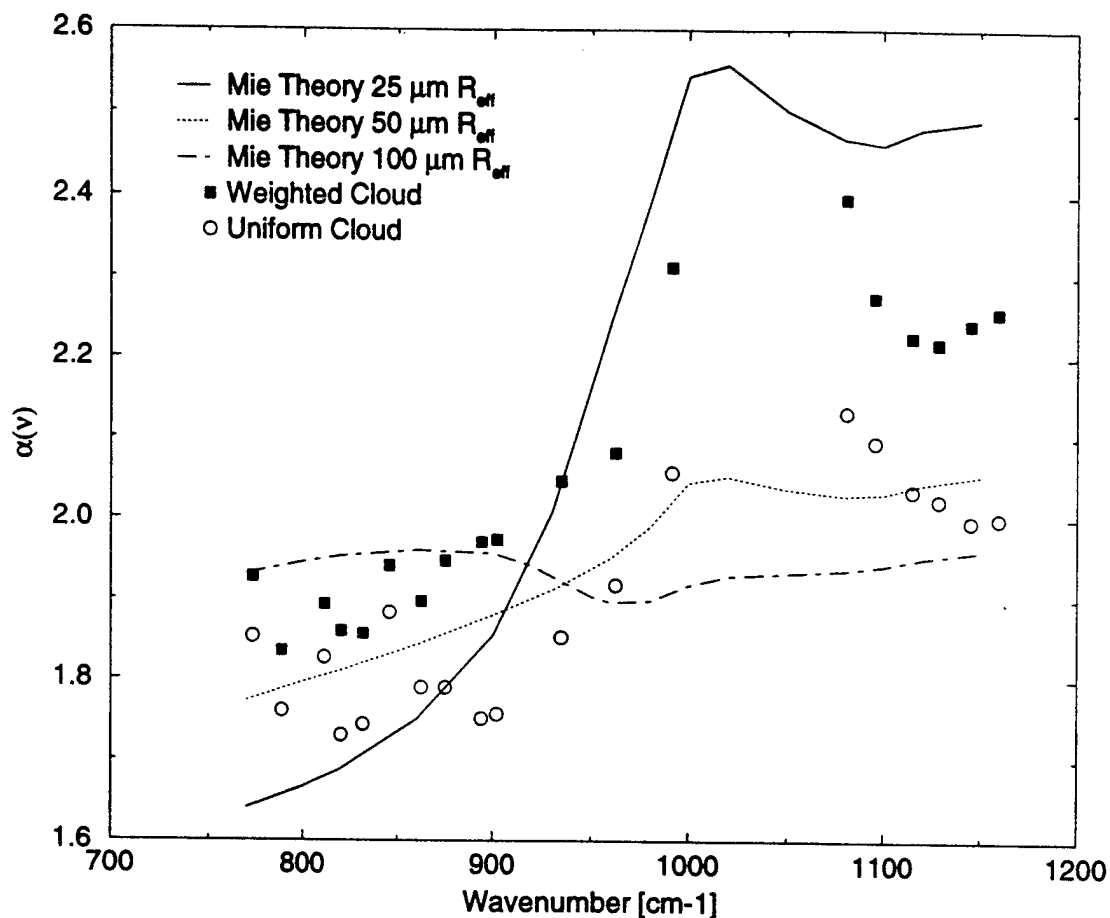


Figure 30: Similar to Figure 22, but updated with $\alpha(\nu)$ using weighted data from all cases. The weighted data (solid squares) produces values that are more consistent with the Mie theory results. The data implies an average radius of about 35 μm , assuming spherical particles. Individual spectral results for the experimental data are given in Tables 4 and 5.

The data from all cases, except 26 October 1995, were combined to determine the effectiveness of iterating $\alpha(\nu)$ from a weighted cloud distribution, relative to the uniform cloud solution, and compared to Mie theory. The weighted results are shown in Figure 30 (solid squares) and demonstrate less scatter than the unweighted results (open circles). The weighted results are also more consistent with the Mie theory calculations, indicating a mean particle effective radius of roughly 35 to 40 μm , assuming spherical particles. Table 5 lists $\alpha(\nu)$ for the weighted cloud experimental solutions for each of the microwindow regions.

Table 5: HSRL:AERI Derived $\alpha(\nu)$ for Weighted Cloud

Microwindow ν [cm^{-1}]	$\alpha(\nu)$	Microwindow ν [cm^{-1}]	$\alpha(\nu)$
773.12	1.7396	934.88	1.9731
788.55	1.6888	962.37	2.0332
811.21	1.7337	991.78	2.2421
820.13	1.7189	1080.97	2.2804
831.70	1.7263	1095.68	2.2210
845.69	1.8035	1115.21	2.1915
862.32	1.7759	1128.71	2.1730
875.10	1.8292	1145.34	2.1738
894.14	1.8774	1159.56	2.1762
902.10	1.8805		

It is necessary to stress the importance of the Gamma correction on the data in the previous figures. The downwelling atmospheric column radiance within a microwindow, given optically thin cirrus or clear conditions, is small relative to optically thick cirrus. As a result, the FASCOD3P calculated radiance from below the cloud dominates the HSRL derived radiance from within the cloud for optically thin or clear conditions. The disagreement between AERI measured radiance and FASCOD3P calculated radiance is significant for these cases. The Gamma technique, detailed in Section 2.1.2, accounts for the difference between AERI and FASCOD3P radiances under clear conditions to correct this problem for

all conditions. Figure 31 illustrates the relative radiance difference and absolute brightness temperature difference due to the Gamma correction for 17 November 1994 data. This is shown as a function of time given a variable, HSRL measured, visible optical depth.

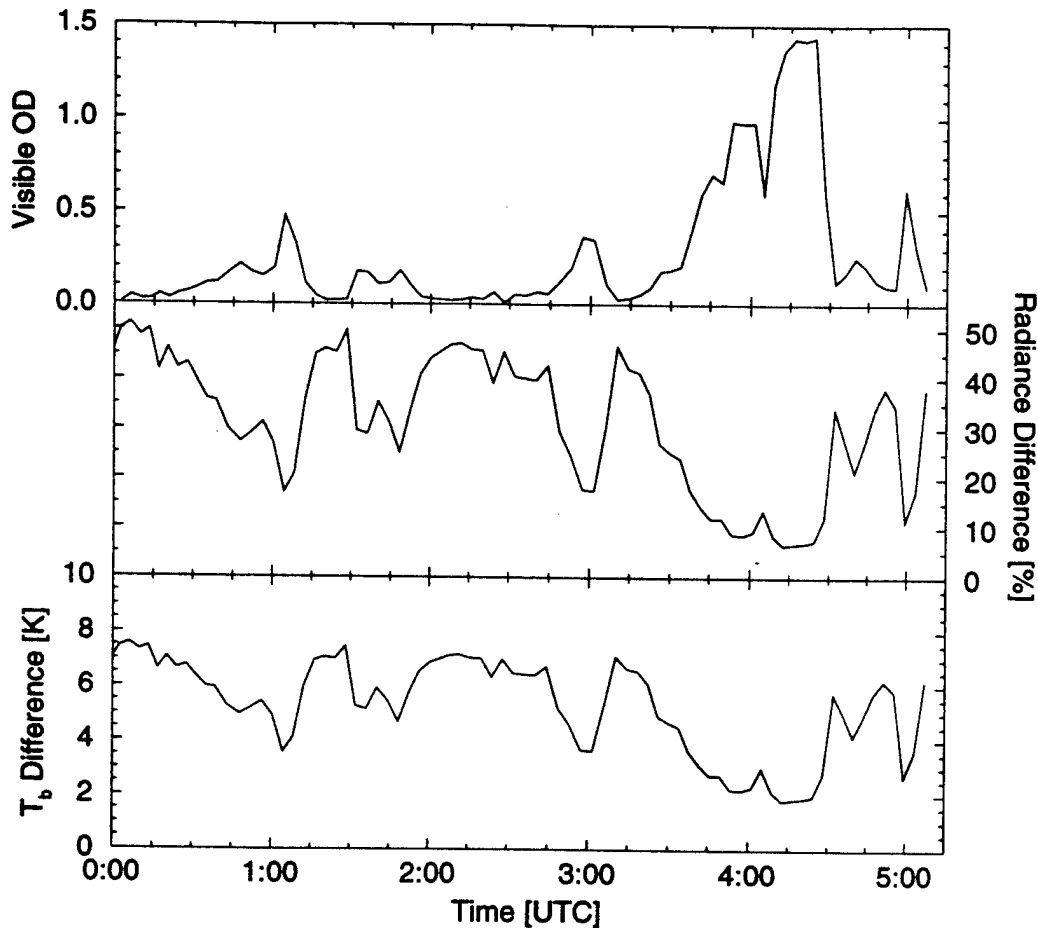


Figure 31: Effects of Gamma correction on HSRL derived brightness temperature for 17 November 1994 data. The upper curve illustrates the HSRL measured visible optical depth. The middle curve shows the contribution of FASCOD3P calculated clear sky radiance relative to the total column. The lower curve gives the absolute difference in brightness temperature that would result without the use of the Gamma correction. The radiance and brightness temperature curves are for the 1096 cm^{-1} microwindow.

The upper curve in Figure 31 indicates the HSRL measured visible optical depth as a function of time. This demonstrates the magnitude of error for optically thin relative to optically thick cirrus. Note that the Gamma corrected radiance, middle curve, can contribute as much as 50 percent of the total column radiance. That implies that the AERI measured clear sky radiance and FASCOD3P calculated clear sky radiance differ by two fold. Although the absolute radiance difference is small, the effect is large for optically thin cirrus or clear conditions. The total difference in HSRL derived brightness temperature is given in the lower curve of Figure 31, resulting in over 7 K difference for clear sky conditions. The radiance and brightness temperature differences are given for the 1096 cm^{-1} microwindow region.

The errors associated with the brightness temperature calculations are similar to those for the optical depth inversions given in Section 4.1. The remainder of this section will detail the magnitude of expected error given the FASCOD3P uncertainties shown in Figure 20. Figure 32 illustrates the FASCOD3P derived clear sky radiance relative to HSRL derived column radiance within the 934 cm^{-1} microwindow for data acquired on 9–10 November 1995. The model clear sky radiance contributes up to 50 percent of the total derived radiance for optically thin cirrus conditions prior to 00:00 UTC. Note that the AERI measured clear sky column radiance near 23:30 UTC is similar to the FASCOD3P calculated values, as expected.

Figure 33 shows the HSRL derived brightness temperature and expected error corresponding to the measured radiance and expected error given in Figure 20. The data corresponds to an HSRL measured visible optical depth of 0.5 for data acquired on 17 November 1994. The upper figure gives the HSRL measured brightness temperature (lower curve) and maximum expected brightness temperature (upper curve) based on FASCOD3P calculations derived from radiosonde uncertainties. The lower figure illustrates the absolute brightness temperature difference of the upper figure. This further suggests the importance of FASCOD3P calculations and radiosonde uncertainties to the final data products.

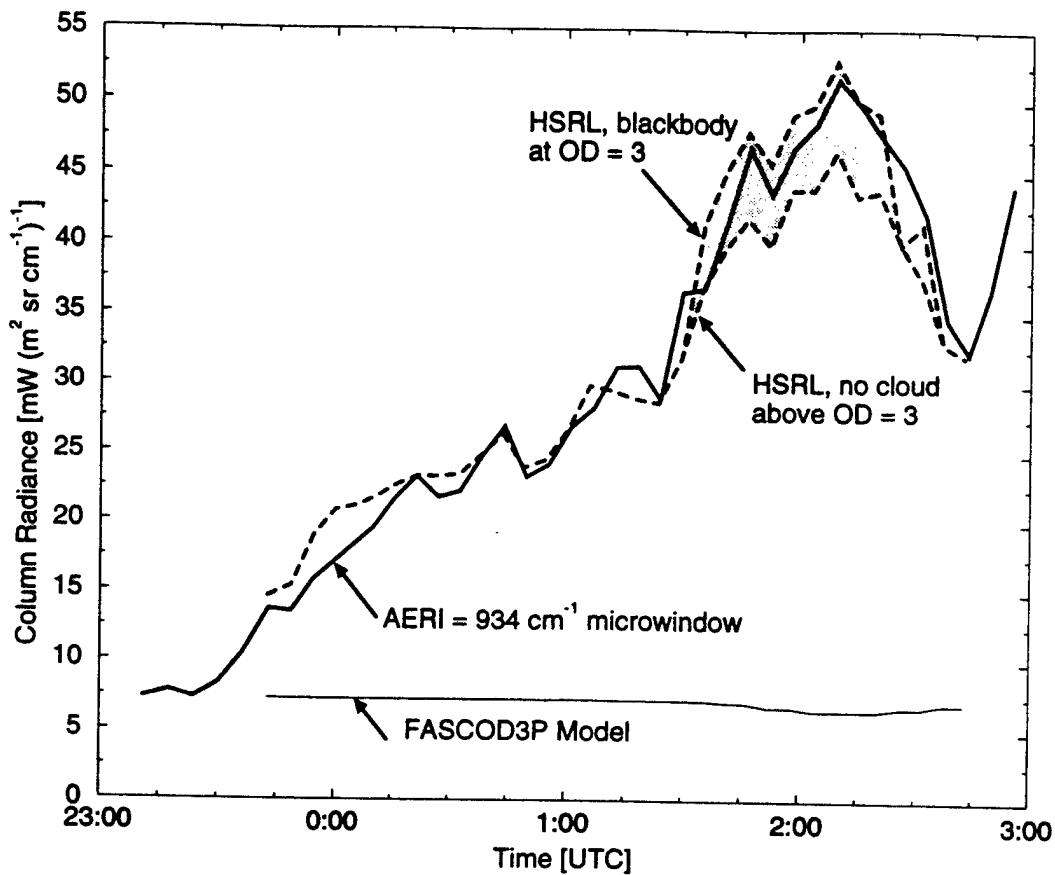


Figure 32: Comparison of measured and derived radiances for 9–10 November 1995. FASCOD3P contribution is shown to gauge the magnitude of clear sky radiance relative to cloud values. The decrease in FASCOD3P calculated radiance occurs with the decrease in cloud base altitude. HSRL derived values are indicated by the dashed lines, where the shading depicts opaque cloud cover.

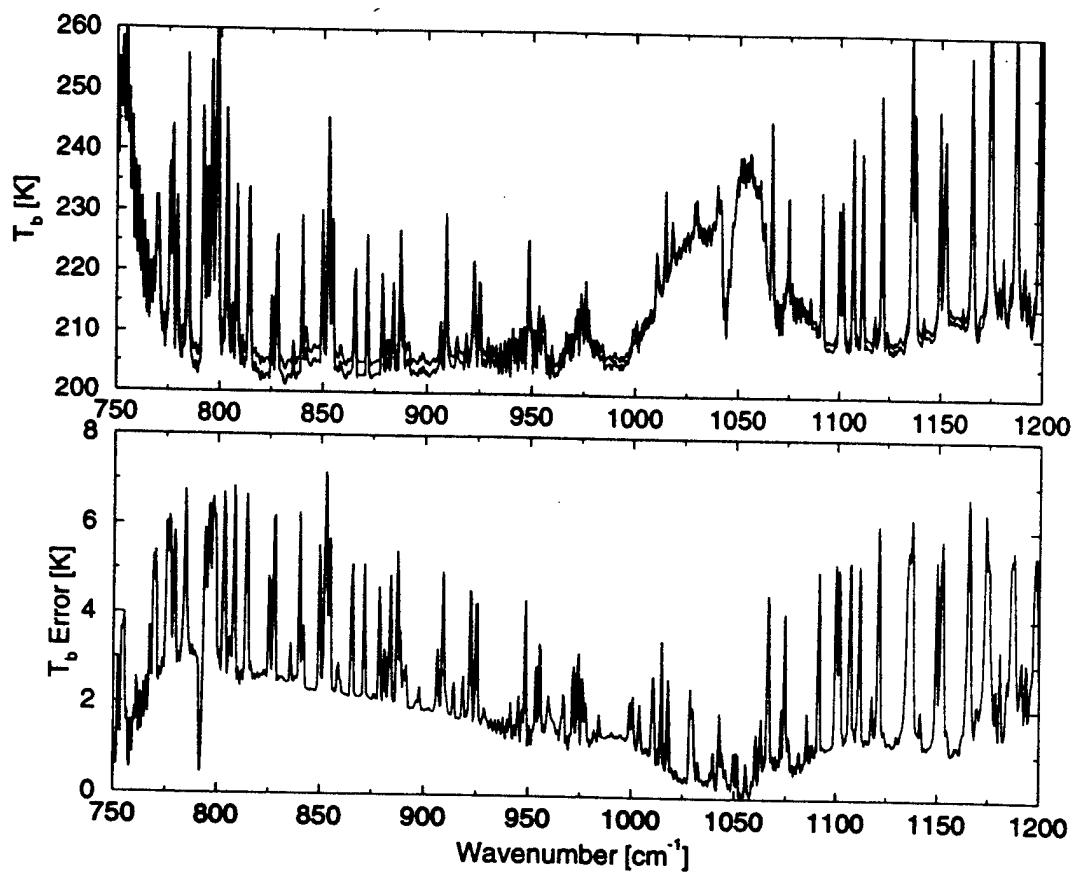


Figure 33: Upper figure shows HSRL derived brightness temperature (lower line) and maximum expected brightness temperature (upper line), given the radiance errors illustrated in Figure 20, for data acquired on 17 November 1994. The lower figure gives the absolute brightness temperature difference for the values shown in the upper figure. The resultant error is calculated for an AERI measured IR optical depth of 0.5

5 Conclusion

An increased understanding of cirrus clouds is necessary to improve current climate models. This includes atmospheric and environmental factors which drive the formation of cirrus, database maintenance of regional and seasonal cirrus coverage on a global scale, and the effect of cirrus on radiative transfer calculations. The research discussed presently focused on the radiative effect of cirrus and, if continued, would lend to a seasonal analysis.

Independent remote sensing at visible and infrared wavelengths, using ground based high spectral resolution lidar (HSRL) and interferometry (AERI), respectively, produced cirrus cloud optical depth and atmospheric column brightness temperature measurements for Madison, WI. A series of 19 infrared microwindows, spectral regions between water vapor absorption lines, were compared to visible lidar measurements. Local atmospheric temperature and dewpoint temperature information was acquired by releasing a radiosonde. Clear sky radiance was calculated using the FASCOD3P line-by-line transmission model.

Trends in the measured optical depth and downwelling brightness temperature were consistent. However, differing instrument field of views and atmospheric dwell-times are limiting features and apparent in portions of the data. Despite these limitations, the HSRL derived brightness temperatures compared favorably with AERI measurements, typically within 5 K over a 100 K temperature range. Visible and infrared optical depths also exhibited good correlation. The HSRL has an upper limit visible optical depth measurement bound of approximately 3.0, defined by the transmitter and detector capabilities. Similarly, the upper bound of AERI calculated infrared optical depth occurs between 2.5 and 3.0; where small deviations in the cloud radiance yield large changes in the optical depth.

Radiosonde and FASCOD3P model uncertainties for infrared data and multiply scattered return for visible data also introduced an important error contribution. Atmospheric water vapor and aerosol loading within the first few kilometers above

the surface introduced a spectral bias to the AERI measured radiance. This affected the minimum resolvable optical depth that could be measured by the AERI, and was corrected by scaling the clear atmospheric radiance and transmittance accordingly. The FASCOD3P calculated clear sky radiance can yield significant errors in the data inversion if not corrected relative to AERI measured clear sky data. The resulting difference between FASCOD3P and AERI radiances was shown to account for over 50 percent of the total column radiance for optically thin cirrus and clear conditions. This produced greater than 7 K differences in the derived brightness temperatures. Overall, spectrally dependent radiance errors ranged from 1 to 8 percent of the total cloud radiance. This corresponded to uncertainties in brightness temperature of 0.5 to 3 K for uniform transmissive cloud cover. An approach was given to estimate the brightness temperature for opaque conditions, resulting in a 10 K difference between the transmissive and opaque calculations. The radiance errors yielded a maximum infrared optical depth deviation of ± 0.1 for a measured value of 0.9. Multiple scattering was shown to account for as much as 20 percent of the HSRL aerosol return signal, which resulted in an underestimation of the HSRL measured visible optical depth.

The visible to infrared optical depth ratio, $\alpha(\nu)$, results were determined by two separate approaches: calculate the visible and infrared optical depths, then determine the ratio; and calculate the downwelling radiance using the HSRL visible optical depth, while iterating the optical depth ratio until the radiance matched the AERI value. Analysis of the unweighted data sets required constraints for optically thin (visible OD < 0.1) and thick (visible OD > 2.0) cases. Iteration of $\alpha(\nu)$ for the weighted cloud was shown to be inconsistent below a visible optical depth of 0.5. Data below this value was not used in the spectral analysis.

Iteration of the optical depth ratio was expected to achieve superior results because the derived values are based on a weighted cloud extinction cross-section, and the data from each instrument is coupled. The other approach assumes a uniform extinction cross-section throughout the cloud, where the optical depth solution is instrument independent. These techniques can be extended to calculate

the upwelling radiance which would be measured by space-borne instrumentation by applying a top-down solution of the radiative transfer equation, assuming the atmosphere does not become opaque due to optically thick cloud cover.

The weighted approach yielded a decreased scatter in the $\alpha(\nu)$ results, which indicated a small bias relative to Mie theory. It was concluded that the direction of the bias was due to instrumental field of view and dwell-time differences, which dominated the combined multiple-scatter and FASCOD3P errors. Implementation of a telescope on the AERI would improve the field of view difference between the instruments. This would increase the light gathering power of the AERI, thereby allowing a minimization in the field of view given similar data acquisition times. Spatial and temporal errors are inherently coupled as the atmosphere is advected through the instrumental field of view. The current approach does not account for AERI calibration times when comparing the AERI and HSRL data. Limiting the HSRL data to AERI atmospheric view times would further improve the instrument correlation.

Particle size spectral dependence was also a factor and the data was shown to agree with Mie theory for ice spheres. A spectral region with a minimum particle size sensitivity near 920 cm^{-1} was suggested by Mie theory calculations. The optical depth ratios for the combined cases were spectrally similar to $35 \mu\text{m}$ radius ($50 \mu\text{m}$ assuming a uniform cloud) ice spheres.

The measured visible to infrared cirrus cloud optical depth ratio can be used in climate models. A parameterization over the entire infrared atmospheric window would require a mean visible to infrared ratio of 1.9 based on 50 to $100 \mu\text{m}$ radius particles. This value could be scaled based on Mie theory results if a mean particle size of the cirrus could be obtained. The large change in ice absorption across the infrared spectrum resulted in a particle size dependence, which could be important to climate models for smaller particles. As the particle size decreased, there was a greater dependence on particle size across the infrared window. The visible to infrared optical depth ratio varied from 1.9 (for $100 \mu\text{m}$ radius ice spheres) to 2.5 (for $25 \mu\text{m}$ radius ice spheres) between 1000 and 1150 cm^{-1} . However, analysis of

ice crystals smaller than 25 μm radius should be performed for validation to the Mie theory ice sphere results.

Observation of contrails formed as a result of jet engine exhaust would allow study of smaller sized particles, relative to cirrus cloud particles. A case study similar to the one presented in this thesis for cirrus would provide a spectral comparison of visible to infrared optical depths. This could further confirm the particle size dependence suggested by Mie theory for ice spheres. It would also show the radiative impact of jet engine exhaust pollution near large airports.

The acquisition of additional data would be useful to complement the current data set, and to improve the statistical analysis relative to Mie theory. A total of 7 of the 8 data sets given in Table 3 were useful in the analysis. The remaining case, 2 December 1995, was useless for cirrus study due to an opaque water cloud below the cirrus cloud layer. The data inversion process fails for water cases because the optical depth of water droplets is large relative to ice crystals. This results in a large optical depth gradient over 200 to 300 m. The current algorithm is based on the FASCOD3P vertical resolution of 64 data points, which yields a layer thickness of 100 to 500 m for a strong to weak dewpoint temperature gradient, respectively. This implies that the depth of the water cloud deck would have the proper resolution. Nonetheless, it is a problem that can be resolved with additional cases and is beyond the scope of this thesis, which is focused on cirrus clouds.

Errors associated with FASCOD3P radiance and transmittance calculations within the water vapor continuum might be decreased by utilizing the high spectral resolution data sets. HSRL measured aerosol backscatter cross-section and depolarization, coupled with AERI radiance measurements, could provide the information required to yield a vertically weighted atmospheric transmittance to correct for the FASCOD3P column radiance relative to AERI measured values. This would improve the current approach, which uses the Gamma correction to apply a uniform correction to the transmissivity.

A AERI Microwindow Regions

A number of regions exist between atmospheric absorption lines which can be observed by the high spectral resolution of the AERI, see Table 6. These 'microwindows' comprise the least absorbing regions within the spectral bandpass of the instrument.

Table 6: AERI Microwindow Regions

Window	Start Window [cm^{-1}]	End Window [cm^{-1}]
1	770.969	774.827
2	785.917	790.739
3	809.061	812.919
4	815.330	824.491
5	828.348	834.617
6	842.814	848.118
7	860.172	864.030
8	872.227	877.531
9	891.996	895.853
10	898.264	905.497
11	929.606	939.731
12	959.983	964.323
13	985.056	998.075
14	1076.670	1084.867
15	1092.100	1098.850
16	1113.316	1116.691
17	1124.406	1132.603
18	1142.246	1148.032
19	1155.265	1163.462

Figures 34 through 36 note these regions and illustrate the change in AERI measured radiance due to the presence of cirrus (upper curve) relative to a clear atmosphere (lower curve). Aerosol loading (e.g., wind blown dust, increased humidity, industrial effluence) will also yield higher microwindow emission.

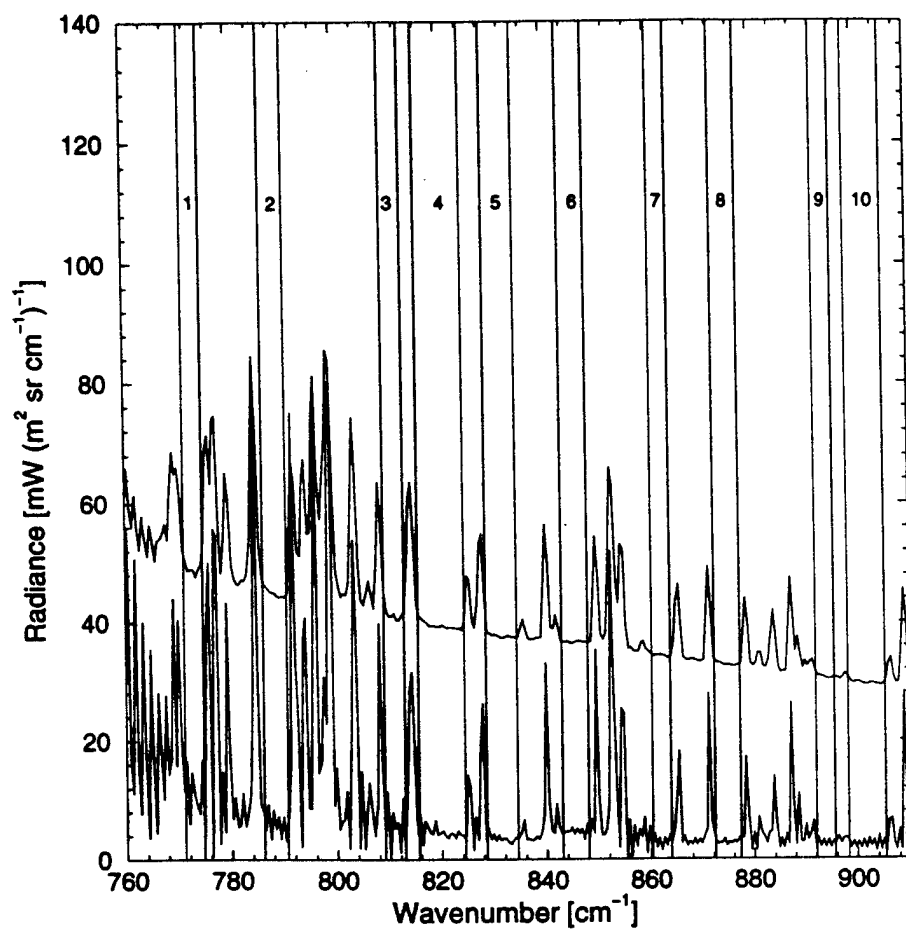


Figure 34: A visualization of AERI microwindow regions listed in Table 6, where the upper curve represents a cirrus case and the lower a clear atmosphere, 760 through 910 cm^{-1} .

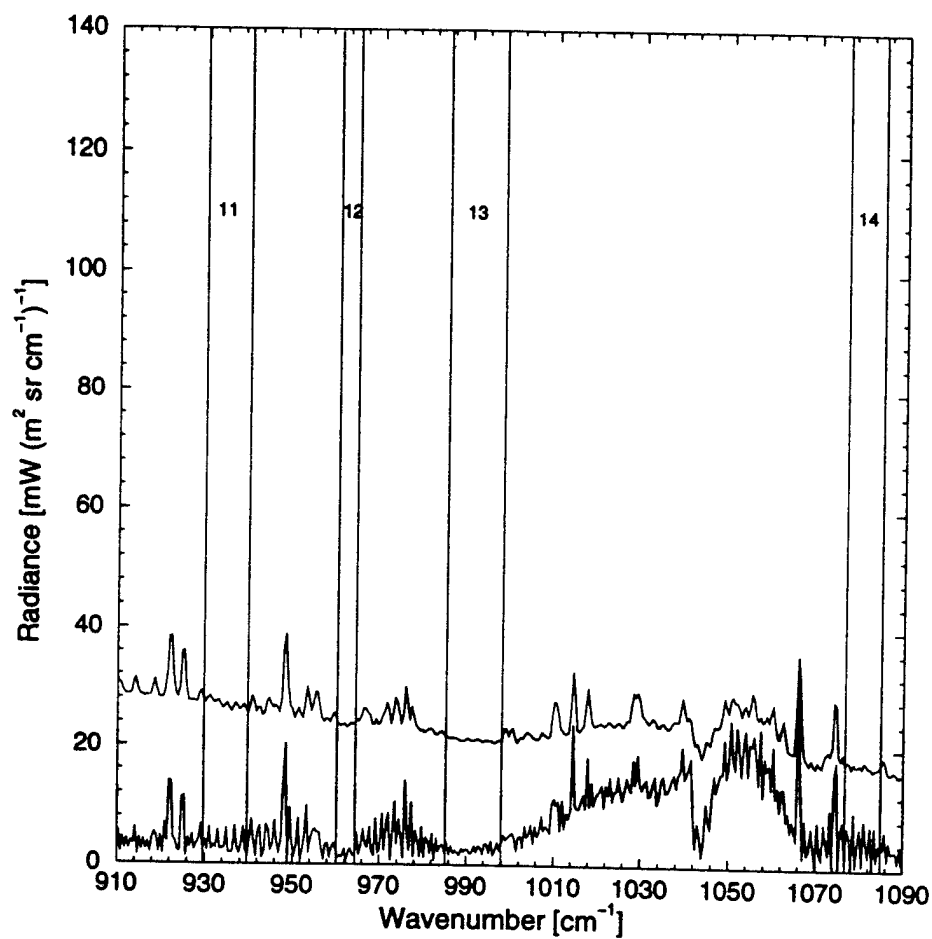


Figure 35: Spectral continuation of Figure 34, see previous caption, 910 through 1090 cm^{-1} .

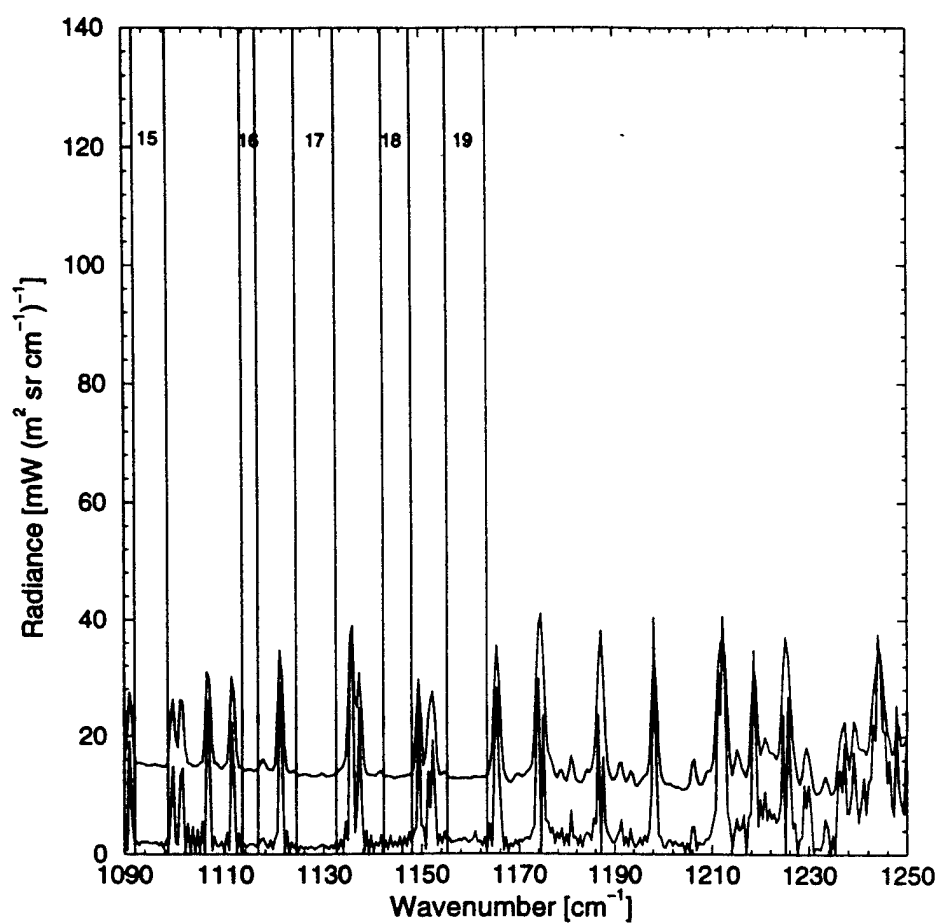


Figure 36: Continuation of Figure 35, see previous caption, 1090 through 1250 cm^{-1} .

B Brightness Temperature Linear Fit

The calculation of a brightness temperature within a spectral bandpass is inconsistent with the true temperature; where the error increases with larger bandpass. This is a result of solving

$$T_b(\nu) = \frac{hc\nu}{k \ln \left[\frac{2hc^2\nu^3}{B(\nu, T(p))} + 1 \right]},$$

based on a single wavenumber representation of the given bandpass.

A correction can be applied by assuming a linear representation of the temperature in the Planck function, such that

$$T_b(\nu) = a + b T'_b(\nu);$$

where a and b are the y-intercept and slope, respectively, determined with a least squares fit over an expected temperature range using the central bandpass wavenumber, ν_c .

For ground-based measurements of downwelling radiance in the atmospheric window, a typical brightness temperature range is between 150 and 270 K; dependent upon cloud base altitude and optical depth. The theoretical radiance, integrated over the spectral bandpass, is calculated in 1 K increments in the given temperature domain. Brightness temperature, $T_b(\nu_c)$, is determined using the theoretical radiance and ν_c . A least squares fit to these values is performed to yield the necessary adjustment; where the corrected form is represented as

$$T'_b(\nu) = \frac{1}{b} \left[\frac{hc\nu}{k \ln \left[\frac{2hc^2\nu^3}{B(\nu, T(p))} + 1 \right]} - a \right],$$

Figure 37 illustrates the relative error (upper figure) and percent error (lower figure) in deriving the brightness temperature from radiance data in a spectral bandpass. Corrected and uncorrected values are represented by the solid and dashed curves, respectively, using a bandpass of 909 to 1000 cm^{-1} (10 to 11 μm) over the temperature domain 150 to 270 K.

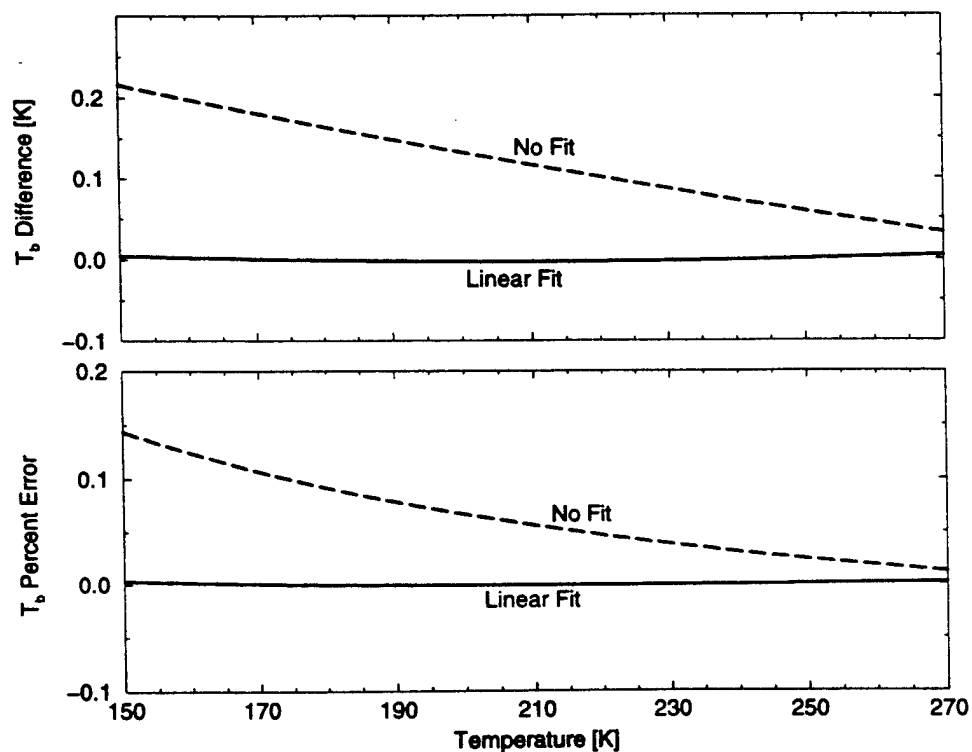


Figure 37: A comparison of broadband brightness temperature using parameterized Planck function linear in temperature (solid line) and standard Planck function (dashed line); each using the mean wavenumber, relative to the theoretical value. The upper figure represents temperature difference from theoretical, while the lower gives percent error.

C FASCOD3P Use

The FASCOD3P model is used to infer clear sky radiance and transmissivity of the atmosphere from the surface to cloud base. Figure 38 illustrates a typical FASCOD3P input file. In this example a bottom-up calculation is performed to determine radiance and transmission to an altitude of 13.8 km.

```

$ (DHD) AERI/HSRL
HI=1 F4=1 CN=1 AE=0 EM=1 SC=0 FI=0 PL=0 TS=0 AT=1 MG=0 LS=0 MS=0 XS=0 0 0
750.000 1250.000 .000 .000 .000 .000 .000 .000
.000 1.000
0 2 43 0 1 7 1 .000 .000 .000 360.000
0.330 13.765 0.000
0.359 0.579 0.978 1.197 1.631 2.031 2.249 2.517
2.732 2.949 3.020 3.171 3.434 3.544 3.691 3.833
3.973 4.114 4.257 4.396 4.653 5.023 5.242 5.346
5.823 6.499 6.894 7.203 7.430 7.727 8.393 8.872
9.396 10.084 10.793 11.351 11.542 11.935 12.178 12.338
12.988 13.114 13.765
43 sond_951026_msn_00.dat
0.359 972.800 288.550 AA FA33333
271.750 360.000
0.579 940.000 285.150 AA FA33333
271.650 360.000
0.978 903.100 283.550 AA FA33333
269.150 360.000
1.197 879.600 281.550 AA FA33333
268.750 360.000
1.631 834.200 277.750 AA FA33333
267.350 360.000
>
> Similar lines deleted...
>
12.988 166.000 215.550 AA FA33333
202.550 360.000
13.114 162.700 215.650 AA FA33333
202.250 360.000
13.765 146.800 215.450 AA FA33333
199.850 360.000

```

Figure 38: Portion of a typical FASCOD3P 'TAPE5' data file. It is used to set various model parameters and input atmospheric temperature and water vapor profiles as a function of altitude.

The input file is comprised of three sub-sections: model calculation parameters, representative altitude levels, and the atmospheric aerological profile determined from radiosonde data at the chosen altitude levels (Anderson and Chetwynd, 1992). A \$ symbol indicates the beginning of the input file, followed by an 80-character information header. The second row determines various parameters used by the model, summarized in Table 7.

Table 7: FASCOD3P Input File: Row 2

Parameter	Value	Definition
HI	1	Use Voigt profile
F4	1	Use 25 cm^{-1} from line center
CN	1	Default for atmospheric calculations
AE	0	No aerosol calculations
EM	1	Calculate radiance and transmittance
SC	0	Default
FI	0	Default
PL	0	Default
TS	0	Default
AT	1	Atmosphere
MG	0	Default, merge data to output file
LS	0	No laser parameters
MS	0	No multiple scattering
XS	0	No cross-sections

Rows 3 through 6 indicate boundaries: spectral, spatial, and direction of calculation. The first two terms in row 3 are the spectral limits; from 750 to 1250 cm^{-1} for this example. The following terms in row 3 relate to the spectral linewidth and strength to use for various cases; each set to .000 to accept the default values. Row 4 sets the boundary temperature and emissivity; 0.000 and 1.000, respectively for space observation from the earth's surface. Table 8 lists the row 5 settings. Row 6 indicates begin (H1) and end (H2) altitudes and slant angle; 0.330 through 13.765 km for a zenith view (.000).

Table 8: FASCOD3P Input File: Row 5

Value	Definition
0	User supplied profile (radiosonde)
2	Path, from H1 to H2 (row 6)
43	Levels in profile, maximum of 64
0	Default, zero absorber if less than 0.1% of total
1	Short printout
7	Default, number of molecular species
1	Write layer data to output file
.000	Default, earth radius = 6371.23 km
.000	Default, altitude of space = 100 km
.000	Default, use mean frequency for refractive geometry
360.000	Mixing ratio (ppmv) for CO ₂

The next several rows, 7 through 12 in this case, suggest the altitude levels which best represent the radiosonde temperature and moisture profile; where roughly 500 data points are reduced to approximately 50. A 24 character information header, used to infer the number of points and filename of the complete radiosonde data file, separates the altitude level listing from the radiosonde data.

The remaining rows describe the radiosonde data corresponding to each altitude level; where two rows are used for each level. Information is given as follows: altitude (km); pressure (mb); temperature (K); units indicator, AA, for this row; and units indicator, FA33333, for next row. The following line: dewpoint temperature (K), and CO₂ mixing ratio (ppmv). The AA specifies pressure and temperature units. FA33333 implies: F, dewpoint units; A, CO₂ units; and 33333, default to value for model mid-latitude winter atmosphere for the remaining 5 atmospheric species (O₃, N₂O, CO, CH₄, and O₂). This is repeated for each altitude. A % symbol indicates end of file. The HITRAN92 atmospheric transmission database is the source for the FASCOD3P transmission data.

D Parameterization of Cirrus Reflectance

A phase function can be determined from Mie theory if given the particle size distribution, particle phase, optical depth, and wavenumber. If a particle size distribution is assumed under cirrus conditions for a given microwindow region, the optical depth remains the only unknown.

Reflectance was calculated for a series of optical depths for each microwindow region; where the IR optical depth varied from 0.01 through 5.0. The upper limit is beyond the capabilities of the lidar and is an acceptable cut-off.

Figure 39 shows a plot of reflectance as a function of the IR optical depth; which is subsequently fit with a sixth-order polynomial to determine a parameterization for the reflectance for the given optical depth range. Data shown is at 772 cm^{-1} . The calculated reflectance for the given assumptions varies from 0 to 0.52%, among all microwindows.

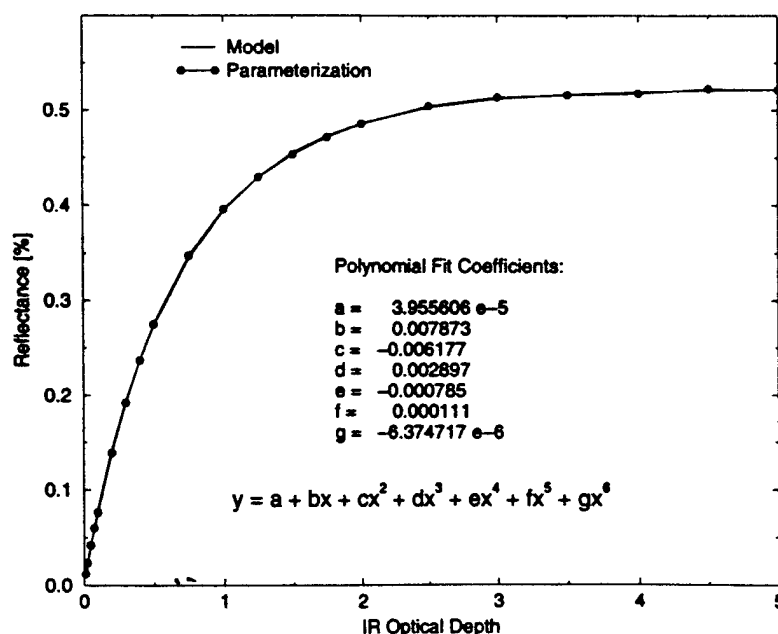


Figure 39: Reflectance as a function of IR optical depth and a sixth-order polynomial fit for the microwindow region centered at 772 cm^{-1} . The fit is required to parameterize reflectance to allow optical depth inversion from the IR RTE.

The coefficients for each microwindow region are given in Table 9 for completeness, such that

$$r(\delta_{cld}) = a + b \delta_{cld} + c \delta_{cld}^2 + d \delta_{cld}^3 + e \delta_{cld}^4 + f \delta_{cld}^5 + g \delta_{cld}^6;$$

where the reflectance is valid for infrared optical depths between 0 and 5, and the spectral dependence is implied.

Table 9: Reflectance Fit Coefficients

μwindow (cm^{-1})	a $\times 10^{-5}$	b $\times 10^{-3}$	c $\times 10^{-3}$	d $\times 10^{-3}$	e $\times 10^{-4}$	f $\times 10^{-4}$	g $\times 10^{-6}$
773	3.9556	7.8733	-6.1774	2.8969	-7.8505	1.1149	-6.3747
788	3.8503	7.6638	-6.0055	2.8156	-7.6313	1.0839	-6.1990
811	3.6348	7.1907	-5.6321	2.6428	-7.1704	1.0194	-5.8339
820	3.5399	6.9738	-5.4638	2.5656	-6.9656	0.9908	-5.6724
831	3.5093	6.6325	-5.2271	2.4700	-6.7406	0.9624	-5.5254
846	3.2853	6.1136	-4.8293	2.2878	-6.2555	0.8944	-5.1399
862	3.0069	5.4711	-4.3383	2.0628	-5.6558	0.8102	-4.6621
875	2.7645	4.9264	-3.9209	1.8710	-5.1439	0.7382	-4.2533
894	2.3410	3.9045	-3.1262	1.4978	-4.1250	0.5921	-3.4095
902	2.1395	3.4956	-2.8113	1.3524	-3.7352	0.5372	-3.0979
935	1.2622	1.8554	-1.5322	0.7510	-2.0987	0.3041	-1.7628
962	1.3547	1.9466	-1.6173	0.7948	-2.2233	0.3223	-1.8688
992	1.9235	2.8994	-2.3775	1.1578	-3.2208	0.4653	-2.6902
1081	2.4633	4.0218	-3.2373	1.5550	-4.2874	0.6158	-3.5472
1096	2.4832	4.0746	-3.2745	1.5712	-4.3288	0.6214	-3.5784
1115	2.5223	4.1853	-3.3529	1.6056	-4.4185	0.6338	-3.6486
1129	2.5462	4.2579	-3.4040	1.6281	-4.4778	0.6422	-3.6958
1145	2.5693	4.3299	-3.4540	1.6498	-4.5338	0.6499	-3.7389
1159	2.5818	4.3689	-3.4799	1.6607	-4.5613	0.6536	-3.7596

References

- Ackerman, S. A., Smith, W. L., Spinhirne, J. D., and Revercomb, H. E. (1990): The 27-28 October 1986 FIRE IFO Cirrus Case Study: Spectral Properties of Cirrus Clouds in the 8-12 μm Window. *Mon. Wea. Rev.*, **118**, pp. 2377-2388.
- Anderson, G. P. and Chetwynd, J. H. (1992): *FASCOD3 Preliminary Version: FASCD3P*. Dept. of the Air Force, Phillips Laboratory (AFSC), Hascom Air Force Base, Massachusetts 01731-5000.
- Cachorro, V. E., de Frutos, A. M., and Casanova, J. L. (1987): Absorption by oxygen and water vapor in the real atmosphere. *Appl. Opt.*, **26**, pp. 501-5.
- Chappelaz, J., Blunler, T., Reynaud, D., Barnola, J. M., Schwander, J., and Stauffer, B. (1993): Synchronous changes in atmospheric CH_4 and Greenland climate between 40 and 8 kyr BP. *Nature*, **366**, pp. 443-5.
- Clough, S. A. (1995): The water vapor continuum and its role in remote sensing. In *OSA Remote Sensing Proceedings*. OSA, Salt Lake City, pp. 76-8.
- Clough, S. A., Kneizys, F. X., Shettle, E. P., and Anderson, G. P. (1986): Atmospheric radiance and transmittance: FASCOD2. In *Proceedings of the Sixth Conference on Atmospheric Radiation*. American Meteorological Society, Boston, MA, pp. 141-4.
- Collard, A. D., Ackerman, S. A., Smith, W. L., Ma, X., Revercomb, H. E., Knuteson, R. O., and Lee, S.-C. (1995): Cirrus Cloud Properties Derived from High Spectral Resolution Infrared Spectrometry during FIRE II. Part III: Ground-Based HIS Results. *J. Atmos. Sci.*, **52**, pp. 4264-75.
- Deirmendjian, D. (1969): *Electronic scattering on spherical polydispersions*. American Elsevier Publishing.

- Eloranta, E. W. (1993): A Practical Model for the Calculations of Multiply Scattered Lidar Returns. In *OSA Remote Sensing Proceedings*. OSA, Salt Lake City.
- Eloranta, E. W. and Piironen, P. (1996): Measurements of Particle Size in Cirrus Clouds with the High Spectral Resolution Lidar. In *8th International Workshop on Multiple Scattering Lidar Experiments*. MUSCLE 8, Quebec, Canada.
- Eloranta, E. W. and Piironen, P. K. (1992): Adaption of the University of Wisconsin High Resolution Lidar for polarization and multiple scattering measurements. In *Sixteenth International Laser Radar Conference, Cambridge, MA*. NASA Conference Publication 3158, pp. 353-6.
- Eloranta, E. W. and Shipley, S. T. (1982): *Atmospheric Aerosols, A Solution for Multiple Scattering*. Ardash Depeek, Ed., Spectrum Press.
- Feltz, W. (1994): Meteorological Applications of the Atmospheric Emitted Radiance Interferometer (AERI). Master's thesis, University of Wisconsin - Madison.
- Genthon, C., Barnola, J. M., Reynaud, D., Lewis, C., Jouzel, J., Barkov, N. I., Kotkevich, Y. S., and Kotlyakov, V. M. (1987): Vostok ice core: climatic response to CO₂ and orbital forcing changes over the last climatic cycle. *Nature*, **366**, pp. 414-8.
- Grant, W. B. (1990): Water vapor absorption coefficients in the 8-13- μ m spectral region: a critical review. *Appl. Opt.*, **29**, pp. 451-62.
- Grund, C. and Eloranta, E. (1994): Personal communication with Edwin Eloranta.
- Hansen, J. E. (1971): Multiple Scattering of Polarized Light in a Planetary Atmosphere. Part II: Sunlight Reflected by Terrestrial Water Clouds. *J. Atmos. Sci.*, **28**, pp. 1400-26.

- Hess, M. and Wiegner, M. (1994): COP: a data library of optical properties of hexagonal ice crystals. *Appl. Opt.*, **33**, pp. 7740-6.
- Liou, K. N., Takano, Y., Ou, S. C., Heymsfield, A., and Kreiss, W. (1990): Infrared Transmission Through Cirrus Clouds: A Radiative Model for Target Detection. *Appl. Opt.*, **29**, pp. 1886-1896.
- Measures, R. M. (1992): *Laser Remote Sensing: Fundamentals and Applications*. Krieger Publishing Co., Florida.
- Piironen, A. K. and Eloranta, E. W. (1995): Accuracy Analysis of Wind Profiles Calculated from Volume Imaging Lidar Data. *J. Geophys. Res.*, **100**, pp. 25559-67.
- Piironen, P. (1994): *A High Spectral Resolution Lidar Based on an Iodine Absorption Filter*. PhD thesis, University of Joensuu, Department of Physics.
- Piironen, P. and Eloranta, E. W. (1994): Demonstration of a high-spectral-resolution lidar based on an iodine absorption filter. *Opt. Lett.*, **19**, pp. 234-6.
- Plass, G. N. and Kattawar, G. W. (1971): Radiative transfer in water and ice clouds in the visible and infrared regions. *Appl. Opt.*, **10**, pp. 738-48.
- Platt, C. M. R. (1973): Lidar and radiometric observations of cirrus clouds. *J. Atmos. Sci.*, **30**, pp. 1191-204.
- Platt, C. M. R. (1979): Remote sounding of high clouds: I. Calculation of visible and infrared optical properties from lidar and radiometer measurements. *J. Appl. Met.*, **18**, pp. 1130-43.
- Platt, C. M. R. and Dilley, A. C. (1979): Remote sounding of high clouds: II. Emissivity and cirrostratus. *J. Appl. Met.*, **18**, pp. 1144-50.
- Poellot, M. R. and Henderson, B. (1994): FIRE Cirrus II Mission Summary and Data Report. Technical report, University of North Dakota Citation, Department of Atmospheric Sciences.

- Revercomb, H. E., Best, F. A., Dedecker, R. G., Dirkx, T. P., Herbsleb, R. A., Knuteson, R. O., Short, J. F., and Smith, W. L. (1993): Atmospheric emitted radiance interferometer (AERI) for ARM. In *Fourth Symposium on Global Change Studies*. AMS 73rd Annual Meeting, Anaheim, CA, pp. 46-9.
- Revercomb, H. E., Best, F. A., Knuteson, R. O., Whitney, B. A., Dirkx, T. P., Dedecker, R. G., Garcia, R. K., van Delst, P., Smith, W. L., and Howell, H. B. (1996): Atmospheric Emitted Radiance Interferometer (AERI), Part I: Status, Basic Radiometric Accuracy, and Unexpected Errors and Solutions. In *Proceedings of the Sixth Atmospheric Radiation Measurement (ARM) Science Team Meeting*. ARM Sixth Annual Meeting, San Antonio, TX.
- Rossow, W. B. and Lacis, A. A. (1990): Global, Seasonal Cloud Variations from Satellite Radiance Measurements. Part II: Cloud Properties and Radiative Effects. *J. Climate*, **3**, pp. 1204-1253.
- Rothman, L. S., Gamache, R. R., Goldman, A., Brown, L. R., Toth, R. A., Pickett, H. M., Poynter, R. L., Flaud, J.-M., Carny-Peyret, C., Barbe, A., Husson, N., Rinsland, C. P., and Smith, M. A. H. (1987): The HITRAN database: 1986 edition. *Appl. Opt.*, **26**, pp. 4058-97.
- Schneider, S. H. (1990): The global warming debate heats up: an analysis and perspective. *Bull. Amer. Met. Soc.*, **71**, pp. 1292-1304.
- Smith, W. L., Knuteson, R. O., Revercomb, H. E., Best, F., Dedecker, R., and Howell, H. (1993): GB-HIS: A Measurement System for Continuous Profiling of Boundary Layer Thermodynamic Structure. In *8th Symposium on Meteorological Observations and Instrumentation*. AMS, 73rd Annual Meeting, Anaheim, CA, pp. J180-3.
- Smith, W. L., Ma, X. L., Ackerman, S. A., Revercomb, H. E., and Knuteson, R. O. (1993): Remote sensing cloud properties from high spectral resolution infrared observations. *J. Atmos. Sci.*, **50**, pp. 1708-20.

STATISTICS ON THE OPTICAL PROPERTIES OF CIRRUS CLOUDS MEASURED WITH THE HIGH SPECTRAL RESOLUTION LIDAR

E. W. Eloranta and P. Piironen

*University of Wisconsin
1225 W. Dayton St., Madison, WI 53706, USA*

1. Abstract

This paper presents statistics derived from one year of cirrus cloud observations with the University of Wisconsin High Spectral Resolution Lidar (HSRL). The HSRL provides calibrated vertical profiles of atmospheric optical depth, backscatter cross section, extinction cross section and depolarization. The measurement technique allows rigorous computation of error bounds for all observations.

2. Instrumentation

The lidar signal backscattered from molecules is spectrally broadened by the Doppler shift resulting from the thermal motion of the molecules. Light scattered from aerosols shows little spectral broadening from the slow Brownian motion of the aerosols. The University of Wisconsin High Spectral Resolution Lidar (HSRL) measures backscatter cross sections and optical depth of clouds by separating the Doppler-broadened molecular backscatter return from the unbroadened aerosol return¹⁻³. The molecular signal is used as a calibration target with a backscatter cross section that can be computed from an independent temperature profile. This calibration avoids the need for information on the ratio of backscatter to extinction and boundary values of the extinction. It thus avoids the ambiguities and numerical instabilities encountered when calibrated measurements are attempted with traditional lidars.

3. Observation Schedule

The HSRL was operated when cirrus was present during the overpass of the NOAA 12 or 13 satellite. Observations were made between February 4, 1994 and December 8 1994. On each day, the decision to operate was based on the presence of visual cirrus clouds or an indication of approaching cirrus on GOES 7 imagery. Decisions to operate were made approximately two hours prior to the satellite pass. The data set includes nearly every case with visual cirrus. Only a few days with cirrus were missed during the entire year. Both AVHRR and GOES images were archived for nearly all data cases. Data from 51 days were used in this study. On each day the lidar was operated for at least one hour. The longest data session was 5 hours.

4. Analysis

The raw lidar data consists of 3 second integrations. For this study we have generated 3 minute averages of these profiles in order to increase the signal to noise ratio of the data and to decrease the total number of data points. The data set includes 1621 data profiles consisting of measurements at 15 meter intervals in the altitude range between 200 m and 35 km.

At first glance it appears easy to define what comprises a cloud. However, close examination shows that cloud cover statistics are very sensitive to how cloudy air is distinguished from clear air. Cloud boundaries are often not distinct and cloud elements that easily identified as clouds are joined by a gradation of cloud densities that merge smoothly with haze and other clear air aerosol clouds. In this study we use a threshold based on the ratio of backscattering from particulates to molecular backscattering to define the presence of cloud. Depolarization measurements allow identification of cloud phase⁴. Strong depolarization indicates the presence of non-spherical particles (ie. ice). Very small depolarizations indicate the presence of spherical scatters (ie. water droplets).

5. Results

Figure 1 shows the depolarization measured for this data set as a function of temperature. These data were used to determine depolarization thresholds which were used to distinguish ice, water, and mixed phase clouds.

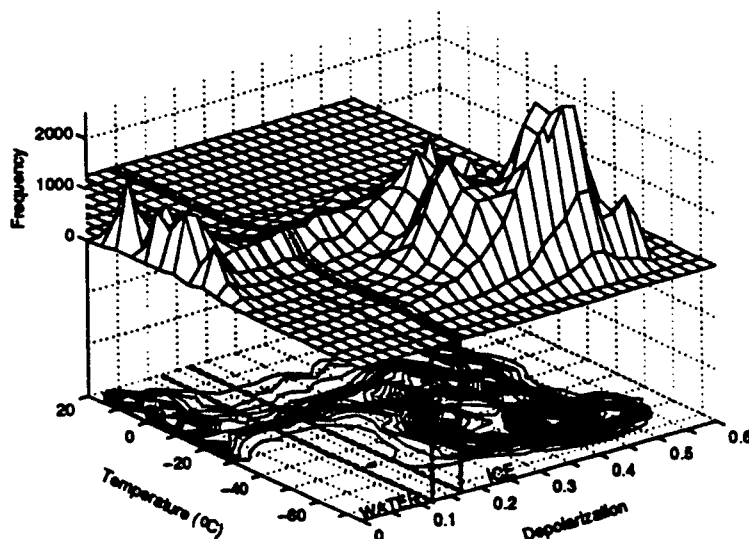


Figure 1. A contour plot and a 3-elevation map of depolarization as a function of temperature for all data points having an aerosol backscatter greater than the molecular backscatter.

Notice that at temperatures below -40°C , where water can not exist in the liquid state, all except one data point have depolarizations greater than 0.17. Also notice that at temperatures above freezing, the number of data points with depolarization above 0.12 become very small. Examination of HSRL altitude vs. time images suggest that those few points with temperatures above freezing and with depolarization greater than 0.12 represent snow falling into a melting layer or depolarization caused by multiple scattering in a dense water layer.

Based on this plot, all data points with depolarization greater than 0.17 have been classified as signal returns from ice clouds. Data points with depolarizations between 0.12 and 0.17 are identified as mixed phase clouds and points less than 0.12 are identified as water.

Figure 2 shows the probability distribution of backscatter cross sections observed in this experiment. Clouds are separated into ice, water and mixed phase clouds.

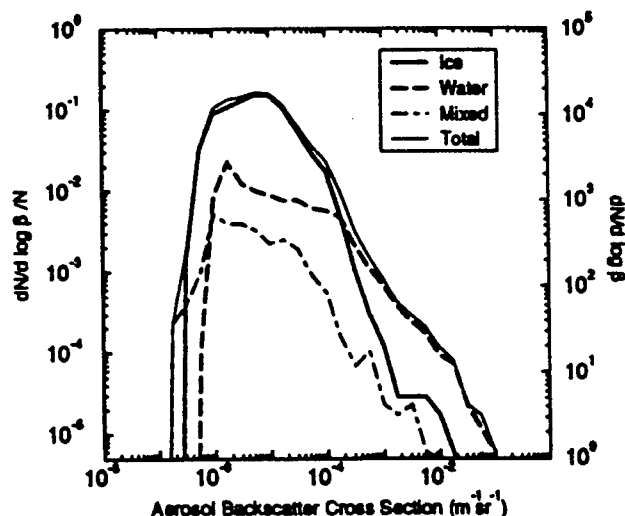


Figure 2. The probability distribution of backscatter cross sections in clouds measured in the current experiment. Only data points where the ratio of aerosol to molecular backscatter is greater than one are presented. Separate plots are shown for ice, water and mixed phase clouds. A combined curve for all cloud types is also presented.

Figure 2 shows a backscatter cross section of approximately $10^{-6} m^{-1} str^{-1}$ for most cirrus clouds. Very few cirrus clouds have backscatter cross sections of greater than $10^{-4} m^{-1} str^{-1}$. The probability of occurrence of water clouds continues to rise as the backscatter cross section decreases. This is due the presence of aerosol scattering in the profiles. Most aerosol particles are small solution droplets which generate small depolarizations and are thus classified as water clouds in this study. Probability distributions computed with a scattering ratio threshold of 0.1 show that the number of ice clouds continues to decrease with decreasing cross section and that the number of water clouds continues to increase.

Because observation days were selected on basis of cirrus cloud cover the combined probability distribution shows much smaller contributions from water clouds than would be found in an unbiased sample.

5. Other results

The oral paper will also present probability distributions of optical depth measurements, cloud altitudes and cloud temperatures. Measurements of multiply scattered lidar signals will be presented along with particle size measurements derived from these observations. Preliminary results from the recent SBIRS intensive observation period will also be presented.

-
1. S. T. Shipley, D.H. Tracy, E. W. Eloranta, J. T. Trauger, J. T. Sroga, F. L. Roesler, and J. A. Weinman, "High resolution lidar to measure optical scattering properties of atmospheric aerosols. 1: Theory and instrumentation," *Appl. Opt.* **22**, 3716-3724 (1983)
 2. P. K. Piironen, and E. W. Eloranta, "Demonstration of a high-spectral resolution lidar based on an iodine absorption filter," *Opt. Lett.* **19**, 234-236 (1994).
 3. C. J. Grund, and E. W. Eloranta, "University of Wisconsin High Spectral Resolution Lidar," *Optical Engineering* **30**, 6-12 (1991).
 4. K. Sassen, "The polarization technique for cloud research: a review and current assesment", *Bull. Am. Soc.*, **72**, 12, 1848-, (1991).

An Error Analysis for High Spectral Resolution Lidar Measurements

E. W. Eloranta and P. Piironen

University of Wisconsin

1225 W. Dayton Street, Madison, Wisconsin 53706, USA

Phone: 608-262-7327 · Fax: 608-262-5974

Email: eloranta@lidar.ssec.wisc.edu, paivi@hsrl.ssec.wisc.edu

The University of Wisconsin High Spectral Resolution Lidar (HSRL) provides calibrated vertical profiles of the backscatter cross section, extinction cross section, depolarization, and optical depth.^{1,2} Unlike values obtained from conventional lidars, these measurements do not require a priori assumptions relating backscatter and extinction cross sections and they do not involve numerically unstable inversion algorithms.

The HSRL divides the received lidar return into separate aerosol and molecular signals with two receiver channels. A beam splitter sends part of the received light directly to a photomultiplier tube. The rest of the light is directed through an I_2 absorption filter before it is detected with a second photomultiplier. Only the Doppler broadened spectral wings of light scattered by air molecules pass through the I_2 filter while both aerosol and molecular signals reach the other detector.^{2,3}

The molecular backscatter from an aerosol free atmosphere can be calculated using an independently measured temperature profile and Rayleigh scattering theory. Thus, a comparison of the observed molecular lidar return and the computed molecular backscatter profile provides a direct measurement of the optical depths between all points in the lidar profile. The derivative of the optical depth curve provides the extinction cross section. The aerosol backscatter cross section is determined from the ratio of the measured aerosol backscatter to the measured molecular backscatter multiplied by the computed molecular cross section. Separate depolarization measurements are made for aerosol and molecular signal components.

Since the derivation of optical parameters does not require the use of an assumed backscatter/extinction relationship, it is possible to rigorously compute confidence limits on all measurements. This poster will provide estimates of errors introduced into HSRL measurements by: 1) Photon statistics, 2) Uncertainties in the assumed atmospheric temperature profile, 3) Uncertainties in the spectral bandpass of the filter used to separate the aerosol and the molecular signals, 4) Nonlinearities

in photon counting caused by photomultiplier after-pulsing and pile up, and 5) Range dependent errors caused by misalignment between the receiver field of view and the transmitted laser beam.

Figure 1 shows a typical time altitude cross section of calibrated backscatter cross section measurements from the HSRL. Profiles derived from this data set will be used in the error analysis.

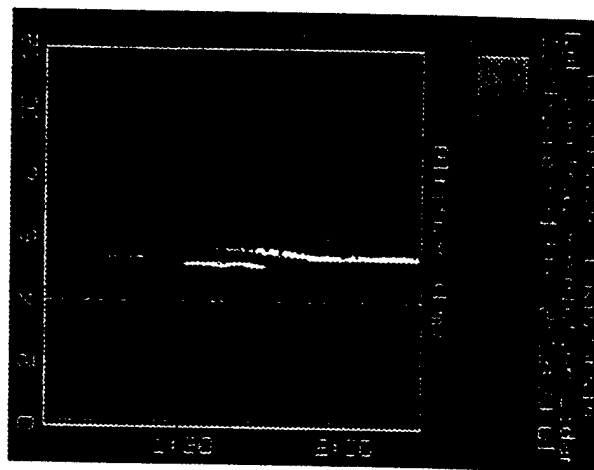


Figure 1. An altitude vs time plot of the calibrated backscatter cross section observed on November 11, 1993 between 1:05 and 2:13 UT. A cirrus cloud is seen between the altitudes of 6.5 and 10 km. Ice crystal virga between 4 and 5.5 km is seen falling from an altostratus water cloud near 5.5 km.

Figure 2 presents the molecular lidar return derived from the HSRL measurements. Computations of the errors introduced by photon statistics in the I_2 absorption filter channel (labeled M) and the combined aerosol and molecular channel (labeled A+M) are also shown. The curves labeled C_{am} and C_{mm} show errors introduced by uncertainties in the spectral line shape of the backscatter spectrum and the spectral transmission of the two HSRL data channels. For altitudes between 4 and 12 km the errors are dominated by photon statistics. Below 4 km the accuracy is limited by errors in C_{mm} . The C_{mm} error is dominated by uncertainty in the Doppler width

of the backscattered spectrum caused by errors in the temperature profile. We have assumed a 5°K temperature error because we used the Green Bay, WI radiosonde temperature profile. It was measured $\sim 190\text{ km}$ from our Madison, WI site. The error was estimated by comparing a series of soundings from Green Bay, WI which is NE of Madison with simultaneous soundings from Peoria, IL which is $\sim 270\text{ km}$ SSW of Madison.

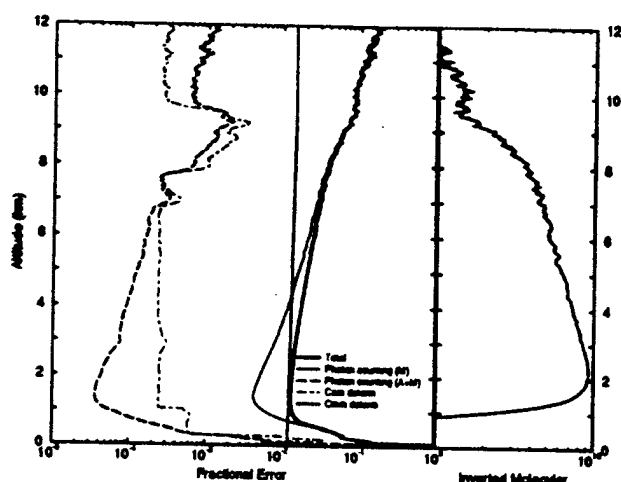


Figure 2. Contributions to the error in the molecular lidar return computed from HSRL signals measured between 1:05 and 1:08 UT on November 11, 1993. The right panel shows the molecular lidar return as a function of altitude. The left panel shows the fractional errors introduced from various sources. Between 8 and 9.5 km the molecular return decreases rapidly due to attenuation in the cirrus cloud.

Figure 3 shows the optical depth and contributions to the error in the optical depth for the data shown in figures 1 and 2. Above 6.5 km the error is dominated by uncertainties in the number of photons counted in the I_2 filter channel (labeled M in the figure). Below the cloud, where the extinction cross section is very small, the error is dominated by uncertainty in the Rayleigh backscatter profile computed from the temperature profile. Attenuation is measured from the difference between the computed and the observed molecular profiles. When attenuation is small these differences are small and the fractional error becomes large. The C_{mm} uncertainty is primarily caused by errors in the spectral width of the backscattered signal. It also provides significant errors in the low altitude part of this profile. This is also due to the 5°K error in temperatures caused by the distant temperature sounding. Errors caused by photon statistics in the combined aerosol-molecular channel and the C_{am} term produce negligible effects in this case.

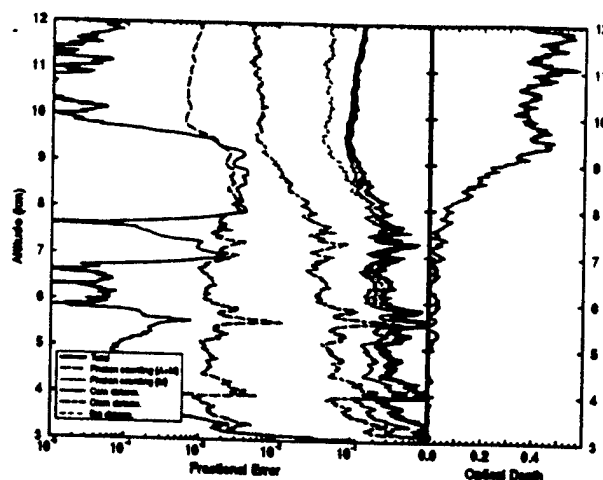


Figure 3. Contributions to error in the optical depths measured between 1:05 and 1:08 UT on November 11, 1993. The optical depth as a function of altitude is shown on the right. The left panel shows the fractional error introduced by various sources.

Currently, HSRL errors are dominated by uncertainties caused by photon counting statistics and errors in the atmospheric temperature profile. Both of these can be reduced in future measurements. The average power transmitted by the HSRL was only $\sim 100\text{ mW}$ when these measurements were acquired. We have since increased the power to $\sim 200\text{ mW}$ and future systems are likely to emit several Watts. Radiosonde temperature uncertainties are normally assumed to be $\sim 1^\circ\text{K}$ instead of the 5°K we have assumed for our profiles which were acquired at a distance of $\sim 190\text{ km}$. A local temperature sounding will reduce this error source.

Acknowledgments

Support for this work has been provided by Department of Energy grant DE-FG02-90ER61058 and Office of Naval Research grant N00014-91-J-1558. Support to P.K. Piironen was provided by the Foundation of Maj and Tor Nessling, and the University of Joensuu, Finland.

References:

1. Grund, C.J. and E.W. Eloranta, 1991: The University of Wisconsin High Spectral Resolution Lidar, *Optical Engineering* 30, 6-12.
2. Piironen, P. and E. W. Eloranta, 1994: Demonstration of an iodine absorption filter based high spectral resolution lidar, *Optics Letters*, 19, 234.

3. Eloranta, E. W. and P. Piironen, High Spectral Resolution Lidar Measurements of Extinction and Particle Size in Clouds., *Conference on Optical Remote Sensing of the Atmosphere* Feb. 3-12, 1995, Salt Lake City, UT.

DEPOLARIZATION MEASUREMENTS WITH THE HIGH SPECTRAL RESOLUTION LIDAR

E. W. Eloranta and P. Piironen

University of Wisconsin

1225 W. Dayton Street, Madison, Wisconsin 53706, USA

Phone: 608-262-7327 Fax: 608-262-5974

Email: eloranta@lidar.ssec.wisc.edu, paivi@hsrl.ssec.wisc.edu

Many investigators have used depolarization of lidar returns to characterize atmospheric particles¹. This paper describes modifications to the University of Wisconsin High Spectral Resolution Lidar which permit very precise depolarization measurements in addition to optical depth, backscatter cross section, and extinction cross section measurements made by the instrument^{2,3}.

The HSRL rotates the polarization of the transmitted laser pulse by 90° on every other pulse (see figure 1). This allows measurement of the parallel and cross polarized lidar returns without the use of separate detectors for the two polarizations. The parallel return is measured on the first pulse and the perpendicular return on the second pulse. The HSRL operates at a pulse repetition rate of 4 kHz. The parallel and perpendicular returns are summed in separate buffers. Each profile consists of the sum of 4000 pulses of each polarization. Since only 250 μ s separates individual laser pulses, it is possible to compute depolarizations from successive pulses without having the wind change the particles in the sample volume. Because the optical path and detector are the same for both polarizations, the depolarization ratios can be measured without the need to calibrate the relative sensitivity of the two channels.

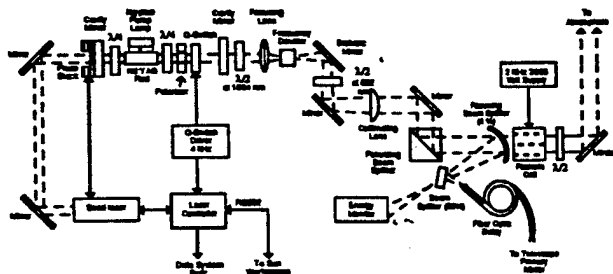


Figure 3. The transmitter section of the HSRL. The transmitted polarization is rotated by 90° between successive pulses by a Pockels cell.

Accurate measurements depend only on the linearity of the detector, the polarization purity of the transmitter, and the cross polarized leakage of the receiver polarization filter. The photon counting system of the HSRL is very linear. Pile-up and after-pulsing corrections are applied to all data; however, low after-pulsing

photomultipliers and high bandwidth counting electronics make the corrections very small for all returns except those from dense low altitude water clouds. Measurements of the polarization of the laser output show residual cross-polarizations of $\sim 0.1\%$ when measured with a polarization cube which is specified to have a 0.1% cross polarization rejection. Model calculations suggest that the cross polarization response of the receiver is also less than 0.1% with the major portion of the error resulting from the ellipticity of light reflected from the primary and secondary aluminized mirrors of the 0.5 m diameter Dall-Kirkham receiving telescope. Thus, although we have not devised a rigorous experimental test of the total cross polarization leakage in the system, we expect that it is $\sim 0.1\%$.

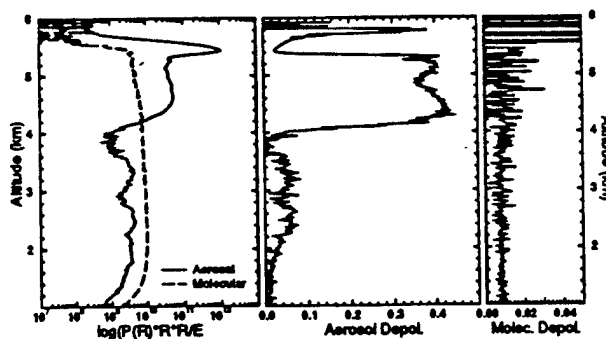


Figure 2. Range-squared corrected aerosol and molecular lidar returns from aerosols (0 - 4 km), ice crystal virga (4-5.2 km), a water cloud (5.4-5.7 km) and a cirrus cloud (5.7-5.8 km) are shown on the left. Particulate depolarizations are shown in the center and molecular depolarizations on the right.

Because the HSRL separates the lidar return into aerosol and molecular contributions, the aerosol and molecular depolarizations can be measured separately. Figure 2 shows separated aerosol and molecular profiles observed with the HSRL on November 11, 1993 between 1:55 and 2:01 UT. Ice crystal virga (at altitudes between 4.0 and 5.2 km) is falling out of a thin water cloud located at altitudes between 5.4 and 5.7 km. Below 4 km, the backscatter from aerosols is weaker than from molecules. The depolarization of the ice is nearly constant between 34% and 42%. At the base of the wa-

ter cloud the depolarization drops to 2% as result of scattering from spherical droplets. Higher in the cloud the depolarization increases, apparently as the result of multiple scattering and the presence of ice. Because the HSRL receiver field of view is only $160 \mu\text{radians}$, multiple scattering depolarization appears to be under 10% in nearly all clouds we have observed. The 30% depolarization at the top of the water cloud is due to the presence of ice at the cloud top. Figure 3 summarizes the depolarizations measured in clouds on 14 days between Aug. 2 and Nov 11, 1993. High depolarization ratios easily distinguish ice clouds from water clouds which produce much smaller depolarization.

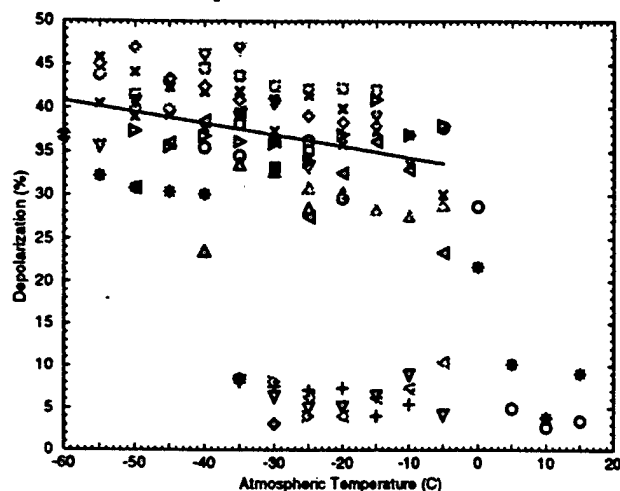


Figure 3. Depolarization as a function of temperature for particulate scattering in clouds.

Notice that all clouds colder than the -40°C homogeneous nucleation temperature of water are ice. Above 0°C all returns show low depolarizations. Although spherical water droplets are expected to yield no depolarization from single scattering, this plot shows depolarizations up to 10% in clouds which appear to be water clouds. Since many of these clouds are observed to have ice crystal virga falling from their bases, it is apparent that at least part of the increased depolarization is due to ice in mixed phase clouds. For mixed phase clouds the scattering from water droplets dominates the scattering cross section; thus, the depolarization is closer to that of pure water clouds than of cirrus. Inside water clouds we see a characteristic increase of depolarization with penetration depth caused by the presence of multiple scattering. For cases studied thus far, it appears that the $160 \mu\text{radian}$ angular field of view of the HSRL limits multiple scattering induced depolarization to less than 10% in water clouds. We are surprised to find no water cloud depolarizations less than 0.8%, although it is clear that the HSRL can detect smaller values.

The molecular depolarization measured by the HSRL is constant at a value of 0.7% to 0.8% when viewed with a 1 nm filter bandpass. This is larger than expected

for Cabanne line depolarization since the filter admits a small fraction of the closest rotational Raman lines and the I_2 filter of HSRL blocks the center of the Cabanne line³. When the filter is removed and the laser is tuned off the I_2 filter, rotational Raman scattering increases the molecular depolarization increases to 1.5%.

With traditional lidars, aerosol depolarization measurements are complicated by the presence of molecular scattering which often dominates the received signal in clear air. Since the HSRL separately measures the aerosol depolarization, accurate measurements can be obtained. Figure 4 presents a histogram of aerosol depolarizations observed below the clouds from the data set used to compile figure 3.

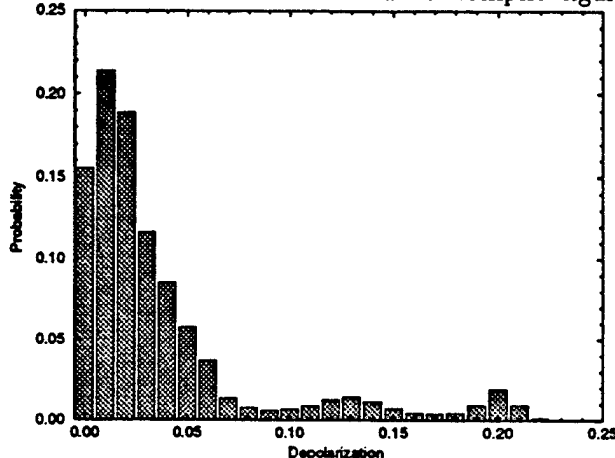


Figure 4. The probability of occurrence of depolarizations for aerosol scattering between altitudes of 500 m and cloud base. Data points consist of 5 min averages of data in 15 m range bins. Statistics include only points with backscatter ratios greater than 0.2.

ACKNOWLEDGMENTS

This work was supported by grants from the Office of Naval Research (N00014-91-J-1558) and the National Aeronautics and Space Administration (NAG-1-882).

REFERENCES

1. Sassen, K., 1991: The Polarization Lidar Technique for Cloud Research: A Review and Current Assessment, *Bulletin of Am. Meteor. Soc.*, 72, 1848.
2. Grund, C.J., and E.W. Eloranta, 1991: University of Wisconsin High Spectral Resolution Lidar, *Optical Engineering*, 30, 6-12.
3. Piironen, P. and E. W. Eloranta, 1994: Demonstration of an iodine absorption filter based high spectral resolution lidar, *Optics Letters*, 19, 234.
4. Eloranta, E. W. and P. Piironen, 1994: *Proceedings of the 17th ILRC*, July 25-29, 1994, Sendai Japan.

HIGH SPECTRAL RESOLUTION LIDAR MEASUREMENTS OF MULTIPLE SCATTERING.

E. W. Eloranta and P. Piironen

University of Wisconsin

1225 W. Dayton Street, Madison, Wisconsin 53706, USA

Phone: 608-262-7327 Fax: 608-262-5974

Email: eloranta@lidar.ssec.wisc.edu, paivi@hsrl.ssec.wisc.edu

Calculations show that the multiply scattered lidar signal is strongly dependent on: 1) the angular Field Of View (FOV) of the receiving telescope, 2) the small angle forward peak in the scattering phase function and 3) the scattering cross section profile in the cloud. If the scattering cross section profile can be measured, multiple scattering measurements may allow measurement of the forward diffraction peak width. This would provide particle size information. Traditional aerosol lidar systems do not provide sufficient information to measure the extinction or backscatter cross section without using assumed relationships between the backscatter and extinction cross section. A boundary value specifying the extinction at one point in the cloud is also required.

The University of Wisconsin High Spectral Resolution Lidar (HSRL) provides unambiguous measurements of backscatter cross section, backscatter phase function, depolarization, and optical depth^{1,2}. This is accomplished by dividing the lidar return into separate particulate and molecular contributions. The molecular return is then used as a calibration target. We have modified the HSRL to use an I₂ molecular absorption filter to separate aerosol and molecular signals². This allows measurements in dense clouds. Useful profiles extend above the cloud base until the two-way optical depth reaches values between 5 and 6; beyond this, photon counting errors become large. The spectrometer channels have a 0.16 mr FOV; the small FOV suppresses multiple scattering errors in the retrieved optical parameters.

In order to observe multiple scattering, the HSRL includes a channel which records the combined aerosol and molecular lidar return simultaneously with the spectrometer channel measurements of optical properties. The angular field of view of this Wide Field Of View (WFOV) channel is controlled by the system computer and it can be adjusted from 0.22 mr to 4 mr. This channel is rapidly sequenced between several aperture sizes to record the FOV dependence of the lidar return. The system calibration and signals recorded in the spectrometer channels are sufficient to allow removal of the molecular return from the WFOV signal. The depolarization of light received in the WFOV channel is also measured.

HSRL measurements from a water cloud are shown in

figure 1. The lidar returns in the WFOV channel divided by the return in the 0.16 mr spectrometer channel are plotted. The measured backscatter cross section profile is also shown. The increased contribution of multiple scattering with increased field of view is easily seen.

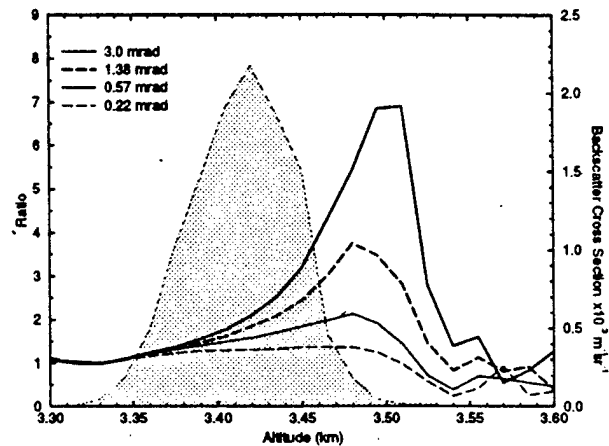


Figure 1. Ratios of the WFOV signals to the signal in the 0.16 mrad spectrometer channel. WFOV acceptance angles of 0.22, 0.57, 1.38 and 3.0 mrad are shown. The backscatter cross section is shaded.

This paper describes HSRL multiple scattering measurements from both water and ice clouds. These include signal strengths and depolarizations as a function of receiver field of view. All observations include profiles of extinction and backscatter cross sections. Measurements are also compared to predictions of a multiple scattering model based on small angle approximations.

Acknowledgements

This work was supported by grants from the Office of Naval Research (N00014-91-J-1558) and the National Aeronautics and Space Administration (NAG-1-882).

References

1. Grund, C.J., and E.W. Eloranta, 1991: University of Wisconsin High Spectral Resolution Lidar, *Optical Engineering*, 30, 6-12.
2. Piironen, P., and E. W. Eloranta, 1994: Demonstration of an iodine absorption filter based high spectral resolution lidar, *Optics Letters*, 19, 234.

Remote Particle Size Measurements with the University of Wisconsin High Spectral Resolution Lidar

E.W. Eloranta and P.K. Piironen
University of Wisconsin
1225 W. Dayton
Madison, Wisconsin 53706

This paper presents computations and preliminary measurements demonstrating the possibility of remotely measuring particle sizes in clouds with the University of Wisconsin High Spectral Resolution Lidar(HSRL). Particle size measurements are based on observations of multiply scattered contributions to the HSRL return.

Calculations show that the multiply scattered lidar return is dependent on the angular field of view of the lidar receiver. As the receiver field of view increases, the multiply scattered contribution to the lidar return increases. The rate at which this increase occurs is dependent on: 1) the beam divergence of the laser transmitter, 2) the range dependence of the scattering cross section in the cloud, 3) and the scattering phase function of the cloud particles. The HSRL provides direct measurements of the scattering cross section which are not available from conventional lidars. Models show that the multiply scattered lidar return variation with receiver field of view is strongly dependent on the angular width of the forward diffraction peak in the scattering phase function. For scattering from a particle of diameter, d , which is large compared to the wavelength, λ , the angular width of the phase function, $\Theta \sim \lambda/d$. Thus, measurements of the diffraction peak width offer information about particle size. Previous studies of the solar aureole suggest that under favorable conditions as many as 5 independent pieces of information on the particle size distribution may be derived from measurements of the forward diffraction peak. Much of this information is potentially available from the multiply scattered lidar return.

This paper presents comparisons between HSRL observations of multiple scattering and model results. The dependence of multiple scattering on particle size is demonstrated and the potential applications of this measurement approach are discussed.

VISIBLE AND INFRARED RADIATIVE RELATIONSHIPS AS MEASURED BY SATELLITE AND LIDAR

Donald Wylie, Walt Wolf and Edwin Eloranta

University of Wisconsin-Madison
Madison, WI 53706

1. INTRODUCTION

The impact of cirrus clouds on the heat balance of the earth is dependent on their reflectivity of solar radiation and their absorptivity of terrestrial radiation. These clouds can either contribute to radiative warming or cooling depending on the ratio of their visible reflectance to their infrared absorption. Any prediction of cloud cover changes that accompany climate change, will have to know whether the visible/IR radiative characteristics of the clouds will also change. Few measurements of cirrus have been made where data from both the visible and IR were collected simultaneously. Most cloud studies have used only one portion of the spectrum.

The best studies of the visible and IR radiative properties of ice clouds have been Platt (1979) using a vertically pointing IR radiometer next to a visible lidar and Minnis et al. (1990) which combined satellite and lidar data. Platt (1979) studied several cases of cirrus clouds and found a ratio of the visible/IR optical depths of 2.0:1. Minnis et al. (1990) studied one case from the FIRE experiment and found the visible/IR ratio to be slightly higher, 2.1:1. Modelling of radiative properties of ice crystals suggest that the visible/IR ratio can vary from 1.8 to 4.0 (Minnis et al., 1993).

One of the largest problems for any cirrus cloud study is the large spatial variability of clouds. Vertically pointing lidars sample only the part of the cloud that drifted over them while satellites see the gradients in the horizontal field. Lidars have a very narrow beam, < 1 m in width while satellite radiometers have field of views (FOV) of 1 to 20 km. For this study, we used a scanning lidar to make volume imagery of cirrus clouds similar to the satellite view of the clouds.

2. MEASUREMENT TECHNIQUE

To obtain the visible optical depths of cirrus, the High Spectral Resolution Lidar

(HSRL) and the Volume Imaging Lidar (VIL) of the University of Wisconsin-Madison were used. The HSRL is a unique instrument that measures the backscatter of the lidar pulse by particulate matter separately from the backscatter of air molecules. A spectrally narrow pulse of 0.6μ from a NdYg lidar is transmitted. The returning radiation scattered by air molecules will be spectrally doppler broadened while that from particles will not. Measurements of both the doppler broadened and non-broadened backscatter are made. The backscatter from air molecules allows a direct determination of the strength of the lidar pulse reaching each level of the cloud. Extinction and optical depth of the cloud can be determined without assumptions of the attenuation along the beam path. More precise measurements of the visible radiative quantities of the clouds can be made this way.

To understand radiative scattering in clouds, the large horizontal and vertical variations in cloud structure have to be measured. The HSRL lidar samples only a small portion of the cloud - a column about 30 centimeters wide. The GOES satellite IR sensors have a horizontal resolution of 10.8 km at Madison, WI. To account for FOV differences, the horizontal structure of the clouds were measured by the VIL.

The VIL produced visible backscatter images of the clouds by scanning across the wind. Time advection was used to construct a horizontal image of visible backscatter from the VIL data over a one hour period. The HSRL was used to calibrate the VIL signal into backscatter cross sections of particulates. The backscatter cross sections were related to extinction by a constant backscatter phase function determined from the HSRL data. This process produced a three dimensional image of visible extinction in the cirrus clouds over a one hour period.

The extinction volume image was then transformed to an image of optical depth in the same viewing geometry as the

GOES satellite. Optical depths were formed from the integral of extinction along the path in which the GOES scanner view this volume. The optical depth image was originally produced with a 1 km (satellite nadir) resolution. This image was then shifted to align with the satellite IR image to account for error in the satellite registration system. The lidar visible optical depth image then was averaged to an 8 km (satellite nadir) image for direct comparison to the satellite IR image. This gave coincident fields of views from both satellite and lidars in the same geometry with a horizontal resolution of 10.8 km per pixel.

IR optical depths were extracted from the GOES image using calculations of the IR transmittance of the clouds using the IR radiance of the cloud, the radiance of cloud free FOV's and radiances calculated from the temperature of the mean vertical level of the cloud. The VIL data were used to determine the cloud level. Rawinsonde observations were made at Madison at the same time as these data.

All data were taken in the vicinity of Madison, WI on 1 December, 1989. The VIL was located 24 km west of the HSRL. The VIL scanned both crosswind and nearly downwind over the HSRL. Data were taken from 19:35 UTC (13:35 Local) to 21:20 UTC (15:20 L). During this time a large mass of cirrus clouds moved in from the west-northwest with an approaching cold front. Madison, WI was under cloud free sky during the morning and proceeded to total overcast by the end of this period. Two lidar images were constructed from 1 hour records. More details on the data taken can be found in Ackerman et al. (1993).

3. RESULTS

An example of the structure of the clouds from the VIL is shown in Figure 1. A thick cloud mass from 6.8 to 9.0 km is apparent from 8 km south to 20 km north of the VIL. Other thin broken layers are apparent both north and south of the large mass. This is typical of the different forms of cirrus sampled on 1 Dec, 89. The first clouds to reach Madison were vertically thin and horizontally broken. A few dense lines with evidence of precipitating virga also were found in the VIL volume. Later thicker

cirrus moved in with virga that spanned the 2.2 km shown in Fig. 1.

The satellite and VIL image was divided into regions of similar cloud characteristics. The VIL cross sections were used as the primary division tool. The GOES image had little detail in the IR. The lidar visible optical depth image at 1 km showed many line and sheet structures. Cloud thickness, the presence of multiple layers and the intensity of precipitating virga were used to segregate different cloud forms.

The visible/IR optical depths are shown in Fig. 2. Most of the data are near the 2:1 line shown in the image. These data loosely agree with theory and the other past measurements. However, the visible/IR optical depth ratio appears to increase for thicker precipitating cirrus. Clouds with dense precipitating virga have ratios below the 2:1 line (visible/IR > 2). Cloud areas of highest reflectivity had solid lidar returns over 2 km depth with occasional embedded layers of extremely high reflectivity. The horizontal variations in cloud reflectivity were seen in the IR satellite imagery but with far less detail than the lidar images. The lower resolution of the satellite IR sensor smoothed some of these variations. However, the lidar data show that visible reflectivity had wide range of values with large vertical and horizontal detail.

4. REFERENCES

- Ackerman, S. A., E. W. Eloranta, C. J. Grund, R. O. Knuteson, H. E. Revercomb, W. L. Smith and D. P. Wylie, 1993: University of Wisconsin Remote Sensing Pilot Experiment. Bull. A.M.S.
- Minnis, P., D.F. Young, K. Sassen, J.M. Alvarez and C.J. Grund, 1990: The October 27-28 1986 FIRE IFO Cirrus Case Study: Cirrus parameter relationships derived from satellite and lidar data. Mon. Wea. Rev., 118, 2402-2425.
- Minnis, P., K.N. Liou and Y. Takano, 1993: Inference of cirrus cloud properties using satellite-observed visible and infrared radiances. Part I: Parameterization of radiance fields, J. Atm. Sci., 50, 1279-1304.

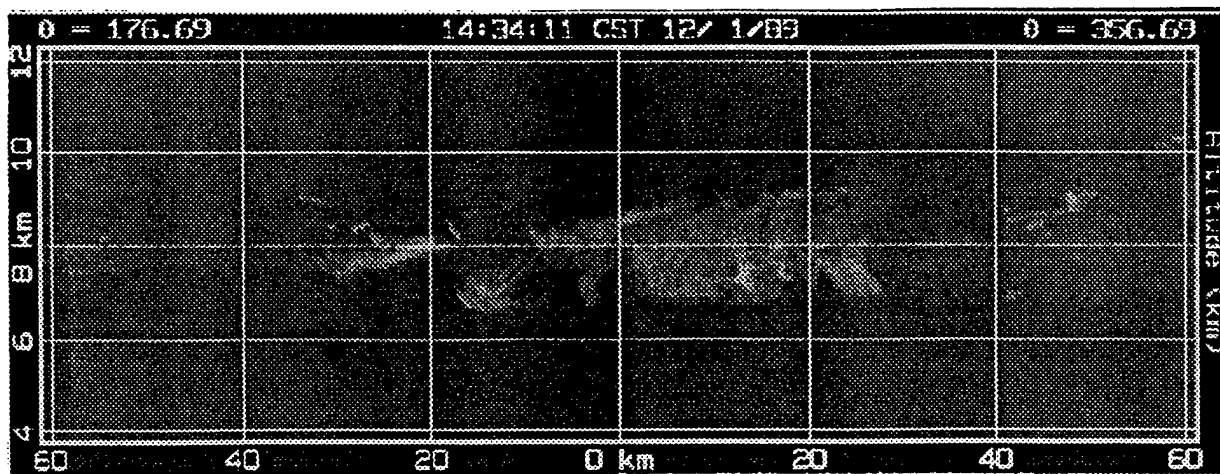


Figure 1: A Volume Imaging Lidar (VIL) cross wind section taken at 20:34 UTC (14:34 local). Scan directions were azimuths of 177° and 357° . Orientation is south to north.

VAS - VIL Optical Depth Comparison

December 1, 1989 (19:35-21:20 GMT)

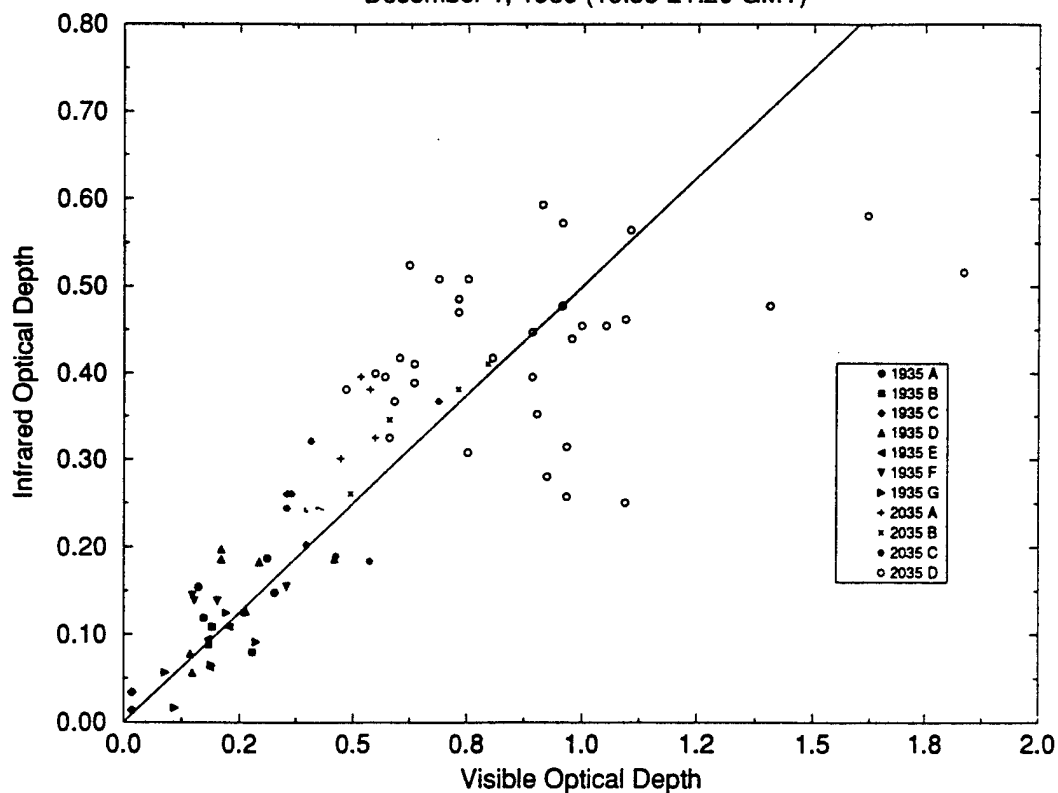


Figure 2: Scatter plot of the visible and IR optical depths of cirrus clouds using coincident lidar and satellite data.

An I₂ absorption filter based High Spectral Resolution Lidar for measurement of the optical properties of aerosols and clouds

Edwin W. Eloranta and Paivi Piironen

University of Wisconsin

1225 W. Dayton St.

Madison, WI 53706

Tel 608-262-7327

FAX 608-262-5974

EMAIL eloranta@lidar.meteor.wisc.edu

Submit to:

Atmospheric Propagation and Remote Sensing III

Chair: Walter A. Flood

Presentation: Oral

Standard lidar returns contain insufficient information to measure scattering or extinction cross sections without recourse to questionable assumptions. The University of Wisconsin High Spectral Resolution Lidar (HSRL) addresses this problem by dividing the lidar signal into separate molecular and aerosol returns. The molecular return is then used as a calibration target. Thermal motions of the molecules Doppler broaden the molecular return and this spectral difference is used to separate it from the aerosol return. In the past, a 15 cm diameter Fabry-Perot etalon operating at a spectral resolution of more than 10^6 separated the spectrally broadened signal. This worked well for studies of clear air aerosols and thin cirrus clouds. However, in dense

clouds aerosol scattering becomes $\sim 10^3$ larger than molecular scattering. In these cases the spectral transmission of the etalon must be known to at least 1 part in 10^4 ; otherwise, the signals can not be completely separated. Since drift of the Fabry-Perot etalon produced errors of ~ 1 part in 10^3 , it was not possible to probe dense clouds.

To overcome this problem, we have replaced the Fabry-Perot etalon with an I_2 molecular vapor absorption filter. This 43 cm long room temperature filter transmits only 0.08% of the aerosol return to the molecular channel. Since this cross talk is very stable, aerosol and molecular components can be separated in dense clouds. Successful operation is achieved for two-way optical depths up to 6. This paper will describe the new HSRL configuration which thermally tunes an injection-seeded, frequency-doubled Nd-YAG laser to an I_2 absorption line. Frequency control is maintained by a digital servo loop which monitors laser light transmitted through a second absorption cell. The system also employs a unique scheme which provides depolarization measurements with errors as small as 0.1%. A separate receiver channel simultaneously measures the changes in received signal as a function of the angular field of view of the receiving telescope. This channel provides measurements of multiply scattered return which yields particle size measurements.

The new HSRL configuration has been used to observe a wide variety of atmospheric targets. Measurements of backscatter cross section, optical depth, depolarization, backscatter phase function and particle size will be presented.

Biography: Dr. Edwin W. Eloranta is a senior scientist at the University of Wisconsin-Madison. His degrees, awarded by the University of Wisconsin, are: BS, Physics 1965, MS, Meteorology 1967, and PhD, Meteorology 1972. He is a fellow of the American Meteorology Society.

A Practical Model for the Calculation of Multiply Scattered Lidar Returns

Edwin W. Eloranta
University of Wisconsin
1225 W. Dayton
Madison, Wisconsin 53706

Introduction

Lidar results are typically analyzed using an equation which assumes all photons contributing to the return have been singly scattered. Lidar pulses returned from clouds often encounter large optical depths within a short distance of the cloud boundary and many of the received photons are likely to result from multiple scattering. This paper presents an equation to predict the multiply scattered return. The equation is easy to solve on a small computer and allows specification of the scattering cross section and the scattering phase function as a function of penetration depth into the cloud. Atmospheric clouds are made of particles large compared to the wavelength of visible and near infrared lidars. Optical absorption by particles is typically negligible at these wavelengths. The solution derived in this paper applies to these conditions. The derivation is an approximation which considers only the contribution due to multiple small angle forward scatterings coupled with one large angle scattering which directs the photon back towards the receiver.

Scattering phase function

The phase function is approximated as a Gaussian function of scattering angle for forward scattering events. This choice is convenient because after a series of small angle scatterings the spatial (or angular) distribution of photons remains a Gaussian. This fact considerably simplifies integration of the multiple scattering equations. A Gaussian phase function is specified by two parameters: a value at a scattering angle of zero, $P(0)$, and a mean square angular width, Θ_s^2 . When a computed, or measured phase function, $P_{true}(\theta)$, is available the parameters of the Gaussian approximation can be defined as:

$$\frac{P(\theta)}{4\pi} = \frac{P_{true}(0)}{4\pi} \exp\left(-\frac{\theta^2}{\Theta_s^2}\right) \quad (1)$$

where:

$$\Theta_s^2 = \frac{2}{P_{true}(0)}$$

This approximation provides a particularly robust description of the forward phase function since it provides correct values in the limiting cases. The phase function at zero scattering angle exactly matches the true value, $P(0) = P_{true}(0)$, and the area under the forward peak matches the value of expected by diffraction theory: $\int_0^{4\pi} \frac{P(\theta)}{4\pi} d\Omega = \frac{1}{2}$. The result of applying this approximation to the C1 model phase function calculated by Deirmendjian(1969) is shown in figure 1.

Near the backscatter direction the phase function is assumed to be isotropic. The value is a function of the order of scattering and is computed from a weighted average of the actual phase function values near 180°.

$$P_{n\pi}(R) = \frac{1}{n\pi} \int_0^\infty P(\pi - \theta, R) \int_{-d}^d \frac{1}{\Theta_s(x)^2} \exp\left(-\frac{\theta^2}{n\Theta_s(x)^2}\right) \beta_s(x) x dx d\theta \quad (2)$$

Where: n is the order of scattering, $\tau = \int_0^d \beta_s(x) dx$ and β_s is the scattering cross section per unit volume.

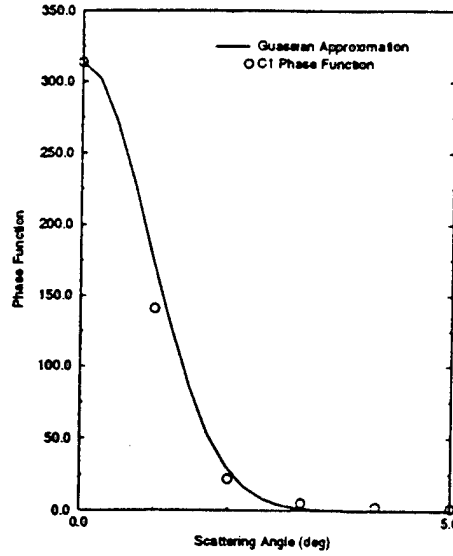


Figure 1. A comparison of the Gaussian approximation to the forward scatter phase function and the exact values computed by Deirmendjian for the C1 model particle distribution illuminated by a wavelength of 450 nm.

Multiple scattering geometry

This model assumes the lidar geometry shown in figure 2.

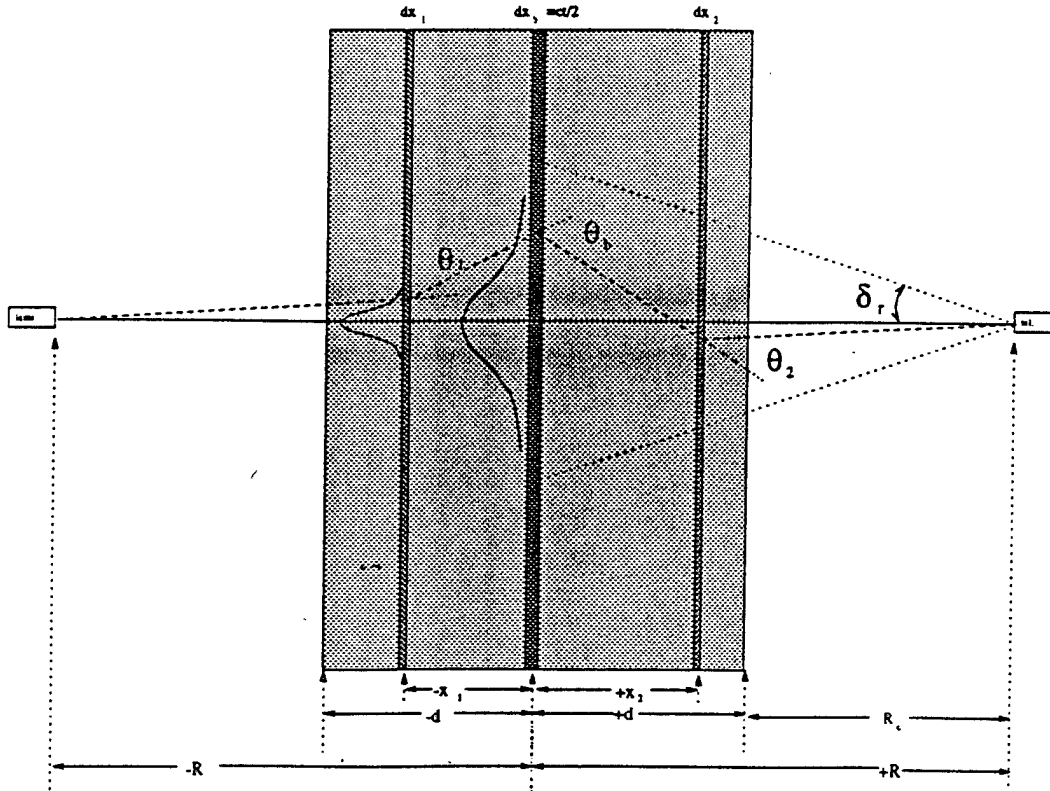


Figure 2. Multiple scatter geometry for a cloud located at a distance R_c from the lidar. For clarity of presentation the propagation path has been unfolded such that the photon return path is separated from the path of the outgoing pulse. In this coordinate system the single scattering slab is placed at the origin, the laser at $-R$ and the receiver at R .

δ_r = Receiver half angle field of view.
 $R = ct/2$ = Distance from the lidar to the single scatter event.
 t = Time after emission of the laser pulse.
 R_c = Distance from the lidar to the cloud base.
 Θ_s^2 = Mean-square angle for single scattering.
 d = Penetration distance into cloud = $R - R_c$.

Equation 3 describes the ratio of n^{th} order scattering, $P_n(R)$, to single scattering, $P_1(R)$. The derivation of this equation assumes: 1) a Gaussian forward scatter phase function described by equation 1. 2) a backscatter phase function which is isotropic near 180° and has a value given by equation 2. 3) the extra path length produced by the small angle deflections is negligible such that the multiply scattered return is not delayed with respect to the single scatter return. 4) the transmitted laser beam is a Gaussian function of angle. 5) multiply scattered photons returned to the receiver have encountered only one large angle scattering event.

$$\frac{P_n(R)}{P_1(R)} = \frac{P_{n\pi}(R)}{P(\pi, R)} \frac{1}{2^{n-1}} \int_{-d}^d \beta_s(x_1) \int_{x_1}^d \beta_s(x_2) \int_{x_2}^d \beta_s(x_3) \cdots \int_{x_{n-2}}^d \beta_s(x_{n-1}) \int_{x_{n-1}}^d \beta_s(x_n) \left(1 - \exp \left(- \frac{\delta_r^2 R^2}{x_1^2 \Theta_s^2(x_1) + x_2^2 \Theta_s^2(x_2) + \cdots + x_{n-1}^2 \Theta_s^2(x_{n-1}) + \delta_r^2 R^2} \right) \right) dx_1 dx_2 dx_3 \cdots dx_{n-1} \quad (3)$$

Where: $P(\pi, R)$ is the phase function at range, R , and a scattering angle of 180° and where the angular distribution of the laser beam is $\propto \exp(-\frac{\theta^2}{\delta_r^2})$.

Figure 3 shows calculations of lidar returns from a cloud with a base altitude of 5 km. The scattering cross section varies with penetration depth while the scattering phase function is assumed to be given by the Deirmendjian C1 model illuminated with a wavelength of 700 nm. The lidar is assumed to have a 5 mr receiver field of view and a transmitter divergence of 1 mr. (both full angles).

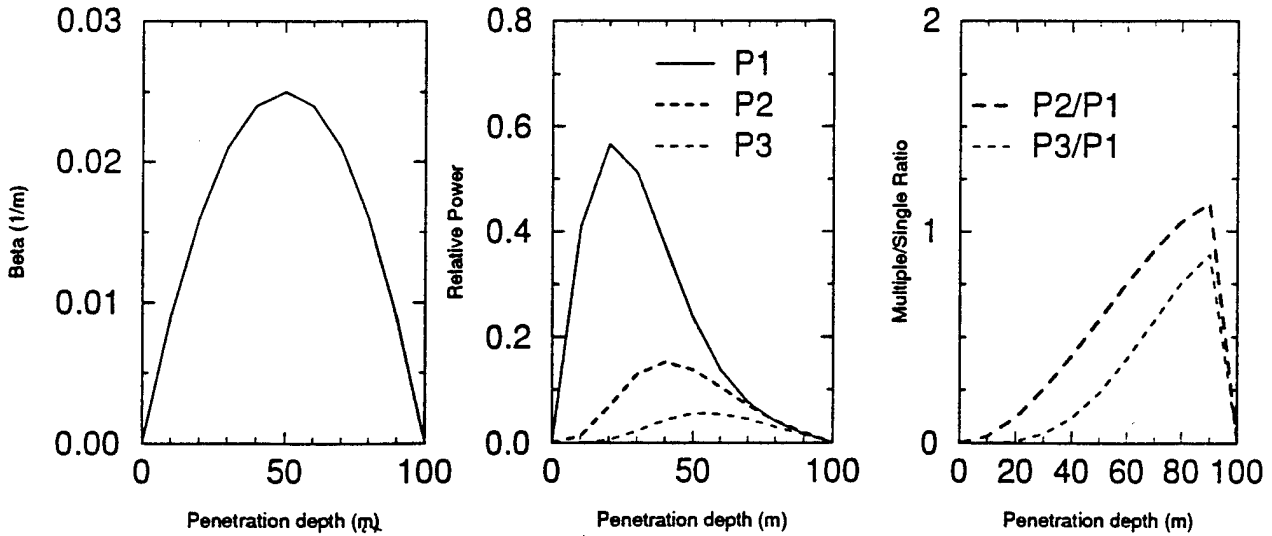


Figure 3. The first three orders of scattering from a cloud with a parabolic range distribution of scattering cross section. The left panel shows the range dependence of the scattering cross section. The center panel shows relative return powers in the first three orders of scattering and the right panel shows the ratios of second and third order scattering to single scattering. The backscatter phase function values for this case are independent of range and have values $\frac{P(\pi)}{4\pi} = .05$, $\frac{P_{2\pi}}{4\pi} = .035$ and $\frac{P_{3\pi}}{4\pi} = .034$

Second order multiple scattering can be computed by an exact integration over all possible double scatter combinations. The model presented above has been used to compute the double scatter contribution for the exact computations presented by Eloranta (1972). The results of this comparison are shown in figure 4.

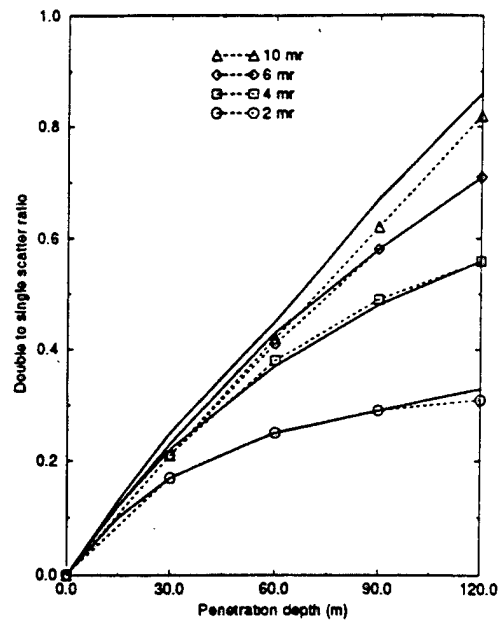


Figure 4. A comparison of small angle approximations and exact double scatter calculations for several receiver fields of view. The double scatter calculations are from Eloranta(1972). Results are for the following case: a cloud base altitude of 1 km, Deirmendjian C1 model phase function, transmitter full angle divergence of 1 mr, and a wavelength of 700 nm. The solid lines are the results of the current model with curves shown for receiver fields of view of 2 mr, 4 mr, 6 mr and 10 mr. Overlaid dashed lines with symbols show the exact values for the same fields of view.

Results obtained from equation 3 provide remarkable agreement with the exact calculations even though this model does not include contributions due to photons which encounter more than one large angle scattering. This is partially due to the fact that lidar receivers typically view a spot on the cloud base with a transverse dimension which has an optical depth of less than 1. Thus, photons scattered laterally are very likely to be outside of the field of view before a second scattering. The small value of the phase function for scattering angles near 90° makes their return into the field of view unlikely. For the narrow angular acceptance angles used in most lidar systems this approximate model for multiple scattering is also expected to provide accurate results for higher order scattering. In cases where the receiver views a spot on the cloud which has a transverse optical depth larger than 1, this approximation is expected to provide a lower bound to the contribution of each order of scattering.

Acknowledgements

Support for this work has been provided by Department of Energy grant DE-FG02-90ER61058 and Office of Naval Research grant N00014-91-J-1558.

References:

- Deirmendjian, D., 1969: *Electromagnetic Scattering on Spherical Polydispersions* Elsevier. New York
- Eloranta, E.W., 1972: *Calculation of Doubly Scattered Lidar Returns*. PhD thesis. University of Wisconsin, 115pp.

Initial Data from a New High Spectral Resolution Lidar

E.W. Eloranta and P.K. Piironen
University of Wisconsin
1225 W. Dayton
Madison, Wisconsin 53706

Introduction

The University of Wisconsin High Spectral Resolution Lidar (HSRL) has been recently redesigned for operation in an electronics semi-trailer van (ref 1). The HSRL can now be deployed in support of field experiments. This paper presents initial observations with the new configuration along with an analysis of measurement accuracy.

New measurement capabilities have been added; these include: observation of the signal variation with angular field of view, and observation of depolarization in all data channels. Depolarization measurements have been implemented by transmitting orthogonal linear polarizations on alternate laser pulses. Pulses are transmitted at 250 μ s intervals such that the lidar observes the same ensemble of particles for both polarizations. Orthogonal polarizations are measured with a single detector per channel (see figure 2). Since the optical components and detector gains are identical for the two polarizations the measured depolarization ratios are independent of these factors and the system delivers very precise depolarizations. A new data channel with a computer controlled aperture allows measurements of multiple scattering as a function of receiver field of view. Since the field of view variation is dependent on the size of the scattering particles it is expected that this will allow remote measurements of cloud particle size. Other technical improvements in the new system include active control of spectrometer temperatures, greatly increased mechanical stability, an increased receiver aperture, injection of calibration signals into the signal profiles to allow continuous monitoring of system calibration drifts, and extensive computer control of system operations.

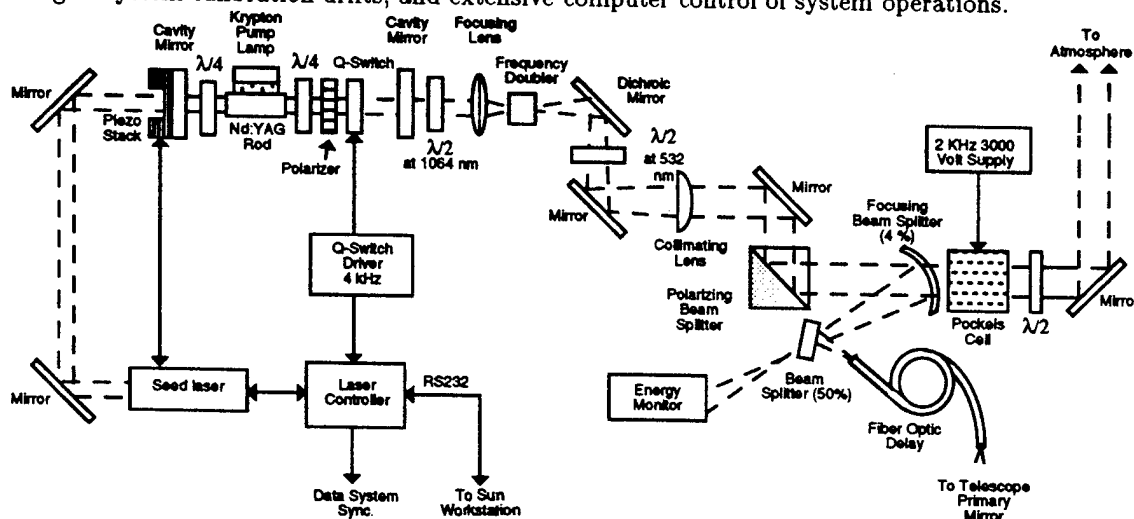


Figure 1: HSRL transmitter schematic. The transmitted polarization is rotated by 90° between successive laser pulses by a Pockels cell. A sample of each transmitted laser pulse is extracted by a beam splitter, delayed in an optical fiber and then injected into the receiver to monitor system calibration.

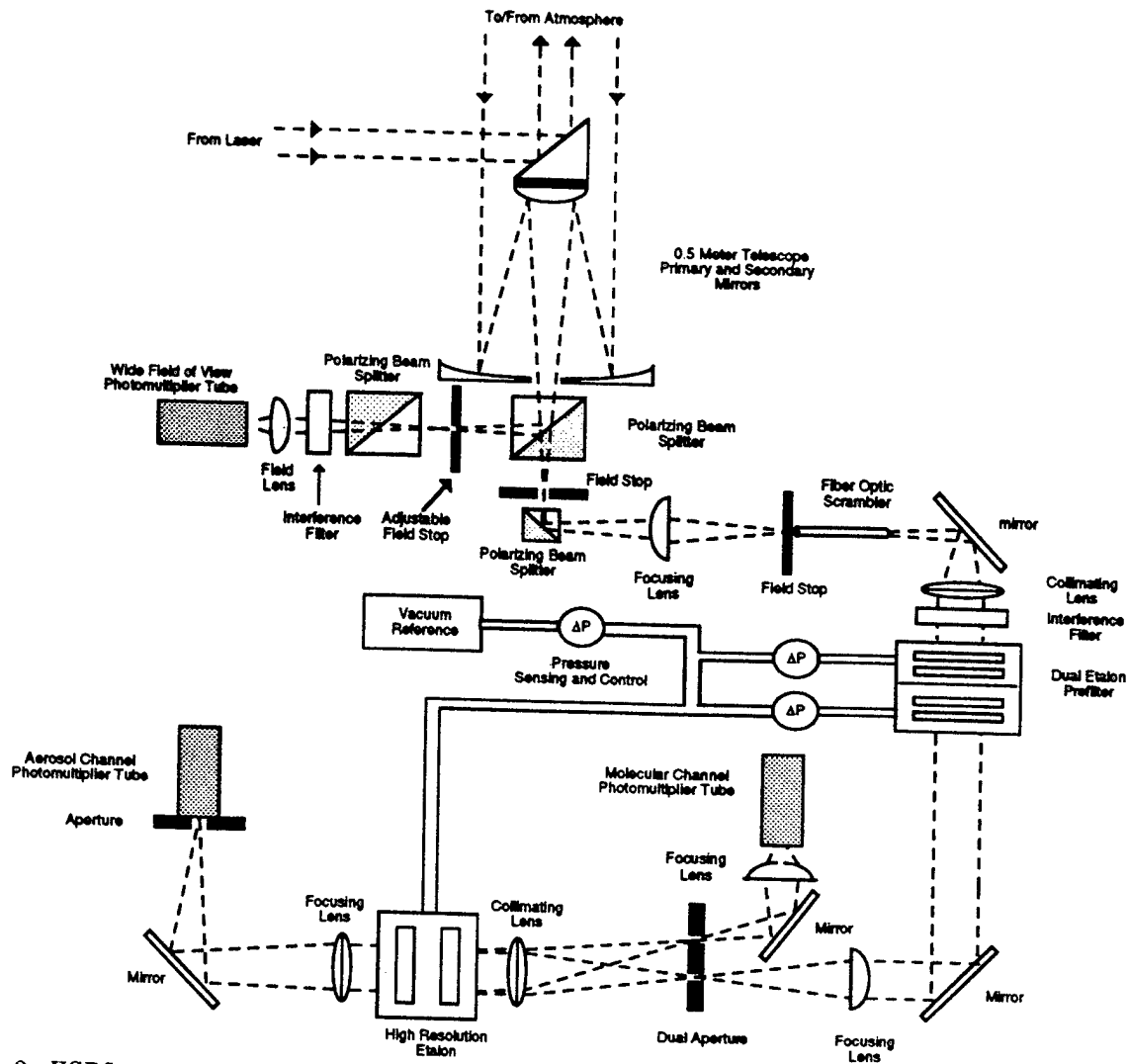


Figure 2: HSRL receiver schematic. A polarizing prism at the output of the receiving telescope separates orthogonal linear polarizations between the wide field of view channel and the spectrometer channels of the HSRL. Since the polarization of the transmitted pulse alternates between successive laser pulses each channel alternately receives parallel and perpendicular polarization components.

Backscatter Cross Section Measurements

The HSRL divides the lidar return into separate molecular and aerosol returns. The Doppler broadening of the molecular return caused by the thermal motion is used to distinguish molecular scattering from aerosol scattering. Computing the ratio of aerosol scattering to molecular scattering and computing the molecular scattering from an independently measured density profile provides calibrated aerosol backscatter cross section measurements. These differ from estimations of backscatter cross sections made with conventional single channel lidars: they do not require an assumed relationship between backscatter and extinction and they do not require an initial value of the scattering cross section. Furthermore the inversion is not subject to the numerical instabilities encountered in single channel lidar inversions.

Figure 3 shows separate aerosol and molecular lidar returns observed on Sept 30, 1992 along with calibrated backscatter cross sections derived for that case.

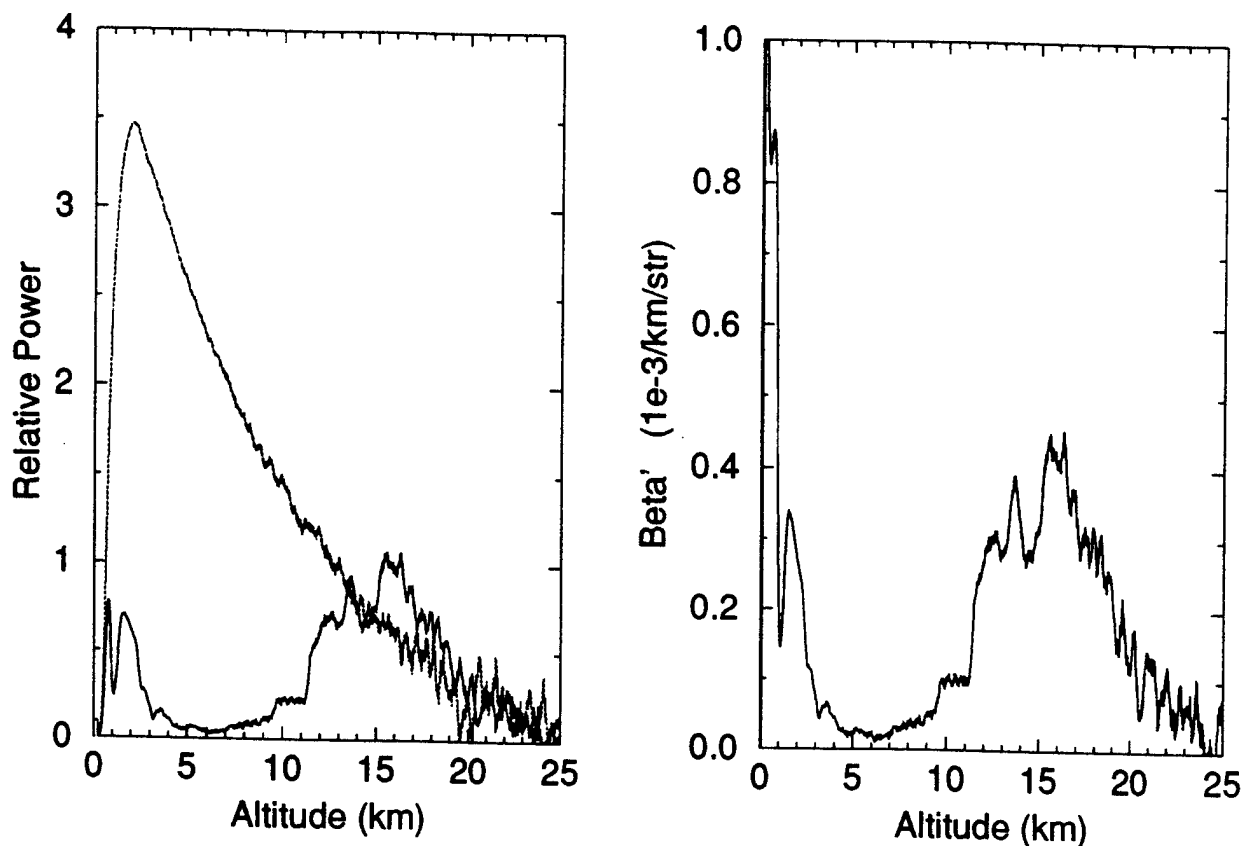


Figure 3: Separated aerosol (solid line) and molecular (dashed line) returns measured on Sept 30, 1992 are shown in the left panel. Calibrated backscatter cross sections derived from this data are shown in the right panel. Notice the strong stratospheric aerosol layer remaining from the Mt. Pinatubo eruption.

Polarization Measurements

Separate depolarization measurements can be made in both the "molecular" and "aerosol" channels of the HSRL while simultaneously observing the depolarization in the wide field of view channel. Calibrations show that the system contributes a depolarization of less than 0.1%. The molecular and aerosol channel signals can be inverted to separate aerosol and molecular depolarizations. This serves to demonstrate the accuracy of the HSRL depolarization measurements and to clearly show the depolarization due to aerosol particles.

Figure 4 shows inverted molecular depolarizations for the data presented in figure 3 along with a separate case showing ice and water cloud depolarization measurements. The right panel of figure 4 shows HSRL returns from a super-cooled water cloud (at an altitude of 5 km) and from ice crystal precipitation falling from this cloud (between altitudes of 3.3 and 4.8 km). The received signals polarized parallel and perpendicular to the transmitted polarization are shown along with the depolarization ratio. Notice that the depolarization observed in the clear air below the cloud is approximately 1% and thus very near the depolarization expected for molecular depolarization of the Cabannes line. Depolarization in the ice crystal virga is $\sim 32\%$. Also note that the water cloud depolarization is approximately 2% indicating that for this cloud the 200 microradian field-of-view of the HSRL effectively suppresses depolarization caused by multiple scattering.

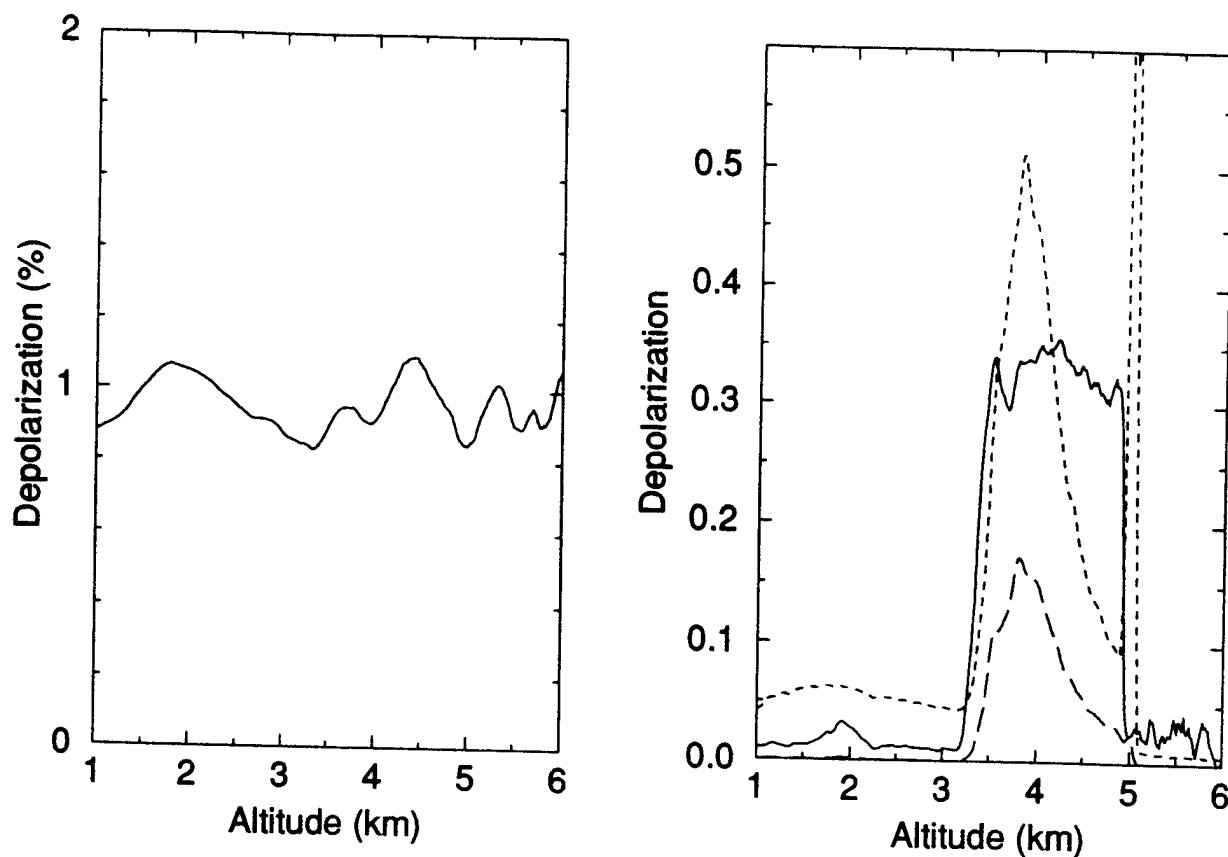


Figure 4: Depolarization measurements. The left panel shows inverted molecular depolarizations for the lidar returns presented in figure 3. Notice the small values of the depolarization; these are consistent with the depolarization expected for the Cabannes line of molecular scattering and support HSRL calibrations showing system depolarizations of less than 0.1%. The right panel shows cloud depolarizations. The un-inverted molecular returns with polarization parallel and perpendicular to the transmitted polarization are shown as short dashed and long dashed lines respectively. The depolarization is shown as a solid line.

Acknowledgements

Support for this work has been provided by Department of Energy grant DE-FG02-90ER61058 and Office of Naval Research grant N00014-91-J-1558. Support to P.K. Piironen was provided by the Foundation of Maj and Tor Nessling, and the University of Joensuu, Finland.

References:

- Grund, C.J. and E.W. Eloranta, 1991: The University of Wisconsin High Spectral Resolution Lidar, *Optical Engineering* 30, 6-12.

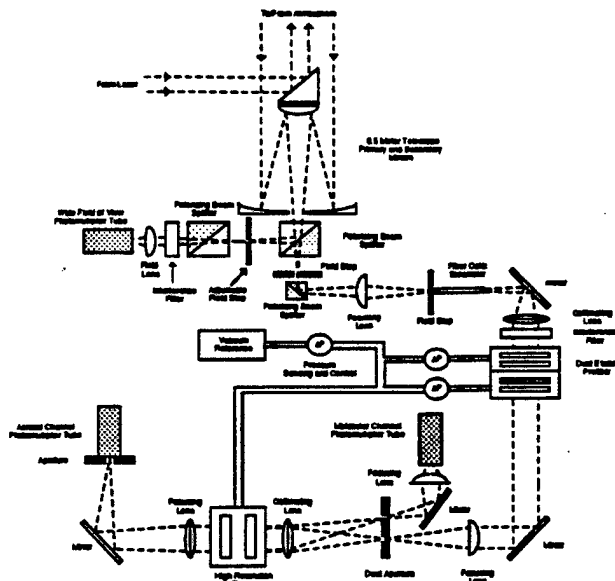


Figure 2. HSRL receiver schematic. Notice the polarizing prism at the output of the receiving telescope which alternates parallel and perpendicular polarizations between the wide-field-of-view and high resolution channels as the transmitter polarization is switched.

The depolarization measurement capability is implemented to provide extremely precise measurements. The transmitted polarization is rotated 90° between alternate laser pulses by a Pockels cell. Calibrations test show that the residual cross polarization in the transmitted beam has been reduced to $\leq 0.1\%$ of the parallel component. Separate depolarization measurements can be made in both the molecular and aerosol channels of the HSRL while simultaneously observing the depolarization in the wide field of view channel. Because both polarization components are observed with the same detector and receiver optics, no calibration is required to make accurate measurements of the depolarization ratio. Photon counting detection also provides linear detector response over a very large dynamic range. The small time separation between laser pulses (250 microsecond) insures that the both polarization components are measured from the same ensemble of scattering particles.

In order to increase the dynamic range of the HSRL we have designed new photon counting electronics to enable count rates near 1 GHz while accumulating counts in up to 8,192 100 ns range bins. These counters have thus far been tested to count rates of over 250 MHz. Full utilization

of these counters awaits the installation of phototubes providing shorter single photon pulses than the EMI model 9860 currently employed.

HSRL returns from a super-cooled water cloud (at an altitude of 5 km) and from ice crystal precipitation falling from this cloud (between 3.2 and 4.9 km) are shown in figure 3. The received signals polarized parallel and perpendicular to the transmitted polarization are shown along with the depolarization ratio. Returns from the ice crystals show characteristically large depolarizations ($\sim 33\%$) while water cloud depolarization is $\sim 2\%$. The small depolarization in the water cloud shows that 240 microradian field-of-view of the high resolution channels have suppressed multiple scattering.

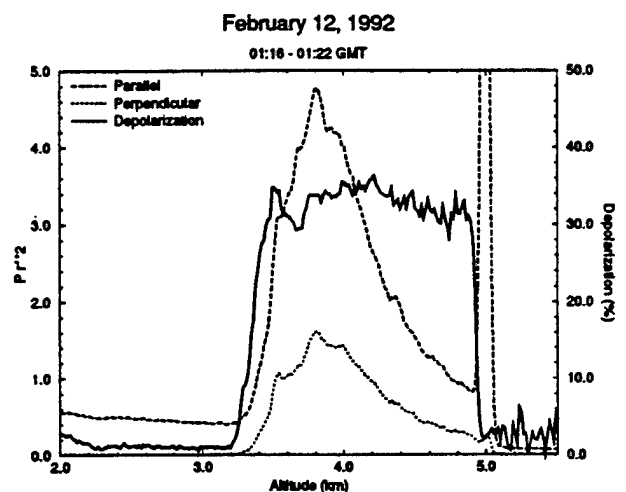


Figure 3. HSRL signals and depolarization observed from a water cloud (4.9-5.1 km) and ice-crystal virga falling from the cloud (3.2-4.9 km). Notice the high depolarization for the ice crystals and the low depolarization in the water cloud.

Observations of clear air scattering show the precision of the HSRL depolarization measurements. Figure 4 shows clear air measurements made on July 15, 1992. Notice that the depolarization is $\sim 0.8\%$ and thus very near the depolarization expected for molecular depolarization of the Cabannes line.

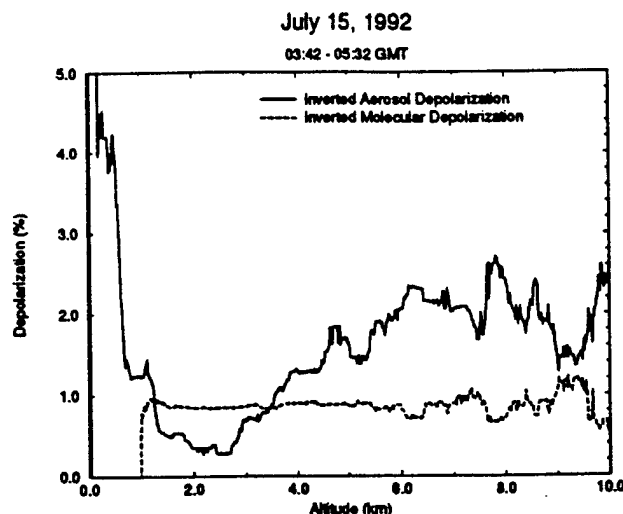


Figure 4. Depolarization of the separated molecular and aerosol lidar returns. Notice that the molecular return is constant and very close the the $\sim 0.8\%$ expected from molecular scattering.

The HSRL easily provides measurements through the stratospheric aerosol layer. Figure 5 shows separated molecular and aerosol profiles between altitudes of 2 and 26 kilometers. The Mt. Pinatubo aerosol layer is seen between altitudes of 15 and 23 kilometers. The large dynamic range of the HSRL photon counting electronics allows these profiles to be acquired over the entire altitude range without gain switching or use of high and low gain channels.

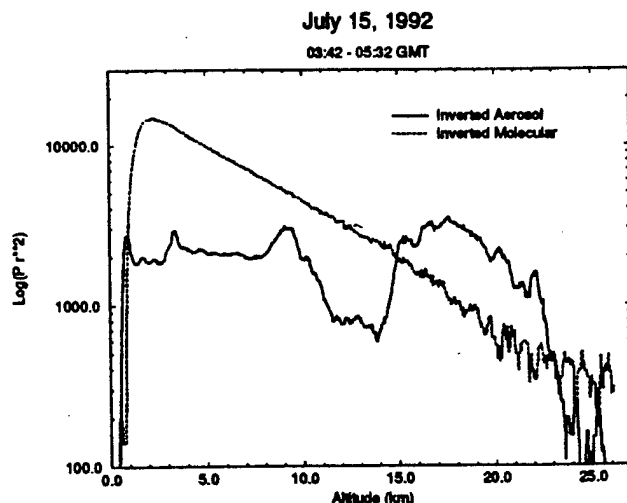


Figure 5. Separated molecular and aerosol scattering profiles showing returns from 2 km through the Mt. Pinatubo aerosol layer.

Acknowledgements

This work was supported by grants from the Dept. of Energy (DE-FG01-90ER61058), the National Aeronautics and Space Administration (NAG-1-882) and the Office of Naval Research (N00014-91-J-1558).

References

- Shipley, S.T., D.H. Tracy, E.W. Eloranta, J.T. Soga, F.L. Roeseler, and J.W. Weinman, 1983: High Spectral Resolution Lidar to Measure Optical Scattering Properties of Atmospheric Aerosols. 1: Theory and Instrumentation, *App. Optics*, 22, 3716-3724.
- Grund, C.J. and E.W. Eloranta, 1991: University of Wisconsin High Spectral Resolution Lidar, *Optical Engineering*, 30, 6-12.
- Eloranta, E.W. and S.T. Shipley, 1982: A Solution for Multiple Scattering, *Atmospheric Aerosols*, Adarsh Depeek, Ed., Spectrum Press.